

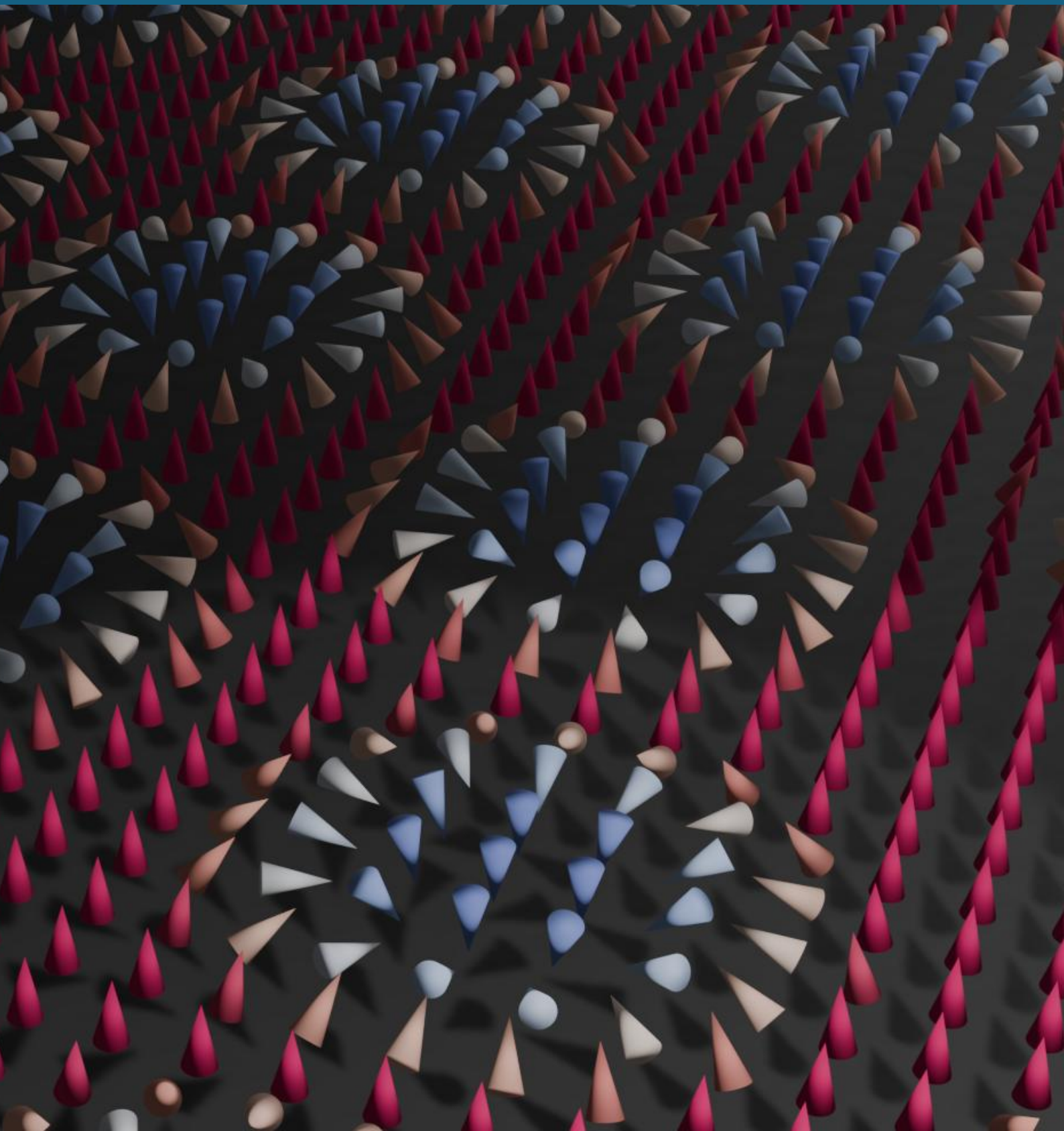
Dissertation | Raphael Gruber

JOHANNES GUTENBERG
UNIVERSITÄT MAINZ



Skyrmions in Motion

Thermal Dynamics and Ordering in 2D



Skymions in Motion – Thermal Dynamics and Ordering in 2D

JOHANNES GUTENBERG
UNIVERSITÄT MAINZ



Dissertation

zur Erlangung des Grades
"Doktor der Naturwissenschaften"
am Fachbereich Physik, Mathematik und Informatik (FB 08)
der Johannes Gutenberg-Universität Mainz

Raphael Gruber

geb. in Hof
Mainz, den 29.08.2025

Eigenständigkeitserklärung

Hiermit erkläre ich, dass ich die vorliegende Arbeit selbstständig verfasst und keine anderen als die angegebenen Quellen und Hilfsmittel benutzt habe.


Im Anhang C.3 habe ich die verwendeten KI-Tools sowie die verwendeten Prompts dokumentiert. Kollaborationen mit Kolleg:innen sind an den entsprechenden Stellen gekennzeichnet. Sämtliche wörtlichen oder sinngemäßen Übernahmen und Zitate sind kenntlich gemacht und nachgewiesen. Ich versichere, dass ich keine Hilfsmittel verwendet habe, deren Nutzung die Gutachter explizit ausgeschlossen haben.

Mit Abgabe der vorliegenden Leistung übernehme ich die Verantwortung für das eingereichte Gesamtprodukt. Die Richtigkeit übernommener Aussagen und Inhalte habe ich nach bestem Wissen und Gewissen geprüft.

Ich habe die Arbeit nicht zum Erwerb eines anderen Leistungsnachweises in gleicher oder ähnlicher Form eingereicht. Mir ist bekannt, dass ein Verstoß gegen die genannten Punkte prüfungsrechtliche Konsequenzen hat und insbesondere dazu führen kann, dass die Studien- und Prüfungsleistung als mit „nicht bestanden“ bewertet wird.

Mainz, den 29.08.2025

© Raphael Gruber, 2026

Sofern nicht anders gekennzeichnet, steht diese Dissertation unter der  **CC BY 4.0** Creative Commons Attribution 4.0 International License.

Für die in dieser Arbeit enthaltenen veröffentlichten Artikel gelten die jeweils separat angegebenen Copyright- und Lizenzbedingungen.

Datum der mündlichen Prüfung: 16.12.2025

Preface

This thesis contains the results of my PhD in the Kläui-Lab at the Johannes Gutenberg-Universität Mainz. With this thesis, I aim to document the knowledge that I gained during my PhD. In particular, I hope to provide all the information that is necessary to understand my (or *our*) work, and to be able to reproduce the findings, focussing on the equipment that I have used and that is available in the Kläui-Lab.

The main results of this thesis are already published as articles in scientific journals or as preprint on arXiv. I have experienced that those articles are often referred to in scientific discussions – both in the international community as well as within the lab. Therefore, I base my thesis on those articles and include them in the formatted version as documentation of the main results. I therefore aim to provide the framework around those articles, connecting the published main results among each other and to the progress in the related fields and groups.

The work behind the articles includes however also a lot of additional results and various experimental approaches, which are typically not specified in detail in the published articles. Moreover, I have experienced that theses are very often read in parts only and not as a whole work – in order to understand and reproduce those results and procedures, for instance from a specific article. Therefore, I include for every article an additional section entitled “Additional Results and Experimental Remarks”, where I describe the background information that I gathered within the last years. In particular, I provide the experimental details that I followed in order to realize the experiments and which I consider useful to know for future students. Also, I present additional results which are maybe only of minor importance and thus omitted in the article, but which I consider instructive when investigating the system in detail or when comparing the results to related experiments.

For the experiments and samples, I also provide links to the corresponding electronic labbook entries for maximum reproducibility. Please note that access is only possible for Kläui-Lab members. To access the entries, click the link in the pdf version of this thesis or – if reading the print version or in case links do not work – log in to the labbook and search for the specified entry ID.

And now: dive deep into 2D physics :)

Abstract



Abstract — English Version

Magnetic skyrmions are chiral magnetic spin textures of non-trivial topology, whose topological stabilization allows them to be treated as quasi-particles.

Owing to their nanoscale size and efficient means of manipulation, skyrmions have attracted considerable research interest as potential information carriers in future low-power data storage and data processing devices. However, reliable device operation requires strict conditions on performance, thermal stability, and robustness against external perturbations, which remain challenging to achieve. Consequently, exploring the static and dynamic properties of skyrmions, as well as their interactions with each other and the host material, is an ongoing and central topic of spintronics research.

A major factor limiting skyrmion dynamics is pinning, caused by material inhomogeneities that induce non-uniform magnetic properties. In this thesis, I show that skyrmions in CoFeB thin-film multilayer stacks experience a continuous two-dimensional energy landscape, leading to pronounced pinning effects. Pinning is dominated by the skyrmion boundary, implying that skyrmions cannot be fully described as point particles, but that their finite size and shape play a decisive role. Consequently, the pinning strength depends sensitively on skyrmion size. Since the skyrmion size can be tuned efficiently by magnetic field excitations, oscillating fields periodically modulate the skyrmion radius, thereby reducing effective pinning and enabling depinning. Under such conditions, the diffusion coefficient increases by up to two orders of magnitude compared to thermal diffusion without external driving. The chosen magnetic CoFeB multilayer composition stabilizes skyrmions of approximately 1 μm diameter near room temperature, allowing for direct optical imaging with Kerr microscopy. This provides unique access to the thermal dynamics of individual skyrmions and their collective behavior. Beyond their relevance for spintronic applications, such micrometer-sized skyrmions in nanometer-thin films constitute an ideal model system to study fundamental two-dimensional physics. In particular, dense skyrmion arrangements exhibit Kosterlitz-Thouless-Halperin-Nelson-Young (KTHNY) phase behavior and the corresponding phase transitions. I demonstrate that skyrmion lattices can form spontaneously in these systems, although the non-flat energy landscape prevents the emergence of true quasi-long-range order. Instead, multiple lattice domains of distinct orientation develop, separated by effectively pinned domain boundaries that impose boundary conditions on the surrounding lattice.

By confining skyrmion lattices to finite geometries, such boundary conditions can

also be imposed artificially. I show that commensurate hexagonal confinement enhances lattice order and favors uniform orientation, whereas non-commensurate geometries lead to multi-domain configurations with suppressed order. Furthermore, I show that skyrmion lattices in a solid regime with translational order can be melted into a disordered, isotropic liquid regime through an intermediate hexatic phase exhibiting only orientational order, in agreement with KTHNY theory. The melting transitions can be driven both by shrinking skyrmions, which reduces the packing fraction, and by applying oscillating fields, which enhance diffusive dynamics. Crucially, direct time-resolved imaging enables the identification and tracking of the topological defect dynamics that mediate the melting transitions – the key feature of KTHNY theory.

In summary, this thesis presents experimental studies of thermally diffusing magnetic skyrmions, revealing how they interact with the underlying magnetic energy landscape and how their diffusion can be tuned by external fields. I demonstrate how skyrmion lattices form, respond to geometric confinement, and undergo phase transitions, thereby establishing skyrmions as a unique platform for investigating two-dimensional melting and related fundamental phenomena with unprecedented resolution.



Kurzzusammenfassung — German Version

Magnetische Skyrmionen sind chirale magnetische Spinstrukturen mit Quasiteilchen-Eigenschaften. Ihre nichttriviale Topologie verleiht ihnen dabei besondere Stabilität. Aufgrund ihrer Größe im Nanometer- bis Mikrometerbereich und ihrer effizienten Manipulierbarkeit haben Skyrmionen besonders als potenzielle Informationsträger in künftigen stromsparenden Speicher und Datenverarbeitungsanwendungen das Forschungsinteresse geweckt. Für einen zuverlässigen Gerätebetrieb sind jedoch hohe Anforderungen an Leistung, thermische Stabilität und Robustheit gegenüber äußeren Einflüssen zu erfüllen – Ziele, die bislang schwer zu erreichen sind. Daher bleibt die Untersuchung statischer und dynamischer Eigenschaften von Skyrmionen sowie ihrer Wechselwirkungen untereinander und mit dem Wirtsmaterial ein zentrales Thema der Spintronik Forschung.

Ein wesentlicher Faktor, der die Skyrmionendynamik begrenzt, sind Pinningeffekte, die durch Unregelmäßigkeiten im Material hervorgerufen werden und inhomogene magnetische Eigenschaften verursachen. In dieser Arbeit zeige ich, dass Skyrmionen in dünnen CoFeB-basierten Metallschichten einer kontinuierlichen, zweidimensionalen Energielandschaft ausgesetzt sind, die Pinningeffekte verursacht. Das Pinning betrifft hauptsächlich den Rand der Skyrmionen, sodass diese nicht vollständig als Punktteilchen beschrieben werden können; stattdessen spielen ihre endliche Größe und Form eine entscheidende Rolle. Folglich hängt die Pinningstärke auch von der Skyrmionengröße ab. Da die Skyrmionengröße direkt über das magnetische Feld kontrolliert werden kann, sorgen oszillierende Felder für periodisches Ausdehnen und Schrumpfen der Skyrmionen. Die Änderung des Skyrmionenradius wiederum hilft den Skyrmionen, sich aus der Energielandschaft zu lösen und verringert so das

effektive Pinning. Dabei steigt der Diffusionskoeffizient um bis zu zwei Größenordnungen gegenüber der rein thermischen Diffusion (ohne äußere Anregung) an. Die gewählte magnetische Materialzusammensetzung ermöglicht es, Skyrmionen mit Durchmessern in der Größenordnung von $1\ \mu\text{m}$ bei Raumtemperatur zu stabilisieren, was eine direkte optische Bildgebung mittels Kerr Mikroskopie erlaubt. Dies ermöglicht einen einzigartigen Zugang zur thermischen Dynamik der einzelnen Skyrmionen sowie zu ihrem kollektiven Verhalten. Über die Relevanz für spintronische Anwendungen hinaus stellen solche mikrometer großen Skyrmionen in nanometer dünnen Filmen ein ideales Modellsystem zur Untersuchung fundamentaler zweidimensionaler Physik dar. Insbesondere dichte Skyrmionenarrangements zeigen Kosterlitz Thouless Halperin Nelson Young (KTHNY) Phasenverhalten – und die zugehörigen Phasenübergänge. Ich demonstriere hier, dass in diesen Systemen spontan Skyrmionengitter entstehen können, wobei die Energielandschaft das Auftreten echter quasi langreichweitiger Ordnung verhindert. Stattdessen entwickeln sich mehrere Gitterdomänen mit unterschiedlicher Orientierung, die durch effektiv gepinnte Domänengrenzen voneinander gepinnt werden und so die Randbedingungen für das umgebende Gitter festlegen.


Durch gezieltes Einschränken des Skyrmionengitters auf endliche Geometrien können solche Randbedingungen auch künstlich erzwungen werden. Ich zeige, dass eine kkommensurable, hexagonale Struktur die Gitterordnung verstärkt und eine einheitliche Orientierung begünstigt, während nichtkommensurable Geometrien zu Multidomänenkonfigurationen mit verminderter Ordnung führen. Schließlich demonstriere ich, wie sich ein Skyrmionengitter von einem kristallinen Regime (mit translationaler Ordnung) durch ein intermediäres hexatisches Regime (das nur orientationale Ordnung aufweist) in ein ungeordnetes, isotropes flüssiges Regime schmelzen lässt – im Einklang mit der KTHNY Theorie. Das Schmelzen kann sowohl durch Schrumpfen der Skyrmionen (Verringerung der Packungsdichte) als auch durch Anlegen oszillierender Felder (Steigerung der Diffusion) ausgelöst werden. Eine Haupterrungenschaft des Experiments ist, dass die verwendete zeitaufgelöste Videomikroskopie die Identifikation von topologischen Gitterdefekten und die Beobachtung deren Dynamik ermöglicht. Die Defektdynamik ist nämlich charakteristisch für die Schmelzvorgänge und damit das zentrale Merkmal der KTHNY Theorie.

Zusammenfassend präsentiere ich in meiner Dissertation Experimente zu thermisch diffundierenden magnetischen Skyrmionen, beschreibe ihre Wechselwirkungen mit der zugrundeliegenden magnetischen Energielandschaft und zeigt, wie ihre Diffusion durch angelegte Magnetfelder gesteuert werden kann. Ich demonstriere, wie Skyrmionengitter entstehen, auf geometrische Einschränkung reagieren und Phasenübergänge durchlaufen. Dabei etabliere ich Skyrmionen als einzigartige Plattform zur Untersuchung von zweidimensionalen Schmelzphänomenen und verwandten fundamentalen Effekten mit bisher unerreichter Auflösung.

Contents

Contents	1
Introduction	4
I. From Spins to 2D Skyrmion Lattices	6
1. Spins Forming Magnetic Structures	7
1.1. Magnetic Moments and the Micromagnetic Model	7
1.1.1. Magnetic Moments and Magnetization	7
1.1.2. Magnetic Domains and Chiral Domain Walls	7
1.1.3. Magnetic Skyrmions	8
1.2. Energy of a Magnetic System	11
1.2.1. Gibbs Free Energy	11
1.2.2. Magnetic Interactions	11
1.2.2.1. Exchange Interaction	11
1.2.2.2. Dipolar Interaction	14
1.2.2.3. Magnetic Anisotropy	16
1.2.2.4. Zeeman Interaction	17
1.2.2.5. Dzyaloshinskii-Moriya Interaction	18
1.2.3. Stabilizing Magnetic Skyrmions in CoFeB Thin Films	19
1.3. Skyrmion Dynamics	20
1.3.1. Magnetization Dynamics	20
1.3.2. Thermal Skyrmion Diffusion	21
1.3.3. Pinning Effects in a Non-Flat Energy Landscape	22
2. Phases and Phase Transitions in Two Dimensions	25
2.1. Macroscopic Theory of Phase Transitions	25
2.2. KTHNY Theory – A Microscopic Theory of 2D Phases	26
2.2.1. Topological Defects	27
2.2.2. Correlation Functions & 2-Step Melting	29
2.2.3. Defect Energies & Elasticity	31
2.3. 2D Skyrmion Lattices	35
3. Imaging Skyrmions with Kerr Microscopy	37
3.1. Magneto-Optical Kerr Effect	38
3.2. Detecting Skyrmions with Kerr Microscopy	40
3.3. Fabrication of Magnetic Thin Film Samples	43

II. Thermal Skyrmion Diffusion in a Non-Flat Energy Landscape	45
4. Skyrmion Pinning Energetics in Thin Film Systems	46
4.1. Published Article	46
4.1.1. Supplementary Information	56
4.2. Additional Results and Experimental Remarks	61
4.3. Author Contributions	61
5. 300-Times-Increased Diffusive Skyrmion Dynamics and Effective Pinning Reduction by Periodic Field Excitation	63
5.1. Published Article	63
5.1.1. Supporting Information	72
5.2. Additional Results and Experimental Remarks	82
5.2.1. Suitable System for Skyrmion Diffusion Experiments	82
5.2.2. Data Analysis for Diffusion Determination	87
5.2.3. Setup Characterization for Field Oscillations	92
5.3. Author Contributions	94
6. Conclusion – Thermal Skyrmion Diffusion in a Non-Flat Energy Landscape	95
6.1. Summary	95
6.2. Challenges	95
6.3. Outlook	97
III. Formation & Phase Behavior of 2D Skyrmion Lattices	98
7. Overview	99
8. Skyrmion Lattice Domain Formation in a Non-Flat Energy Landscape	104
8.1. Published Article	104
8.1.1. Supplementary Information	113
8.2. Additional Results and Experimental Remarks	118
8.2.1. Establishing Skyrmion Lattice Order in Experiments	118
8.2.2. Skyrmion Lattice Statistics	119
8.2.3. Related Works in Different Systems	120
8.3. Author Contributions	122
9. Skyrmion Lattice Order Controlled by Confinement Geometry	123
9.1. Published Article	123
9.1.1. Supplementary Material	130
9.2. Additional Results and Experimental Remarks	137
9.2.1. Map of Confinement Geometries	137
9.2.2. Stabilizing Skyrmions in Confinement	139
9.2.3. Treatment of Skyrmions Along the System Edge	140
9.3. Author Contributions	142

10. Real-Time Observation of Topological Defect Dynamics Mediating 2D Skyrmion Lattice Melting	143
10.1.  Published Article	143
10.1.1. Supplementary Information	157
10.2. Additional Results and Experimental Remarks	170
10.2.1. Optimizing Skyrmion Lattices for 2D Phase Observations	170
10.2.2. Analysis of 2D Phase Behavior	172
10.2.2.1. Determination of Order	172
10.2.2.2. Measuring Topological Defect Dynamics	178
10.2.2.3. Extraction of Shear and Strain	181
10.2.3. Non-Equilibrium Lattice Dynamics	184
10.3. Author Contributions	187
11. Conclusion – Formation & Phase Behavior of 2D Skyrmion Lattices	189
11.1. Summary	189
11.2. Challenges	189
11.3. Outlook	190
Back Matter	193
A. Overall Conclusion & Outlook	193
B. References	195
B.1. List of Acronyms	211
B.2. List of Figures	212
C. Appendix	214
C.1. Additional Data	214
C.2. Code Availability	217
C.3. Use of Large Language Models	218
C.4. List of Publications with my Contribution	220
C.5. Acknowledgements	222
Curriculum Vitae	223

Introduction

The increasing number of electronic and computing devices for automatization and artificial intelligence demands ever larger amounts of power. As existing techniques approach their performance limits, a new generation of data storage and processing devices must be developed.

Magnetism is already a key enabler of modern technologies [1–3]. For instance, the Giant Magneto-Resistance (GMR) [4, 5] and Tunneling Magneto-Resistance (TMR) [6–8] enabled the development of hard drives [1, 2]. Yet, magnetism can offer more. The research field of spintronics [9] investigates magnetization effects on the nanoscale, where information is carried not by electric charge, as in conventional electronics, but by magnetic states. With a strong focus on device applications, spintronics enables the design of efficient low-power architectures, particularly at the nanoscale.

Among the information carriers that have entered the focus of spintronics are magnetic skyrmions [10–12]. A skyrmion is a chiral magnetic spin texture exhibiting quasi-particle behavior with stability enhanced by its non-trivial topology. Skyrmions can be created, annihilated [13], and moved [14, 15] with high efficiency, making them promising candidates for both storage and computing architectures. Their existence in magnetic compounds further renders them compatible and integrable with CMOS technology.

The existence of magnetic skyrmions was first predicted theoretically [10, 11], and their experimental discovery was reported in 2009 in the bulk crystal MnSi – at cryogenic temperature and large magnetic fields. In the following years, skyrmions were observed in a wide range of materials and experimental conditions [14, 16–19] – including room-temperature observations in ultrathin magnetic multilayers.

A central focus of current skyrmion research is the identification of material systems that allow for efficient operation in everyday devices. Key requirements include stability at practical operating temperatures and magnetic fields, robustness against external stimuli such as magnetic field fluctuations or mechanical stress, and efficient interfaces for reading, writing, and moving skyrmions [20, 21]. Equally important is the investigation of their fundamental behavior, aiming to exploit both static and dynamic properties for future applications [22, 23]. This includes their mutual interactions, their coupling to the host material, and their response to external driving.

In this thesis, I present my research on the thermal dynamics of magnetic skyrmions. Based on Kerr microscopy experiments, I investigate both their static and dynamic properties – contributing to closing the gap in our understanding of intrinsic skyrmion behavior and paving the way toward the development of low-power skyrmionic devices. In Part I, I provide the theoretical background on magnetic

skyrmions (chapter 1), two-dimensional phase behavior (chapter 2), and the experimental methods employed (chapter 3).

In Part II, I investigate the thermal diffusion of magnetic skyrmions in thin-film systems. I analyze pinning effects in a non-flat energy landscape (chapter 4), and show how magnetic field oscillations effectively reduce pinning and enhance skyrmion diffusion (chapter 5).

In Part III, I study the formation and behavior of dense skyrmion arrangements forming two-dimensional lattices. I present results on multidomain lattice formation in a non-flat energy landscape (chapter 8) and under geometric confinement (chapter 9). Finally, I elucidate the topological defect dynamics mediating the two-step melting of a skyrmion lattice from ordered to disordered states (chapter 10).

Part I.

**From Spins to 2D Skyrmion
Lattices**

1. Spins Forming Magnetic Structures

1.1. Magnetic Moments and the Micromagnetic Model

1.1.1. Magnetic Moments and Magnetization

Both the spin and the orbital angular momentum of electrons contribute to a angular momentum called the magnetic moment μ , which are the elementary quantity of the phenomenon magnetism. Thus, magnetism is of purely quantum mechanical origin and depends on the atomic configuration of the underlying material [1].

The magnetization

$$\mathbf{M} = \sum_i \frac{\mu_i}{V_u} \quad (1.1)$$

defines the total magnetic moment per unit volume V_u . The saturation magnetization M_s is the sum of the absolute values of μ_i (in a ferromagnet), corresponding to the maximum possible magnetization when all moments are aligned. Together, we can define the reduced magnetization

$$\mathbf{m} = \frac{\mathbf{M}}{M_s} \quad (1.2)$$

as a unit vector, indicating the magnetization direction [1].

As magnetic moments are local and bound to discrete atomic positions, also the magnetization is discrete in space. However, averaging the magnetization over a mesoscopic scale allows to construct a continuous function $\mathbf{m}(\mathbf{r})$. This continuous modelling is referred to as micromagnetic approximation. Wherever appropriate, this model yields computational advantages due to the description as continuous function. The micromagnetic approximation is valid in a magnetically ordered system, where the system size is much larger than the atomic lattice distance and where structural changes in the magnetization happen on scales larger than the mesoscopic averaging [2].

1.1.2. Magnetic Domains and Chiral Domain Walls

Magnetically ordered areas, in which the magnetization is uniform apart from fluctuations, are called domains. Mostly, a ferromagnet (FM) consists of several domains [1]. The region between two domains is called a domain wall (DW). Inside the DW, the magnetization changes gradually from one to the other domain, yielding a chiral transition. Between two domains of opposite out-of-plane (OOP) magnetization as shown in Fig. 1.1, this chiral transition can happen in two distinct ways: In a Néel

DW, the magnetization rotates out of the plane of the DW; In a Bloch DW, the magnetization rotates within the plane of the DW [24].

In magnetic thin film systems with Dzyaloshinskii-Moriya interaction (DMI) – as studied in this thesis – Néel DWs are mostly favorable [2].

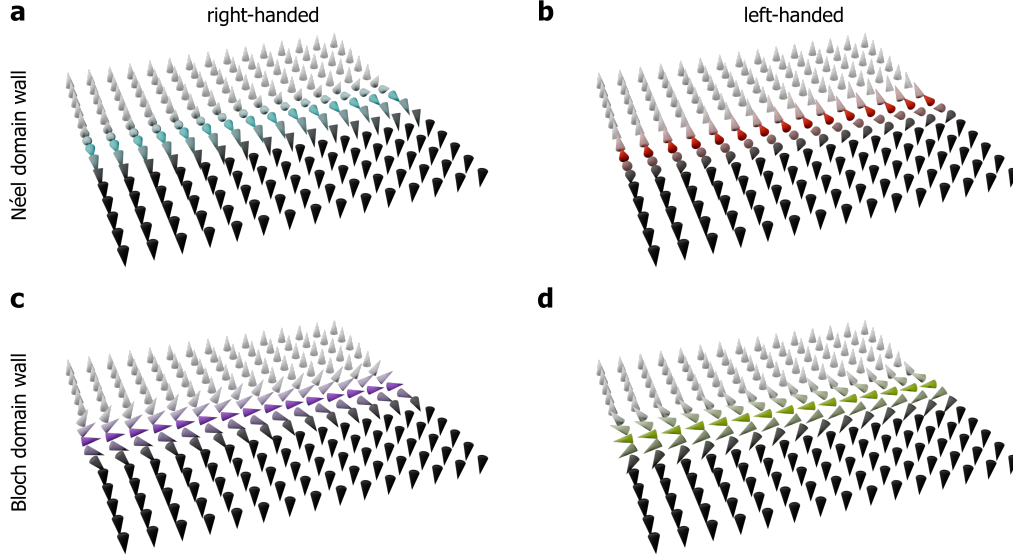


Figure 1.1.: Chiral Domain Walls between OOP Domains. (a) Right-handed Néel, (b) left-handed Néel, (c) right-handed Bloch, (d) left-handed Bloch DW. A superposition of a Bloch and Néel type DW is also possible. The color represents the in-plane (IP) direction, the (color) saturation the IP magnitude and the lightness the OOP magnitude of the magnetization (see Fig. C.1).

1.1.3. Magnetic Skyrmions

A magnetic skyrmion is a topologically protected spin texture characterized by a core domain magnetized opposite to the surrounding background, delineated by a DW exhibiting the same chirality in all radial directions. Depending on the type of DW, both Néel-type and Bloch-type skyrmions can be realized. Magnetization textures for the two types of skyrmions are shown in Fig. 1.2. The uniform chirality of the spin structure gives rise to a well-defined topological winding number [25]

$$Q = \frac{1}{4\pi M_s^3} \int d\mathbf{r} \mathbf{M} \cdot \left(\frac{d\mathbf{M}(\mathbf{r})}{dx} \times \frac{d\mathbf{M}(\mathbf{r})}{dy} \right), \quad (1.3)$$

where $Q = \pm 1$ for a skyrmion. This integer-valued quantity serves as the topological charge of the spin texture [10–12].

Topology, in the context of magnetic textures, classifies configurations based on their topological charge Q . Two states with the same Q can be transformed into one an-

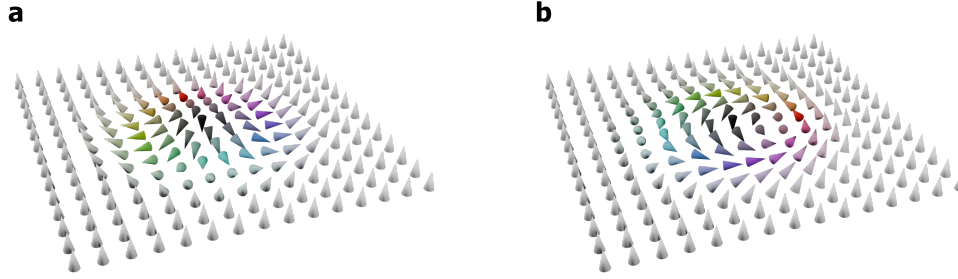


Figure 1.2.: Magnetic Skyrmions. Magnetization texture of (a) a Néel and (b) a Bloch skyrmions. The color represents the IP direction, the (color) saturation the IP magnitude and the lightness the OOP magnitude of the magnetization (see Fig. C.1).

other via continuous deformations, whereas states with different Q are topologically distinct. As a result, a skyrmion with $Q = \pm 1$ is topologically stabilized and cannot be continuously transformed into a uniformly magnetized state ($Q = 0$) [10, 26].

In the idealized micromagnetic approximation, where the magnetization is treated as a continuous field, transforming between topologically distinct states requires a discontinuity – equivalent to an infinite energy barrier. However, in real materials, magnetization is defined on a discrete atomic lattice. Thus, the energy barrier becomes finite and is determined by the energy required to flip individual spins of instance nucleating a Bloch point. While this allows for skyrmion creation or annihilation when sufficient energy is supplied (e.g., via temperature sweeps, magnetic field pulses, or thermal fluctuations), topological protection still imparts a degree of stability [11, 26].

The skyrmion’s emergent properties arise from the collective behavior of many interacting spins. As such, a skyrmion constitutes a quasi-particle – a localized, particle-like excitation of the magnetic system with a well-defined dispersion relation [10, 11, 26]. Magnetic skyrmions were first experimentally observed in the chiral magnet MnSi [12], and subsequently in other bulk materials such as $\text{Fe}_{0.5}\text{Co}_{0.5}\text{Si}$ [16] and Cu_2OSeO_3 [17]. They were later also found in magnetic thin films [14, 18, 19], where reduced dimensionality and interfacial effects give rise predominantly to Néel-type skyrmions, while Bloch-type skyrmions are more common in bulk crystals.

Skyrmions generally occur at different scales ranging from few nanometers [13] to several micrometers [19]. A change in skyrmion size can be realized by both extending the skyrmion core as shown in Fig. 1.3, or by enhancing the width of the skyrmion’s delineating DW. In the CoFeB multilayer stacks used in this thesis, the skyrmion core is typically a few micrometers in diameter, while the DW only spans tens of nanometers [19, 27]. Hence, the magnetization is mostly uniform but only transitions rapidly in a comparably narrow region.

In ultrathin films, with thicknesses down to the sub-nanometer scale, the skyrmion spin texture is approximately uniform across the film thickness, making them effectively two-dimensional quasi-particles [19]. With increasing film thickness or in bulk

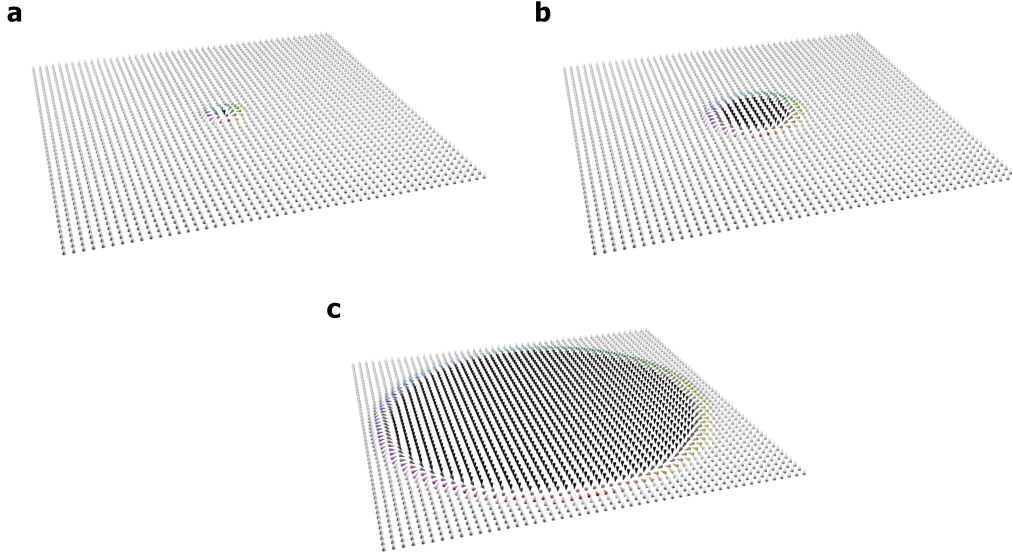


Figure 1.3.: Different Skyrmion Sizes. (a) A magnetic skyrmion consists of a core (black, downwards), which is separated from the FM background (white, upwards) by a delineating chiral DW. The color represents the IP direction, the (color) saturation the IP magnitude and the lightness the OOP magnitude of the magnetization (see Fig. C.1). In (b) the core is extended, moving the DW outwards. Here, the DW thickness stays constant and only the core area is enhanced. The topological winding number Q remains unaffected as it is only determined by the chirality of the DW by the integral over the whole compact structure. In (c), the core is further extended and represents a more extreme case where the DW width is small in comparison to the skyrmion core. This structure is often referred to as bubble skyrmion.

materials, skyrmions become inherently three-dimensional, leading to more complex internal structures. In the simplest case, a skyrmion may form a tube-like structure with constant cross-sectional spin texture across the material [28, 29]. However, even slight material inhomogeneities can cause these tubes to twist, deform, or even split, resulting in the formation of multiple skyrmions at opposite surfaces [28, 29]. Skyrmion tubes can also terminate within the material at Bloch points, giving rise to three-dimensional magnetic objects known as chiral bobbers [30]. Furthermore, in specifically engineered multilayer systems, skyrmion cocoons have been observed, wherein skyrmion tubes span the entire thickness but become significantly constricted near the surfaces [31].

1.2. Energy of a Magnetic System

1.2.1. Gibbs Free Energy

The magnetic structure in a magnetic material forms by minimization of the thermodynamic potential [3]. As commonly, the controlled experimental parameters are the externally applied magnetic field and the temperature, the Gibbs free energy

$$G(p, T) = U + p V - T S \quad (1.4)$$

with internal energy U and system volume V is adequate for describing the system. Stable states can be the global or a local minimum of G . Various interactions contribute to the Gibbs free energy and thus determine the magnetic state of a magnetic system. The most important terms relevant for the work presented in this thesis are discussed in the following section 1.2.2 [3, 32].

1.2.2. Magnetic Interactions

1.2.2.1. Exchange Interaction

Magnetic moments interact quantum-mechanically due to the Coulomb interaction and the Pauli exclusion principle. This so-called exchange interaction is particularly significant for nearest-neighbor electrons [3].

When two electrons i and j are exchanged by the permutation operator \mathcal{P}_{ij} , the anti-symmetric nature of the fermionic wavefunction implies

$$\mathcal{P}\Psi(i, j) = -\Psi(j, i), \quad (1.5)$$

while the charge density remains symmetric:

$$|\Psi(i, j)|^2 = |\Psi(j, i)|^2 \quad (1.6)$$

In general, the total wavefunction may be written as a product

$$\Psi = \phi \chi \quad (1.7)$$

where ϕ is the spatial part and χ the spin part, each depending solely on the spatial coordinates \mathbf{r} and spin coordinates \mathbf{s} , respectively [1, 33].

If the two electrons occupy a bonding orbital, the spatial wavefunction is symmetric:

$$\phi_s = \frac{\psi_i + \psi_j}{\sqrt{2}} \quad (1.8)$$

To satisfy the Pauli exclusion principle, the corresponding spin wavefunction must then be antisymmetric. This configuration corresponds to a singlet state, expressed as:

$$\Psi^{(S)}(i, j) = \phi_s(i, j) \chi_a(i, j) \quad (1.9)$$

Conversely, if the electrons occupy an antibonding orbital, the spatial part is anti-symmetric,

$$\phi_a = \frac{\psi_i - \psi_j}{\sqrt{2}} \quad (1.10)$$

requiring a symmetric spin wavefunction. This triplet state is given by:

$$\Psi^{(T)}(i, j) = \phi_a(i, j) \chi_s(i, j) \quad (1.11)$$

Both ϕ_s and ϕ_a satisfy the time-independent Schrödinger equation

$$\mathcal{H}(i, j) \Psi(i, j) = \left[-\frac{\hbar^2}{2m} (\nabla_i^2 + \nabla_j^2) + V(i) + V(j) \right] \Psi(i, j) = E \Psi(i, j) \quad (1.12)$$

where V is the Coulomb potential and m is the electron mass. Although both are solutions of the same Hamiltonian, they correspond to different eigenenergies. These energies can be computed as

$$E^{(S/T)} = \int d\mathbf{r}_1 \int d\mathbf{r}_2 \phi_{s/a}^* \mathcal{H} \phi_{s/a} \quad (1.13)$$

and the energy difference between the two states defines the exchange constant:

$$J = \frac{E^{(T)} - E^{(S)}}{2} \quad (1.14)$$

A positive exchange constant ($J > 0$) favors parallel spin alignment, leading to ferromagnet (FM) coupling, while $J < 0$ favors antiparallel alignment, corresponding to antiferromagnet (AFM) coupling. The sign and magnitude of J depend on both kinetic and Coulombic contributions [1, 2, 32].

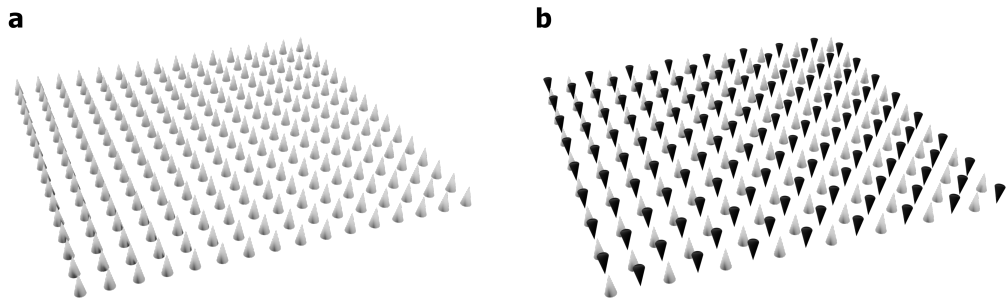


Figure 1.4.: Magnetic Exchange Coupling. (a) $J > 0$ leads to FM coupling favoring parallel spin alignment while (b) $J < 0$ favors antiparallel alignment in the AFM coupling. White and black denote spins pointing up- and downwards, respectively.

The interaction energy between two spins can be directly written as

$$E = -\frac{2J}{\hbar^2} \mathbf{s}_i \cdot \mathbf{s}_j \quad (1.15)$$

where \mathbf{s}_i denotes a (continuous) spin at site i . In many-electron systems, the Heisenberg model generalizes this interaction through an effective Hamiltonian

$$\mathcal{H}_{\text{ex}} = - \sum_{i,j} J_{ij} \mathbf{S}_i \cdot \mathbf{S}_j \quad (1.16)$$

with \mathbf{S}_i denoting the spin *operator* at site i . The factor of two is absorbed into J_{ij} , and each spin pair is only counted once [1]. If only nearest-neighbor interactions are considered, the Hamiltonian simplifies to

$$\mathcal{H}_{\text{ex}} = -J \sum_{\langle i,j \rangle} \mathbf{S}_i \cdot \mathbf{S}_j \quad (1.17)$$

where J is a constant parameter for all nearest-neighbor pairs [1, 2].

In micromagnetic theory, the discrete spins are replaced by a continuous unit magnetization vector field $\mathbf{m}(\mathbf{r})$. The ferromagnetic tendency to minimize spin misalignment is then described by an energy term penalizing spatial gradients of \mathbf{m} [2]:

$$E_{\text{ex}} = A \int_V d\mathbf{r} [(\nabla \mathbf{m}_x)^2 + (\nabla \mathbf{m}_y)^2 + (\nabla \mathbf{m}_z)^2] \quad (1.18)$$

where A is the exchange stiffness constant. In terms of microscopic parameters, A is given by

$$A = \frac{c_s J S^2}{a} \quad (1.19)$$

with lattice spacing a , spin magnitude S , and a structure-dependent factor c_s ($c_s = 1$ for simple cubic, $c_s = 2$ for body-centered cubic, $c_s = 4$ for face-centered cubic lattices) [2].

For systems lacking cubic symmetry, A becomes a second-rank tensor A_{kl} , and the exchange energy takes the generalized form [2]:

$$E_{\text{ex}} = \int_V d\mathbf{r} \sum_{ikl} A_{kl} \frac{\partial m_i}{\partial r_k} \frac{\partial m_i}{\partial r_l} \quad (1.20)$$

Because the exchange interaction strongly couples adjacent spins, it is essential for establishing magnetic order, including FM domain formation [2]. Above a critical temperature – the Curie temperature T_C – thermal fluctuations disrupt this order. A stronger exchange interaction corresponds to a higher T_C [1].

The exchange stiffness A is temperature-dependent and often modeled by the empirical relation

$$\frac{A(T)}{A(0)} = \left(\frac{M_s(T)}{M_s(0)} \right)^\nu \quad (1.21)$$

where $M_s(T)$ is the saturation magnetization at temperature T , and ν is a scaling exponent. In mean-field theory, $\nu = 2$, but empirical studies often report smaller values. For instance, in hexagonal Co, $\nu \approx 1.8$ [34].

1.2.2.2. Dipolar Interaction

Every magnetic moment generates a magnetic stray field, which interacts with surrounding magnetic moments. The energy required to sustain this stray field is commonly referred to as stray field energy or magnetostatic energy [1, 2].

The dipolar interaction energy between two magnetic moments, $\boldsymbol{\mu}_1$ and $\boldsymbol{\mu}_2$, separated by a vector \mathbf{r} , is given by

$$E_{\text{dip}} = \frac{\mu_0}{4\pi r^3} \left(\boldsymbol{\mu}_1 \cdot \boldsymbol{\mu}_2 - \frac{3(\boldsymbol{\mu}_1 \cdot \mathbf{r})(\boldsymbol{\mu}_2 \cdot \mathbf{r})}{r^2} \right), \quad (1.22)$$

which highlights the long-range and anisotropic nature of this interaction. In a many-body system, all magnetic moments are, in principle, mutually coupled via dipolar interactions. Due to their long-range character, these interactions cannot generally be neglected. While they are negligible in the limits of monolayers or infinitely large systems [2, 24], the dipolar interactions are relevant in materials as studied in this thesis [35].

The collective stray field generated outside the sample by the ensemble of magnetic moments is referred to as the stray field. From a distance, the superposition of all dipolar contributions approximates the field of a single effective dipole with the same net moment. Internally, the system also experiences a magnetic field – the demagnetizing field – which opposes the magnetization and is defined as [1]

$$\mathbf{H}_{\text{demag}} = \frac{1}{\mu_0} \mathbf{B} - \mathbf{M}. \quad (1.23)$$

In the absence of external fields and applied currents, Maxwell's equations yield

$$\nabla \times \mathbf{H}_{\text{demag}} = 0, \quad (1.24)$$

allowing us to express the demagnetizing field in terms of a scalar magnetic potential ϕ :

$$\mathbf{H}_{\text{demag}} = -\nabla \phi. \quad (1.25)$$

Additionally, applying Gauss's law for magnetism,

$$0 = \nabla \cdot \mathbf{B} = \mu_0 \nabla \cdot (\mathbf{H}_{\text{demag}} + \mathbf{M}), \quad (1.26)$$

we obtain

$$\nabla \cdot \mathbf{H}_{\text{demag}} = -\nabla \cdot \mathbf{M} = -\nabla^2 \phi, \quad (1.27)$$

which shows that the scalar potential ϕ satisfies Poisson's equation [1, 2].

The general solution of this equation is

$$\phi(\mathbf{r}) = \frac{1}{4\pi} \left(\int_V d\mathbf{r}' \frac{\rho(\mathbf{r}')}{|\mathbf{r} - \mathbf{r}'|} + \int_{\partial V} d\mathbf{r}' \frac{\sigma(\mathbf{r}')}{|\mathbf{r} - \mathbf{r}'|} \right), \quad (1.28)$$

where the volume magnetic charge density is defined as

$$\rho(\mathbf{r}) = -\nabla \cdot \mathbf{M}, \quad (1.29)$$

and the surface magnetic charge density as

$$\sigma(\mathbf{r}) = \mathbf{M}(\mathbf{r}) \cdot \mathbf{n}(\mathbf{r}), \quad (1.30)$$

with \mathbf{n} denoting the surface normal vector at the boundary ∂V [1, 2].

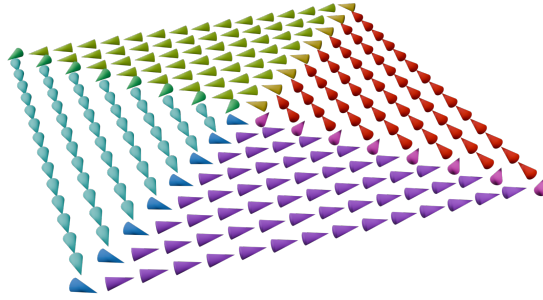


Figure 1.5.: Flux Closure State. Magnetization alignment with the edges of the system minimizes magnetic surface charges σ , while the magnetization pointing along a closed contour reduces magnetic volume charges ρ at the same time. The resulting spin structure is called a flux closure state or Landau state. The color represents the IP direction, the (color) saturation the IP magnitude and the lightness the OOP magnitude of the magnetization (see Fig. C.1)

Combining Eq. 1.25 and Eq. 1.28, the corresponding energy contribution to the Hamiltonian is

$$\mathcal{H}_{\text{dip}} = -\frac{\mu_0}{2} \int_V \mathbf{dr} \mathbf{M}(\mathbf{r}) \cdot \mathbf{H}_{\text{demag}}(\mathbf{r}) = -\frac{\mu_0}{2} \int_V \mathbf{dr} \mathbf{H}_{\text{demag}}^2(\mathbf{r}), \quad (1.31)$$

where the second equality holds in the absence of externally applied magnetic fields. As this energy is always positive, the system minimizes it by reducing both surface and volume magnetic charges, as implied by Eq. 1.28 [1, 2].

In ellipsoids with uniform magnetization, the demagnetizing field $\mathbf{H}_{\text{demag}}$ is also spatially uniform [3]. However, in general geometries, particularly non-ellipsoidal samples, dipolar interactions tend to favor non-uniform magnetization structures. In such cases, the demagnetizing field is related to the magnetization via

$$(H_{\text{demag}})_i = -N_{ij} M_j, \quad (1.32)$$

where N_{ij} are components of the demagnetization tensor $\underline{\mathbf{N}}$, which satisfies $\text{Tr}(\underline{\mathbf{N}}) = 1$ [2].

In thin films, an OOP magnetization is energetically unfavorable from the perspective of dipolar interactions, as it gives rise to large surface magnetic charges and correspondingly strong stray fields. Instead, the dipolar interaction favors an IP orientation of the magnetization. This geometry-dependent preference of the magnetization orientation is commonly referred to as shape anisotropy, [2, 24].

1.2.2.3. Magnetic Anisotropy

Magnetic anisotropies lead to a preferred alignment of magnetization with specific axes or planes [1, 2, 24].

The magnetocrystalline anisotropy causes such preferred alignment with crystallographic symmetry axes. The total energy of the overall electron wavefunction depends on the overlap of the constituting orbitals. If the atomic wavefunctions are anisotropic and cause non-spherical orbitals, the alignment of the orbitals is crucial to minimize the overlap and thus energy [24, 32]. The alignment of the orbitals is however coupled to the spin alignment via spin-orbit coupling (SOC). Thus, the magnetization favors alignment such that the orbital overlap is optimized. The magnetocrystalline anisotropy can favor spin alignment along various axes and planes, depending on the crystal symmetry and orbital shape [1, 2]. In the case of a uniaxial magnetocrystalline anisotropy, alignment along one crystallographic axis is preferred – e.g., the z -axis. It contributes to the free energy as

$$E_{\text{ani}}^{\text{uni}} = - \int dV K_1 \frac{M_z^2}{M_s^2} + \mathcal{O}(M_z^4) \quad (1.33)$$

with a positive anisotropy constant K_1 . The omitted higher-order terms are all of even power: due to the crystal symmetry, only the alignment with an axis is favorable, independent of the magnetization direction. The z -axis is therefore called an easy axis. If $K_1 < 0$, magnetization alignment along the z -axis is unfavorable and the system thus exhibits an easy-plane anisotropy for the xy -plane, while the z -axis becomes a so-called hard axis [2].

Besides the crystalline structure of a material itself, also interfaces with other materials can induce a similar magnetic anisotropy, the so-called interface anisotropy. The corresponding energy term

$$E_{\text{ani}}^{\text{i-uni}} = - \int dV \frac{K_i}{d} \frac{M_z^2}{M_s^2} + \mathcal{O}(M_z^4) \quad (1.34)$$

with an anisotropy constant K_i and depending on the layer thickness d of the ferromagnetic material. The anisotropy is commonly expressed by the uniaxial interfacial isotropy constant $K_u = \frac{K_i}{d}$. Such interfacial uniaxial anisotropy can arise in ferromagnetic films at interfaces with oxides (such as CoFeB/MgO) due to hybridization of the $3d$ orbitals d_{x^2} , d_{xz} and d_{yz} with the p_z orbital of oxygen [36–39]; or at the interfaces with heavy metals like due to hybridization of the $3d$ and the $5d$ orbitals of Co and Pt, respectively [40].

Interfacial uniaxial anisotropy is a key ingredient in magnetic thin film systems since it enables perpendicular magnetic anisotropy (PMA) and thus OOP magnetization in thin films, even though the dipolar interaction would favor in-plane magnetization, what is referred to as shape anisotropy. Since in polycrystalline films as studied in this thesis, there is no net IP magnetocrystalline anisotropy, the effective anisotropy

$$K_{\text{eff}} = K_u - K_s = \frac{K_i}{d} - \frac{1}{2} \mu_0 M_s^2 \quad (1.35)$$

is a trade-off of the shape anisotropy K_s and the interfacial uniaxial anisotropy. Consequently, positive values of K_{eff} lead to PMA while IP magnetization is favored for negative values [41].

Besides the magnetic layer thickness d , also the temperature T is a crucial factor deciding on the anisotropy constants K_i and K_1 . Both follow a temperature dependence

$$\left(\frac{K(T)}{K(T=0)} \right) = \left(\frac{M_s(T)}{M_s(T=0)} \right)^c \quad (1.36)$$

with a material-dependent scaling exponent c ($c=2$ in mean-field approximation) [42–44]. The transition point in d or T , where the system flips from preferring OOP magnetization to preferring IP alignment is called the spin reorientation transition (SRT) [2, 41]. Due to the strong temperature dependence of the anisotropy, also the SRT is changing strongly with T [42–44].

Additional to the crystal structure (magnetocrystalline anisotropy), also crystal deformations affect the overlap of orbitals. Therefore, an induced strain can control the preferred orientation and induce a magnetoelastic anisotropy [2].

1.2.2.4. Zeeman Interaction

Magnetic moments interact with externally applied magnetic fields \mathbf{B}_{ext} . Thereby, the associated energy

$$E_Z = -\boldsymbol{\mu} \cdot \mathbf{B}_{\text{ext}} \quad (1.37)$$

for every magnetic moment $\boldsymbol{\mu}$ is minimized, when it aligns with \mathbf{B}_{ext} [3, 32].

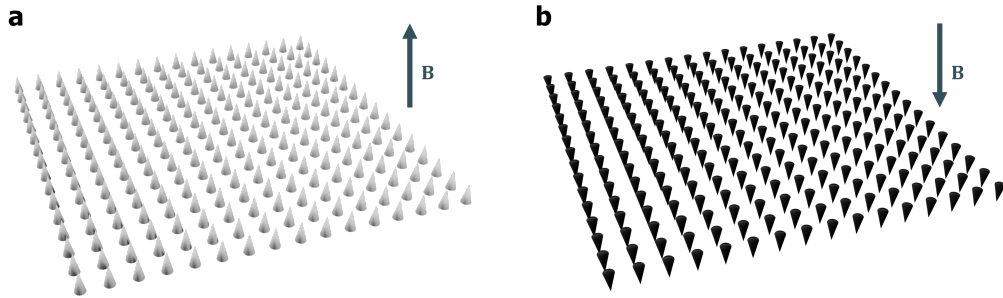


Figure 1.6.: Magnetization Alignment with External Field. The magnetization follows the externally applied magnetic field \mathbf{B} , for instance to point (a) upwards or (b) downwards.

The corresponding energy of a many-particle system contains simply the sum over all moments. Considering the magnetization as a continuous function in the micromagnetic approximation, the sum turns into an integral over the whole system volume V and yields a contribution

$$\mathcal{E}_Z = - \int_V d\mathbf{r} \mathbf{M}(\mathbf{r}) \cdot \mathbf{B}_{\text{ext}} \quad (1.38)$$

to the energy of the system [2].

When flipping the magnetization from pointing upwards to downwards by reorientation of \mathbf{B} , the magnetization exhibits hysteresis. The dependence of the net magnetization on the magnetic field is thereby governed by all the present interactions and their magnitudes [24].

1.2.2.5. Dzyaloshinskii-Moriya Interaction

In systems with broken inversion symmetry, an antisymmetric exchange interaction arises, commonly referred to as Dzyaloshinskii-Moriya interaction (DMI) [45, 46]. In contrast to the symmetric exchange interaction described in section 1.2.2.1, DMI favors canting of neighboring spins. The interaction arises due to SOC leading to a Hamiltonian

$$\mathcal{H}_{\text{DMI}} = \mathbf{D}_{ij} \cdot (\mathbf{S}_i \times \mathbf{S}_j) \quad (1.39)$$

coupling neighboring spins \mathbf{S}_i and \mathbf{S}_j . Thereby, the DMI vector \mathbf{D}_{ij} determines a preferred direction of the canting and therefore leads not only to spin canting, but also to a preferred handedness, being the basis for chiral spin structures, such as chiral DW and skyrmions. The strength of the DMI is primarily set by the SOC strength of the involved atoms, whereas the direction follows from the symmetry of the system [1, 2, 24].

DMI can arise as a bulk effect in non-centrosymmetric compounds. The broken inversion symmetry is necessary, as the Hamiltonian has to reflect the system symmetry: For systems with inversion symmetry, we obtain $\mathbf{D}_{ij} = \mathbf{D}_{ji}$ for symmetry reasons, while Eq. 1.39 generally yields $\mathbf{D}_{ij} = -\mathbf{D}_{ji}$ (because of the cross product) – consequently, $\mathbf{D}_{ij} = \mathbf{D}_{ji} = 0$ for inversion-symmetric materials. An example of a bulk material with finite DMI are the B20 compounds MnSi [12, 47], Fe_{0.5}Co_{0.5}Si [17] and FeGe [18].

Similarly, also material interfaces cause broken inversion symmetry. In that case, the SOC of the layer adjacent to the ferromagnet determines the DMI strength. Therefore, especially interfaces of ferromagnets with heavy metals (which have large SOC) yield sizable DMI. For an interface in the z -plane, the interfacial DMI (iDMI) vector takes the form $\mathbf{D}_{ij} = \frac{d}{|\mathbf{r}_{ij}|} \mathbf{r}_{ij} \times \mathbf{e}_z$ where \mathbf{r}_{ij} is the connecting vector of two atoms in the FM layer and d determines strength and direction of the vector [48]. Using the micromagnetic description, the iDMI yields a contribution

$$E_{\text{DMI}} = \frac{D}{M_s^2} \int dV M_z(\mathbf{r}) \nabla \mathbf{M}(\mathbf{r}) - \mathbf{M}(\mathbf{r}) \nabla M_z(\mathbf{r}) \quad (1.40)$$

to the energy of the system. Thereby, D is the DMI constant, which can be expressed by the DMI strength d , the film thickness t and the atomic lattice constant a as $D \propto \frac{d}{at}$. As the iDMI is an interface effect, it is effectively suppressed for increasing layer thickness t of the ferromagnet and therefore especially relevant for magnetic thin

films [25]. The sign of D – and thus, the preferred chirality of spin canting – is determined by the stacked materials and the stacking order [49].

The DMI exhibits a similar temperature dependence as the (symmetric) exchange interaction A [50]. Therefore, the periodicity of spin spirals $\lambda \propto \frac{A}{D}$ remains often effectively independent of temperature [50].

1.2.3. Stabilizing Magnetic Skyrmions in CoFeB Thin Films

The interactions present in a magnetic system, along with their respective magnitudes, determine its equilibrium state. The interactions discussed in section 1.2.2 permit the existence of skyrmions in the Ta/CoFeB/Ta/MgO/Ta thin film multilayer stacks used in this thesis. In addition to the exchange interaction, which underpins the FM order, the interplay between PMA and the DMI is crucial. Achieving a suitable balance between PMA and DMI poses a central challenge in sample fabrication. Moreover, the dipolar interaction plays a non-negligible role in shaping the magnetization texture and its stability [35].

Skyrmions may exist either as metastable states or as ground states. In both cases, the experimental parameters, particularly the temperature T and the applied magnetic field B , must support the existence of skyrmions as local or global energy minima. Under appropriate conditions, skyrmions can emerge spontaneously [11, 51]. However, in many cases, transitioning from an arbitrary initial state to a skyrmionic configuration requires surmounting an energy barrier to establish the characteristic topological structure [14, 19].

A variety of methods have been developed to induce skyrmion formation across different material systems. Energy input can be provided, for instance, via local heating from laser pulses or electrical currents [52–54]. Alternatively, local magnetic fields [55–57] or electric fields [19, 58, 59] can be used to write or delete individual skyrmions. Additionally, spin-orbit torques arising from electrical currents can induce the formation of skyrmions [13, 60]. Local material inhomogeneities, where magnetic parameters are spatially modified (see section 1.3.3), can further facilitate the spontaneous or externally stimulated nucleation of skyrmions [61, 62].

In this thesis, an alternative and well-established method is employed to generate skyrmions in CoFeB-based multilayer stacks [19, 63, 64]. The sample is first brought into a parameter regime where skyrmions are energetically stable by adjusting T and B . Subsequently, a strong IP magnetic field is applied to rotate the magnetization into the film plane [19]. Full saturation of the magnetization IP is not necessary; rather, the field must be sufficiently strong to transiently suppress the PMA. Rapid removal of the IP field then allows the PMA to reassert itself, leading to the formation of OOP magnetic domains. Provided the system is not trapped in a competing OOP configuration, this procedure enables the random nucleation of skyrmions distributed across the sample. Notably, the magnitude of the applied IP field pulse provides control over the number and density of generated skyrmions.

1.3. Skyrmion Dynamics

1.3.1. Magnetization Dynamics

The energy contributions in a magnetic system determine the equilibrium magnetization state at $T = 0$ K and form the basis for deriving the effective magnetic field

$$\mathbf{H}_{\text{eff}} = -\frac{1}{\mu_0} \frac{\delta E[\mathbf{M}]}{\delta \mathbf{M}} \quad (1.41)$$

defined via the functional derivative of the total energy functional $E[\mathbf{M}]$ with respect to the magnetization \mathbf{M} in the continuum limit.

This effective field exerts a torque

$$\boldsymbol{\tau} = \mu_0 \mathbf{M} \times \mathbf{H}_{\text{eff}} = -\frac{1}{\gamma} \frac{d\mathbf{M}}{dt} = \frac{d\mathbf{L}}{dt} \quad (1.42)$$

on the magnetization, which can be interpreted as the rate of change of the angular momentum \mathbf{L} associated with the magnetization, according to Newton's second law. Here, $\gamma = \frac{g e}{2 m_e}$ is the gyromagnetic ratio, with g the Landé g-factor, e the elementary charge, and m_e the electron mass [1, 2].

The resulting time evolution of the magnetization under the influence of \mathbf{H}_{eff} is governed by

$$\frac{d\mathbf{M}}{dt} = -\mu_0 \gamma \mathbf{M} \times \mathbf{H}_{\text{eff}}, \quad (1.43)$$

which describes the precession of the magnetic moments around the effective field. However, this precession alone conserves the total energy and therefore cannot drive the system toward its equilibrium state. To account for relaxation, Landau and Lifshitz introduced a phenomenological damping term, yielding the Landau-Lifshitz (LL) equation:

$$\frac{d\mathbf{M}}{dt} = -\mu_0 \gamma \mathbf{M} \times \mathbf{H}_{\text{eff}} - \frac{\lambda}{M_s} \mathbf{M} \times (\mathbf{M} \times \mathbf{H}_{\text{eff}}), \quad (1.44)$$

where λ is a damping constant and M_s denotes the saturation magnetization. The damping term allows the magnetization to relax towards alignment with the local effective field [2].

Using a Lagrangian formulation, Gilbert later derived an alternative expression for the dynamics – the implicit Landau-Lifshitz-Gilbert (LLG) equation

$$\frac{d\mathbf{M}}{dt} = -\mu_0 \gamma \mathbf{M} \times \mathbf{H}_{\text{eff}} - \frac{\alpha}{M_s} \mathbf{M} \times \frac{d\mathbf{M}}{dt} \quad (1.45)$$

where α is the Gilbert damping factor. In the limit of small α , the LL and LLG equations become equivalent [65].

In addition to field-induced dynamics, thermal fluctuations at finite temperatures introduce stochastic variations in the magnetization. These fluctuations can be

modeled as thermal white noise and enter the system according to the fluctuation-dissipation theorem. While the average temperature $\langle T \rangle$ remains constant in the canonical ensemble, the instantaneous temperature undergoes random fluctuations. Because this thermal noise affects the system's energy – like the damping – it plays a critical role in enabling the system to reach equilibrium.

The LLG equation can be used to simulate the magnetization dynamics of various magnetic structures. Software packages such as *mumax* [66] solve these equations numerically by computing \mathbf{H}_{eff} at each step. However, for complex spin textures or large-scale systems, such simulations can become computationally intensive – or even infeasible – due to memory and time constraints [67].

1.3.2. Thermal Skyrmion Diffusion

Thermal spin fluctuations at finite temperature can induce motion of skyrmions as collective spin configurations stabilized by their topological properties. Since temperature introduces thermal white noise into the system, this motion manifests as random diffusion [19].

The dynamics of a quasi-particle skyrmion – treated as a rigid steady-state spin texture i with velocity \mathbf{v}_i – can be described by the Thiele equation [68–71]

$$\tilde{\gamma}\mathbf{v}_i - G\mathbf{e}_z \times \mathbf{v}_i = \sum_j \mathbf{F}_{\text{sk}}(\mathbf{r}_i - \mathbf{r}_j) + \mathbf{F}_{\text{ext}} + \mathbf{F}_{\text{th}} \quad (1.46)$$

with phenomenological forces \mathbf{F} in a dynamical force equation. Here, $\tilde{\gamma}$ denotes the effective damping constant, and G is the gyrocoupling constant. I use the notation $\tilde{\gamma}$ to avoid confusion with the gyromagnetic ratio (γ) introduced in Eq. 1.43. The term $G\mathbf{e}_z \times \mathbf{v}_i$ represents the Magnus force acting on the skyrmion [69]. The right-hand side of Eq. 1.46 includes the sum of interaction forces from surrounding skyrmions j , \mathbf{F}_{sk} , additional external forces \mathbf{F}_{ext} such as drive fields, and the stochastic thermal contribution \mathbf{F}_{th} [70, 71].

The Thiele equation as presented in Eq. 1.46 is specifically adapted to magnetic skyrmions, which are well-approximated as point-like particles due to their compact, rotationally symmetric structure and topological stability [70, 71]. The effective damping is given by $\tilde{\gamma} = \frac{1}{2}\alpha \text{Tr}(\underline{\mathcal{D}})$ and is derived from the dissipation tensor $\underline{\mathcal{D}}$, with components

$$\mathcal{D}_{ij} = \frac{M_s}{\tilde{\gamma}d} \int d\mathbf{r} \left(\frac{\partial \mathbf{m}}{\partial r_i} \cdot \frac{\partial \mathbf{m}}{\partial r_j} \right) \quad (1.47)$$

as determined by the magnetization texture $\mathbf{m}(\mathbf{r})$. This texture also defines the gyrocoupling tensor $\underline{\mathcal{G}}$ [68, 72], with components

$$\mathcal{G}_{ij} = \frac{M_s}{\tilde{\gamma}d} \int d\mathbf{r} \mathbf{m} \cdot \left(\frac{\partial \mathbf{m}}{\partial r_i} \times \frac{\partial \mathbf{m}}{\partial r_j} \right) \quad (1.48)$$

In the case of a skyrmion in the xy -plane, this yields a scalar gyrocoupling

$$G = \mathcal{G}_{xy} = \frac{M_s}{\tilde{\gamma}d} 4\pi Q \quad (1.49)$$

with Q denoting the winding number (see Eq. 1.3) [72].

The Thiele equation describes overdamped dynamics without inertia and corresponds to Brownian motion. From this, the diffusion coefficient

$$D = k_B T \frac{\tilde{\gamma}^2}{\tilde{\gamma}^2 + G^2} \quad (1.50)$$

can be derived for a rotationally symmetric skyrmion [72].

In Brownian dynamics, the mean squared displacement (MSD)

$$\text{MSD}(t) = \langle [\mathbf{r}(t) - \mathbf{r}(0)]^2 \rangle = 2dDt \quad (1.51)$$

is linear in time t , with d denoting the dimensionality of the system. This relation enables experimental extraction of the diffusion coefficient D through direct tracking of skyrmion trajectories and fitting according to Eq. 1.51 [19].

As seen in Eq. 1.46, a critical contribution to skyrmion dynamics is the skyrmion-skyrmion interaction potential $U_{\text{sk}}(r)$. While in general such interactions may exhibit both attractive and repulsive components [73–75], the skyrmions in the CoFeB multi-layer stacks used in this thesis experience a purely repulsive interaction [70, 71] from other skyrmions. Yuqing Ge and Jan Rothörl [70] applied real-space imaging in combination with the iterative Boltzmann inversion (IBI) method to experimentally determine this skyrmion-skyrmion interaction potential. The data can be well described by either an exponential decay or a power-law potential of the form $U_{\text{sk}}(r) \propto r^{-n}$, with an exponent $n \approx 8$, depending on the specific system and configuration.

Together, the Thiele equation and the experimentally determined skyrmion interaction potential $U_{\text{sk}}(r)$ provide a robust foundation for modeling experimental systems using Brownian dynamics simulations. This is typically implemented via molecular dynamics frameworks and enables quantitative analysis of skyrmion behavior at finite temperature [70, 71].

1.3.3. Pinning Effects in a Non-Flat Energy Landscape

Local inhomogeneities in magnetic materials give rise to spatial variations in the energy landscape experienced by spin textures. These inhomogeneities may stem from lattice defects, impurities, doping, grain boundaries or general variations in crystallinity within the bulk of a crystal. Additionally, structural features such as interfacial roughness or variations in layer thickness can induce such energetic modulations. Depending on the specific origin and nature of the inhomogeneity, various magnetic parameters – such as the exchange stiffness, magnetic anisotropy, or DMI – can be locally affected. The resulting non-uniform energy landscape creates energetically favorable and unfavorable regions for magnetic spin structures [23].

Magnetic skyrmions, which consist of a topologically protected core and a surrounding delineating DW, are particularly susceptible to such energy variations. The phenomenon in which a skyrmion preferentially resides at specific spatial locations is referred to as a pinning effect. These pinning forces may be attractive, repulsive, or a

combination of both, depending on the interaction mechanisms and material parameters involved. While numerous theoretical models have been proposed to explain skyrmion pinning, experimental verification remains a topic of ongoing research [23]. First-principles calculations for PdFe bilayers on an Ir substrate have shown that the presence of atomic impurities – either embedded within or deposited atop the surface layer – can lead to attractive potentials, or to a mixed interaction characterized by long-range attraction and short-range repulsion [76]. Related studies have investigated the influence of adatoms arranged in specific geometries, such as dimers and trimers, revealing that the resulting skyrmion interaction can be tuned to be either repulsive, attractive, or hybrid in nature [77].

Substitutional defects, in which host atoms are replaced by foreign atoms, have also been studied using density functional theory. These substitutions have been shown to yield either attractive or repulsive potentials for skyrmions, depending on the specific element used [78]. Similarly, the absence of atoms (i.e., vacancies) has been modeled using micromagnetic simulations and effective quasi-particle equations of motion. These models predict short-range attractive and long-range repulsive interactions for skyrmions in the presence of spin vacancies [79].

Analytical models have further demonstrated that spatial modulations of the strength of the DMI and the perpendicular magnetic anisotropy (PMA) can give rise to complex pinning forces exhibiting both attractive and repulsive components [80]. Micromagnetic simulations have confirmed such pinning effects for modulated anisotropy landscapes [81], and similar effects have been reported for modulations in the exchange stiffness due to local variations in electron density [82, 83].

Experimental observations in ultrathin films have revealed that pinning is often dominated not by single-atom impurities but rather by grain boundaries within the polycrystalline film structure [14]. Subsequent simulations have shown that increasing the grain size can reduce the pinning strength [60].

In CoFeB-based thin film multilayers, the energy scale of pinning sites can be comparable to thermal excitation energies at room temperature. Under such conditions, skyrmions may overcome pinning barriers via thermal activation and exhibit stochastic motion. Experimental studies have observed this behavior as Brownian-like diffusion, which is not purely isotropic but modulated by the underlying energy landscape. This results in a hopping-like diffusion process, which has been leveraged for novel computing approaches. For instance, thermally driven skyrmion motion has been utilized as a passive reshuffling mechanism in bit stream decorrelation, and as an automatic reset function in non-conventional computing architectures, such as Boolean logic gates [84] and gesture recognition systems [85]. Moreover, controlled diffusion can serve as a transport mechanism in token-based computing [86].

In general, pinning effects lead to anisotropic and non-linear skyrmion dynamics, often requiring external driving forces for depinning. This can impair the reliability of skyrmion-based data storage or processing devices. However, pinning can also be harnessed beneficially – for instance, as an intrinsic reset mechanism in computing [84, 85], or to enable guided skyrmion motion along predefined tracks [87, 88].

To enable such guided motion, the energy landscape of a material can be artificially

1. Spins Forming Magnetic Structures

tailored. Focused ion beam irradiation has been employed to irreversibly modify magnetic parameters and thereby control skyrmion pinning sites and allow guided skyrmion motion [88]. Similarly, recent studies have demonstrated the feasibility of using optical laser writing to effectively tune the local energy landscape [89].

2. Phases and Phase Transitions in Two Dimensions

2.1. Macroscopic Theory of Phase Transitions

According to the second law of thermodynamics, a system tends to evolve toward a state of minimal free energy. This principle governs a wide range of physical phenomena, including spin ordering (see section 1.2), atomic arrangements in solids, and the configuration of quasi-particles such as skyrmions. At constant temperature, the relevant thermodynamic potential is the Helmholtz free energy, defined as $F = U - TS$. Minimization of F can occur through two distinct mechanisms: by decreasing the internal energy U , or by increasing the entropy S [3, 32, 90].

The equilibrium state thus represents a compromise between energetic stability and entropic disorder. A reduction in internal energy generally promotes order, favoring low-temperature phases that exhibit reduced – often discrete – symmetry. At higher temperatures, however, entropy becomes the dominant term, favoring disordered phases with increased symmetry. A familiar example is the water–ice transition: in its solid phase, ice adopts a hexagonal lattice with discrete translational and rotational symmetries. In contrast, liquid water exhibits macroscopic isotropy, due to the random distribution of molecules. An analogous situation arises in spin systems such as a FM: above the Curie temperature T_C , the system resides in a disordered, paramagnetic phase with full rotational symmetry. Below T_C , spontaneous magnetization breaks this symmetry, yielding an ordered ferromagnetic phase [1, 3, 91].

In general, two classes of phase transitions are distinguished. First-order transitions are characterized by latent heat – a finite, often large energy difference between the two phases at the transition temperature. During such a transition, both phases coexist while latent heat is exchanged, until the transformation is complete. In contrast, second-order (or continuous) phase transitions proceed without latent heat. These are marked by a diverging correlation length and the emergence of an order parameter, which is zero in the disordered phase and finite in the ordered phase. A canonical example is the FM-to-paramagnet transition: in the ferromagnetic phase, the magnetization is finite and decreases continuously with increasing temperature. At T_C , the magnetization vanishes, and the system becomes disordered. At this critical point, the magnetic susceptibility diverges, reflecting the long-range correlations that emerge in the system [3, 91].

The phase behavior of a system is governed by external parameters such as temperature, pressure, and density. Changes in these variables affect macroscopic response functions – such as magnetic susceptibility or elastic moduli – which often exhibit

discontinuities or singular behavior at phase transitions [91]. On macroscopic scales, these properties depend on the nature of interparticle interactions, spatial order, and thermal energy. Microscopically, transitions from ordered to disordered phases are accompanied by increased lattice defects, vibrational entropy, and excitation of dynamical modes. These modes are intimately linked to phase behavior: for example, in a liquid, sound waves are purely longitudinal, as the absence of long-range order precludes support for shear stresses [90–92].

Despite extensive study, the microscopic mechanisms driving many phase transitions remain only partially understood [92]. Analytical solutions to the equations of state for three-dimensional (3D) interacting systems remain inaccessible, and theoretical treatment often relies on phenomenological models. Near criticality, such models suggest that microscopic details are largely irrelevant to macroscopic behavior – a concept formalized by the theory of universality [91, 92].

In two-dimensional (2D) systems, the situation is markedly different. A key distinction arises from the role of long-wavelength fluctuations. While such fluctuations are energetically suppressed in infinite 3D systems, they become thermally accessible in 2D. According to the Mermin–Wagner theorem [93, 94], these fluctuations prohibit the existence of true long-range positional order in 2D crystals: lattice displacements diverge with system size. As a result, only quasi-long-range order (QLRO) is possible. In such systems, discrete rotational symmetries remain intact, but the Bragg peaks in the structure factor are broadened, reflecting algebraic rather than exponential decay of correlations [95–98].

2.2. KTHNY Theory – A Microscopic Theory of 2D Phases

A microscopic theory of 2D phases and phase transitions was developed by Kosterlitz, Thouless, Halperin, Nelson and Young (KTHNY theory) [95, 97–99]. Their description is based on the emergence of topological defects in the lattice as discussed in the following sections.

Kosterlitz-Thouless-Halperin-Nelson-Young (KTHNY) phase behavior has been observed for lattices of superconducting vortices, colloids or skyrmions. It is therefore accessible for a range of different systems, but the phase behavior depends on several parameters, such as the interaction potential present in the system [100].

Accordingly, also other theories of 2D melting exist. Alternative approaches suggest first-order phase transitions and are based on the formation of grain boundaries [101, 102] or the condensation of geometrical defects [103, 104]. Also metastability of the hexatic phase [105, 106] has been observed. While fluctuations and finite-size effects in hard core potentials play an important role [107, 108], more long-range interactions are less affected by fluctuations and show second-order transitions [109].

2.2.1. Topological Defects

In a perfect two-dimensional hexagonal crystal, each lattice particle has $N = 6$ nearest neighbors, as illustrated in Fig. 2.1a. However, when even a single particle is sufficiently displaced, the nearest-neighbor connections between neighboring particles are altered, resulting in the formation of topological defects. Any particle for which $N \neq 6$ constitutes such a defect. These defects are considered topological objects because their existence is encoded in the connectivity of the lattice; they cannot be removed unless they annihilate with another defect of opposite topological charge, such as in a dislocation pair composed of a 5–7 defect [92].

In Fig. 2.1b, a local shearing of four adjacent particles alters a single neighbor connection, thereby creating a pair of oppositely oriented dislocations. These dislocations form a bound pair and are topologically stable [91].

Such a local distortion does not necessarily disrupt the global lattice symmetry, provided the two dislocations remain tightly bound. If further displacements are introduced in the vicinity of the dislocation pair, the two defects may separate. This process is visualized in Fig. 2.1c and d, where the propagation of a dislocation is achieved by successively continuing the local shear. As the separation increases, the lattice lines between the two dislocations become increasingly bent. While the lattice spacing is locally perturbed, the global orientation of the lattice remains nearly preserved [90].

The orientation of each dislocation is determined by its Burgers vector \mathbf{b} . In Fig. 2.1e, the gray path is constructed by taking four steps in each of the three lattice directions in a counterclockwise manner. In a defect-free lattice, this would form a closed loop. However, in the presence of a dislocation, an additional step equal to \mathbf{b} is required to close the path. This Burgers vector is independent of the exact path taken, provided no other defects are enclosed. Since the configuration originates from a defect-free lattice, the total Burgers vector must sum to zero. Consequently, the Burgers vectors of the two dislocations exactly cancel, and a dislocation cannot arbitrarily reorient [91].

Further local rearrangements of particle positions, as shown in Fig. 2.1f, can convert one of the dislocations into an isolated defect – a disclination – along with a nearby cluster of three particles. This cluster can be interpreted as the combination of a dislocation and a disclination. Due to the underlying topology, the Burgers vectors of this disclination and the associated cluster cancel that of the remaining dislocation, which remains unaltered. This emphasizes that significant local distortions are required for a disclination to emerge [91, 92].

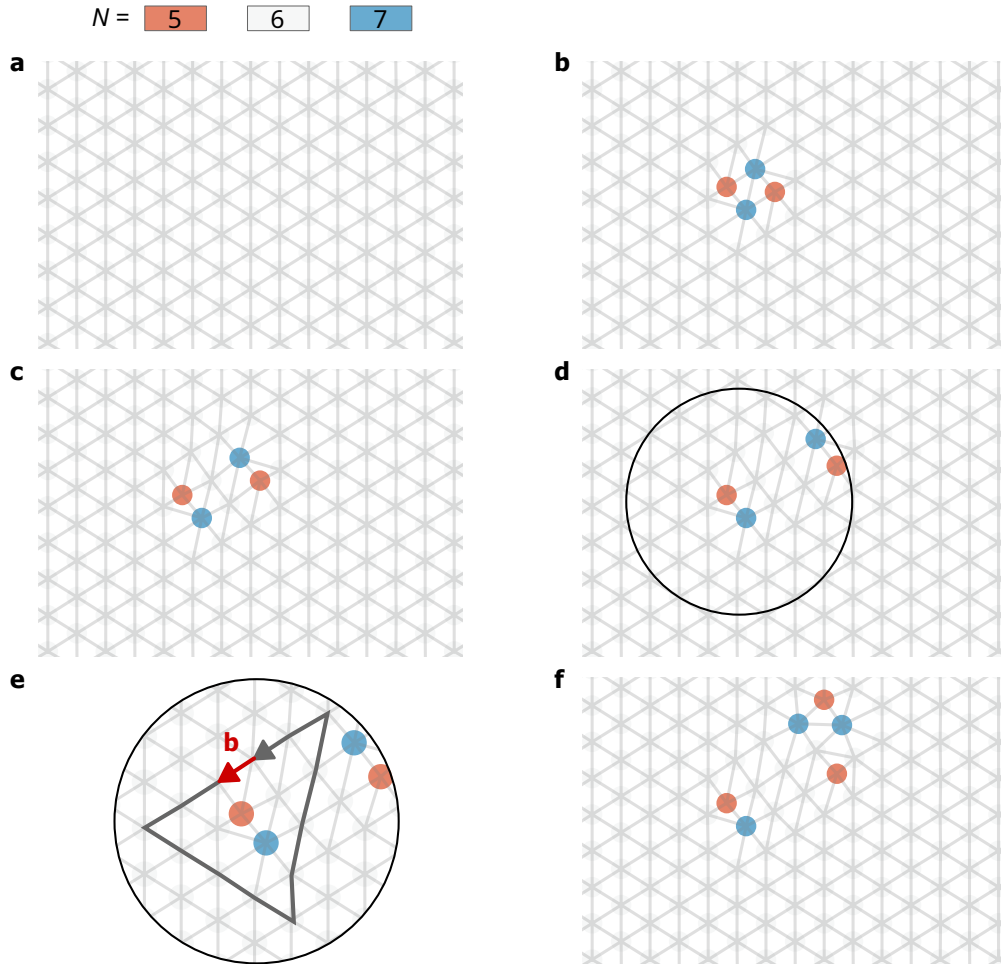


Figure 2.1.: Illustration of Dislocations. (a) In an ideal hexagonal lattice, each particle has $N = 6$ neighbors. The gray net illustrates the neighbor connections and each site is colored according to its N . (b) Local twisting of lattice sites changes one neighbor connection, generating a dislocation pair (5–7 defects) with opposite orientation. (c–d) If the twisting also affects (c) the next or (d) second-next site, the dislocations separate by one or two lattice sites. (e) Further distortion can yield an isolated defect, a disclination. (f) The orientation of a dislocation is defined by the Burgers vector \mathbf{b} . In a perfect lattice, a closed path formed by four steps in each of the three lattice directions encloses no area. Around a dislocation, this path fails to close and requires an additional vector \mathbf{b} .

Although the disclinations in Fig. 2.1f remain locally compensated by nearby defects, a more extreme case is presented in Fig. 2.2a and b. There, isolated $N = 5$ and $N = 7$ disclinations are embedded in otherwise defect-free regions. The resulting deformation of the lattice causes the lattice lines to bend, leading to a globally undefined

orientation of the hexagonal lattice.

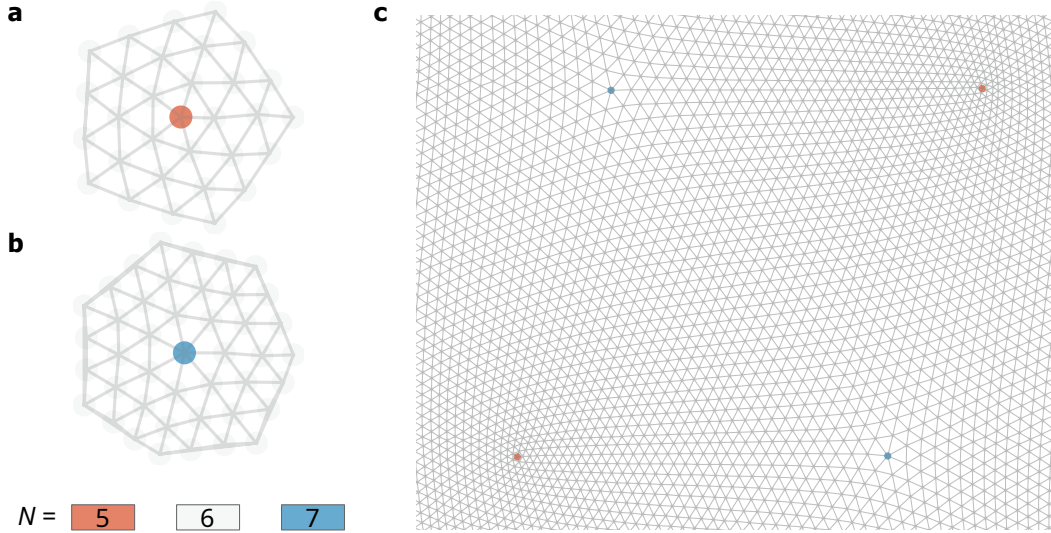


Figure 2.2.: Illustration of Disclinations. (a) Isolated $N = 5$ and (b) $N = 7$ disclinations in an otherwise perfect hexagonal lattice lead to bent lattice lines and undefined global orientation. The gray net illustrates the neighbor connections and each site is colored according to its number of neighbors N . (c) Four separated disclinations originating from a dislocation pair, spanning a finite region. Although the dislocation has disintegrated, the overall topological charge is still balanced, and global lattice order is preserved outside the defect region.

The extreme case of a dislocation pair dissociating into four isolated disclinations is shown in Fig. 2.2c. In this configuration, maintaining the dislocation requires substantial distortion of both the lattice spacing and orientation, indicative of a breakdown of long-range order. Nevertheless, as long as the total topological charge remains neutral – as in this case – the lattice outside the region spanned by the disclinations remains ordered. Only when defects fully dissociate – either by diverging spatially or interacting with new defect structures (as seen in Fig. 2.1f) on arbitrarily large length scales –, the global lattice order becomes compromised [98, 99].

2.2.2. Correlation Functions & 2-Step Melting

KTHNY theory describes the emergence of QLRO in two-dimensional systems as a consequence of the proliferation of topological defects. Notably, it predicts an intermediate hexatic phase between the solid and isotropic liquid phases. In the solid phase, only bound dislocation pairs – localized lattice distortions – are present. At a critical temperature T_1 , these pairs unbind into free dislocations, marking the breakdown of translational lattice order and the onset of the hexatic phase. However,

this intermediate phase retains orientational QLRO and does not yet exhibit the full isotropy of a liquid. Only at a second transition temperature T_2 does the system fully melt into an isotropic liquid, characterized by the unbinding of dislocations into disclinations and the proliferation of defect clusters [97–99].

The degree of order in the system is characterized through correlation functions. The translational correlation function

$$G_T(r = |\mathbf{r}_j - \mathbf{r}_k|) = \langle e^{i\mathbf{G} \cdot (\mathbf{r}_j - \mathbf{r}_k)} \rangle \quad (2.1)$$

evaluates the spatial correlation between particles j and k separated by $r = |\mathbf{r}_j - \mathbf{r}_k|$ via a reciprocal lattice vector \mathbf{G} , averaged over all particle pairs. For practical evaluation, $G_T(r)$ is computed by binning the distances r . In the solid phase, G_T decays algebraically as $G_T(r) \propto r^{-\eta_T}$ with $\eta_T < \frac{1}{3}$. At the transition into the hexatic phase, the exponent reaches its critical value $\eta_T = \frac{1}{3}$. In the hexatic and liquid phases, translational QLRO is lost, and G_T decays exponentially as $\propto \exp(-r/\zeta_T)$, with ζ_T denoting the translational correlation length [92, 97, 98].

Despite the disappearance of translational QLRO at T_1 , the system can retain orientational QLRO. The local orientational order parameter

$$\psi_6(\mathbf{r}_j) = \frac{1}{N} \sum_{k=1}^N e^{-i6\theta_{jk}} \quad (2.2)$$

quantifies, for each particle j at position \mathbf{r}_j , the degree to which the angles θ_{jk} formed with its N nearest neighbors match a hexagonal symmetry. Here, θ_{jk} is the angle between the horizontal axis and the vector $\mathbf{r}_j - \mathbf{r}_k$. The argument of the complex number ψ_6 defines the local lattice orientation as $\alpha(\mathbf{r}_j) = \arg[\psi_6(\mathbf{r}_j)] / 6$ [92, 97, 98]. The construction of ψ_6 and its associated orientation α are illustrated in Fig. 2.3.

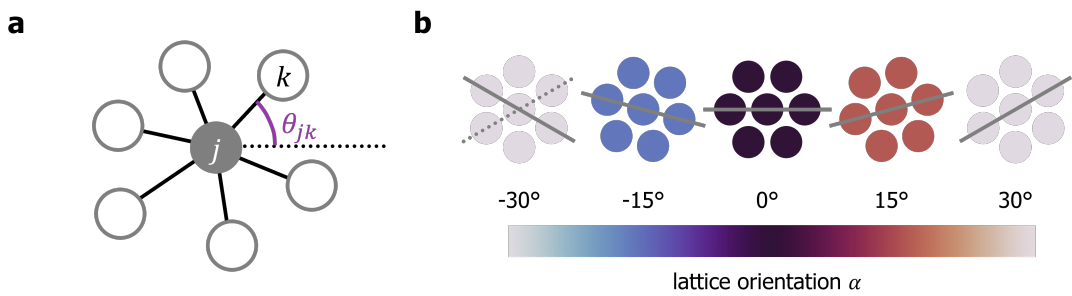


Figure 2.3.: Hexagonal Lattice Order. (a) The local orientational order parameter $\psi_6(\mathbf{r}_j)$ for particle j is computed from the angles θ_{jk} between the horizontal axis (dotted line) and the bond vectors to its neighbors k (black lines). (b) The Euler angle of ψ_6 determines the local lattice orientation α . The shown examples depict different local 6-fold configurations, with the orientation α indicated by solid gray lines. Due to the sixfold symmetry of the hexagonal lattice, the examples at -30° and 30° are equivalent (dotted gray line), justifying the use of a cyclic color bar.

The spatial correlation of ψ_6 values defines the orientational correlation function

$$G_6(r = |\mathbf{r}_j - \mathbf{r}_k|) = \langle \psi_6^*(\mathbf{r}_j) \psi_6(\mathbf{r}_k) \rangle \quad (2.3)$$

after averaging over all particle pairs j, k . In the solid phase, G_6 remains constant with increasing r . Upon entering the hexatic phase, it decays algebraically as $\propto r^{-\eta_6}$ with $\eta_6 < \frac{1}{4}$. At the transition to the liquid phase, η_6 reaches its critical value of $\frac{1}{4}$, after which G_6 also decays exponentially, $\propto \exp(-r/\xi_6)$, indicating the loss of orientational QLRO [92, 97, 98].

In general, both translational and orientational correlation functions exhibit the universal form

$$G(r) \propto \begin{cases} r^{-\eta} \cdot \exp\left(-\frac{r}{\xi}\right), & \text{critical (QLRO) phase with } \xi \rightarrow \infty \\ \exp\left(-\frac{r}{\xi}\right), & \text{disordered phase} \end{cases} \quad (2.4)$$

comprising both algebraic and exponential components. The algebraic term, governed by the exponent η , exists only in the critical phase exhibiting QLRO, where the correlation length ξ diverges. Consequently, the exponential term becomes negligible, and a pure power-law behavior is observed [91, 92, 97, 98].

Temporal correlations of orientational QLRO further reflect the phase behavior. The orientational time correlation function

$$G_6(\tau) = \langle \psi_6^*(t) \psi_6(t + \tau) \rangle \quad (2.5)$$

is obtained by correlating the local ψ_6 values of individual particles at time t and at a delayed time $t + \tau$, averaged over all particles [110]. Its behavior mirrors that of the spatial correlation: constant in the solid phase, algebraic in the hexatic phase, and exponential in the liquid. At the liquid transition temperature T_2 , the time correlation reaches its critical exponent $\eta_\tau = \frac{1}{8}$. As such, $G_6(\tau)$ provides equivalent insight into phase behavior as $G_6(r)$, although its computation requires full access to individual particle trajectories [110].

In summary, the melting of a two-dimensional solid proceeds in two distinct steps: translational QLRO is lost at T_1 , and orientational QLRO at T_2 , giving rise to the intermediate hexatic phase that retains only orientational QLRO between T_1 and T_2 [97–99]. This two-step melting is a unique feature of 2D systems. In three dimensions, the loss of translational QLRO simultaneously destroys orientational QLRO, precluding a hexatic analogue [91, 92]. In 2D, however, the presence and nature of the hexatic phase depend sensitively on system-specific factors such as the interaction potential, which also influence the type of phase transition observed [100].

2.2.3. Defect Energies & Elasticity

The deformation of a lattice – whether homogeneous or localized as topological defects – requires energy. A displacement field assigns to each particle a displacement

vector \mathbf{u} from its ideal lattice position, which defines the strain tensor $\underline{\epsilon}$ with components

$$\epsilon_{ij} = \frac{1}{2} (\partial_i u_j + \partial_j u_i), \quad (2.6)$$

constructed from the spatial derivatives of the displacement components u_i [3, 32]. Exemplary lattice deformations associated with different tensor components are illustrated in Fig. 2.4.

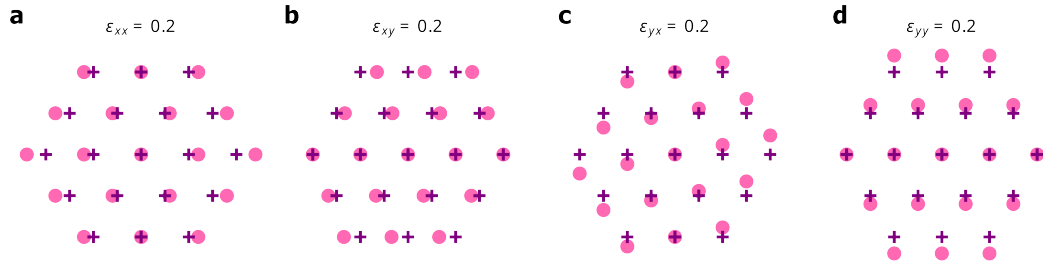


Figure 2.4.: Strained Lattices. Non-zero entries in the strain tensor $\underline{\epsilon}$ deform an originally ideal hexagonal lattice (purple crosses), producing distorted positions (pink dots). The four independent components cause (a) uniaxial strain along x , (b) shear deformation in x , (c) shear deformation in y , and (d) uniaxial strain along y . All other components are zero in the respective configurations.

The associated free energy density of a deformed hexagonal 2D crystal is given by

$$f = \frac{1}{2} \lambda \epsilon_{ii} \epsilon_{jj} + \mu \epsilon_{ij} \epsilon_{ji} = \frac{1}{2} B \epsilon_{ii}^2 + \mu \left(\epsilon_{ij} - \frac{1}{2} \delta_{ij} \epsilon_{kk} \right)^2, \quad (2.7)$$

where λ and μ are the Lamé coefficients and summation over repeated indices is implied. The second form results from a decomposition of the strain tensor into a scalar (dilatational) and a traceless symmetric (shear) part, introducing the bulk modulus $B = \lambda + \mu$. The bulk modulus B quantifies the energy cost of uniform area changes, while the shear modulus μ governs energy contributions from shape changes at constant area [92].

Alternative elastic descriptors include Young's modulus

$$K = \frac{4B\mu}{B + \mu}, \quad (2.8)$$

which characterizes elongation under uniaxial stress, and the Poisson ratio

$$\sigma = \frac{B - \mu}{B + \mu}, \quad (2.9)$$

which couples lateral contraction to uniaxial elongation [91].

In the hexatic phase, orientational fluctuations of the local bond directions are dominant and are captured by the angular field $\theta(\mathbf{r})$. The corresponding elastic energy is described by the Hamiltonian

$$\mathcal{H}_A = \frac{1}{2}K_A \int d\mathbf{r} |\nabla\theta(\mathbf{r})|^2, \quad (2.10)$$

with K_A denoting Frank's constant. In contrast, in the isotropic liquid phase, the only non-vanishing elastic response is the compressibility [92].

Since topological defects necessarily involve local lattice distortions at the scale of the lattice constant r_0 , their energetic cost is controlled by the elastic constants [97–99]. For a dislocation α located at position \mathbf{r}_α , the lattice displacement field can be approximated by its Burgers vector \mathbf{b}_α , which encapsulates the net lattice mismatch. Additionally, a short-range contribution arises from the dislocation core and is captured by the core energy E_{core} , which generally requires a microscopic treatment. The total interaction energy of a system of dislocations is then given by

$$\begin{aligned} \mathcal{H}_{\text{disloc}} = & -\frac{r_0^2 K}{4\pi} \frac{1}{2} \sum_{\alpha \neq \alpha'} \left[\mathbf{b}_\alpha \cdot \mathbf{b}_{\alpha'} \ln \left(\frac{|\mathbf{r}_\alpha - \mathbf{r}_{\alpha'}|}{r_0} \right) - \frac{[\mathbf{b}_\alpha \cdot (\mathbf{r}_\alpha - \mathbf{r}_{\alpha'})][\mathbf{b}_{\alpha'} \cdot (\mathbf{r}_\alpha - \mathbf{r}_{\alpha'})]}{(\mathbf{r}_\alpha - \mathbf{r}_{\alpha'})^2} \right] \\ & + E_{\text{core}} \cdot \sum_{\alpha} |\mathbf{b}_\alpha|^2, \end{aligned} \quad (2.11)$$

where the first term describes the long-range interaction depending on the separation and orientation of dislocation pairs, and the second term accounts for the core energy [91, 92].

Neglecting the angular interaction in Eq. 2.11, one obtains the effective interaction potential between two dislocations as

$$U_{\text{disloc}}(r) = c_{\text{disloc}} \ln \left(\frac{r}{r_0} \right) = \frac{Kr_0^2}{4\pi} \ln \left(\frac{r}{r_0} \right), \quad (2.12)$$

explicitly linking the interaction strength to Young's modulus K [91, 92].

Disclination interactions, by contrast, depend both on the distribution of disclinations and the presence of dislocations, which act to screen these interactions. The resulting interaction potential is

$$U_{\text{discl}}(r) = c_{\text{discl}} \ln \left(\frac{r}{r_0} \right) = \frac{K_A \pi}{18} \ln \left(\frac{r}{r_0} \right), \quad (2.13)$$

with K_A governing the interaction strength, highlighting the relevance of orientational elasticity [91, 92].

The interplay between elastic constants and defect energetics becomes particularly significant when considering the thermally driven unbinding of defect pairs. The mean squared separation of such a pair is given by

$$\langle r^2 \rangle = \frac{\int d\mathbf{r} r^2 \exp \left(-\frac{U(r)}{k_B T} \right)}{\int d\mathbf{r} \exp \left(-\frac{U(r)}{k_B T} \right)} = \frac{2k_B T - c}{4k_B T - c} r_0^2, \quad (2.14)$$

which diverges when the interaction strength c equals $4k_B T$. This divergence marks the unbinding of the defect pair and defines the associated phase transition. Accordingly, the unbinding of dislocations – corresponding to the solid-hexatic transition – occurs at

$$T_1 = \frac{K r_0^2}{16\pi k_B}, \quad (2.15)$$

as derived from Eq. 2.12. The unbinding of dislocation pairs to isolated dislocations automatically destroys translational QLRO as collective displacement of the intermediate particles is necessary to maintain the dislocations as indicated in Fig. 2.1d. Similarly, the hexatic-liquid transition, driven by disclination unbinding, takes place at

$$T_2 = \frac{K_A \pi}{72k_B}, \quad (2.16)$$

according to Eq. 2.13. The unbinding of dislocations to disclinations eventually also requires significant bending of the lattice lines as indicated in Fig. 2.1f and Fig. 2.2, which causes orientational QLRO to vanish [91, 97–99].

In summary, the emergence, unbinding, and proliferation of topological defects are fundamentally governed by the elastic properties of the system. Enhanced elastic compliance facilitates defect formation, and conversely, the presence of defects modifies the elastic response – establishing a dynamic feedback between elasticity and defect-mediated phase transitions, [91, 92].

2.3. 2D Skyrmion Lattices

Skyrmions have been shown to arrange in hexagonal two-dimensional (2D) lattices, both in bulk materials [12, 16, 17, 111] and in thin films [18, 112, 113].

In thin films with thicknesses down to the sub-nanometer scale, the exchange length typically exceeds the layer thickness, resulting in an approximately uniform magnetic structure across the film. Consequently, skyrmions with diameters of up to several micrometers exhibit quasi-2D behavior [14, 18, 112]. In contrast, skyrmions in bulk materials form extended tubes with complex three-dimensional (3D) configurations [114], limiting the applicability of strictly 2D models to their phase behavior. In most skyrmion-hosting systems, the applied magnetic field B and temperature T serve as tunable external parameters that influence the stability and arrangement of skyrmions. In bulk systems, such tuning can enable the formation of skyrmions [12, 17] or allow control over skyrmion density and inter-skyrmion interactions, which in turn affect the degree of 2D lattice order [111].

A central challenge in investigating the phase behavior of skyrmion lattices lies in their observation and detection (see chapter 3). Techniques such as small-angle neutron scattering [12, 115] and ac susceptibility measurements [116] provide indirect insights, while direct real-space imaging is achieved via Lorentz transmission electron microscopy (LTEM) [16, 111], magnetic force microscopy (MFM) [113], or Kerr microscopy [112]. Among these, Kerr microscopy (see section 3.2) offers several advantages: it enables real-time imaging with millisecond time resolution, is non-invasive, and does not perturb the magnetic configuration. However, its spatial resolution is diffraction-limited to a few hundred nanometers, requiring the skyrmions under investigation to be sufficiently large.

This constraint is met in the micrometer-sized skyrmions in CoFeB-based thin film multilayers studied in this thesis. In these systems, the skyrmion size [64, 117, 118] and density [27, 64, 112] can be tuned by adjusting the magnetic field. Additionally, the temperature controls both the spin dynamics and the underlying magnetic parameters, thereby influencing the stability and density of skyrmions [112]. A sufficiently high temperature is required to stabilize a dense and periodic skyrmion lattice. However, excessive thermal fluctuations increase entropy and may destroy lattice order. Striking this balance represents a fundamental challenge in sample fabrication, where slight variations in material composition or growth conditions can critically determine whether a skyrmion lattice can form.

Another key challenge in stabilizing ordered skyrmion lattices in thin films arises from the non-flat energy landscape, which gives rise to pinning effects [112, 113]. These effects generally hinder lattice formation; weak pinning may still allow 2D crystalline order, while stronger pinning can suppress order entirely [23]. Notably, such pinning can expand the narrow parameter space where the intermediate hexatic phase occurs, thus facilitating access to this unique regime and enabling its detailed exploration [23, 119]. In addition, the roughness of the energy landscape contributes to heterogeneities in the skyrmion ensemble, including shape deformations, size polydispersity, and spatially varying diffusion behavior – all of which present

further limitations for sample optimization.

The effective interaction potential between skyrmions [70] exhibits a form compatible with KTHNY-type melting behavior [100]. Importantly, recent investigations in CoFeB thin films have shown that this potential is only weakly sensitive to changes in skyrmion density [120], allowing for the system to remain within the regime where KTHNY transitions occur. Thus, the skyrmion packing fraction – a key determinant of the phase state [100] – can be dynamically controlled via the applied magnetic field without significantly altering the interaction potential.

This in-situ dynamic tunability of skyrmion size and density, combined with their inherent diffusive dynamics, makes skyrmions a uniquely suitable system for studying 2D phase transitions. Compared to other systems exhibiting KTHNY behavior, such as colloidal suspensions and superconducting vortices, skyrmions offer unique experimental control and time resolution. In superconducting systems, vortex imaging is typically performed via scanning tunneling spectroscopy, which provides high spatial resolution but is limited in temporal resolution – thereby restricting access to dynamical information [121–123]. In colloidal systems, optical video microscopy allows real-time tracking of particle trajectories, but achieving thermal equilibrium can require hours [124], and the 2D character is only approximated by suspending the particles at fluid interfaces [124, 125].

In summary, skyrmion lattices in CoFeB thin films provide a promising and highly tunable platform for investigating 2D phase behavior – particularly KTHNY transitions – with real-time access to both structural and dynamical observables (see chapter 3).

3. Imaging Skyrmions with Kerr Microscopy

Imaging skyrmions is essential for investigating their static and dynamic properties, forming the foundation for both fundamental research and towards application design. Depending on the technique employed, imaging can be performed in either real space or use reciprocal space measurements to reconstruct real-space information, each imposing distinct experimental conditions on the sample and its magnetic structures [1, 126].

X-rays offer high spatial resolution, enabling the visualization of magnetic textures at the nanometer scale. However, conventional x-ray imaging typically requires exposure times on the order of several seconds to minutes to achieve sufficient contrast. Coherent correlation imaging techniques can mitigate this limitation by resolving state fluctuations and, in some cases, enabling single-shot imaging. Both reciprocal space methods such as small-angle x-ray scattering and real-space reconstructions via holography are available. Nevertheless, these approaches often demand specialized sample preparation, including deposition on membranes for transmission-mode imaging. Moreover, x-ray-based methods generally require access to a synchrotron facility, representing a significant experimental bottleneck [126].

Real-space imaging at the nanoscale can alternatively be achieved using Lorentz transmission electron microscopy (LTEM), which offers direct visualization of magnetic structures but is typically limited in temporal resolution [111, 126].

Magnetic force microscopy [126] constitutes another real-space imaging technique, operating as a scanning probe method. A cantilever equipped with a magnetic tip scans the sample surface, with tip deflections caused by local stray fields – originating from the sample’s magnetization – being measured. This technique can resolve structures at nanometer resolution – however, it suffers from limited temporal resolution due to its sequential scanning nature. Additionally, since the tip interacts with the stray field, it can inadvertently perturb or modify the magnetic configuration of the sample [1].

For magnetic structures with length scales on the order of hundreds of nanometers to micrometers, optical techniques can be employed. In particular, imaging based on the magneto-optical Kerr effect (MOKE) [127] in dedicated optical microscopes – so-called Kerr microscopes – provides an effective and accessible solution. One of the main advantages of Kerr microscopy is its simplicity: it enables rapid imaging without requiring specialized infrastructure and can be implemented in a standard laboratory environment. The method is suitable for samples with relatively smooth surfaces (typically nanometer-scale roughness) and magnetization that in-

teracts strongly enough with light to yield sufficient contrast [126, 127]. In the following sections, I detail how Kerr microscopy is employed in the experiments presented in this thesis.

3.1. Magneto-Optical Kerr Effect

Light is an electromagnetic wave characterized by oscillating magnetic (\mathbf{B}) and electric (\mathbf{E}) fields, and a propagation direction \mathbf{k} , all mutually orthogonal [3]. Magneto-optical effects describe the interaction between light and additional electromagnetic fields, such as the magnetization within a magnetic material [24].

The propagation of light through matter is governed by Maxwell's equations, where the displacement field

$$\mathbf{D} = \epsilon_0 \mathbf{E} + \mathbf{P} = \underline{\epsilon} \mathbf{E} \quad (3.1)$$

captures the material's electric response via the vacuum permittivity ϵ_0 , the electric polarization \mathbf{P} , and the material-specific permittivity tensor $\underline{\epsilon}$ [3]. In general, $\underline{\epsilon}$ is complex and depends on the material's symmetry. For cubic crystals, it reduces to the form

$$\underline{\epsilon} = \epsilon_0 \begin{pmatrix} 1 & iQm_z & -iQm_y \\ -iQm_z & 1 & iQm_x \\ iQm_y & -iQm_x & 1 \end{pmatrix} + \begin{pmatrix} B_1 m_x^2 & B_2 m_x m_y & B_2 m_x m_z \\ B_2 m_x m_y & B_1 m_y^2 & B_2 m_y m_z \\ B_2 m_x m_z & B_2 m_y m_z & B_1 m_z^2 \end{pmatrix} \quad (3.2)$$

where the Voigt constant Q describes the linear magneto-optical response (i.e., the Kerr effect), and the second-order contributions are characterized by the material-specific constants B_1 and B_2 (Voigt effect) [24]. As B_1 and B_2 typically have magnitudes on the order of 10^{-4} , they are negligible for the present discussion and will not be considered further [127].

The MOKE manifests as circular birefringence, in which left- and right-circularly polarized light propagate with different refractive indices, resulting in anisotropic refraction. Since linearly polarized light is a superposition of two circularly polarized waves of opposite handedness, the linear MOKE also influences linearly polarized beams. Combining Eq. 3.1 with the linear magneto-optical term in Eq. 3.2, one obtains

$$\mathbf{D} = \epsilon_0 (\mathbf{E} + iQ \mathbf{m} \times \mathbf{E}), \quad (3.3)$$

which resembles the action of a Lorentz force acting on the electronic response [126]. This cross product introduces a polarization component perpendicular to \mathbf{m} [127].

The precise influence of the MOKE on the polarization state of the incident electric field \mathbf{E}_i depends on the experimental geometry. The polar, longitudinal, and transverse configurations are illustrated schematically in Fig. 3.1. The skyrmion-hosting systems investigated in this thesis exhibit PMA, with the magnetization predominantly oriented OOP, corresponding to the polar MOKE configuration (Fig. 3.1a). For an incident polarization \mathbf{E}_i lying within the incidence plane yz , the birefringence introduces a Kerr-induced rotation, resulting in an elliptical polarization state upon

reflection. The reflected polarization vector \mathbf{E}_r is governed by the displacement field \mathbf{D} in Eq. 3.3. In the polar geometry, \mathbf{E}_r is rotated by the Kerr angle θ_K with respect to the ideal mirror-reflected polarization \mathbf{E}_i' (i.e., the case for zero magnetization) [24]. The effect is maximized at an incidence angle $\alpha = 90^\circ$, where $\mathbf{E}_i \perp \mathbf{m}$, enhancing the cross product in Eq. 3.3. For typical values of $Q \approx 0.003$, Kerr rotations are of the order of milliradians; however, under certain conditions, rotations exceeding $\theta_K > 1^\circ$ have been observed [127].

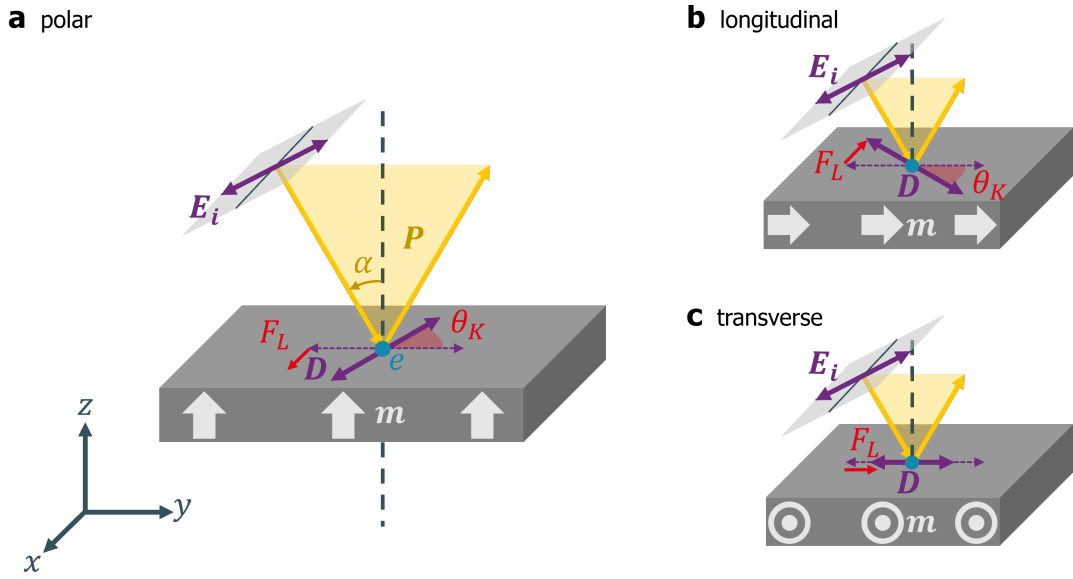


Figure 3.1.: Magneto-Optical Kerr Effect. (a) Linearly polarized light with electric field \mathbf{E}_i impinges on the sample at an angle α with a plane of incidence P aligned with the yz -plane. In the polar configuration, the magnetization \mathbf{m} points along the z -axis. As \mathbf{E}_i induces electron oscillations, \mathbf{m} introduces an effective Lorentz force \mathbf{F}_L as described by Eq. 3.3. This causes the displacement field \mathbf{D} to rotate by the Kerr angle θ_K , yielding a reflected polarization \mathbf{E}_r rotated with respect to \mathbf{E}_i . (b) In the longitudinal configuration, $\mathbf{m} \parallel \mathbf{e}_y$ lies within the plane of incidence and again produces a Kerr rotation. (c) In the transverse configuration, where $\mathbf{m} \parallel \mathbf{e}_x$, the z -component of \mathbf{E}_i does not lead to a polarization rotation but modifies the magnitude $|\mathbf{D}|$.

Different geometries provide complementary access to the MOKE. In the longitudinal configuration (Fig. 3.1b), both the magnetization \mathbf{m} (along the y -axis) and the electric field \mathbf{E}_i lie in the plane of incidence, resulting in a Kerr rotation similar to the polar case. In contrast, in the transverse configuration – where the magnetization \mathbf{m} is IP along the x -axis and thus $\mathbf{m} \perp \mathbf{E}_i$ (Fig. 3.1c) – the effect manifests as a change in reflectivity without a polarization rotation. Here, the MOKE is observed as a modulation in the reflected intensity and therefore modulates the sample's reflectivity [126].

3.2. Detecting Skyrmions with Kerr Microscopy

Because the magnetization of a material alters the polarization of reflected light in a direction-dependent manner, the MOKE effect can be exploited to generate magnetic contrast. For optimal contrast, the sample surface must be smooth, and the magnetic layer should lie close to the surface. This ensures sufficient penetration depth of the incident light to probe the magnetic structures of interest. Fig. 3.2 shows a schematic of a Kerr microscope setup [127].

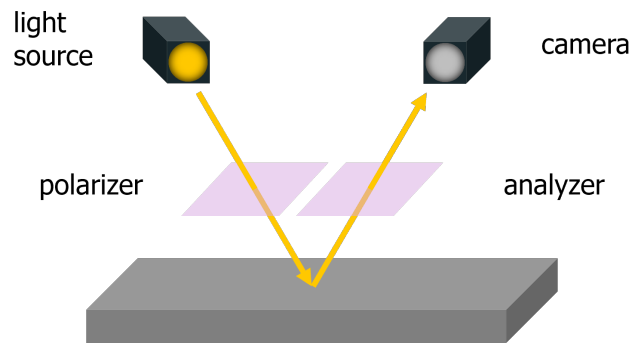


Figure 3.2.: Schematic of a Kerr Microscope. Light from a light source is first polarized linearly in a polarizer. When reflected by a magnetic material, the polarization is altered as illustrated in Fig. 3.1. An analyzer filters one polarization component of the reflected light along, such that the intensity detected by the camera establishes contrast for domains of differently oriented magnetization.

Linear incident polarization \mathbf{E}_i is established by placing a polarizer between the light source and the sample. An analyzer positioned in the reflected beam path – between the sample and the camera – detects changes in polarization \mathbf{E}_k induced by the magnetization vector \mathbf{m} . In the polar configuration, the analyzer is typically adjusted such that one magnetization direction (e.g., pointing out-of-plane and upwards) yields minimal detected intensity, while the opposite direction (downwards) produces maximum intensity [128].

For the experiments presented in this thesis, a commercially available Kerr microscope manufactured by *evico magnetics GmbH* was used. The light source consists of an array of blue LEDs, each coupled to a glass fiber that transmits the light into the microscope. The optical unit, which includes the polarizer, aligns and focuses the incident beam onto the sample. The complete beam path for this microscope is illustrated in Fig. 3.3. After reflection, the light – now elliptically polarized due to the magneto-optical effect – passes through a compensator, which converts it back into linear polarization. The analyzer then filters one polarization component to extract the magnetic contrast. The resulting beam is directed to a CCD camera that records the reflected intensity [128, 129].

The microscope’s LED array consists of eight individually selectable sources. Each LED is positioned such that selecting a specific LED defines the incidence plane of

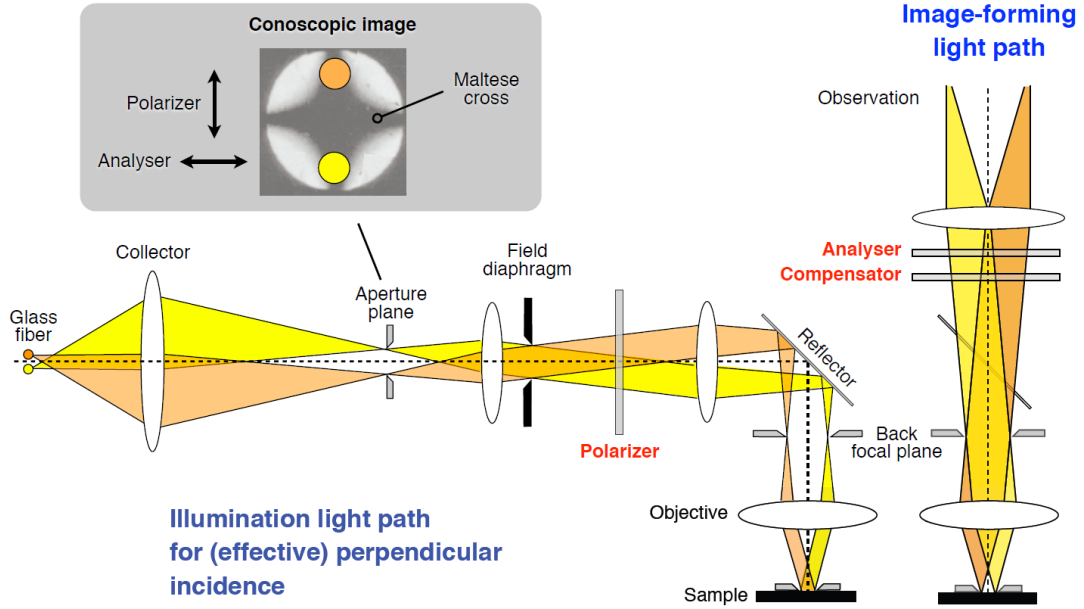


Figure 3.3.: Beam Path of the *evico* Kerr Microscope. Light enters the microscope from the left and passes through the polarizer and an optical unit, which focuses the light onto the sample. The path of the reflected light is depicted separately on the right to ensure better readability. The reflected beam passes the analyzer and compensator to establish magnetic contrast and is then directed onto the camera for imaging. From Ref. [129].

the beam. The incidence angle is nearly normal to the sample surface, making the system optimized for the polar configuration. Selecting a single LED always yields sensitivity to the out-of-plane (OOP) magnetization component. However, this also introduces a finite sensitivity to in-plane (IP) components – either transverse or longitudinal – depending on the incidence plane. By simultaneously illuminating the sample with two opposing LEDs, the polar components remain unchanged while the IP components acquire opposite signs. Summing the images from both configurations cancels the IP contribution, isolating the pure OOP contrast [129, 130].

Imaging pure longitudinal or transverse magnetization is more challenging, as it requires suppression of the polar contribution. This is achieved by subtracting images obtained from opposing LEDs. To do so, the microscope alternates between two opposite LEDs, recording their signals sequentially. The resulting difference image isolates the desired IP magnetization contrast [129, 130].

The setup also includes a set of independently controlled electromagnets for applying external magnetic fields. An in-plane coil is capable of generating magnetic fields up to 200 mT and is primarily used for skyrmion nucleation, as discussed in section 1.2.3. However, the coil generating out-of-plane fields is the primary one used in nearly all measurements. This coil provides the field necessary to stabilize skyrmions

and control their size and density. It is specially designed for precise field control with sub-microtesla resolution, as the skyrmions in the studied CoFeB thin films are extremely sensitive to such small field variations. Depending on the measurement, different coils are used: air-core coils (up to $\approx 2 \mu\text{T}$) or soft-iron-core coils (up to $\approx 15 \mu\text{T}$), with the latter introducing only minimal hysteresis. A Peltier element placed directly on the coil core serves as the sample holder, enabling fine control over sample temperature while keeping it as close as possible to the coil center to ensure field homogeneity. Magnetic field calibration is performed using a Hall probe placed at the sample position, allowing precise and reproducible field control. A Pt100 sensor mounted directly on the Peltier element – adjacent to the sample – enables accurate temperature measurement and regulation, maintaining fluctuations below 0.1 K [64]. To further stabilize the temperature, the microscope is enclosed in a laminar flow box. Prior experiments revealed that the local sample temperature is highly susceptible to environmental disturbances: each person working near the microscope increased the temperature by approximately 0.5 K within 15–30 min, and even walking past the setup could lead to a sudden drop of similar magnitude. While a PID temperature controller could, in principle, correct such fluctuations by adjusting the heating current, such active feedback often perturbs an otherwise equilibrated setup. The laminar flow box thus plays a crucial role in maintaining a stable thermal environment. The Peltier element permits control of the sample temperature within a range of approximately 285 to 370 K. The lower bound is limited by condensation, which typically begins near 285 K, depending on ambient humidity, while the upper limit is constrained by the efficiency of the Peltier element [19, 112].

All image data for the experiments were acquired using a *Hamamatsu ORCA-03G* CCD camera. With a 2×2 binning configuration, the camera delivers an effective resolution of 672×512 pixels (excluding legend) at a maximum frame rate of 16 fps, with a typical exposure time of 62.5 ms. Binning modes of 4×4 and 8×8 enable higher frame rates of up to 27 fps and 43 fps, respectively, at the cost of reduced spatial resolution by factors of 2 and 4 along each axis.

For automated skyrmion detection, I employed the *trackpy* Python package [131, 132]. The algorithm identifies local intensity maxima (or minima, if inverted) by fitting a 2D Gaussian kernel. Two primary parameters govern detection: *diameter*, which defines the feature size and kernel scale, and *separation*, which sets the minimum distance between features. Additional parameters such as *percentile* (minimum relative peak intensity) and *minmass* (minimum integrated intensity) are particularly useful for refining detection in cases where noise or poor contrast limit performance with default settings.

Experimental Note

Over the past years, a machine-learning based approach has been developed in our group to detect skyrmions, specifically in Kerr microscopy videos [133]. The trained *UNET* model can detect skyrmions efficiently and precisely without requiring explicit parameter choices. However, at the moment, *trackpy* still outperforms the *UNET* for

certain conditions. For linking skyrmion occurrences to trajectories, *trackpy* [131, 132] thus remained the state-of-the-art method.

3.3. Fabrication of Magnetic Thin Film Samples

Magnetic materials – whether hosting skyrmions or not – can be deposited via various deposition techniques. For the multilayer stacks investigated in this thesis, deposition was performed using a *Singulus Rotaris* magnetron sputtering system.

Sputtering is a physical vapor deposition technique that enables the continuous transfer of material from a target – serving as the source – to a substrate, under ultra-high vacuum conditions [134, 135] (here: $<1 \times 10^{-9}$ mbar). The deposition chamber is filled with Argon gas, and a voltage – either constant (DC) or alternating (RF) – is applied to the target. This induces ionization and forms a plasma near the target. The Argon ions are accelerated towards the target, dislodging individual atoms through momentum transfer [134, 136]. A magnetic field near the target region enhances electron confinement, thereby increasing the frequency of ionizing collisions with Argon atoms and improving plasma stability. The liberated atoms then travel ballistically through the chamber and condense on the substrate surface [134, 136]. Upon arrival, the atoms reorganize – ideally – into smooth, homogeneous thin films, which can be either crystalline or amorphous. The structural properties of the resulting layer can be tuned by adjusting the sputtering power and Argon pressure, which in turn influence the deposition rate and energy of the adatoms [134, 137].

The multilayer stacks used in this thesis (and in similar studies conducted in the Kläui group) are typically of the form Ta/CoFeB/Ta/MgO/Ta [19, 63, 112]. The ferromagnetic layer CoFeB, with a thickness of approximately 0.8 nm to 1 nm, serves as the functional magnetic material. The composition $\text{Co}_{20}\text{Fe}_{60}\text{B}_{20}$ has been found to yield exceptionally smooth films with homogeneous magnetic properties, which is critical for achieving low pinning and a flat energy landscape conducive to skyrmion dynamics. The bottom Ta layer functions as a heavy metal base that induces iDMI in the adjacent CoFeB layer. For optimal interfacial quality and to promote smooth growth, Ta thicknesses in the range of 4 nm to 5 nm are commonly employed. The CoFeB/MgO interface provides the PMA required to stabilize skyrmions in the thin-film geometry. A thin Ta dusting layer, inserted between CoFeB and MgO, enables further tuning of PMA, DMI, and the effective energy landscape [19, 63, 112]. This layer is subatomic in average thickness (typically 0.05-0.09 nm) and consists of discontinuous islands of a few atoms, randomly distributed across the sample [138]. A final top Ta layer serves as a capping layer to protect the stack from oxidation. Instead of Ta, also other materials can be used. In particular, we have started using the transparent material HfO_2 as capping in order to optimize the magnetic contrast. However, I have made the experience that samples with HfO_2 instead of Ta capping may lead to faster aging effects in terms of changing magnetic properties at identical measurement conditions. As substrates, both Si/SiO₂ and SiN wafers are used, with

minor variations in substrate composition possibly influencing the magnetic properties of the film.

The ability to deposit ultrathin layers – including submonolayer dusting layers [138] – with high smoothness is one of the main advantages of magnetron sputtering. The multilayer structures are thus optimized such that skyrmions emerge at temperatures close to room temperature, with micrometer-scale diameters suitable for Kerr microscopy, and in an energy landscape as flat as possible to minimize pinning and enable thermal diffusion [19, 63, 112].

Thin films are typically deposited onto substrates of several millimeters in lateral dimensions. For the study of skyrmions in confined geometries or wire-like structures – as relevant for device applications – patterning of the magnetic stack is required.

One common method for patterning is based on physical removal of material outside the desired geometry via electron beam lithography (EBL) [139]. The process begins with spin-coating a resist onto the sample. A focused electron beam then exposes the resist according to a predefined pattern with nanometer-scale precision. The exposure modifies the resist by polymerization, rendering the exposed areas resistant to subsequent processing. Development in a suitable solvent removes the unexposed resist. The remaining resist protects the underlying material during ion beam etching, which removes all unprotected regions of the stack. Finally, the resist is stripped using a strong solvent (e.g., acetone), leaving behind only the patterned magnetic structure [139].

Contributions

The sample deposition and patterning was done by my lab colleagues. Their contributions are described in detail in the Author Contribution section of every project.

Alternatively, patterning can be achieved without physical removal of material by altering the magnetic properties through local irradiation. Techniques such as focused ion beam (FIB) irradiation [88] or optical microwriting [89] deposit energy into specific regions of the film. At sufficiently high power, this energy input irreversibly transforms the originally FM layer into a non-magnetic phase. In this way, the functional magnetic structure is defined by spatially modulating the magnetic properties, rather than the physical geometry, of the film [88, 89].

Part II.

**Thermal Skyrmion Diffusion in a
Non-Flat Energy Landscape**

4. Skyrmion Pinning Energetics in Thin Film Systems

4.1. Published Article

Publication Information


The following article is published in *Nature Communications*:

Skyrmion pinning energetics in thin film systems

Raphael Gruber, Jakub Zázvorka, Maarten A. Brems, Davi R. Rodrigues, Takaaki Dohi, Nico Kerber, Boris Seng, Mehran Vafaei, Karin Everschor-Sitte, Peter Virnau & Mathias Kläui

Nature Communications **13**, 3144 (2022).

DOI: [10.1038/s41467-022-30743-4](https://doi.org/10.1038/s41467-022-30743-4)

Copyright Information:  CC BY 4.0 Creative Commons Attribution 4.0 International License

Editorial Note: The blue header/footer bars were added for inclusion in this dissertation and are not part of the original publication.

Contributions









The author contributions for this project and article are described in detail in section 5.3.

ARTICLE


<https://doi.org/10.1038/s41467-022-30743-4>

OPEN

Skyrmion pinning energetics in thin film systems

Raphael Gruber ¹, Jakub Zázvorka ², Maarten A. Brems ¹, Davi R. Rodrigues ^{1,3,4}, Takaaki Dohi ¹, Nico Kerber ¹, Boris Seng^{1,5}, Mehran Vafaei^{1,6}, Karin Everschor-Sitte ^{1,4,7}, Peter Virnau¹ & Mathias Kläui ¹✉

A key issue for skyrmion dynamics and devices are pinning effects present in real systems. While posing a challenge for the realization of conventional skyrmionics devices, exploiting pinning effects can enable non-conventional computing approaches if the details of the pinning in real samples are quantified and understood. We demonstrate that using thermal skyrmion dynamics, we can characterize the pinning of a sample and we ascertain the spatially resolved energy landscape. To understand the mechanism of the pinning, we probe the strong skyrmion size and shape dependence of the pinning. Magnetic microscopy imaging demonstrates that in contrast to findings in previous investigations, for large skyrmions the pinning originates at the skyrmion boundary and not at its core. The boundary pinning is strongly influenced by the very complex pinning energy landscape that goes beyond the conventional effective rigid quasi-particle description. This gives rise to complex skyrmion shape distortions and allows for dynamic switching of pinning sites and flexible tuning of the pinning.

¹Institute of Physics, Johannes Gutenberg-Universität Mainz, Staudingerweg 7, Mainz 55128, Germany. ²Institute of Physics, Faculty of Mathematics and Physics, Charles University, Ke Karlovu 5, Prague 12116, Czech Republic. ³Dipartimento di Ingegneria Elettrica e dell'Informazione, Politecnico di Bari, Via E. Orabona 4, Bari 70125, Italy. ⁴Faculty of Physics, University of Duisburg-Essen, Lotharstraße 1, Duisburg 47057, Germany. ⁵Institut Jean Lamour, UMR CNRS 7198, Université de Lorraine, 2 allée André Guinier, Nancy 54011, France. ⁶Singulus Technologies AG, Hanauer Landstraße 103, Kahl am Main 63796, Germany. ⁷Center for Nanointegration Duisburg-Essen (CENIDE), University of Duisburg-Essen, Carl-Benz-Straße 199, Duisburg 47057, Germany. ✉email: klaui@uni-mainz.de

Magnetic skyrmions are topologically stabilized chiral magnetic structures which are stabilized by bulk or interfacial Dzyaloshinskii-Moriya interaction (DMI)^{1–3}. Due to their quasi-particle nature, skyrmions are of special interest in research for their promising applications^{4–8}. In particular, skyrmions are suggested as information carriers in data storage devices^{9,10} and logic devices^{6,8,11,12} since they can be moved deterministically and efficiently by ultralow current densities due to spin-orbit and spin-transfer torques. Recently, the diffusive motion of skyrmions due to thermal excitations was demonstrated in thin-film multilayers which makes them applicable for nonconventional computing^{13–16} and leads to 2D phases and phase transitions^{17,18}.

While for strongly driven fast skyrmion motion, pinning effects are expected to be small¹⁹, pinning effects have been shown to play a crucial role in most skyrmion-based spintronic device proposals. For racetrack memories, for example, pinning may be used as notches to maintain a fixed distance between skyrmions^{12,20}. Also nonconventional computing proposals such as reservoir computing require strong pinning of the skyrmions^{21,22}. The key step to realizing such nonconventional computing in skyrmion textures is to obtain the appropriate pinning strength for which one needs a method to quantify and then understand the pinning effects. Moreover, in applications, which rely on skyrmion diffusion, such as Brownian computing and probabilistic computing, pinning effects are of crucial importance as the pinning strength is often comparable to the scales of thermal excitation and thus impacts the operation of skyrmion-based devices^{14,15}. Pinning or more precisely a nonflat energy landscape for skyrmions occurs in skyrmion systems where different interactions on similar energy scales appear. Pinning effects due to local changes in the material parameters compete with magnetic interactions and have a strong impact on the static and dynamic skyrmion properties⁴ such as the shape and profile of skyrmions in the static ground state and during motion^{23,24}. In particular also properties of skyrmion motion and dynamic effects such as the skyrmion Hall effect^{24,25} are strongly affected by the distribution of pinning sites leading potentially to different skyrmion Hall angle dependences on the skyrmion size^{26,27}. The local material inhomogeneities leading to local variations of the magnetic parameters define an energy landscape²³ which can qualitatively impact the dynamics depending on the details of the pinning^{14,24,26}.

Skyrmion pinning in general is an open question and hence, quantifying and understanding the nature of the pinning experimentally is crucial²³. So far there have been only first attempts to characterize pinning strengths by measuring the driving forces required to unpin the skyrmion from a specific point in space²⁸. Furthermore, energy landscape dependences on pinning effects have been studied, but limited to skyrmions of sizes similar to the grains of the sample^{22,29,30}.

In particular, the current understanding of pinning is primarily based on micromagnetic simulations or on theoretical predictions considering effective potentials or the rigid particle description of skyrmions^{23,31–39}. Several mechanisms have been considered to be responsible for pinning effects and give plausible origins for the wide range of pinning strength occurring in various materials at different external parameters²³. These mechanisms include local changes of the magnetic parameters induced by variations in anisotropy³¹, exchange interaction^{32,33} or DMI³⁴ and the impact of missing spins, atomic impurities³⁵ or surface adatoms^{36,37}. Depending on the mechanism, defects attracting^{32,35–38} and repelling^{35–38} the skyrmion center or even exhibiting a combined behavior of attraction and repulsion^{36,37} have been predicted and established the conventional picture of skyrmion center pinning. Thereby, the skyrmion center has been used to describe the

position of the skyrmion with respect to a pinning site as centered or off-center. These theoretical predictions have been based on micromagnetic simulations^{31–34,38}, first principle calculations^{35–37} or the equations of motion for a quasi-particle model³⁹ with partly contradicting claims about the mechanism of the pinning. Even though previous investigations have noticed an influence of deformations of skyrmions, a thorough investigation and solid understanding of the mechanism is still missing^{30,33,38}. Experimentally, little work is available with in particular strong pinning reported in thin films^{28,29,40–43} where explanations for pinning have been based on grain boundaries that are expected to occur in the polycrystalline films and thus pinning has so far always been considered to be a static property of the sample. However, these predictions and possible explanations have not been explored in detail experimentally. In particular, the effective potential or rigid quasi-particle descriptions typically used for skyrmions have neglected their complex spin structure with a core as well as a delineating domain wall boundary both being deformable and do not allow for a description of many of the complex pinning properties observed experimentally.

In this paper, we experimentally explore the skyrmion pinning behavior present in a thin film system. We develop a method to ascertain the energy landscape for skyrmions quantitatively and, by magnetic microscopy we reveal the details of the spatially resolved skyrmion pinning. We show in our analysis of the pinning mechanism that one has to go beyond a simplified quasi-particle model as skyrmion pinning arises from the domain walls allowing us to understand the complex skyrmion pinning observed in multilayer samples and we demonstrate that skyrmion pinning can be tuned on-the-fly by switching certain pinning sites on and off.

Results

Skyrmion energy landscape. We start by probing the spatial dependence of the skyrmion pinning strength in a Ta(5)/Co₂₀Fe₆₀B₂₀(1)/Ta(0.08)/MgO(2) sample (thicknesses in nm, details for sample fabrication in the methods section) as the first important piece of information necessary to understand the pinning is to ascertain the energy landscape. To achieve this, we make use of the unique thermal dynamics of skyrmions that leads to a diffusive random walk motion that explores the full space of the sample¹⁴. We measure spatially resolved the occurrence (dwell time in relation to the full measurement time) and plot in Fig. 1a the probability of pixels being occupied by skyrmions throughout the measurement time (for details, see methods section). These results thus reflect the probability of finding a skyrmion covering a certain area of the sample.

We notice that at specific positions, skyrmions are found over nearly the entire observation time despite the regular re-nucleation procedures in between the single videos (see methods for details). These positions are characterized by localized high peaks of the probability density corresponding to skyrmions being strongly pinned. Other pinning sites show a weaker effect on skyrmions, meaning that they pin the skyrmions for a short period of time and then the skyrmion depins (for instance blue meaning probabilities of 20%). Finally, the very dark blue background corresponds to the area of low probability density where skyrmions occur only in few or single frames throughout the measurement (for further details about the analysis, see Supplementary Note 1 with Supplementary Fig. 1).

Figure 1b shows the energy landscape for the sample area corresponding to the probability distribution from Fig. 1a. We see a non-flat surface with distinct valleys connected to pinning sites and peaks for the positions with few observations. Thus, our method allows us to quantitatively ascertain the full energy

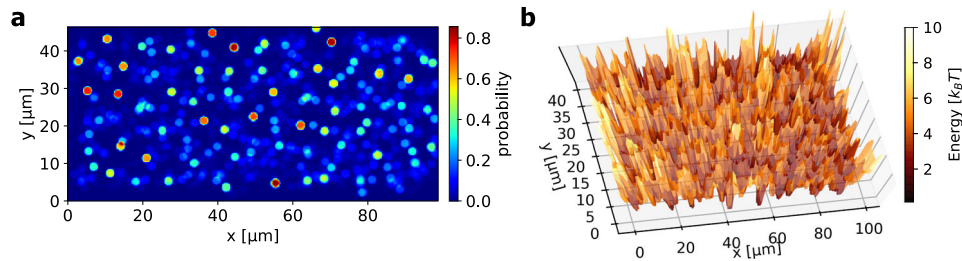


Fig. 1 Skyrmion energy landscape. **a** Occurrences of skyrmions in a $45 \times 100 \mu\text{m}^2$ film are measured at 312.5 K and $-88 \mu\text{T}$. The color scale represents the probability of pixels to be covered by skyrmions throughout the whole measured time. For example, at red positions, skyrmions were present around 80 % of the whole measurement time whereas the dark blue areas are rarely visited. The skyrmions explore the full space of the sample, only few single pixels are never covered by skyrmions. **b** Relative energy landscape surface in $k_B T$ determined from the probability distribution at 312.5 K in (a).

landscape of a sample and these results can then be used to gauge the applicability for nonconventional computing schemes.

Single skyrmion pinning. Having identified the presence of individual pinning sites, the next step is to investigate the underlying pinning mechanism for single skyrmion pinning. To realize this, we focus on a small confinement structure in a Ta(5)/Co₂₀Fe₆₀B₂₀(0.9)/Ta(0.08)/MgO(2) stack (thicknesses in nm, details in the methods section) presenting a non-uniform probability density. We study a single skyrmion in this area, which allows for observing thermal skyrmion dynamics governed only by the energy landscape and excluding any skyrmion-skyrmion interaction effects.

When we analyze the skyrmion probability density map, we find surprisingly that skyrmions of different sizes pin in very different positions. We vary the size (core area) of the skyrmion by up to a factor two using different applied fields at a certain temperature^{26,44}. We start our analysis by the conventional effective potential rigid quasi-particle model investigating the distribution of the positions of the effective center of mass of the skyrmion. All observed skyrmion center occurrences at out-of-plane field values between -43 and $-31 \mu\text{T}$ are shown in a scatter plot in Fig. 2a. The color indicates the size of the skyrmions located at the observed coordinates. The color opacity reflects the probability of finding a skyrmion there. In the measured field range, the mean skyrmion radius varies from $1.27 \mu\text{m}$ at $-43 \mu\text{T}$ up to $1.68 \mu\text{m}$ at $-31 \mu\text{T}$. For comparison, those skyrmion sizes are indicated schematically below the scatter plot in Fig. 2a and in the color code established there. The histogram on the top shows the size distribution from all measurements.

As a key finding we see, that at different magnetic field values we find different pinning sites at which skyrmions are observed to be predominantly positioned. And at each of the pinning sites, the detected skyrmions are of a specific size. Thus, the pinning position of the skyrmion center and the skyrmion size are strongly correlated. To corroborate this concept, we study the probability distributions for skyrmions at distinct field values. Figure 2b–e show histograms of the occurring skyrmion center coordinates for external fields between -39 and $-33 \mu\text{T}$. Also, the size distribution of the skyrmions observed there is depicted with the color code as used before. We find a strong size dependence of the positions where the skyrmion center is pinned. For instance, when we vary the applied magnetic out-of-plane (OOP) field by only $2 \mu\text{T}$ corresponding to a skyrmion size change by 5–8 %, the obtained probability density distribution of the skyrmion center position varies drastically. This means that by varying the field and thus the size, we can switch on and off certain pinning sites and thus tune the pinning on-the-fly.

Skyrmions observed for $-39 \mu\text{T}$ and below are relatively small with an average size $1.33 \mu\text{m}$ and mainly observed to be pinned at

pinning site 1 as depicted in Fig. 2d. Increasing the skyrmion size, Fig. 2c, d show that various other pinning sites become prominent. For the large skyrmions with an average radius of $1.63 \mu\text{m}$ at fields of $-33 \mu\text{T}$ and for higher fields yielding larger skyrmions, only pinning site 3 is effective and skyrmions depin from all other pinning sites. Throughout all measurements, the skyrmions exhibit thermal dynamics and by varying the field we can pin them but also then depin them from all pinning sites. This means that the pinning is flexible and that we can move skyrmions between different positions on-the-fly by tuning their size: once a skyrmion becomes larger or smaller than the characteristic size of a pinning site, this site no longer exhibits pinning behavior. Since there is no pinning site at which the skyrmions are permanently trapped and cannot be depinned from, there is no universal deep minimum energy position with strong attraction and permanent trapping. Hence, we can flexibly tune the position where skyrmions are pinned.

For all investigated skyrmion diameters we identify pinning sites so that the energy landscape is found to be clearly nonflat with the probability density of finding skyrmions being strongly nonhomogeneous. In particular, we see that the distances between the observed pinning sites are smaller or comparable to the skyrmion radius. Hence, the area of a skyrmion core may cover several of the sites 1–4, which correspond to pinning sites for the skyrmion centers of mass. We notice however that for such large skyrmions of micrometer size, the core is homogeneously magnetized. Thus, the translation of the homogeneous core corresponds to a zero mode⁴⁵ and cannot influence the pinning site. In contrast, the skyrmion boundary (SB) corresponds to a large gradient in magnetization and to a nonzero energy density being sensitive to the energy landscape as especially the high energy of the boundaries favors being compensated by low potential regions⁴⁵. Figure 3 provides a schematic of how skyrmions are pinned by the SB in the non-flat potential and how the energetically most favorable position changes with skyrmion size.

Due to a fixed SB, skyrmions of characteristic size still have specific center positions. The corresponding pinning of the center as presented in Fig. 2 and suggested in the conventional picture of rigid particles or effective potentials acting on the centers of skyrmions^{31–38} is therefore an effective approach. For the large skyrmions investigated in this paper, the energy landscape is responsible for a more complex pinning behavior.

Shape of pinned skyrmions. We notice that pinning of the skyrmion governed by the boundary implies not only a size dependence of the skyrmion but also a shape dependence. To understand the mechanism of the pinning, we next study the detailed shape of the skyrmions when they are pinned at different pinning sites. For this we carry out high resolution Kerr

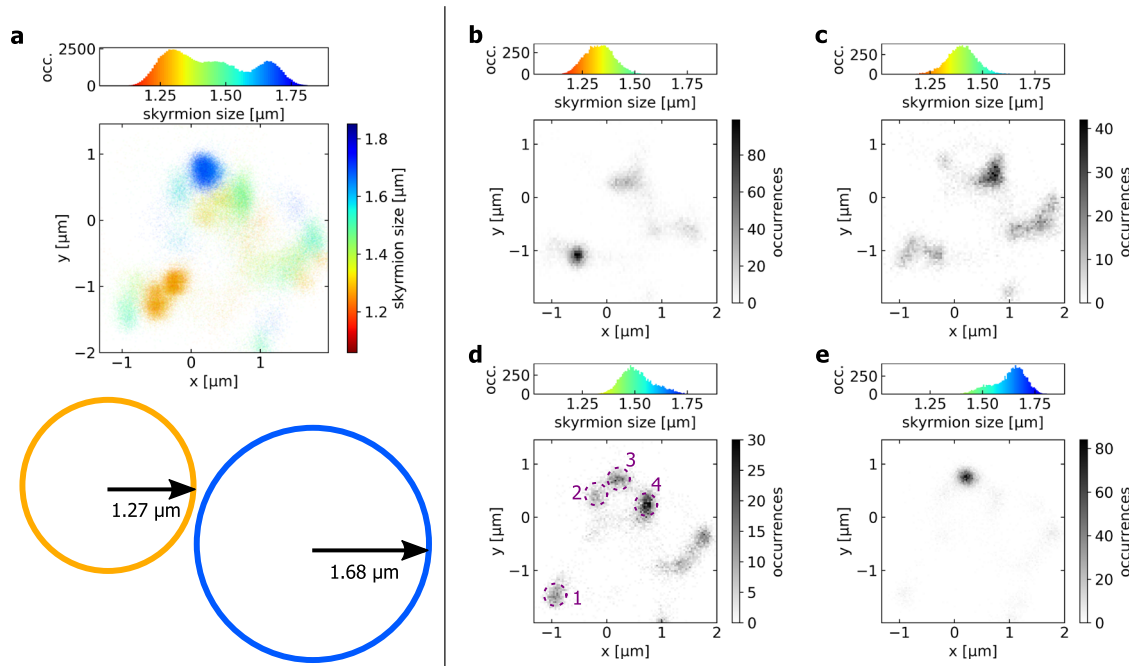


Fig. 2 Skyrmion size dependence of the pinning. **a** Skyrmion occurrences in all measurements at fields between -43 and -31 μT with an average skyrmion size between 1.27 and 1.68 μm with standard deviations of about 5%. Every detected skyrmion is depicted by a scatter plot point at the coordinate of observation. The colors represent the skyrmion size. The color intensity indicates the probability density of finding a skyrmion at a certain position. The top histogram shows the size distribution of all observed skyrmions. The colored circles on the bottom indicate schematically the size relation of the skyrmions among each other and the coordinate frame. **b–e** Histograms of the occurring skyrmion center positions in the same sample area at external fields of **(b)** -39 μT , **(c)** -37 μT , **(d)** -35 μT , and **(e)** -33 μT . The greyscale denotes the number of skyrmion center occurrences at a position. Even for small field changes of 2 μT corresponding to size changes of 5–8% in region depicted by **(b–e)**, the skyrmion distribution varies drastically and skyrmions are pinned at different positions indicating size-dependent pinning sites. In **(d)**, predominant pinning sites are highlighted by the dashed purple circles and labelled with integers 1–4.

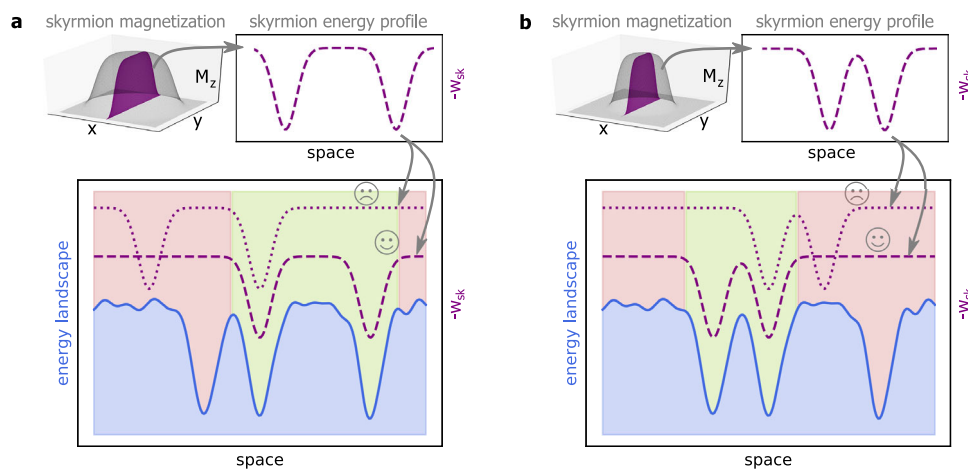


Fig. 3 Schematics of skyrmion pinning in a nonflat energy landscape. **a** The 3D surface schematically shows the magnetization of a skyrmion. The dashed line plot besides shows the negative energy density $-w_{\text{sk}}$ of this skyrmion along a profile as shown by the purple plane. It indicates that the (exchange-) energy density is most important in the domain walls delineating the skyrmion. The bottom part shows an exemplary schematic of a non-flat energy landscape in blue exhibiting three distinct minima. The peaks in energy density of the specific skyrmion match two of the valleys which leads to a favorable state of low energy in the region shaded in green as indicated by the dashed purple line. Other states as in the case of the dotted purple line yield a higher energy and are therefore unfavorable to be pinned at this position as indicated by the red-shaded region. **b** shows a similar scenario for a smaller skyrmion. Here, a minimal energy is achieved at a different position where the skyrmion energy density best matches the energy landscape (dashed purple line in the favorable green region). Hence, the position which was favorable in **(a)** is now in the unfavorable red region.

microscopy. The central coordinate frame in Fig. 4a shows the skyrmion shapes by plotting the positions of the domain walls that constitute the SB for skyrmions at pinning sites 1–4. The SB is defined as the position where the Kerr intensity intersects the mean of the values belonging to the skyrmion core and the

ferromagnetic background. The average Kerr contrast intensity of skyrmions is depicted in the surrounding plots for every pinning site. We see that although the corresponding skyrmion center coordinates deviate, their boundaries coincide in significant parts of the boundary length. To demonstrate the relevance of this

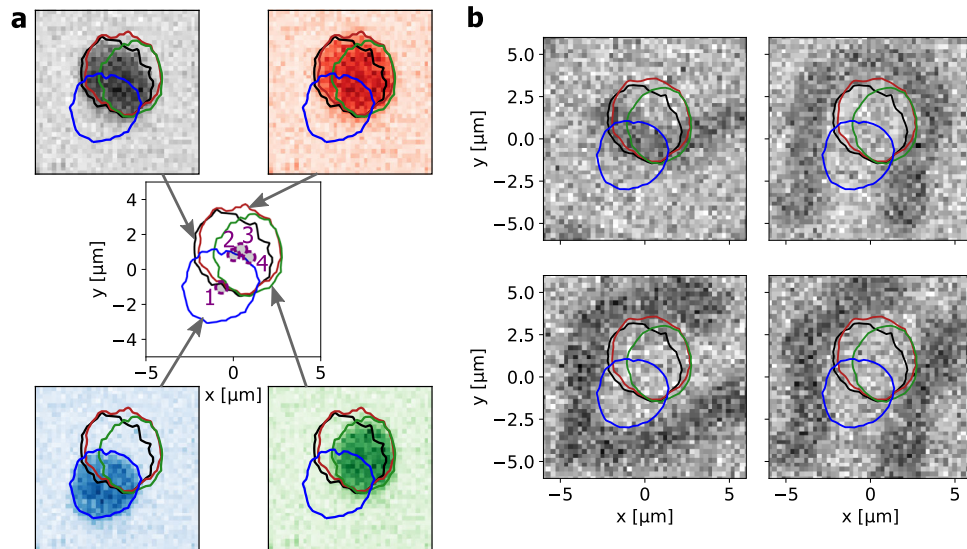


Fig. 4 Pinning of skyrmion boundaries. **a** The central coordinate frame shows the observed skyrmion boundary positions of the skyrmions at $-35 \mu\text{T}$ at pinning sites 1 (in blue), 2 (black), 3 (red) and 4 (green) as introduced in Fig. 2d. The positions of the corresponding skyrmion center coordinates are visualized by the dashed purple circles, which are additionally filled in grey for better visibility. The surrounding plots depict the average intensity for each pinning site with a color scale matching to the boundary color. **b** Kerr microscopy images of arbitrary stripe observations in the same sample area. Black corresponds to magnetization pointing out of the plane while white denotes magnetization pointing into the plane. The previously determined skyrmion boundaries are plotted additionally for comparison. The paths of the skyrmion boundaries fit the domain boundary position of the stripes in significant parts.

effect, we present an additional example for differently sized skyrmions pinned at the same position is presented in Supplementary Note 2 with Supplementary Fig. 2. Note that for such large skyrmions, translation and deformation of the SB in a flat potential require very little energy⁴⁵. Thus, recurring SB positions that coincide between different configurations provide strong evidence that pinning has to be present at the SB. However, the distance between the clearly distinct clusters of pinning sites 1 and sites 2–4 is of the order of or larger than the skyrmion radius and suggests that the difference between the pinning sites cannot be associated solely with a change in shape but the size is crucial. The equilibrium size of a skyrmion is thus governed by the applied magnetic field and temperature, based on the fundamental magnetic material properties^{14,44,46}.

To corroborate this pinning mechanism further, we explore pinning of stripe domains: the pinning mechanism should also be visible when studying domain walls in the stripe domain phase, rather than in the skyrmion phase. By tuning the OOP field and the nucleation process we obtain stripe domains as shown in Fig. 4b in the same confined sample as used for the skyrmion observation (single frame examples of stripe domains originating from different nucleation events). The domain walls of the stripe domains match the contours where the skyrmion domain wall boundaries were observed previously.

Having identified the domain walls at the skyrmion boundary as decisive for the pinning, we finally demonstrate how such a mechanism can arise. We use micromagnetic simulations with an arrangement of regions, which pin the domain wall. Exemplarily, the anisotropy is reduced in these regions as it is the magnetic property most sensitive to structural variations in the film and in particular the interfaces. As shown in Fig. 5, we can reproduce the observed pinning behavior by reducing the perpendicular magnetic anisotropy in three regions which are indicated as red boxes. Similar as in the experiment, the trajectory of a single skyrmion is tracked inside a small confinement and the skyrmion center positions are different when varying the skyrmion size due to the skyrmions being pinned with their boundary. Figure 5a, b shows histograms of the occurring skyrmion center coordinates

for both skyrmion sizes. A strong dependence of the center accumulation positions on the skyrmion size is observed, qualitatively supporting the experimental findings. Moreover, distinct skyrmion center accumulation points are observed although the underlying mechanism is pinning of the skyrmion boundary and not of the skyrmion center. The size of the smaller skyrmion is 5.7 nm meaning that its boundary can overlap only with two of the three pinning areas whereas the boundary of the larger skyrmion can overlap all three areas with a mean size of 10.3 nm. The occurring skyrmion sizes are shown in a histogram for Fig. 5a, b and furthermore, the mean sizes with respect to the coordinate frames used are depicted in Fig. 5c. Note that the SB usually makes up a much larger proportion of the skyrmion for nanometer-sized skyrmions than for the micro-scale skyrmions used experimentally. Given that the domain walls are the most highly energetic part of the skyrmion because of the rapid variation in the magnetization direction on a nm scale as compared to a homogeneously magnetized core of μm extension in the experiment, one can understand why variations in the magnetic properties most strongly influence the pinning of the skyrmion boundary domain walls. Further details on how the skyrmions of different size arrange in the simulation setup are found in Supplementary Note 3 with Supplementary Fig. 3.

Discussion

Our results show that thermal skyrmion dynamics is a powerful method to ascertain the energy landscape of a sample. As a key finding, we demonstrate that the skyrmions explore by thermal dynamics nearly the full area of a state-of-the-art thin-film device and exhibit significant pinning at certain locations with a particular distribution. This highlights that the energy landscape contains distinct minima but virtually no highly repulsive maxima. Since the pinning positions are featured at different temperature and out-of-plane field values, we deduce the behavior to be based on local variations in the materials parameters^{26,47,48} originating from the thin film growth process. As shown in our previous work on such samples, the observed pinning sites in this

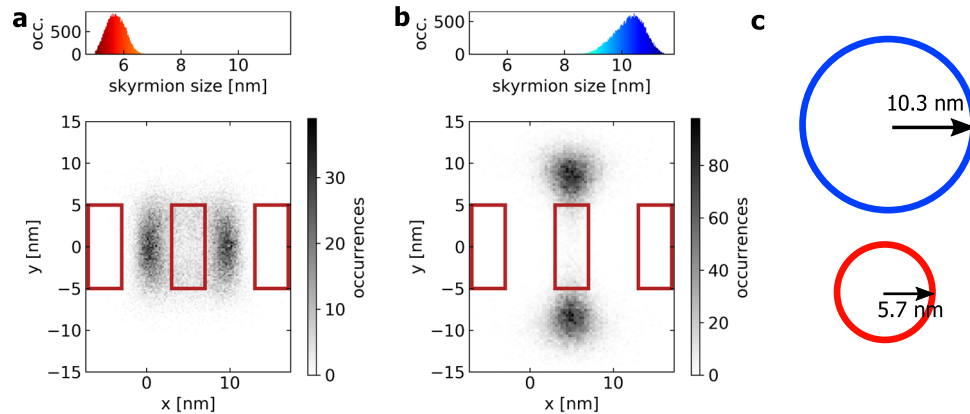


Fig. 5 Skyrmion boundary pinning simulation. Histograms of occurring skyrmion center positions for external out-of-plane fields of (a) 0.15 T and (b) 0.05 T based on micromagnetic simulations. The greyscale represents the number of skyrmion center occurrences at a position. Red boxes indicate the area where the magnetic anisotropy is reduced. The top histograms show the skyrmion size distribution. c Size comparison of the average sizes from (a) and (b). The scaling is identical for (a–c).

sample are weak enough so that driving skyrmions by spin-orbit torques is able to overcome the pinning and move skyrmions¹⁴. So the combination of quantified pinning sites and a possible skyrmion manipulation modes well for applications in non-conventional computing since for instance reservoir computing needs pinning to ensure the reservoir's stability. A quantitative description of the pinning strengths and locations, as obtained in this work, gives access to the reservoir's performance, in particular regarding the reservoir's complexity, memory, and its nonlinearity^{22,49}.

We find that the pinning sites, at which skyrmion centers are located, vary drastically with the skyrmion size. In particular since the skyrmion size can be directly tuned by the applied external field at a fixed temperature^{14,26,44,46}, this observation allows for an experimental control of the skyrmion pinning sites that goes beyond the previously assumed static pinning energy landscape. In particular, we can actively manipulate the efficiency of the pinning sites by varying the skyrmion diameter and thus tune the effectiveness of single pinning sites: once the size of the skyrmion is incommensurate with the pinning site, the pinning site is effectively shut off. This allows for an unprecedented engineering of the skyrmion energy landscape on-the-fly during device operation, which might prove useful for a possible application with tunable pinning as theoretically suggested²³.

By magnetic microscopy, we find that the spacing between the distinctly observable positions where center positions of differently sized skyrmions accumulate, is sometimes smaller than the skyrmion radius. The experimental evidence shows that the observed effects cannot arise due to the pinning of the skyrmion core, which is uniform over an area exceeding the distances of the pinning sites. Instead, the skyrmion pinning originates from a mechanism that pins the domain walls at the skyrmion boundary (SB). From the direct observation of SB position, we conclude that the observed pinning sites arise due to the SB being pinned along certain complex contours. We furthermore note that since the obtained distinct regions where the skyrmion tends to be pinned are much smaller than the homogeneous core of the skyrmion, the skyrmion is not pinned at a point-like grain but rather by a distribution of points within a region of at least the size of the skyrmion. Due to characteristic occurring sizes, still distinct skyrmion center positions arise but are not very meaningful measures for the present pinning. In general, pinning yields a spatially varying additional energy contribution for the equilibrium state compared to the case without pinning and thus impacts the skyrmion shape. At a constant applied field, a

distribution of skyrmion sizes is observed and in particular, it becomes clear that the detailed energy landscape is responsible for the size and shape of a skyrmions occurring at a specific position. Finally, we can conclude that this mechanism is decisive for the position that the skyrmion is pinned at and determines the path of the contour along which the SB is positioned. From the shape-determining SB pinning mechanism, we especially deduce that conventional rigid particle descriptions or effective potentials are not sufficient to portray the actual complex pinning mechanism.

Since the thermal excitation is competing with the pinning energy on the same energy scale, the skyrmion is able to move in the sample region in the non-flat energy landscape. Moreover, it can undergo size changes of on average 5–10 %. Increasing its size, a skyrmion can match two different pinning features with different sections of its boundary. For example, while skyrmions at sites 2 and 4 show approximately the same size of around 1.5 μm , site 3 yields characteristic values above 1.7 μm . Thereby, the energy difference arising from the size variation occurring even at a fixed field can be explained by a compensation due to the pinning. In particular, both states featuring different skyrmion size and pinning are accessible by the thermal fluctuations present. Furthermore, we clearly observe that not only the size is determined by the pinning, but also the shape. Skyrmions at site 2 are elongated with the average eccentricity of 0.13. The resulting shape can again be well explained by the SB being pinned along a contour as set by the grain level such that an enhanced coincidence of SB and pinning feature may be energetically more favorable than the equilibrium shape in a flat potential. SB pinning introduced in micromagnetic simulations reproduces the size-dependent skyrmion center positions, which cannot arise from previously often assumed pinning due to the skyrmion core. The boundary pinning concept is further corroborated by the analysis of randomly generated static configurations of stripe domains which are shown to share the same boundary positions as the investigated skyrmions.

Since antiskyrmions⁵⁰ are also surrounded by domain walls that delineate the spin structure⁴⁵, the boundary-induced pinning effect should occur analogously to the skyrmion case studied here. In the case of antiferromagnetic skyrmion-like textures^{51,52} however, the specific influence of the magnetic parameters that are unique to (synthetic) antiferromagnets, such as local variations of the antiferromagnetic exchange between the sub-lattices (respectively the RKKY between the two layers) will lead to additional effects^{53,54}.

In conclusion, pinning is a key feature relevant for many skyrmion-based spintronic devices. It allows to control many aspects of skyrmion dynamics such as nucleation, direction of motion, and speed. In racetracks memory concepts, for example, pinning allows to control the inter distance between skyrmions^{12,55–57}. Pinning is even more essential for devices, which exploit skyrmion diffusion as in neuromorphic^{58–60}, probabilistic^{14,61}, reservoir^{22,49} or Brownian computing^{16,62}. Thus, pinning effects must not only be taken into account when realizing applications but certain pinning is actually required for the operation of some non-conventional computing devices and so understanding the pinning is a key requirement to ensure functionality. Whereas in some cases, the particle-like approach with the skyrmion being pinned in the center of site works, we find that in other cases it is the SB, which is pinned – depending on the skyrmion size and stiffness, as well as the energy landscape. Thus, with our findings, the pinning effect can even be exploited in new kinds of applications. For instance, a parameter variation as in terms of the anisotropy or DMI that can be tuned by electric fields or simply by varying the applied external magnetic field as shown here, we can switch on or off pinning at certain sites. This provides a flexible means to control skyrmion dynamics for potential new applications. And by tuning the pinning efficiency, applications such as reservoir computing or other non-conventional computing schemes can be enabled.

Methods

Sample characterization. Multilayer stacks of Ta(5)/Co₂₀Fe₆₀B₂₀(0.9–1)/Ta(0.08)/MgO(2) as used in previous studies^{14,63} are investigated. The values in parentheses indicate the layer thickness in nanometers. After deposition, the stacks are annealed at 250 °C at vacuum pressure to obtain perpendicular magnetic anisotropy.

For the energy landscape analysis, the skyrmions are observed within a confinement structure of 60 × 120 μm². However, the extension of the device is large enough to be treated as continuous film with respect to used skyrmion sizes, the governing diffusion constant and the observation time scales¹⁴.

For the detailed study of magnetic pinning at a certain position, a disc with 17 μm diameter as previously investigated for diffusion in confinement⁶³ is used to ensure a single skyrmion to be present in a specific region.

The stacks were deposited by DC magnetron sputtering with a Singulus Rotaris sputtering tool using a base pressure of 3 × 10^{−8} mbar. With the mentioned tool, the layer thickness can be controlled precisely with a reproducible accuracy of less than 0.01 nm. The stacks used are comparable in terms of the temperature and magnetic field region where skyrmions occur as well as in the obtained skyrmion sizes showing good reproducibility.

All confinement structures were patterned by electron beam lithography (EBL) and Ar ion etching. The samples exhibit perpendicular magnetic anisotropy (PMA) and we confirmed that they host magnetic structures of non-trivial topology demonstrating skyrmion character^{14,63}.

Measurement setup. A commercial *evico magnetics GmbH* Kerr microscope including an in-plane (IP) field coil is used in combination with an electromagnet coil for out-of-plane (OOP) field control which was custom-made at the University of Mainz. For this small coil without magnetic core, a precise current control is used to realize OOP fields of the order of microtesla and with sub-μT precision. The field values are calibrated with a sensitive Hall probe, corrected by the hysteresis offset and reproduced in several measurement series. The magnetic structures are made visible exploiting the polar magneto-optical Kerr effect (MOKE) using a time resolution of 62.5 ms corresponding to 16 frames per second. To enable heating, the sample is placed on a Peltier element and a Pt100 sensor is attached to the Peltier element right next to the sample for temperature control. The temperature stability was ensured to be within 0.1 K.

The samples are heated by a Peltier element to temperatures between 300 and 350 K in order to get stable skyrmion phases exhibiting thermal motion¹⁴.

Investigated skyrmion systems. The skyrmions are nucleated at measurement temperature and OOP field by additionally applying an IP field sweep. During a sweep, a saturating IP field is rapidly switched off to relax spins into an equilibrium state. We are able to control the number of skyrmions in the geometry by the field strength to obtain desired skyrmion densities⁶³.

To quantify and investigate the occurrence of pinning in the continuous sample, an array of many skyrmions is nucleated. The high number of skyrmions helps to acquire statistically relevant skyrmion occurrences throughout the whole region within the observation time. However, the skyrmion density is kept sufficiently low

with the skyrmions appearing at distances of several skyrmion diameters so that a significant influence of repulsive skyrmion-skyrmion interactions on the thermal motion can be ruled out¹⁴. To obtain the necessary statistics to quantify the strength of single pinning sites but also to qualitatively observe where pinning sites occur on the sample, 20 videos of 9600 frames (ten minutes length) each with re-nucleated skyrmions are recorded. The re-nucleations thereby enable the skyrmions to occur at new positions each time. Especially, we ensure that skyrmion nucleation does not occur directly at pinning sites so that skyrmions exhibit significant thermal dynamics before they might eventually become trapped at a strong pinning site and thus the full space of the sample is explored and not limited by repulsive skyrmion-skyrmion interaction¹⁴.

To study the skyrmion dynamics near pinning effects in a thin film, we nucleate a single skyrmion in a disc with 17 μm diameter. In this confined geometry, the skyrmion can explore the energy landscape but cannot escape from the disc. For the analysis of the experiment, we have selected a sample where we find that the skyrmion positions are not homogeneously distributed but influenced by pinning but there is no pinning site, which permanently traps the skyrmion. This furthermore enables to study the skyrmion dynamics even for differently sized skyrmions. The skyrmion was nucleated and recorded for ten minutes (9600 frames) for each skyrmion size related to a certain value of the OOP field value. As the skyrmion is continuously moving between different positions and thus never permanently trapped at a pinning site, multiple nucleation events are not required in this case.

The skyrmion size can directly be tuned by the applied magnetic out-of-plane field^{14,46} and temperature^{14,44}. With our measurement at constant temperature, we can thus tune the average skyrmion size by the external field value^{14,46}. We do not find that the skyrmion is ever leaving the disc or is annihilated inside the disc during the measurements for the field and temperature ranges studied.

Skyrmion imaging and tracking. The videos are acquired with the CCD camera of the microscope, the *trackpy*⁶⁴ package is used to preprocess the frame images and detect the skyrmions. The preprocessing includes both background gradient compensation and noise filtering. The detection is then performed by fitting two-dimensional Gaussian kernels for localized intensities exceeding certain thresholds in terms of intensity and size. The optical spatial resolution of the MOKE microscope (≈300 nm) is better than the skyrmion size but domain boundaries cannot be resolved. Changes in the magnetization lead to a significant intensity edge and the dimensions of the skyrmions can be determined with subpixel accuracy. The validity of those obtained quantities well below the single-pixel range was ensured by a wide variation of the tracking parameters and comparison of intensities of single frames as well as averaged over frames yielding quantitatively identical results. Therefore, a spatial resolution well below 100 nm is reached for the detection of the skyrmion center of mass positions. As the skyrmion size, the gyration radius of the fitted intensity profile is established by the tracking algorithm⁶⁴. Note that this size is smaller than but still a measure for the actual extent of the magnetic texture.

The video contrast is enhanced by the microscope performing background subtraction. Since we have access to both unprocessed images and used background images, sample drifts occurring can be detected at the confinement edge and quantified with precision well below the single-pixel regime. In the analysis, the drift can thus be compensated. Furthermore, comparing the position of the confinement edges for every measurement makes it possible to establish a reference coordinate frame. All detected skyrmion positions are expressed in this coordinate system. There, the observations are compared with all the conducted measurements.

A further important part of the analysis is the detection of skyrmion boundary (domain wall) positions. These cannot be obtained directly from single-frame images since the magnetic contrast in images from the Kerr microscope is too low. The skyrmions observed here are of micrometer size and their center of mass can therefore be detected and located precisely since they cause an average difference in the intensity level over all the several pixels that they cover. However, the domain walls present at the skyrmion boundaries are of widths in the subpixel regime^{14,63}. Therefore, the intensity edge originating from the transition between the skyrmion core and the ferromagnetic background would be expected to occur within one pixel but the present noise prohibits even a skyrmion boundary (SB) detection with pixel accuracy. Nevertheless, the SB can be determined accurately when averaging over similar frames due to gained statistics regarding the position and noise being averaged out. Therefore, the individual frames are assembled in groups such that each group contains skyrmions located at one specific position. The intensities of those frames are then averaged within every group to average out noise. Edge-preserving bilateral filtering is used to further reduce the noise present despite the frame averaging. The position of the SB per pinning site is then obtained as the contour where the filtered intensity profile intersects the mean value between core and ferromagnetic background level. The group elements are selected by skyrmion center coordinates corresponding to the centers of peaks in the probability density distribution. Due to the selection by a small range of center coordinates, we consider only skyrmions with negligible variations and hence ensure that the SB position is preserved in the averaging. Still, at least 350 corresponding to 3.7% of the total observations are considered per pinning site and hence allow for an adequate determination of the SB position.

Micromagnetic simulation setup. To understand and support the experimental findings, nano-scale micromagnetic simulations are performed using the *mumax3* simulation package^{14,65–67}. Similar to the experimental study of the skyrmion inside a small confinement, a single skyrmion is simulated inside a square box with open boundary conditions. The side length is chosen to be about four times the size of the largest simulated skyrmion such that effects of the sample edge are negligible in the central region of the sample. There, different domain wall pinning regions are exemplarily created by locally lowering the effective PMA strength K_{eff} to 20%. The skyrmion size is tuned via an external OOP magnetic field. The system evolves under the finite temperature Landau-Lifschitz-Gilbert equation for 60 μs and is sampled every 1 ns. As in the experimental setup, the *trackpy* package is used for skyrmion detection based on greyscale images of the OOP magnetization⁶⁴.

Typical nano-scale sample parameters were employed for a $128 \times 128 \times 1 \text{ nm}^3$ sample^{68–70}. A cell size of $1 \times 1 \times 1 \text{ nm}^3$ is used and the sample has a saturation magnetization of $M_s = 1 \text{ MA/m}$, exchange stiffness of $A_{\text{ex}} = 15 \text{ pJ/m}$ and Gilbert damping of $\alpha = 0.01$. The demagnetization energy is accounted for by employing an effective PMA strength of $K_{\text{eff}} = K_u - 0.5 \cdot \mu_0 M_s^2$ with $K_u = 1.1 \text{ MJ/m}^3$, which is equivalent to considering an infinite thin film and explicitly calculating the demagnetization field in the case of a homogeneous magnetization^{68,71}. In the presence of skyrmion-type magnetic spin structures, this formalism is however a well-established approximation for performance reasons, while furthermore not leading to boundary effects due to stray fields^{68,71}. The interfacial DMI strength is chosen to $D = 0.95 \cdot D_{\text{crit}}$ with $D_{\text{crit}} = 4 \sqrt{A_{\text{ex}} K_{\text{eff}}} / \pi$ and skyrmions are stabilized by applying external OOP magnetic fields of 0.05 T and 0.15 T for large and small skyrmions, respectively. The pinning areas have a size of $4 \times 10 \text{ nm}^2$ and the temperature is set to 100 K.

Data availability

The data that support the findings of this study are available from the corresponding author upon reasonable request.

Code availability

The codes associated with the evaluation of experimental data and the simulation presented in this paper are available from the corresponding author upon reasonable request.

Received: 4 August 2021; Accepted: 16 May 2022;

Published online: 06 June 2022

References

- Bogdanov, A. & Hubert, A. Thermodynamically stable magnetic vortex states in magnetic crystals. *J. Magn. Magn. Mater.* **138**, 255–269 (1994).
- Mühlbauer, S. et al. Skyrmion Lattice in a Chiral Magnet. *Science* **323**, 915–919 (2009).
- Nagaosa, N. & Tokura, Y. Topological properties and dynamics of magnetic skyrmions. *Nat. Nanotechnol.* **8**, 899–911 (2013).
- Fert, A., Reyren, N. & Cros, V. Magnetic skyrmions: advances in physics and potential applications. *Nat. Rev. Mater.* **2**, 1–15 (2017).
- Finocchio, G., Büttner, F., Tomasello, R., Carpentieri, M. & Kläui, M. Magnetic skyrmions: from fundamental to applications. *J. Phys. Appl. Phys.* **49**, 423001 (2016).
- Zhang, X., Ezawa, M. & Zhou, Y. Magnetic skyrmion logic gates: conversion, duplication and merging of skyrmions. *Sci. Rep.* **5**, 9400 (2015).
- Back, C. et al. The 2020 skyrmionics roadmap. *J. Phys. Appl. Phys.* **53**, 363001 (2020).
- Luo, S. & You, L. Skyrmion devices for memory and logic applications. *APL Mater.* **9**, 050901 (2021).
- Parkin, S. & Yang, S.-H. Memory on the racetrack. *Nat. Nanotechnol.* **10**, 195–198 (2015).
- Fert, A., Cros, V. & Sampaio, J. Skyrmions on the track. *Nat. Nanotechnol.* **8**, 152–156 (2013).
- Luo, S. et al. Reconfigurable Skyrmion Logic Gates. *Nano Lett.* **18**, 1180–1184 (2018).
- Walker, B. W. et al. Skyrmion logic clocked via voltage-controlled magnetic anisotropy. *Appl. Phys. Lett.* **118**, 192404 (2021).
- Everschor-Sitte, K., Masell, J., Reeve, R. M. & Kläui, M. Perspective: Magnetic skyrmions—Overview of recent progress in an active research field. *J. Appl. Phys.* **124**, 240901 (2018).
- Zázvorka, J. et al. Thermal skyrmion diffusion used in a reshuffler device. *Nat. Nanotechnol.* **14**, 658–661 (2019).
- Brems, M. A., Kläui, M. & Virnau, P. Circuits and excitations to enable Brownian token-based computing with skyrmions. *Appl. Phys. Lett.* **119**, 132405 (2021).
- Jibiki, Y. et al. Skyrmion Brownian circuit implemented in continuous ferromagnetic thin film. *Appl. Phys. Lett.* **117**, 082402 (2020).
- Zázvorka, J. et al. Skyrmion Lattice Phases in Thin Film Multilayer. *Adv. Funct. Mater.* **30**, 2004037 (2020).
- Baláz, P., Paściak, M. & Hlinka, J. Melting of Néel skyrmion lattice. *Phys. Rev. B* **103**, 174411 (2021).
- Reichhardt, C. & Reichhardt, C. J. O. Depinning and nonequilibrium dynamic phases of particle assemblies driven over random and ordered substrates: a review. *Rep. Prog. Phys.* **80**, 026501 (2016).
- Wang, J. et al. Controllable transport of a skyrmion in a ferromagnetic narrow channel with voltage-controlled magnetic anisotropy. *J. Phys. Appl. Phys.* **51**, 205002 (2018).
- Prychynenko, D. et al. Magnetic Skyrmion as a Nonlinear Resistive Element: A Potential Building Block for Reservoir Computing. *Phys. Rev. Appl.* **9**, 014034 (2018).
- Pinna, D., Bourianoff, G. & Everschor-Sitte, K. Reservoir Computing with Random Skyrmion Textures. *Phys. Rev. Appl.* **14**, 054020 (2020).
- Reichhardt, C., Reichhardt, C. J. O. & Milosevic, M. V. Statics and Dynamics of Skyrmions Interacting with Pinning: A Review. *ArXiv210210464 Cond-Mat* (2021).
- Litzius, K. et al. Skyrmion Hall effect revealed by direct time-resolved X-ray microscopy. *Nat. Phys.* **13**, 170–175 (2017).
- Jiang, W. et al. Direct observation of the skyrmion Hall effect. *Nat. Phys.* **13**, 162–169 (2017).
- Zeissler, K. et al. Diameter-independent skyrmion Hall angle observed in chiral magnetic multilayers. *Nat. Commun.* **11**, 428 (2020).
- Tan, A. K. C. et al. Visualizing the strongly reshaped skyrmion Hall effect in multilayer wire devices. *Nat. Commun.* **12**, 4252 (2021).
- Hanneken, C., Kubetzka, A., von Bergmann, K. & Wiesendanger, R. Pinning and movement of individual nanoscale magnetic skyrmions via defects. *N. J. Phys.* **18**, 055009 (2016).
- Legrand, W. et al. Room-Temperature Current-Induced Generation and Motion of sub-100 nm Skyrmions. *Nano Lett.* **17**, 2703–2712 (2017).
- Gross, I. et al. Skyrmion morphology in ultrathin magnetic films. *Phys. Rev. Mater.* **2**, 024406 (2018).
- Iwasaki, J., Mochizuki, M. & Nagaosa, N. Universal current-velocity relation of skyrmion motion in chiral magnets. *Nat. Commun.* **4**, 1463 (2013).
- Liu, Y.-H. & Li, Y.-Q. A mechanism to pin skyrmions in chiral magnets. *J. Phys. Condens. Matter* **25**, 076005 (2013).
- Derras-Chouk, A. & Chudnovsky, E. M. Skyrmions near defects. *J. Phys. Condens. Matter* **33**, 195802 (2021).
- Navau, C., Del-Valle, N. & Sanchez, A. Interaction of isolated skyrmions with point and linear defects. *J. Magn. Magn. Mater.* **465**, 709–715 (2018).
- Choi, H. C., Lin, S.-Z. & Zhu, J.-X. Density functional theory study of skyrmion pinning by atomic defects in MnSi. *Phys. Rev. B* **93**, 115112 (2016).
- Lima Fernandes, I., Bouaziz, J., Blügel, S. & Lounis, S. Universality of defect-skyrmion interaction profiles. *Nat. Commun.* **9**, 4395 (2018).
- Arjana, I. G., Lima Fernandes, I., Chico, J. & Lounis, S. Sub-nanoscale atom-by-atom crafting of skyrmion-defect interaction profiles. *Sci. Rep.* **10**, 14655 (2020).
- Müller, J. & Rosch, A. Capturing of a magnetic skyrmion with a hole. *Phys. Rev. B* **91**, 054410 (2015).
- Vizarim, N. P., Reichhardt, C., Venegas, P. A. & Reichhardt, C. J. O. Guided skyrmion motion along pinning array interfaces. *J. Magn. Magn. Mater.* **528**, 167710 (2021).
- Woo, S. et al. Observation of room-temperature magnetic skyrmions and their current-driven dynamics in ultrathin metallic ferromagnets. *Nat. Mater.* **15**, 501–506 (2016).
- Hrabec, A. et al. Current-induced skyrmion generation and dynamics in symmetric bilayers. *Nat. Commun.* **8**, 15765 (2017).
- Akhtar, W. et al. Current-Induced Nucleation and Dynamics of Skyrmions in a Co-based Heusler alloy. *Alloy. Phys. Rev. Appl.* **11**, 034066 (2019).
- Juge, R. et al. Current-Driven Skyrmion Dynamics and Drive-Dependent Skyrmion Hall Effect in an Ultrathin Film. *Phys. Rev. Appl.* **12**, 044007 (2019).
- Zivieri, R. et al. Configurational entropy of magnetic skyrmions as an ideal gas. *Phys. Rev. B* **99**, 174440 (2019).
- Rodrigues, D. R., Abanov, A., Sinova, J. & Everschor-Sitte, K. Effective description of domain wall strings. *Phys. Rev. B* **97**, 134414 (2018).
- Wang, X. S., Yuan, H. Y. & Wang, X. R. A theory on skyrmion size. *Commun. Phys.* **1**, 1–7 (2018).
- Rodrigues, D. R., Everschor-Sitte, K., Gerber, S. & Horenko, I. A deeper look into natural sciences with physics-based and data-driven measures. *iScience* **24**, 102171 (2021).
- Horenko, I., Rodrigues, D., O’Kane, T. & Everschor-Sitte, K. Scalable computational measures for entropic detection of latent relations and their

- applications to magnetic imaging. *Commun. Appl. Math. Comput. Sci.* **16**, 267–297 (2021).
49. Bourianoff, G., Pinna, D., Sitte, M. & Everschor-Sitte, K. Potential implementation of reservoir computing models based on magnetic skyrmions. *AIP Adv.* **8**, 055602 (2018).
 50. Nayak, A. K. et al. Magnetic antiskyrmions above room temperature in tetragonal Heusler materials. *Nature* **548**, 561–566 (2017).
 51. Ross, A. et al. Structural sensitivity of the spin Hall magnetoresistance in antiferromagnetic thin films. *Phys. Rev. B* **102**, 094415 (2020).
 52. Jani, H. et al. Antiferromagnetic half-skyrmions and bimerons at room temperature. *Nature* **590**, 74–79 (2021).
 53. Dohi, T., DuttaGupta, S., Fukami, S. & Ohno, H. Formation and current-induced motion of synthetic antiferromagnetic skyrmion bubbles. *Nat. Commun.* **10**, 5153 (2019).
 54. Legrand, W. et al. Room-temperature stabilization of antiferromagnetic skyrmions in synthetic antiferromagnets. *Nat. Mater.* **19**, 34–42 (2020).
 55. Leliaert, J., Gypens, P., Milošević, M. V., Waeyenberge, B. V. & Mulkers, J. Coupling of the skyrmion velocity to its breathing mode in periodically notched nanotracks. *J. Phys. Appl. Phys.* **52**, 024003 (2018).
 56. Xia, H. et al. Control and manipulation of antiferromagnetic skyrmions in racetrack. *J. Phys. Appl. Phys.* **50**, 293002 (2017).
 57. Suess, D. et al. Spin Torque Efficiency and Analytic Error Rate Estimates of Skyrmion Racetrack Memory. *Sci. Rep.* **9**, 4827 (2019).
 58. Grollier, J. et al. Neuromorphic spintronics. *Nat. Electron.* **3**, 360–370 (2020).
 59. Zhang, X. et al. Skyrmion-electronics: writing, deleting, reading and processing magnetic skyrmions toward spintronic applications. *J. Phys. Condens. Matter* **32**, 143001 (2020).
 60. Song, K. M. et al. Skyrmion-based artificial synapses for neuromorphic computing. *Nat. Electron.* **3**, 148–155 (2020).
 61. Pinna, D. et al. Skyrmion Gas Manipulation for Probabilistic Computing. *Phys. Rev. Appl.* **9**, 064018 (2018).
 62. Nozaki, T. et al. Brownian motion of skyrmion bubbles and its control by voltage applications. *Appl. Phys. Lett.* **114**, 012402 (2019).
 63. Song, C. et al. Commensurability between Element Symmetry and the Number of Skyrmions Governing Skyrmion Diffusion in Confined Geometries. *Adv. Funct. Mater.* **31**, 2010739 (2021).
 64. Allan, D. B., Caswell, T., Keim, N. C. & van der Wel, C. M. *trackpy: Trackpy v0.4.1*. (Zenodo, 2018). <https://doi.org/10.5281/zenodo.1226458>.
 65. Mulkers, J., Van Waeyenberge, B. & Milošević, M. V. Effects of spatially engineered Dzyaloshinskii-Moriya interaction in ferromagnetic films. *Phys. Rev. B* **95**, 144401 (2017).
 66. Leliaert, J. et al. Adaptively time stepping the stochastic Landau-Lifshitz-Gilbert equation at nonzero temperature: Implementation and validation in MuMax3. *AIP Adv.* **7**, 125010 (2017).
 67. Vansteenkiste, A. et al. The design and verification of MuMax3. *AIP Adv.* **4**, 107133 (2014).
 68. Rohart, S. & Thiaville, A. Skyrmion confinement in ultrathin film nanostructures in the presence of Dzyaloshinskii-Moriya interaction. *Phys. Rev. B* **88**, 184422 (2013).
 69. McKeever, B. F. et al. Characterizing breathing dynamics of magnetic skyrmions and antiskyrmions within the Hamiltonian formalism. *Phys. Rev. B* **99**, 054430 (2019).
 70. Miron, I. M. et al. Fast current-induced domain-wall motion controlled by the Rashba effect. *Nat. Mater.* **10**, 419–423 (2011).
 71. Hubert, A. & Schäfer, R. *Magnetic Domains: The Analysis of Magnetic Microstructures*. (Springer-Verlag, 1998).

Acknowledgements

The authors acknowledge funding from TopDyn, SFB TRR 146 (project #233630050), SFB TRR 173 Spin+X (project A01 #268565370 and project B12 #268565370). The work was additionally funded by the Deutsche Forschungsgemeinschaft (DFG, German Research Foundation) Project No. 403502522 (SPP 2137 Skyrmionics) as well as the Emmy Noether project #320163632. This project has received funding from the European Research Council (ERC) under the European Union's Horizon 2020 research and innovation programme under grant agreement No. 863155 (s-Nebula) and No. 856538 (ERC-SyG 3D MAGIC). Open access funding is enabled and organized by Projekt DEAL. J.Z. acknowledges the support of Charles University grant PRIMUS/20/SCI/018.

Author contributions

M.K., P.V., and J.Z. supervised the study. N.K., B.S., and M.V. fabricated and characterized the multilayer samples. R.G. prepared the measurement setup, conducted the experiments using the Kerr microscope and evaluated the experimental data with the help of J.Z.; M.B. performed the micromagnetic simulation with guidance of D.R. and evaluated the simulation data. R.G. prepared the manuscript with the help of M.K., P.V., D.R., K.E., J.Z., M.B., and T.D.; all authors commented on the manuscript.

Funding

Open Access funding enabled and organized by Projekt DEAL.

Competing interests

The authors declare no competing interests.

Additional information

Supplementary information The online version contains supplementary material available at <https://doi.org/10.1038/s41467-022-30743-4>.

Correspondence and requests for materials should be addressed to Mathias Kläui.

Peer review information *Nature Communications* thanks the anonymous reviewer(s) for their contribution to the peer review of this work. Peer reviewer reports are available.

Reprints and permission information is available at <http://www.nature.com/reprints>

Publisher's note Springer Nature remains neutral with regard to jurisdictional claims in published maps and institutional affiliations.



Open Access This article is licensed under a Creative Commons Attribution 4.0 International License, which permits use, sharing, adaptation, distribution and reproduction in any medium or format, as long as you give appropriate credit to the original author(s) and the source, provide a link to the Creative Commons license, and indicate if changes were made. The images or other third party material in this article are included in the article's Creative Commons license, unless indicated otherwise in a credit line to the material. If material is not included in the article's Creative Commons license and your intended use is not permitted by statutory regulation or exceeds the permitted use, you will need to obtain permission directly from the copyright holder. To view a copy of this license, visit <http://creativecommons.org/licenses/by/4.0/>.

© The Author(s) 2022

4.1.1. Supplementary Information

Publication Information


The following Supplementary Information is published with the article in *Nature Communications*:

Skyrmion pinning energetics in thin film systems

Raphael Gruber, Jakub Zázvorka, Maarten A. Brems, Davi R. Rodrigues, Takaaki Dohi, Nico Kerber, Boris Seng, Mehran Vafaei, Karin Everschor-Sitte, Peter Virnau & Mathias Kläui

Nature Communications **13**, 3144 (2022).

DOI: [10.1038/s41467-022-30743-4](https://doi.org/10.1038/s41467-022-30743-4)

Copyright Information:  CC BY 4.0 Creative Commons Attribution 4.0 International License

Editorial Note: The blue header/footer bars were added for inclusion in this dissertation and are not part of the original publication.

Contributions

The author contributions for this project and article are described in detail in section 5.3.

Skyrmion pinning energetics in thin film systems

Supplementary Information

Raphael Gruber¹, Jakub Zázvorka², Maarten A. Brems¹, Davi R. Rodrigues^{1,3,4}, Takaaki Dohi¹, Nico Kerber¹, Boris Seng^{1,5}, Mehran Vafae^{1,6}, Karin Everschor-Sitte^{1,4,7}, Peter Virnau¹, Mathias Kläui*¹

¹ Institute of Physics, Johannes Gutenberg-Universität Mainz, Staudingerweg 7, Mainz 55128, Germany

² Institute of Physics, Faculty of Mathematics and Physics, Charles University, Ke Karlovu 5, Prague 12116, Czech Republic

³ Dipartimento di Ingegneria Elettrica e dell'Informazione, Politecnico di Bari, Via E. Orabona 4, Bari 70125, Italy

⁴ Faculty of Physics, University of Duisburg-Essen, Lotharstraße 1, Duisburg 47057, Germany

⁵ Institut Jean Lamour, UMR CNRS 7198, Université de Lorraine, 2 allée André Guinier, Nancy 54011, France

⁶ Singulus Technologies AG, Hanauer Landstraße 103, Kahl am Main 63796, Germany

⁷ Center for Nanointegration Duisburg- Essen (CENIDE), University of Duisburg-Essen, Carl-Benz-Straße 199, Duisburg 47057, Germany

*E-mail: klaeui@uni-mainz.de

Supplementary Notes

Supplementary Note 1

Supplementary Fig. 1 provides additional information regarding the skyrmion occurrences in the thin film sample. Besides the probability of finding a skyrmion at certain positions, it shows the positions of skyrmions in the beginning and at the end of the observations in Supplementary Fig. 1a. Whereas the newly nucleated skyrmions (blue dots) are evenly spread over the sample, the skyrmions at the end of every video (red dots) are as expected often found at pinning sites. The histograms along the x and y axis indicate furthermore that the skyrmion distribution is uniform along the sample axes throughout the measurement time.

Within the observed area, the positions featuring strong pinning appear evenly spread. The green annotations in Supplementary Fig. 1a exemplarily provide a few distances in micrometers between pinning spots. To study the spatial distribution of pinning sites, we therefore also look at the Fourier transformation of the histogram of skyrmion center positions. The radial dependence of the FFT intensity is depicted in Supplementary Fig. 1b as a function of real space distances. The distances denoted in Supplementary Fig. 1a are indicated by the green solid lines and lay within the FFT region with high intensities. This indicates a range of characteristic distances between positions at which skyrmions appear for a significant amount of time. We therefore conclude the existence of typical lengths under which strong pinning centers occur. In the analysis, we restrict ourselves to the radial dependence of the FFT since the angular distribution is homogeneous meaning that there is no preferred axis in the sample along which pinning sites are observed.

The detailed investigation of the underlying physical reason for this repeated appearance of pinning centers is beyond the scope of this paper. However, since locally varying material parameters result in the occurrence of pinning sites, this effect is potentially featured by a periodic appearance of impurities which can be governed by the physics of the manufacturing procedure of the amorphous multilayer stack. Therefore, the sample growth must be considered when fabricating a stack with specific pinning properties.

Supplementary Note 2

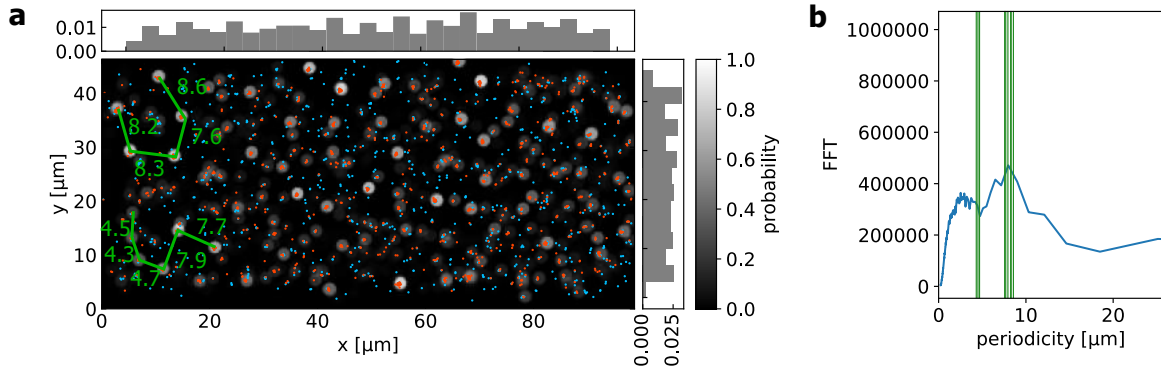
Skyrmions at pinning site 1 can appear at slightly varying positions depending on the skyrmion size. Supplementary Fig. 2a shows skyrmion boundaries for two different occurring skyrmion center of mass positions, which are indicated in Supplementary Fig. 2b. The SB position coincides at one side for both skyrmion sizes indicating a pinned behavior. However, the extension is different on the other side and determined by the size. Therefore, different skyrmion center positions can occur at this particular site (see Supplementary Fig. 2b). The size difference belonging to this variation of the center positions is visible in Supplementary Fig. 2c.

Supplementary Note 3

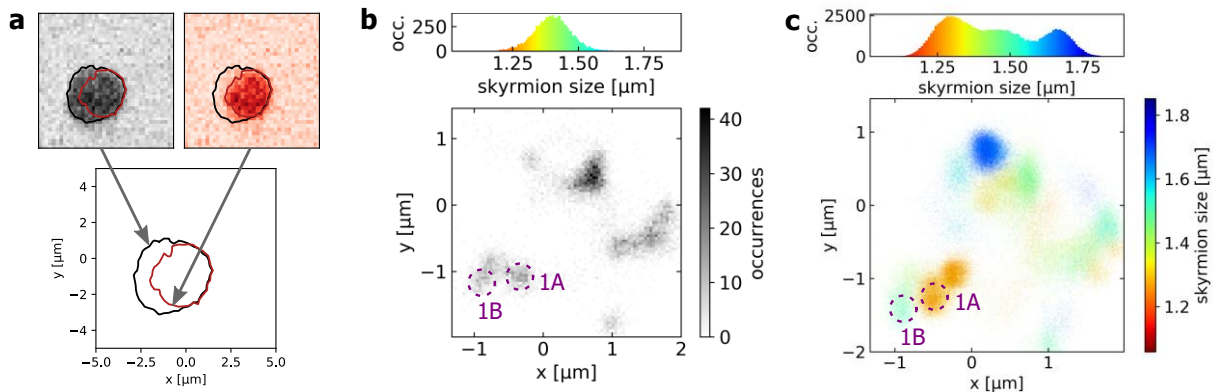
The small skyrmions appear between the regions of lowered anisotropy introduced in the simulation. Supplementary Fig. 3a shows the probability map of skyrmion center occurrences as presented in Fig. 5. Supplementary Fig. 3c,e show the perpendicular magnetization component of two such simulated skyrmions at different positions exemplarily. As proposed by our SB pinning concept, the area with reduced anisotropy is thereby occupied mainly by the SB depicted in white. Similarly, Supplementary Fig. 3b,d,f show the center occurrence probability and magnetization components along the z-direction for two simulated skyrmions, respectively. Now, the large skyrmions do not fit between the boxes anymore with their core. Instead, they arrange above or below to maximize the overlap of their SB with the reduced anisotropy region while keeping the same overlap small for their core.

During that process, the skyrmions are also deformed with average eccentricities of 0.05 and 0.11 for the small and the large skyrmion, respectively.

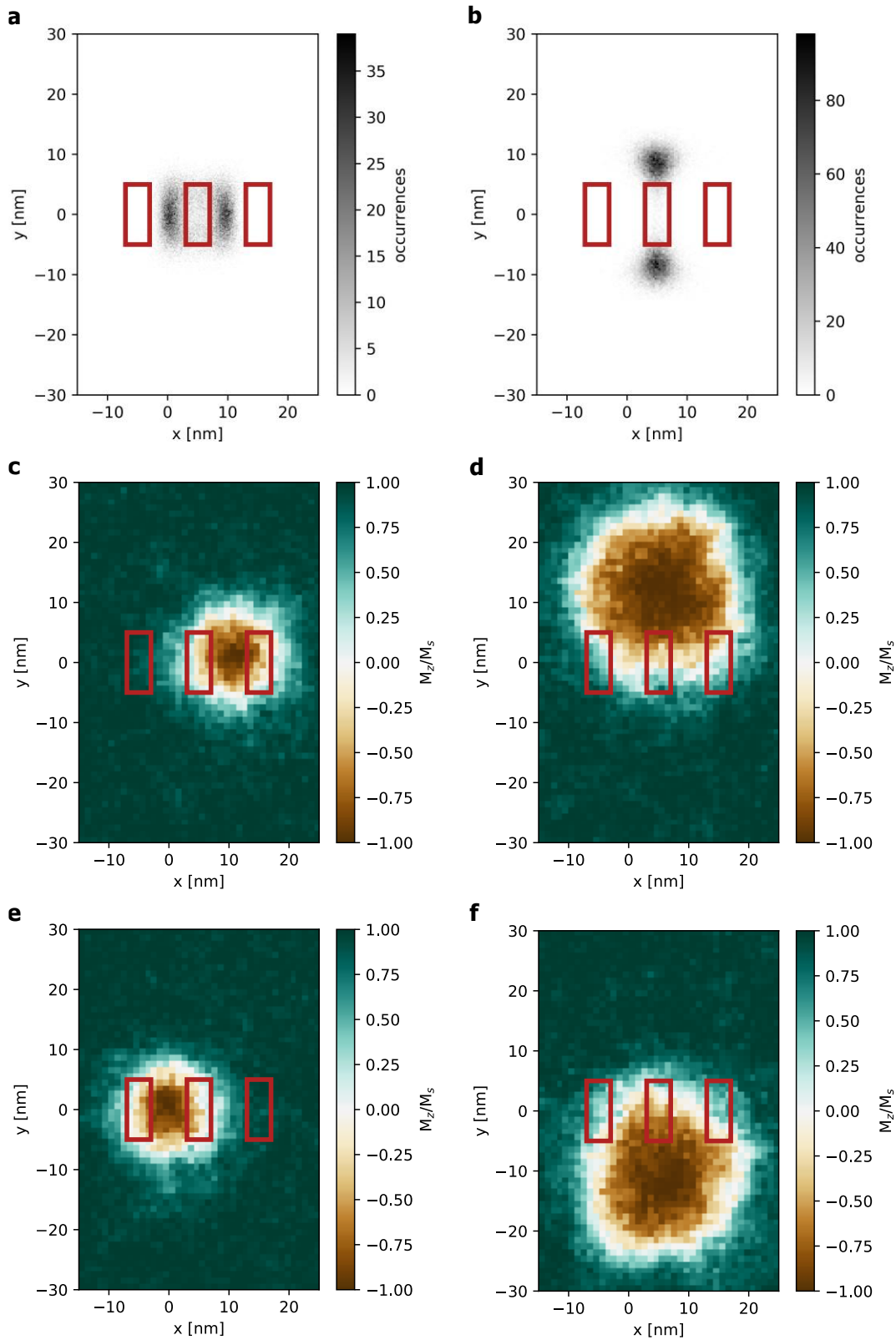
Supplementary Figures



Supplementary Fig. 1. Occurrence of the pinning. (a) The greyscale image shows the probability of skyrmions covering certain pixels as established in Fig. 1. The blue and red scattered spots depict the skyrmion center positions at the beginning and end of every video, respectively. The normalized histograms on the top and right show the uniformity of the x - and y -coordinate distribution of every observed skyrmion center. The green lines with annotations in micrometers show distances between arbitrarily selected pinning sites. In (b), the radial part of the FFT intensities of the skyrmion occurrences from (a) is depicted whereby the frequencies are rescaled to real space distances. The green lines indicate the distances denoted in (a).



Supplementary Fig. 2. Pinning of differently sized skyrmions at same pinning site. (a) The bottom coordinate frame shows the contours of the two distinct skyrmion sizes occurring at the same pinning site during the measurement at $-37 \mu\text{T}$. The above panels show the Kerr intensities of the respective skyrmions analogously to Fig. 4. (b) Skyrmion center occurrence probabilities at $-37 \mu\text{T}$ from Fig. 2c. At the pinning site which was labeled as 1 in the main text, the skyrmion center position can vary slightly depending on the skyrmion size. Two possible positions labeled as 1A and 1B are picked which correspond to the red and black boundaries and intensities shown in (a), respectively. (c) Similarly, the two positions presented in (b) are indicated also in the size dependence plot from Fig. 2a.



Supplementary Fig. 3. Arrangements of skyrmions in boundary pinning simulation. (a-b) Histograms of occurring skyrmion center positions for external out-of-plane fields of (a) 0.15 T and (b) 0.05 T based on micromagnetic simulations as presented in Fig. 5. (c-f) The z-component of the unitary magnetization direction M_z/M_s of simulated skyrmions. The small skyrmions at 0.15 T in (c,e) fit between the pinning areas which are thereby covered by the SB, but not the core. In contrast, the large skyrmions at 0.05 T in (d,f) move to the top and bottom to maximize the overlap of the SB (corresponding to white region) with the area of reduced anisotropy while not covering it with their cores.

4.2. Additional Results and Experimental Remarks

Additional results and methods related to the article in section 4.1 are explained in detail in my Master thesis [140].

Specifically, my Master thesis contains information about:

- the perpendicular alignment of OOP and IP field coils by monitoring the hysteresis shift
- determination of the magnetic background field due to the earth magnetic field as well as due to magnetic fields in the surrounding by analyzing the field offset of the hysteresis loop
- explanation of the background subtraction method for enhanced magnetic contrast
- determination and compensation of physical sample drifts when recording videos with background subtraction
- coordinate mapping for independent measurements of the the same sample area
- analysis of the skyrmion boundary occurrence as shown in the article in section 4.1 [64] as well as for a different sample, where a skyrmion circles around a strong pinning site

4.3. Author Contributions

I performed all the experiments at the Kerr microscope on my own. Previous measurements of similar kind were done by Chengkun Song and analyzed by Maarten A. Brems. The majority of the data analysis shown here was done by me and I also developed the Python code that I used. I specifically performed the skyrmion detection using *trackpy* [131]. With the help of Jakub Zázvorka, I calculated the probability density map of skyrmion occurrences to extract the energy landscape. For the experiments, I analyzed the skyrmion occurrence positions yielding the size-dependent pinning effect. I also developed and performed the analysis of domain boundaries for both skyrmions and stripe domains. Maarten A. Brems had the idea of investigating the effect for stripe domains.

The micromagnetic simulations were performed and analyzed by Maarten A. Brems with the consulting help of Davi R. Rodrigues. The schematic Fig. 3 in section 4.1 [64] was created by me and conceptualized by Maarten A. Brems and myself based on an idea by Karin Everschor-Sitte and. The magnetic multilayer samples were deposited by Mehran Vafaei and Jakub Zázvorka. The patterning of the devices was done by Nico Kerber and Boris Seng.

Davi R. Rodrigues helped with the interpretation of the results and with the paper outline design. He also suggested the micromagnetic simulations. Karin Everschor-Sitte, Peter Virnau and Mathias Kläui supervised and guided this work. Takaaki Dohi provided consulting help as postdoctoral researcher in our skyrmion research group. Peter Virnau and Mathias Kläui contributed as PhD supervisors and principal investigators and provided advice in regular discussions.

5. 300-Times-Increased Diffusive Skyrmion Dynamics and Effective Pinning Reduction by Periodic Field Excitation

5.1. Published Article

Publication Information


The following article is published in *Advanced Materials*:

300-Times-Increased Diffusive Skyrmion Dynamics and Effective Pinning Reduction by Periodic Field Excitation

Raphael Gruber, Maarten A. Brems, Jan Rothörl, Tobias Sparmann, Maurice Schmitt, Iryna Kononenko, Fabian Kammerbauer, Maria-Andromachi Syskaki, Oded Farago, Peter Virnau & Mathias Kläui

Advanced Materials **35**(17), 2208922 (2025).

DOI: [10.1002/adma.202208922](https://doi.org/10.1002/adma.202208922)


Copyright Information:  **CC BY-NC 4.0** Creative Commons Attribution-NonCommercial 4.0 International License

Editorial Note: The blue header/footer bars were added for inclusion in this dissertation and are not part of the original publication.

Contributions

The author contributions for this project and article are described in detail in section 5.3.

Experimental Note

Documentation of my experiments used for this article are available for lab members on *eLabFTW* ( labbook database ID **5834**).

RESEARCH ARTICLE

300-Times-Increased Diffusive Skyrmion Dynamics and Effective Pinning Reduction by Periodic Field Excitation

Raphael Gruber, Maarten A. Brems, Jan Rothörl, Tobias Sparmann, Maurice Schmitt, Iryna Kononenko, Fabian Kammerbauer, Maria-Andromachi Syskaki, Oded Farago, Peter Virnau, and Mathias Kläui*

Thermally induced skyrmion dynamics, as well as skyrmion pinning effects, in thin films have attracted significant interest. While pinning poses challenges in deterministic skyrmion devices and slows down skyrmion diffusion, for applications in non-conventional computing, both pinning of an appropriate strength and skyrmion diffusion speed are key. Here, periodic field excitations are employed to realize an increase of the skyrmion diffusion by more than two orders of magnitude. Amplifying the excitation, a drastic reduction of the effective skyrmion pinning, is reported, and a transition from pinning-dominated diffusive hopping to dynamics approaching free diffusion is observed. By tailoring the field oscillation frequency and amplitude, a continuous tuning of the effective pinning and skyrmion dynamics is demonstrated, which is a key asset and enabler for non-conventional computing applications. It is found that the periodic excitations additionally allow stabilization of skyrmions at different sizes for field values that are inaccessible in static systems, opening up new approaches to ultrafast skyrmion motion by transiently exciting moving skyrmions.

applications in data storage and logic in thin film multilayer systems. The topologically non-trivial magnetic skyrmion texture^[3,4] is stabilized by the Dzyaloshinskii–Moriya interaction (DMI) and exhibits quasi-particle properties.^[3–6] Hence, the skyrmion can serve as stable information carrier in logic^[6–9] and memory^[4,10–12] devices. Thereby, tailoring the skyrmion dynamics is a key asset for efficient device operation. For certain devices, deterministic motion is required, which can be realized by a number of mechanisms including external fields, temperature, as well as their gradients,^[13–17] and by spin torques generated by currents.^[18–26] In the latter case, the skyrmion velocity can be efficiently set by the applied current density. However, skyrmions can also undergo thermally activated diffusion,^[6,27–31] which

1. Introduction

Skyrmions are chiral magnetic structures^[1–4] that are of major scientific interest as they are promising candidates for various


is dependent on temperature and sample-specific material characteristics^[6,27,29] and has been lacking means to control the diffusive motion. Thermal diffusion is desired for various applications in non-conventional computing with the performance scaling with the diffusion. Non-conventional computing has recently moved to the focus of research because it enables low-power realizations of complex computing tasks, for which a special need has become apparent in the context of the enormous power consumption of information technology. In case of skyrmions used in Brownian computing concepts,^[6,9,29,30,32–34] the energy necessary for the actual computation may predominantly be provided as thermal activation from the surrounding. Specifically, skyrmion diffusion has been employed recently in a Brownian reshuffler^[6] as a decorrelation mechanism for probabilistic computing,^[6,8,35] but also in Brownian reservoir computing^[34] and in Brownian token-based computing.^[9,30–32] In all these skyrmion-based computing devices, both operation speed and energy efficiency are heavily dependent on and scaling with the skyrmion diffusion speed: In Brownian token-based computing on the one hand, diffusion is used as propagation mechanism for the skyrmions to search forward paths in token-based computing networks. On the other hand, in Brownian reservoir computing, skyrmion diffusion serves as automatic reset mechanism and is necessary to overcome device imperfections. Even though skyrmion diffusion on the reported time scales^[6] has recently been experimentally demonstrated to successfully enable Brownian reservoir computing,^[34] a faster operation of

R. Gruber, M. A. Brems, J. Rothörl, T. Sparmann, M. Schmitt, I. Kononenko, F. Kammerbauer, M.-A. Syskaki, P. Virnau, M. Kläui
Johannes Gutenberg-Universität Mainz
Institut für Physik
Staudingerweg 7, 55128 Mainz, Germany
E-mail: mathias.klaui@magnetism.ch

I. Kononenko
National Academy of Sciences of Ukraine
Institute of Applied Physics
58 Petropavlivska St., Sumy 40000, Ukraine

M.-A. Syskaki
Singulus Technologies AG
Hanauer Landstraße 103, 63796 Kahl am Main, Germany

O. Farago
Biomedical Engineering Department
Ben Gurion University of the Negev
Be'er Sheva 84105, Israel

 The ORCID identification number(s) for the author(s) of this article can be found under <https://doi.org/10.1002/adma.202208922>.

© 2023 The Authors. Advanced Materials published by Wiley-VCH GmbH. This is an open access article under the terms of the Creative Commons Attribution-NonCommercial License, which permits use, distribution and reproduction in any medium, provided the original work is properly cited and is not used for commercial purposes.

DOI: 10.1002/adma.202208922

such devices or especially processing input signals on shorter time scales—such as for the newly proposed audio recognition^[36]—is only enabled by higher skyrmion diffusion speeds. Unless strongly driven, the skyrmion dynamics has been found to be heavily impacted by size-dependent pinning effects that induce a non-flat effective energy landscape.^[27,37] Thus, pinning causes non-homogeneous probability densities for skyrmion occurrences,^[27] reducing the reliability of conventional skyrmion devices and making device operational properties vary between samples. Thus, pinning leads to unwanted and uncontrolled variations from device to device. Consequently, pinning can impede the functionality of devices relying on deterministic skyrmion motion and has additionally been shown to massively slow down skyrmion diffusion^[6] to the detriment of the performance of diffusion-exploiting devices.^[9] For skyrmion-based neuromorphic computing, skyrmion pinning of an appropriate strength can be an essential source of non-linearity, though one needs to be able to tune the pinning effect so it appropriately competes with other interactions in the system.^[34,38] Hence, there is a clear need for means to control the diffusion and attenuate pinning effects to achieve higher operation reliability and to speed up or even enable specific computations by enhanced diffusion as proposed for pinning-free thermal dynamics.^[39]

Periodic excitations of systems have become a topic of major interest recently as periodic modulation can not only vary the properties in time but even stabilize new states epitomized by Floquet states.^[40] In magnetic systems, periodic drive even in the classical limit has shown to excite eigenmodes—such as the skyrmion breathing mode in the GHz regime—and parametric pumping can be used to manipulate skyrmions.^[41] However, so far the impact on the motion and translational dynamics has not been explored.

In this work, we study how the skyrmion diffusion can be tuned by periodic excitations due to an oscillating out-of-plane magnetic field. In contrast to the well-studied case of static fields,^[6,28] we find that we can directly control the effective

pinning by applying field oscillations. Therefore, the observed effect can be a key enabler for non-conventional computing schemes. We find specifically that the skyrmion diffusion coefficient can be increased by more than two orders of magnitude at a constant temperature. Unlike other methods to tune skyrmion diffusion by external drives, which employ random sequencing of deterministic excitations,^[9] our method does not require to input any external randomness to the system. Instead, we solely rely on deterministic (periodic) excitation in the sub-Hz to kHz regime and exploit the intrinsic system properties. Beyond the drastic increase in the dynamics, we find that qualitatively, the dynamic regime changes from pinning-dominated to approaching free diffusion. Moreover, we observe that during the oscillating field excitation, skyrmions remain stable at field values that lead to much larger and smaller diameters than achievable for stationary field configurations. This observation may lay a foundation for ultrafast skyrmion transport by transiently tuning the size of skyrmions during brief application of spin torques or field gradients to move them.

2. Diffusion Enhanced and Tuned by Magnetic Field Oscillation

We investigate the diffusion of skyrmions in a Ta(4)/Co₂₀Fe₆₀B₂₀(0.85)/Ta(0.08)/MgO(2)/HfO₂(4) multilayer stack exhibiting low pinning.^[6,27] Layer thicknesses are given in nanometers in parentheses. The skyrmion density is controlled by the nucleation sequence including the out-of-plane (OOP) magnetic field and is kept low to suppress skyrmion–skyrmion interactions. The magnetic contrast is established in real time using Kerr microscopy with blue light and a time resolution of 62.5 ms. From the obtained movies, the skyrmions are detected and trajectories are linked with trackpy.^[42] We start by studying the diffusion using our previously established method.^[6,28] Then, we compare this diffusion to the dynamics when additionally applying an oscillating OOP field. **Figure 1a** shows

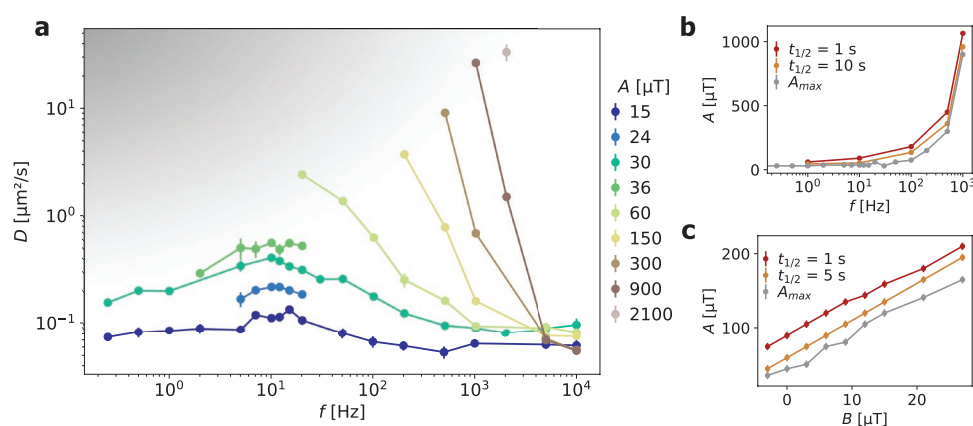


Figure 1. Enhanced skyrmion diffusion and stability in field oscillation. a) The skyrmion diffusion constant D depends on field oscillation frequency f and peak-to-peak amplitude A . Solid lines are guide to the eye along a frequency scan at fixed amplitude. For low frequencies, the maximum applicable field amplitude A_{max} , for which skyrmions do not annihilate, is limited. Therefore, not all amplitudes can be evaluated over the whole frequency range, the inaccessible region is indicated by the gray-shaded area. b) A_{max} (gray) increases with frequency. Higher amplitudes lead to an increasingly fast decay of the number of skyrmions. Amplitudes are shown that correspond to a half-life of 10 (orange) and 1 s (red). c) A_{max} also increases with increasing offset field values (i.e., skyrmion size) while keeping f constant at 100 Hz, as shown by the gray line. Amplitudes leading to half-lives of 5 (orange) and 1 s (red) behave similarly.

how the diffusion coefficient depends on field amplitude and frequency. Generally, larger amplitudes yield a higher diffusion constant. For constant amplitude, however, D increases from the unexcited case up to a peak at $f = (10 \pm 2)$ Hz and decreases again for higher frequencies. By variation of the frequency and amplitude, we can effectively tune the skyrmion diffusion coefficient even at a constant temperature. In particular, we find a maximum increase by a factor of ≈ 330 in the diffusion coefficient comparing excited and unexcited diffusion. And this maximum is currently only limited by the time resolution of our optical detection scheme. As discussed in Note S2 (Supporting Information), such an acceleration in the diffusion can be a key enabler for non-conventional computing by significantly decreasing the mean computation time of, for example, a skyrmion-based microscale Brownian half-adder.^[9]

Next, we discuss the mechanism of the diffusion enhancement effect due to size oscillations in the context of skyrmion boundary pinning. Previous investigations have shown (both experimentally and micromagnetically) that the position where a skyrmion is pinned at a fixed external field without applied oscillation is often not favorable when the skyrmion becomes smaller or larger.^[27] Thus, when the size of the skyrmion is changed by an out-of-plane field,^[6,27,43] the effective pinning energy landscape changes as well and new pinning positions become favorable.^[27] We note that the change in size due to field oscillations up to the kHz regime is qualitatively different from the skyrmion breathing mode,^[41] possibly leading to only segments of the skyrmion boundary moving to expand the skyrmion.^[27]

During the field oscillation, the skyrmion with its varying size experiences a variety of different effective energy landscapes, some of which may make it easier for the skyrmion to escape from its current position by thermal diffusion, and thus effectively depin the skyrmion. We note that the diffusion enhancement is generally larger when the oscillation amplitude is larger. We attribute this effect to a stronger variation of the skyrmion size making a broader range of energy landscapes accessible such that skyrmions become more likely to experience a low-pinning landscape. However, note that we cannot apply oscillations of arbitrary amplitude for every frequency due to skyrmions decaying differently rapidly. This stability effect is discussed in detail in the following Section 3. Sometimes, during the increased-size half-cycle, the boundary of the skyrmion may stick to a distant strong boundary pinning site and then contract toward this pinning site and thereby also increase diffusion. However first, the latter effect cannot explain why the diffusion coefficient decreases in the high-frequency limit. Second, we observe an increase in diffusion even if the skyrmion size during the oscillation never exceeds a given static size. In particular, the diffusion coefficient at a static field of 21 μT is $D = (0.105 \pm 0.006) \mu\text{m}^2 \text{s}^{-1}$, which is smaller than the diffusion coefficient for an oscillating field $\approx 30 \mu\text{T}$ with peak-to-peak amplitude of 15 μT , which is $D = (0.121 \pm 0.004) \mu\text{m}^2 \text{s}^{-1}$ even though the field is never reduced to values $< 21 \mu\text{T}$. This effect can also not be explained solely by expansion and pinning of the skyrmion boundary but requires consideration of thermal effects as discussed above.

Moreover, the change in diffusion depends clearly on the oscillation frequency. In the low-frequency limit, the size-

change-induced depinning is on the same timescale as the thermal depinning; therefore, the resulting diffusion coefficient approaches the unexcited case (limit toward 0 Hz). Therefore, those very low frequencies are in general not able to cause significant diffusion enhancement. In the high-frequency limit, the time interval during which the skyrmion remains in a possible low-pinning energy landscape is too short to significantly move away from its current position by thermal diffusion. It remains close to the position where it has been pinned and thus, high frequencies are not suitable to cause effective depinning either. In between these two limits, there exists a regime where, due to the change in size, the skyrmion temporarily is in a low-pinning energy landscape and can diffuse away from the position where it is pinned when it has a different size. Imagine—without loss of generality—the skyrmion is currently at a position where pinning is strong at small sizes but weak at much larger sizes. Assume that during a certain time interval as part of the field oscillation, the skyrmion is large enough such that it feels only weak pinning. Then, it thermally diffuses to a position where large skyrmions are pinned strongly, but very small skyrmions are pinned weakly. When the size is reduced, the skyrmion is weakly pinned and can diffuse again to a position where small skyrmions are pinned strongly. Thereby, the total diffusion is effectively increased.

To corroborate the proposed general concept of depinning of domain walls due to field excitations, we additionally analyze stripe domains in oscillating magnetic fields. We find that in analogy to the case of skyrmions, the stripes (or more specifically, the domain walls at their boundaries) move more for applied excitations, in particular for higher field amplitudes. Kerr microscopy data visualizing the effect can be found in Figure S2 (Supporting Information). To stress the scope of the effect beyond the specific system presented here, we furthermore analyze the influence of field excitations on various skyrmion systems. Plots similar to the one in Figure 1a are presented in the Supporting Information for a system with comparable skyrmion density but stronger pinning (Figure S3a, Supporting Information) as well as for a very dense skyrmion system (Figure S3b, Supporting Information) showing qualitatively consistent behavior. We note that in confined geometries such as wires, the size variations of the skyrmions due to field oscillations may be limited by the device edge effects. In Figure S3c (Supporting Information) however, we show that even in a wire geometry with a width of 1.8 skyrmion diameters, we can still enhance the diffusion by a factor of nearly 100. Hence, the mechanism of periodic field excitations is not strongly suppressed by geometrical confinements. Therefore, it appears widely applicable to as well as useful for a variation of different skyrmion systems and for several devices based on skyrmion diffusion in different geometries.

3. Skyrmion Stability in Oscillating Field

Next, we discuss the effect of the magnetic field oscillations on the stability of the skyrmions. In response to the magnetic field, the skyrmions vary their size during the oscillations. At constant external fields, we find that in our sample, skyrmions are only existing as a stable phase in the field range from

21 to 63 μT . For higher fields, skyrmions become too small and annihilate on time scales of <1 s whereas for lower fields, skyrmions start expanding into stripes as previously observed.^[31] When applying field oscillations, we choose a field offset that is inside this field range. We note however that we can apply field oscillation amplitudes of the order of milliteslas, hence orders of magnitude beyond what is applicable in the static case, when going to frequencies in the kHz regime: for low oscillation frequencies, the maximum applicable amplitude A_{max} without leading to a significant amount of skyrmions annihilations is coinciding well with the field region at which skyrmions are stable at static fields. However, beyond 10 Hz, A_{max} increases clearly with frequency. For frequencies in the kilohertz regime, even amplitudes of hundreds of microteslas can be applied even though the sample reaches saturation at 150 μT already in the static case. In Figure 1b, A_{max} as well as the field amplitudes corresponding to half-lives of 10 and 1 s are shown as function of the frequency.

We furthermore find that A_{max} is dependent on the offset field. Figure 1c shows A_{max} as well as the field amplitudes corresponding to half-life times of 5 and 1 s for varying offset fields. In particular, A_{max} increases with increasing offset. Thus, A_{max} increases with the average skyrmion size. We find that large skyrmions become stripe-like when the field is decreased to values <21 μT . In contrast, when starting with the smallest stable skyrmions and increasing the magnetic field to values >63 μT , the skyrmions annihilate.

We conclude that skyrmions start annihilating when their size drops below a threshold value. The skyrmion annihilation process is thermally activated and small skyrmions below this size threshold are not stable anymore but still require additional energy to overcome the topological stabilization energy barrier to annihilate. This leads to a finite probability of annihilation and an exponential decay of the number of skyrmions. Hence, the speed at which the skyrmions decay depends on the time interval during which the size is below the threshold for stability. However, the fraction of a time-span for which the field is below a certain value depends on the amplitude only, not on the frequency. Therefore, we conclude that the skyrmion permanently adjusts itself to the non-flat energy landscape leading to a multi-step process approaching the small skyrmion state, such that the long-term decay rate is indeed dependent on the oscillation period time. Hence, the enhanced stability of skyrmions in field oscillation is a consequence of pinning effects.

Potentially, the ability to briefly change the size of skyrmions beyond their static stability limits is promising for ultrafast skyrmion motion. As the skyrmion velocity depends on its size, one can enhance the size of a skyrmion briefly while generating spin-torques by injecting a current pulse to induce much faster motion than accessible within the static stability limits.

4. Effective Reduction of Pinning Effects

For the case of excitation with an amplitude of $A = 30$ μT we experimentally observe a maximum diffusion constant increase of $\approx 300\%$ compared to the case without excitation. In contrast, the diffusion we would obtain by keeping the skyrmion small all the time by statically applying the lower bound size of the

field oscillation is only 31% higher than the diffusion at the offset field. Moreover, increased diffusion based on the non-linear dependence of the dissipation tensor on the skyrmion size derived by Schütte et al.^[39] can only account for an increase of 1.6%. The corresponding calculation as well as the experimentally determined relations between magnetic field, skyrmion size, and diffusion constant can be found in Note S1 and Figure S1 (Supporting Information). Therefore, we conclude that the main reason for the enhanced diffusion cannot be the non-linear size dependence of the dissipation tensor. Instead, we propose that the periodic size change effectively reduces the skyrmion pinning. Recently, a strong size dependence of skyrmion pinning has been reported,^[27] allowing one to attenuate the influence of certain pinning sites by changing the skyrmion size. Finally, we note that skyrmions have been found to exhibit hopping-like diffusion in a non-flat energy landscape due to the pinning effect^[6,27] in contrast to the expected free diffusion of Brownian particles.^[44]

Similar to our analysis in the previous work,^[27] we ascertain the spatially resolved occurrence map with and without excitation as described in the Experimental Section. We observe in Figure 2a,c that with applied oscillating field, the occurrence map is significantly more homogeneous indicating an overall flatter energy landscape and thus lower effective pinning. At a constant field of 30 μT , large parts of the sample are never visited within 10 min of measurement. Utilizing a field oscillation of 2100 μT peak-to-peak amplitude at 2 kHz however, we can tune the system such that almost every pixel of the video hosts the center of a skyrmion at least once within the same time. The data shown in Figure 2a,c are limited to the occurrences within 10 min for both plots to allow for comparison. The full gathered statistics for the unexcited case in Figure 2a as well as the corresponding spatially resolved energy landscapes are provided in Figures S4 and S5 (Supporting Information), respectively. Kerr microscopy data corresponding to the unexcited and excited case are shown in Videos S1 and S2 (Supporting Information), respectively. We conclude that by oscillation of the out-of-plane field, we can strongly attenuate the effective skyrmion pinning and enable a rather uniform movement of skyrmions anywhere in the sample.

The ability to tune the pinning energy landscape is of importance for skyrmion-based neuromorphic computing such as reservoir computing^[34,38] since pinning is a valuable source of the required non-linearity of the system but must be of the order of other interactions in the system for efficient operation. Moreover, the effectively flattened energy landscape with more isotropic skyrmion movement reduces variations between equivalent devices and thus increases or even ensures the operation reliability but also the potential for applications.

Figure 2b,d displays two sets of trajectories comparing the unexcited case with the amplitude-frequency pair from Figure 1a yielding the highest diffusion. We find that with increasing amplitude of oscillation, the diffusion becomes less hopping-like and approaches isotropic free diffusion. Note that the scales of Figure 2b,d is different as more strongly diffusing skyrmions cover more of the sample area within the same time.

This now calls for a final analysis, where we check whether there is not just a quantitative but really a qualitative difference in the type of diffusive motion as discussed above. To

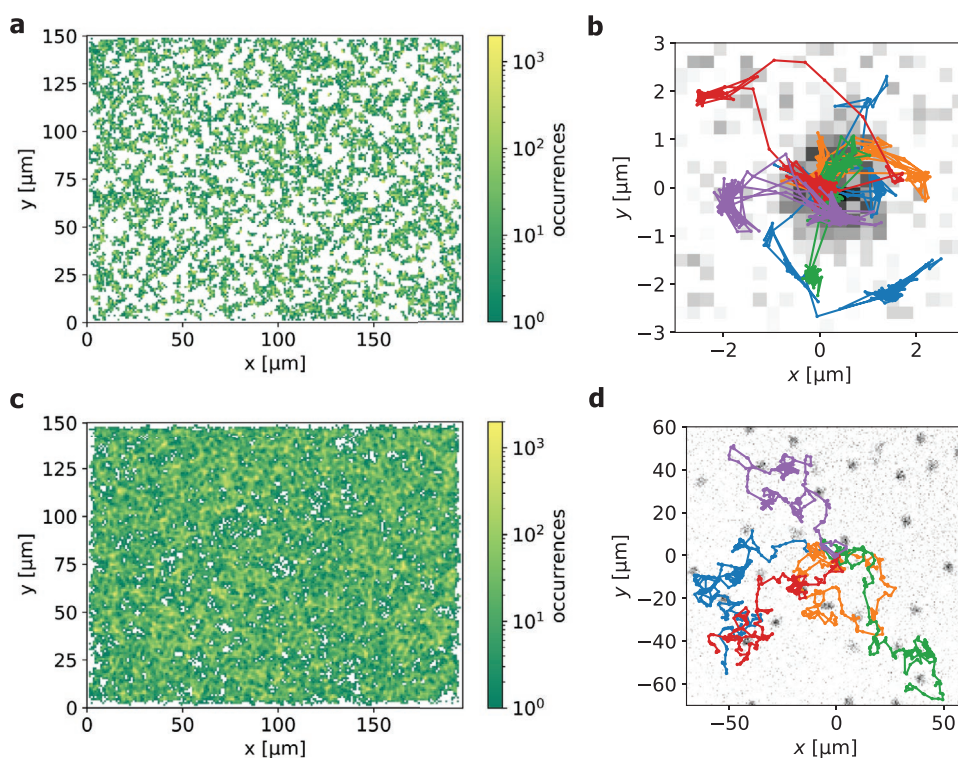


Figure 2. Skyrmion movement with and without periodic field excitation. a) The positions of skyrmion occurrences at a static field of 30 μT over 10 min are found at distinct places while large parts of the sample are never visited. b) Example trajectories with respect to the coordinate origin of the case in (a) show a clear hopping behavior. Each color represents one skyrmion. The grayscale background depicts a single Kerr microscopy frame image of one of those skyrmions at the coordinate origin. c) Analogously, the occurrence histogram—for the same time interval as in (a)—as well as d) example trajectories are evaluated for a magnetic field oscillating $\approx 30 \mu\text{T}$ with a frequency of 2 kHz and a peak-to-peak amplitude of 2100 μT . During the excitation, the skyrmions travel over larger distances and explore nearly the whole sample. As in (b), a single Kerr microscopy frame image with one of the respective skyrmions in the center is used as grayscale background.

understand and quantify the difference between the dynamics with and without excitation, we analyze the distributions of the skyrmion displacements after 2 s to gauge the system's relative proximity to the free diffusion limit. In a classical freely diffusing system, each component of the displacement should be Gaussian distributed. The absolute displacement should consequently follow a Rayleigh distribution

$$p(\Delta x) \sim \Delta x e^{-\frac{\Delta x^2}{2\sigma^2}} \quad (1)$$

Figure 3a,b shows the displacement in x -direction and the absolute displacement, respectively, after 2 s as histograms for the excited case established in Figure 2c, which corresponds to a magnetic field oscillating around an offset value = 30 μT with a frequency of 2 kHz and a peak-to-peak amplitude of 2100 μT . We find that the measured x -displacement distribution is composed of two contributions: The sharp peak around zero displacement (labeled as A) reflects the marginal movement in the vicinity of pinning sites, for example, in a harmonic well. The wider part (label B) corresponds to the quasi-free motion leading to larger displacements and is the dominating component here. Since both contributions are expected to exhibit random motion, we fit a sum of two Gaussians to the distribution in Figure 3a. Because the two regimes A and B are

separated such that pinned skyrmions are found in regime A for both x and y displacement (while free-like motion correspondingly leads to regime B for both dimensions), we fit the 2D case in Figure 3b with a sum of two Rayleigh distributions accounting for each A and B. The fitted distributions are clearly in good agreement to the observed displacements, endorsing the random walk nature of the skyrmions for both the motion within pinning sites and the quasi-freely diffusing regime. That is, we indeed see a qualitatively different, free-like type of diffusion—in contrast to the hopping motion observed in previous investigations.^[6,28] The small additional peak present at displacements of $\approx 4 \mu\text{m}$ in Figure 3b is a consequence of skyrmions hopping from one pinning site to a close neighboring pinning site once. It arises as soon as the neighboring pinning site is in reach of the skyrmion boundary during the size oscillation. We observe that the peak position is related to the skyrmion size and the characteristic distances between pinning sites, which have been discovered previously as a consequence of the sample fabrication.^[27] Quantitatively, the peak is of minor importance and not generic but sample-specific and therefore omitted in the fit. Furthermore, we note that a small net motion component due to a slight field gradient shifts the regime B of the x -displacement slightly to negative values. For the unexcited case from Figure 2a, we observe in comparison that the peak around zero displacement corresponding to movement

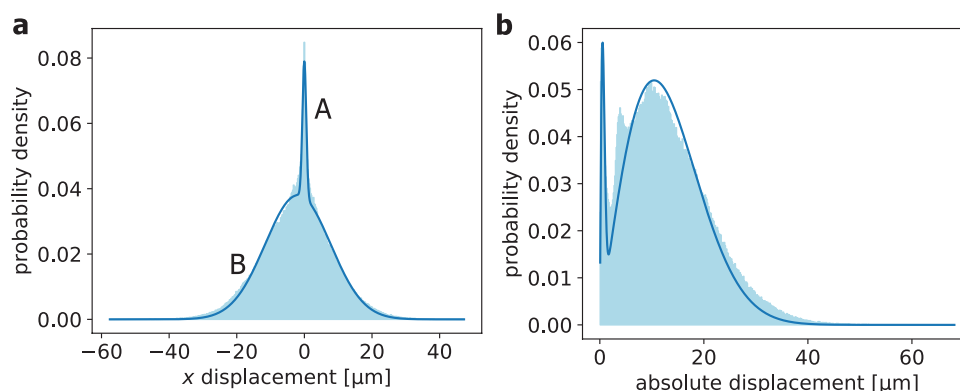


Figure 3. Skyrmion displacement distributions. a) The x -components and b) absolute values of skyrmion displacements within 2 s under a field oscillation at 2 kHz with a peak-to-peak amplitude of 2100 μT around an offset field of 30 μT are shown as histogram in light blue. The peak around zero displacement (labeled as A) represents movements within the pinning site whereas the wider distribution (labeled as B) corresponding to further displacements belongs to the quasi-free diffusive behavior. The shift of the wider distribution B in (a) toward negative values reveals a slight net motion due to a small field gradient throughout the sample. In good agreement with the experimental data, a sum of two Gaussian distribution accounting for each A and B is fitted to the 1D case in (a) as this behavior is expected for Brownian-like random walk independently for both regimes. Analogously, a sum of two Rayleigh distributions is fitted as the 2D equivalent in (b). The small additional peak at displacements $\approx 4 \mu\text{m}$ arises from skyrmions hopping to close neighboring pinning sites.

within pinning sites dominates whereas hopping between pinning sites leads to only slightly larger displacements. The corresponding plots are provided in Figure S6 (Supporting Information). Note that the displacement distributions in Figure 3 and Figure S6 (Supporting Information) are taken for the same, finite time scale and the component-wise displacement distribution will converge to a Gaussian in both in the limit of infinite timescales. For the strongly excited case shown in Figure 3, we conclude however that the observed diffusion is governed by a diffusive motion close to free diffusion leading to large displacements.

5. Conclusion

We demonstrate a mechanism to tune the diffusive dynamics of skyrmions in a magnetic thin film by an oscillating magnetic field. We show that we can enhance the diffusion by two orders of magnitude, limited only by the time resolution limit of our imaging technique and with the potential to drastically speed up skyrmion-based non-conventional computing methods originating from Brownian computing and reservoir computing paradigms. When the diffusion is enhanced, we find that the energy landscape becomes effectively flattened corresponding to a reduction of the effective pinning. In accordance with the recently reported strong size dependence of the pinning, we can conclude that the effectiveness of pinning sites is strongly reduced as the skyrmions undergo significant size changes, which compensates for sample specific pinning landscapes and hence suppresses undesirable effects resulting from device-to-device variations. In the analysis of the dynamics, we can identify a qualitative difference: when strongly excited, the skyrmion diffusion is dominated by Brownian motion approaching free diffusion while in the case of no or weak excitation, hopping displacements within the pinning site are dominating. During the field oscillation, we find that skyrmions remain stable even when exposed to magnetic fields at which they immediately

annihilate without oscillation. The enhanced stability is also traced back to pinning mediated effects and can be a key enabler to tune skyrmion properties by size changes and thus enhance operation reliability of skyrmion devices. Therefore, our findings present a method to tune and drastically enhance speed and operation reliability of skyrmion-based non-conventional computing devices and open up an unexplored gateway to ultrafast and efficient skyrmion transport.

6. Experimental Section

Sample Characterization: The investigated material was a Ta(4)/Co₂₀Fe₆₀B₂₀(0.85)/Ta(0.08)/MgO(2)/HfO₂(4) multilayer stack with layer thicknesses given in nanometers in the parentheses. The piece of $10 \times 10 \text{ mm}^2$ size was deposited with a *Singulus Rotaris* magnetron sputtering tool at a base pressure of 3×10^{-8} mbar. Thereby, the layer thicknesses were reproducible with an accuracy of better than 0.01 nm and the surface roughness was found to be $<1 \text{ nm}$. The interface between the ferromagnetic Co₂₀Fe₆₀B₂₀(0.85) and the MgO(2) causes the sample to exhibit perpendicular magnetic anisotropy, which was tuned by the Ta(0.08) interlayer.^[6] The saturation magnetization ($M_s = (0.46 \pm 0.02) \text{ MA m}^{-1}$) and effective anisotropy constant ($K_{\text{eff}} = (41 \pm 3) \text{ kJ m}^{-3}$) were determined from a hard axis hysteresis loop with anisotropy field $B_s = (179 \pm 10) \text{ mT}$ using a superconducting quantum interference device. From this, a magnetic domain wall width of $\Delta = (16 \pm 1) \text{ nm}$ was calculated for a typical exchange stiffness of $A = (10 \pm 1) \text{ pJ m}^{-1}$.^[6] The Ta(4)/Co₂₀Fe₆₀B₂₀(0.85) interface provides interfacial DMI that was measured for similar stacks to be $D \approx (0.30 \pm 0.08) \text{ mJ m}^{-2}$.^[6,28,45] The HfO₂(4) was used as capping to prevent the sample from oxidation while still allowing for good imaging contrast due to being optically transparent. The out-of-plane hysteresis loop of the used sample is shown in Figure S7 (Supporting Information). The topologically non-trivial structure of the observed skyrmionic bubbles was confirmed by studying the displacements using spin-orbit torques as well as by evaluating the spin structure in micromagnetic simulations, proving that indeed chiral skyrmions are studied.^[6,27,28]

Measurement Setup: Magnetic contrast was established using the polar magneto-optical Kerr effect (MOKE) in a commercially available Kerr microscope from evico magnetics GmbH. Magnetic fields in in-plane (IP) as well as out-of-plane (OOP) direction can be applied by

separate and perpendicularly aligned electromagnetic coils. The OOP magnet was custom-made and constructed to generate small fields with sub-microtesla precision. Directly on top of the coil, there was a Peltier element for sample temperature regulation, where a Pt100 heat sensor was used to observe the actual temperature directly next to the sample with accuracy and stability better than 0.1 K. The whole setup was housed additionally in a thermally stabilized flow box. Magnetic structures and hystereses were characterized between 315 and 330 K. For the diffusion measurements, the sample temperature was kept constant at 319.0 K, where skyrmions were found in various densities and stable between 21 and 63 μT OOP field and exhibiting thermal diffusion. The magnetic field values were calibrated by a sensitive Hall probe and external fields were corrected by the hysteresis offset. The OOP field was found to be constant and reproducible with a gradient at the sample position of $<0.01 \mu\text{T} \mu\text{m}^{-1}$. For the field oscillation, the OOP coil was supplied by an Agilent 33250A Arbitrary Waveform Generator and the current through the coil was checked with an oscilloscope. Data was acquired by a CCD camera as gray-scale videos with a field of view of $200 \times 150 \mu\text{m}^2$ at 16 frames per second with a time resolution of 62.5 ms.

The skyrmions were nucleated at a fixed OOP field by applying a saturating IP field pulse such that skyrmions form as stable state when the IP field was switched off and the spins relax into OOP domains. The number of skyrmions (i.e., the skyrmion density) was controlled by the IP and OOP field value. The skyrmion size was directly tuned by the OOP field at constant temperature.

Skyrmion Detection and Tracking: From the grayscale videos, the frames were preprocessed and skyrmions were detected using the trackpy package.^[42] The detection was performed by a 2D Gaussian fit into local intensity maxima exceeding threshold values for both maximum intensity values, intensity peak size, and integrated intensity within the fit region. The magnetic contrast between opposite magnetized domains yields the required significant intensity edges. The contrast was further enhanced by applying background subtraction with respect to a saturated state. Due to the detection fit over a large pixel number and beyond the skyrmion core, the skyrmion center can be determined with accuracy below the optical resolution of the microscope ($\approx 300 \text{ nm}$) as previously reported.^[27] Originating from the tracking procedure, the skyrmion size refers to the radius of gyration of the fitted Gaussian kernel.

All measurements were performed in one run and at the same position on the sample. Since the sample size exceeds the field of view by more than one order of magnitude, the skyrmion system was treated as infinite allowing boundary effects to be neglected. However, one could still map positions between the single videos due to topographic defects at the sample surface and the performed background subtraction with a static background image. From the subtracted images, it was deduced that the sample drift throughout the measurement series was $<300 \text{ nm}$, which means that indeed all measurements were performed at the same sample position.

Investigating Skyrmion Dynamics—Diffusion Coefficients, Occurrence Maps, and Displacement Distributions: The diffusion coefficients in Figure 1 have been calculated based on the skyrmion trajectories using the relation $\langle[\Delta x(\Delta t)]^2\rangle = 2dD\Delta t$. Here, $[\Delta x(\Delta t)]^2$ is the squared spatial displacement during the time Δt , $d = 2$ is the dimension of the system and D is the diffusion coefficient. Angled brackets indicate the average over the individual skyrmions as well as over different sections of each trajectory with length Δt (sliding window method). The diffusion coefficient D was calculated by fitting the well-sampled regions of $\langle[\Delta x(\Delta t)]^2\rangle$ with $2dD\Delta t$ for 3 to 5 videos of 1 min length for each amplitude-frequency pair and averaging over the values for each video. The uncertainty of the diffusion coefficient was estimated using the standard error of the mean.

Occurrence maps were calculated from the tracked skyrmion center positions in videos with equal experimental conditions. Tracked positions were put into bins with a bin width of $1 \mu\text{m}$ resulting in an occurrence landscape that was plotted logarithmically for readability. Some bins were never visited by a skyrmion leading to incomplete sampling of the landscape. To improve comparability between experiments with and without applied field, the number of points in both maps were kept

equal by using only part of the statistics recorded for skyrmions without an applied field.

Distributions of displacements were calculated by determining the displacement of a skyrmion after $\Delta t = 2 \text{ s}$. As for the diffusion constant, the sliding window method and multiple videos were used to improve the statistics. The values were then divided into equally distributed bins in a histogram. While the instantaneous velocities were experimentally inaccessible, the distributions of displacements to gauge the two systems' relative proximity to the free diffusion limit on the same timescale could still be compared. The shape of this distribution depends on the time Δt , so a time was chosen that was long enough to contain both, movement between pinning sites as well as skyrmions staying at their place.

Supporting Information

Supporting Information is available from the Wiley Online Library or from the author.

Acknowledgements

The authors are grateful to the Deutsche Forschungsgemeinschaft (DFG, German Research Foundation) for funding this research: Project number #403502522-SPP 2137 Skyrmionics, SFB TRR 173 Spin+X (project A01 #268565370 and project B12 #268565370), SFB TRR 146 (project #233630050). The authors further acknowledge funding from TopDyn, and this project has furthermore received funding from the European Union's Horizon 2020 research and innovation programme under grant no. 863155 (s-Nebula), grant no. 856538 (3D MAGIC) and under the Marie Skłodowska-Curie grant agreement no. 860060 (MagnEfi). M.B. was supported by a doctoral scholarship of the Studienstiftung des deutschen Volkes.

Open access funding enabled and organized by Projekt DEAL.

Conflict of Interest

The authors declare no conflict of interest.

Author Contributions

R.G. prepared the measurement setup and performed the Kerr microscopy measurements with the help of T.S.; I.K., F.K., and M.A.S. fabricated the multilayer sample. R.G., M.B., and J.R. evaluated the experimental data and prepared the manuscript supported by P.V. and M.K.; O.F. helped with the interpretation of the results. J.R., M.B., and M.S. provided the theoretical calculations. The study was supervised by M.K. and P.V.; all authors commented on the manuscript.

Data Availability Statement

The data that support the findings of this study are available from the corresponding author upon reasonable request.

Keywords

diffusion, non-conventional computing, pinning, skyrmions, spintronics

Received: September 27, 2022

Revised: January 30, 2023

Published online: March 18, 2023

- [1] A. Bogdanov, A. Hubert, *J. Magn. Magn. Mater.* **1994**, *138*, 255.
- [2] S. Mühlbauer, B. Binz, F. Jonietz, C. Pfleiderer, A. Rosch, A. Neubauer, R. Georgii, P. Böni, *Science* **2009**, *323*, 915.
- [3] W. Jiang, G. Chen, K. Liu, J. Zang, S. G. E. te Velthuis, A. Hoffmann, *Phys. Rep.* **2017**, *704*, 1.
- [4] K. Everschor-Sitte, J. Masell, R. M. Reeve, M. Kläui, *J. Appl. Phys.* **2018**, *124*, 240901.
- [5] P. Huang, T. Schönenberger, M. Cantoni, L. Heinen, A. Magrez, A. Rosch, F. Carbone, H. M. Rønnow, *Nat. Nanotechnol.* **2020**, *15*, 761.
- [6] J. Závorka, F. Jakobs, D. Heinze, N. Keil, S. Kromin, S. Jaiswal, K. Litzius, G. Jakob, P. Virnau, D. Pinna, K. Everschor-Sitte, L. Rózsa, A. Donges, U. Nowak, M. Kläui, *Nat. Nanotechnol.* **2019**, *14*, 658.
- [7] X. Zhang, M. Ezawa, Y. Zhou, *Sci. Rep.* **2015**, *5*, 9400.
- [8] D. Pinna, F. Abreu Araujo, J.-V. Kim, V. Cros, D. Querlioz, P. Bessiere, J. Droulez, J. Grollier, *Phys. Rev. Appl.* **2018**, *9*, 064018.
- [9] M. A. Brems, M. Kläui, P. Virnau, *Appl. Phys. Lett.* **2021**, *119*, 132405.
- [10] A. Fert, V. Cros, J. Sampaio, *Nat. Nanotechnol.* **2013**, *8*, 152.
- [11] S. Parkin, S.-H. Yang, *Nat. Nanotechnol.* **2015**, *10*, 195.
- [12] X. Zhang, G. P. Zhao, H. Fangohr, J. P. Liu, W. X. Xia, J. Xia, F. J. Morvan, *Sci. Rep.* **2015**, *5*, 7643.
- [13] X. Yu, F. Kagawa, S. Seki, M. Kubota, J. Masell, F. S. Yasin, K. Nakajima, M. Nakamura, M. Kawasaki, N. Nagaosa, Y. Tokura, *Nat. Commun.* **2021**, *12*, 5079.
- [14] Y. Chen, Z. Li, Z. Zhou, Q. Xia, Y. Nie, G. Guo, *J. Magn. Magn. Mater.* **2018**, *458*, 123.
- [15] F. Büttner, C. Moutafis, M. Schneider, B. Krüger, C. M. Günther, J. Geilhufe, C. v. K. Schmising, J. Mohanty, B. Pfau, S. Schaffert, A. Bisig, M. Foerster, T. Schulz, C. a. F. Vaz, J. H. Franken, H. J. M. Swagten, M. Kläui, S. Eisebitt, *Nat. Phys.* **2015**, *11*, 225.
- [16] Y. Liu, N. Lei, C. Wang, X. Zhang, W. Kang, D. Zhu, Y. Zhou, X. Liu, Y. Zhang, W. Zhao, *Phys. Rev. Appl.* **2019**, *11*, 014004.
- [17] X. Wang, W. L. Gan, J. C. Martinez, F. N. Tan, M. B. A. Jalil, W. S. Lew, *Nanoscale* **2018**, *10*, 733.
- [18] F. Jonietz, S. Mühlbauer, C. Pfleiderer, A. Neubauer, W. Münzer, A. Bauer, T. Adams, R. Georgii, P. Böni, R. A. Duine, K. Everschor, M. Garst, A. Rosch, *Science* **2010**, *330*, 1648.
- [19] X. Z. Yu, N. Kanazawa, W. Z. Zhang, T. Nagai, T. Hara, K. Kimoto, Y. Matsui, Y. Onose, Y. Tokura, *Nat. Commun.* **2012**, *3*, 988.
- [20] S. Woo, K. Litzius, B. Krüger, M.-Y. Im, L. Caretta, K. Richter, M. Mann, A. Krone, R. M. Reeve, M. Weigand, P. Agrawal, I. Limesh, M.-A. Mawass, P. Fischer, M. Kläui, G. S. D. Beach, *Nat. Mater.* **2016**, *15*, 501.
- [21] S. Komineas, N. Papanicolaou, *Phys. Rev. B* **2015**, *92*, 064412.
- [22] J. Iwasaki, M. Mochizuki, N. Nagaosa, *Nat. Commun.* **2013**, *4*, 1463.
- [23] A. Hrabec, J. Sampaio, M. Belmeguenai, I. Gross, R. Weil, S. M. Chérif, A. Stashkevich, V. Jacques, A. Thiaville, S. Rohart, *Nat. Commun.* **2017**, *8*, 15765.
- [24] K. Litzius, I. Limesh, B. Krüger, P. Bassirian, L. Caretta, K. Richter, F. Büttner, K. Sato, O. A. Tretiakov, J. Förster, R. M. Reeve, M. Weigand, I. Bykova, H. Stoll, G. Schütz, G. S. D. Beach, M. Kläui, *Nat. Phys.* **2017**, *13*, 170.
- [25] K. Litzius, J. Leliaert, P. Bassirian, D. Rodrigues, S. Kromin, I. Limesh, J. Závorka, K.-J. Lee, J. Mulkers, N. Kerber, D. Heinze, N. Keil, R. M. Reeve, M. Weigand, B. Van Waeyenberge, G. Schütz, K. Everschor-Sitte, G. S. D. Beach, M. Kläui, *Nat. Electron.* **2020**, *3*, 30.
- [26] R. Juge, S.-G. Je, D. S. de Chaves, L. D. Buda-Prejbeanu, J. Peña-García, J. Nath, I. M. Miron, K. G. Rana, L. Aballe, M. Foerster, F. Genuzio, T. O. Montes, A. Locatelli, F. Maccherozzi, S. S. Dhesi, M. Belmeguenai, Y. Roussigné, S. Auffret, S. Pizzini, G. Gaudin, J. Vogel, O. Boulle, *Phys. Rev. Appl.* **2019**, *12*, 044007.
- [27] R. Gruber, J. Závorka, M. A. Brems, D. R. Rodrigues, T. Dohi, N. Kerber, B. Seng, M. Vafaei, K. Everschor-Sitte, P. Virnau, M. Kläui, *Nat. Commun.* **2022**, *13*, 3144.
- [28] N. Kerber, M. Weißhofer, K. Raab, K. Litzius, J. Závorka, U. Nowak, M. Kläui, *Phys. Rev. Appl.* **2021**, *15*, 044029.
- [29] T. Nozaki, Y. Jibiki, M. Goto, E. Tamura, T. Nozaki, H. Kubota, A. Fukushima, S. Yuasa, Y. Suzuki, *Appl. Phys. Lett.* **2019**, *114*, 012402.
- [30] Y. Jibiki, M. Goto, E. Tamura, J. Cho, S. Miki, R. Ishikawa, H. Nomura, T. Srivastava, W. Lim, S. Auffret, C. Baraduc, H. Bea, Y. Suzuki, *Appl. Phys. Lett.* **2020**, *117*, 082402.
- [31] M. Goto, H. Nomura, Y. Suzuki, *J. Magn. Magn. Mater.* **2021**, *536*, 167974.
- [32] J. Lee, F. Peper, S. D. Cotofana, M. Naruse, M. Ohtsu, T. Kawazoe, Y. Takahashi, T. Shimokawa, L. B. Kish, T. Kubota, *Int. J. Unconv. Comput.* **2016**, *12*, 341.
- [33] R. Ishikawa, M. Goto, H. Nomura, Y. Suzuki, *Appl. Phys. Lett.* **2021**, *119*, 072402.
- [34] K. Raab, M. A. Brems, G. Beneke, T. Dohi, J. Rothörl, F. Kammerbauer, J. H. Mentink, M. Kläui, *Nat. Commun.* **2022**, *13*, 6982.
- [35] K. Wang, Y. Zhang, V. Bheemarasetty, S. Zhou, S.-C. Ying, G. Xiao, *Nat. Commun.* **2022**, *13*, 722.
- [36] R. Msiska, J. Love, J. Mulkers, J. Leliaert, K. Everschor-Sitte, arXiv:2209.13946, **2022**.
- [37] C. Reichhardt, C. J. O. Reichhardt, M. V. Milošević, *Rev. Mod. Phys.* **2022**, *94*, 035005.
- [38] D. Pinna, G. Bourianoff, K. Everschor-Sitte, *Phys. Rev. Appl.* **2020**, *14*, 054020.
- [39] C. Schütte, J. Iwasaki, A. Rosch, N. Nagaosa, *Phys. Rev. B* **2014**, *90*, 174434.
- [40] T. Oka, S. Kitamura, *Annu. Rev. Condens. Matter Phys.* **2019**, *10*, 387.
- [41] M. Lonsky, A. Hoffmann, *APL Mater.* **2020**, *8*, 100903.
- [42] D. B. Allan, T. Caswell, N. C. Keim, C. M. van der Wel, soft-matter/trackpy: Trackpy v0.5.0, Zenodo: 4682814, **2021**.
- [43] X. S. Wang, H. Y. Yuan, X. R. Wang, *Commun. Phys.* **2018**, *1*, 31.
- [44] R. Brown, *Philos. Mag.* **1828**, *4*, 161.
- [45] N. Kerber, D. Ksenzov, F. Freimuth, F. Capotondi, E. Pedersoli, I. Lopez-Quintas, B. Seng, J. Cramer, K. Litzius, D. Lacour, H. Zabel, Y. Mokrousov, M. Kläui, C. Gutt, *Nat. Commun.* **2020**, *11*, 6304.

5.1.1. Supporting Information

Publication Information


The following Supporting Information is published with the article in *Advanced Materials*:

300-Times-Increased Diffusive Skyrmion Dynamics and Effective Pinning Reduction by Periodic Field Excitation

Raphael Gruber, Maarten A. Brems, Jan Rothörl, Tobias Sparmann, Maurice Schmitt, Iryna Kononenko, Fabian Kammerbauer, Maria-Andromachi Syskaki, Oded Farago, Peter Virnau & Mathias Kläui

Advanced Materials **35**(17), 2208922 (2025).

DOI: [10.1002/adma.202208922](https://doi.org/10.1002/adma.202208922)


Copyright Information:  CC BY-NC 4.0 Creative Commons Attribution-NonCommercial 4.0 International License

Editorial Note: The blue header/footer bars were added for inclusion in this dissertation and are not part of the original publication.

Contributions

The author contributions for this project and article are described in detail in section 5.3.

Experimental Note

Documentation of my experiments used for this article are available for lab members on *eLabFTW* ( labbook database ID [5834](#)).

ADVANCED MATERIALS

Supporting Information

for *Adv. Mater.*, DOI: 10.1002/adma.202208922

300-Times-Increased Diffusive Skyrmion Dynamics and
Effective Pinning Reduction by Periodic Field Excitation

*Raphael Gruber, Maarten A. Brems, Jan Rothörl, Tobias
Sparmann, Maurice Schmitt, Iryna Kononenko, Fabian
Kammerbauer, Maria-Andromachi Syskaki, Oded
Farago, Peter Virnau, and Mathias Kläui**

300-Times-Increased Diffusive Skyrmion Dynamics and Effective Pinning Reduction by Periodic Field Excitation

Supporting Information

Raphael Gruber¹, Maarten A. Brems¹, Jan Rothörl¹, Tobias Sparmann¹, Maurice Schmitt¹, Iryna Kononenko^{1,2}, Fabian Kammerbauer¹, Maria-Andromachi Syskaki^{1,3}, Oded Farago⁴, Peter Virnau¹, Mathias Kläui*¹

¹Institute of Physics, Johannes Gutenberg-Universität Mainz, Staudingerweg 7, Mainz 55128, Germany

²National Academy of Sciences of Ukraine, Institute of Applied Physics, 58 Petropavlivska St., 40000 Sumy, Ukraine

³Singulus Technologies AG, Hanauer Landstraße 103, 63796 Kahl am Main, Germany

⁴Biomedical Engineering Department, Ben Gurion University of the Negev, Be'er Sheva 84105, Israel

* Email: klaeui@uni-mainz.de

Supporting Note 1 – Micromagnetic Calculation of Size Dependent Diffusion Tensor

To obtain information about the relation between skyrmion size and skyrmion diffusion one can use micromagnetic calculations. Micromagnetic simulations akin to the ones in a previous study^[1] show that the width of the domain wall is approximately constant for differently sized skyrmions created by different applied fields in our material stacks and that the domain wall width is always much smaller than the radius of the skyrmion while the size of the skyrmions depends roughly linearly on the field. The same parameters^[1] are employed as for the sample Ta(5)/Co₂₀Fe₆₀B₂₀(1)/Ta(0.08)/MgO(2)/Ta(5) that is very similar to the one in this study, Ta(4)/Co₂₀Fe₆₀B₂₀(0.85)/Ta(0.08)/MgO(2)/HfO₂(4). The layer thicknesses in nanometers are given in parentheses. In the systems used in this work, the damping αD_T is in general significantly larger than the Magnus force amplitude G . Therefore, we can simplify the formula for the diffusion constant from Schütte et al.^[3] to a Taylor series to first order

$$D = k_B T \frac{\alpha D_T}{G^2 + (\alpha D_T)^2} \approx \frac{k_B T}{\alpha D_T} \quad (S1)$$

with reduced temperature $k_B T$, Gilbert damping α , and D_T being half the trace of the dissipative tensor. Temperature and Gilbert damping are independent of the skyrmion size and thus $D \sim D_T^{-1}$.

D_T can be calculated from the spin structure of a skyrmion. We consider a Néel skyrmion with a hyperbolic tangent shaped domain wall, skyrmion radius a and domain wall width b .

$$\begin{aligned} m_x &= \cos(\phi) \sqrt{1 - \tanh^2\left(\frac{r-a}{b}\right)} \\ m_y &= \sin(\phi) \sqrt{1 - \tanh^2\left(\frac{r-a}{b}\right)} \\ m_z &= \tanh\left(\frac{r-a}{b}\right) \end{aligned} \quad (S2)$$

For this spin structure we can calculate the trace elements of the diffusion tensor:

$$\begin{aligned}
D_{xx} = D_{yy} &= \int (\partial_x \vec{S})^2 d^2 r = \int_0^{2\pi} d\phi \int_0^\infty dr r \left[(\partial_x S_x)^2 + (\partial_x S_y)^2 + (\partial_x S_z)^2 \right] \\
&= \int_0^{2\pi} d\phi \int_0^\infty dr r \left[\left(\partial_x \cos \phi \sqrt{1 - \tanh^2 \left(\frac{r-a}{b} \right)} \right)^2 \right. \\
&\quad \left. + \left(\partial_x \sin \phi \sqrt{1 - \tanh^2 \left(\frac{r-a}{b} \right)} + \left(\partial_x \tanh \left(\frac{r-a}{b} \right) \right)^2 \right) \right] \\
&= \int_0^{2\pi} d\phi \int_0^\infty dr r \left[\left((\partial_x \cos \phi)^2 + (\partial_x \sin \phi)^2 \right) \left(1 - \tanh^2 \left(\frac{r-a}{b} \right) \right) \right. \\
&\quad \left. + \left(\partial_x \sqrt{1 - \tanh^2 \left(\frac{r-a}{b} \right)} \right)^2 + \left(\partial_x \tanh \left(\frac{r-a}{b} \right) \right)^2 \right] \\
&= \int_0^{2\pi} d\phi \int_0^\infty dr r \left[\left(\partial_x \frac{x}{r} \right)^2 + \left(\partial_x \sqrt{1 - \frac{x^2}{r^2}} \right)^2 \left(1 - \tanh^2 \left(\frac{r-a}{b} \right) \right) \right. \\
&\quad \left. + \left(\frac{\partial r}{\partial x} \right)^2 \left(\frac{\tanh \left(\frac{r-a}{b} \right)}{b \cosh^2 \left(\frac{r-a}{b} \right) \sqrt{1 - \tanh^2 \left(\frac{r-a}{b} \right)}} \right)^2 + \left(\frac{1}{b \cosh^2 \left(\frac{r-a}{b} \right)} \right)^2 \right] \\
&= \int_0^{2\pi} d\phi \int_0^\infty dr r \left[\left(\left(\frac{1-x^2}{r} - \frac{x^2}{r^3} \right)^2 + \left(\frac{x \left(1 - \frac{x^2}{r^3} \right)}{\sqrt{1 - \frac{x^2}{r^2}}} \right)^2 \right) \left(1 - \tanh^2 \left(\frac{r-a}{b} \right) \right) \right. \\
&\quad \left. + \left(\frac{x}{r} \right)^2 \left(\frac{\tanh^2 \left(\frac{r-a}{b} \right)}{1 - \tanh^2 \left(\frac{r-a}{b} \right)} + 1 \right) \cdot \frac{1}{b^2 \cosh^4 \left(\frac{r-a}{b} \right)} \right] \\
&= \int_0^{2\pi} d\phi \int_0^\infty dr r \left[\left(\left(\frac{1 - \cos^2 \phi}{r} \right)^2 + \left(\frac{\cos \phi \left(1 - \cos^2 \phi \right)}{\sqrt{1 - \cos^2 \phi}} \right)^2 \right) \right. \\
&\quad \left. \cdot \left(1 - \tanh^2 \left(\frac{r-a}{b} \right) \right) + \cos^2 \phi \frac{1}{1 - \tanh^2 \left(\frac{r-a}{b} \right)} \cdot \frac{1}{b^2 \cosh^4 \left(\frac{r-a}{b} \right)} \right] \\
&= \int_0^{2\pi} d\phi \int_0^\infty dr r \left[\left(\left(\frac{1 - \cos^2 \phi}{r} \right)^2 \left(1 + \frac{\cos \phi}{\sin \phi} \right)^2 \right) \frac{1}{\cos^2 \left(\frac{r-a}{b} \right)} \right. \\
&\quad \left. + \cos^2 \phi \cos^2 \left(\frac{r-a}{b} \right) \cdot \frac{1}{b^2 \cosh^4 \left(\frac{r-a}{b} \right)} \right] \\
&= \int_0^{2\pi} d\phi \int_0^\infty dr r \left[\frac{\sin^4 \phi}{r^2} \left(1 + \frac{\cos \phi}{\sin \phi} \right)^2 + \frac{\cos^2 \phi}{b^2} \right] \frac{1}{\cosh^2 \left(\frac{r-a}{b} \right)} \\
&= \int_0^\infty dr \left[\frac{\pi}{r} + \frac{\pi r}{b^2} \right] \frac{1}{\cosh^2 \left(\frac{r-a}{b} \right)}
\end{aligned}$$

$$\begin{aligned}
&= \int_0^\infty dr \frac{\pi}{r \cosh^2\left(\frac{r-a}{b}\right)} + \frac{\pi}{b} \left[r \tanh\left(\frac{r-a}{b}\right) - b \log \cosh\left(\frac{r-a}{b}\right) \right]_0^\infty \\
&= \int_0^\infty dr \frac{\pi}{r \cosh^2\left(\frac{r-a}{b}\right)} + \lim_{r \rightarrow \infty} \frac{\pi}{b} \left[r - b \log\left(\frac{e^{\frac{r-a}{b}}}{2}\right) + b \log \cosh\left(\frac{-a}{b}\right) \right] \\
&= \int_0^\infty dr \frac{\pi}{r \cosh^2\left(\frac{r-a}{b}\right)} + \lim_{r \rightarrow \infty} \frac{\pi}{b} \left[r - b \left(\frac{r-a}{b} - \log 2\right) + b \log \cosh\left(\frac{a}{b}\right) \right]
\end{aligned}$$

arriving at

$$D_{xx} = D_{yy} = \int_0^\infty dr \frac{\pi}{r \cosh^2\left(\frac{r-a}{b}\right)} + \frac{\pi}{b} \left[a + b \log 2 + b \log \cosh\left(\frac{a}{b}\right) \right] \quad (S3)$$

Using the previously mentioned assumption that the skyrmion size a is much larger than the domain wall width b , one can further simplify this calculation using

$$\cosh\left(\frac{a}{b}\right) \approx \frac{1}{2} e^{a/b} \quad (S4)$$

and the fact that the first integral is close to 0 for $a \gg b$:

$$D_{xx} \approx \frac{\pi}{b} \left[a + b \log 2 + b \left(\frac{a}{b} - \log(2)\right) \right] = \frac{2\pi a}{b} \quad (S5)$$

Now we can write $D \sim a^{-1}$. With a being linear in the applied field B , we obtain

$$D = \frac{c_0}{c_1 - B} \quad (S6)$$

as a fitting function to fit to the experimentally determined field dependence of the diffusion constant. The fit gives $c_0 = 8.91 \mu\text{T} \mu\text{m}^2 \text{s}^{-1}$ and $c_1 = 114.33 \mu\text{T}$ and is shown in Figure S1. Here, we ignore both the leftmost and rightmost experimentally determined points. While for the leftmost point, skyrmions decay extremely fast and therefore strongly pinned skyrmions dominate the measurement, the rightmost point already contains some worm domains which are hard to distinguish from skyrmions making the determined diffusion less robust. They lead to increased measured diffusion due to the inherent difficulty of tracking an elongated object with a circular mask.

One can now integrate over one period of the alternating field, arriving at:

$$D = \frac{1}{T} \int_0^T dt \frac{c_0}{c_1 - B_0 - \frac{1}{2} \Delta B \sin\left(\frac{2\pi t}{T}\right)} = \frac{c_0}{\sqrt{(c_1 - B_0)^2 - \left(\frac{1}{2} \Delta B\right)^2}}. \quad (S7)$$

Without oscillations, $\Delta B = 0$ and we get a diffusion constant of $0.1057 \mu\text{m}^2 \text{s}^{-1}$ for $30 \mu\text{T}$. If we now add a change of the applied field of $\Delta B = 30 \mu\text{T}$ (peak-to-peak), we can increase the diffusion to $0.1074 \mu\text{m}^2 \text{s}^{-1}$, which is an increase by 1.6 %. This increase is significantly smaller than the increase in diffusion observed in the experiment.

Supporting Note 2 – Impact of skyrmion diffusion enhancement on the viability of Brownian computing

In a previous work,^[4] the mean computation time of a skyrmion-based Brownian half-adder is estimated using a minimal random walk model. Moreover, the mean computation time is inversely proportional to the diffusion coefficient. Employing the crossing-free skyrmion-suited half-adder layout by Brems et al.^[4] with 5 μm wire lengths, one obtains a mean computation time of about 56.2 min using measured diffusion constant without excitation $D_{\text{unex}} = 0.1 \mu\text{m}^2 \text{s}^{-1}$. In contrast, using the highest diffusion constant with excitation $D_{\text{ex}} = 33.2 \mu\text{m}^2 \text{s}^{-1}$ the mean computation time is reduced to about 10.2 s. Thereby, Brownian computing is much more viable for real applications. Finally, as the oscillating field excitation can be activated and deactivated as necessary leading to a tunability of the diffusion, the hybrid Brownian computing method developed by Brems et al.^[4] can be realized using our system. Compared to using randomly directed spin torques, our excitation method does not rely on an external random number generator.

Supporting Figures

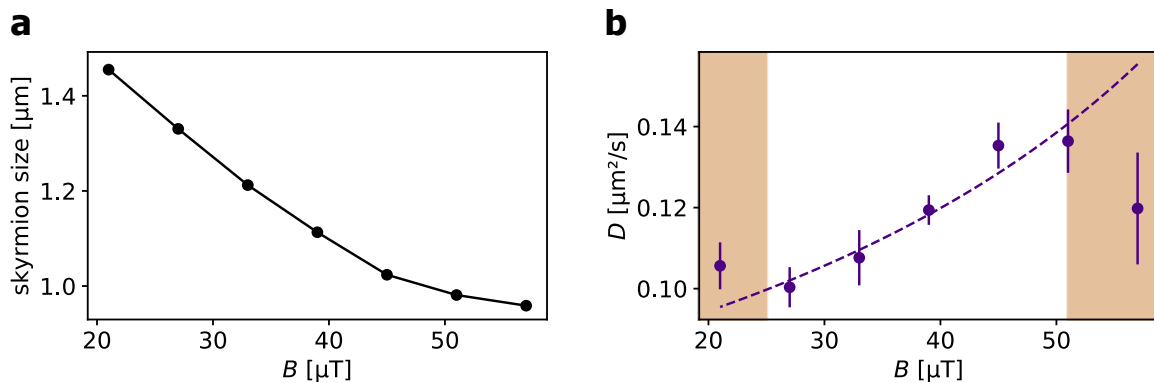


Figure S1. Field effect on skyrmions. (a) The skyrmion size is directly tuned by the applied magnetic field B and increases for large field values. (b) The experimentally determined diffusion coefficient D depends on the skyrmion size and hence the applied field. The orange regions indicate the fields at which skyrmions are not stable. For fields above $63 \mu\text{T}$, skyrmions annihilate on the time scale of several seconds, the annihilation process is faster for higher fields corresponding to smaller skyrmions. For fields of $25 \mu\text{T}$, we notice occasional formations of stripe-like, elongated skyrmions. The formation of stripes increases for lower fields until a pure stripe domain state is reached. The diffusion constant in the region of stable circular skyrmions (white region) is fitted with Equation S6 yielding the dashed purple line with parameters $c_0 = 8.91 \mu\text{T} \mu\text{m}^2 \text{s}^{-1}$ and $c_1 = 114.33 \mu\text{T}$.

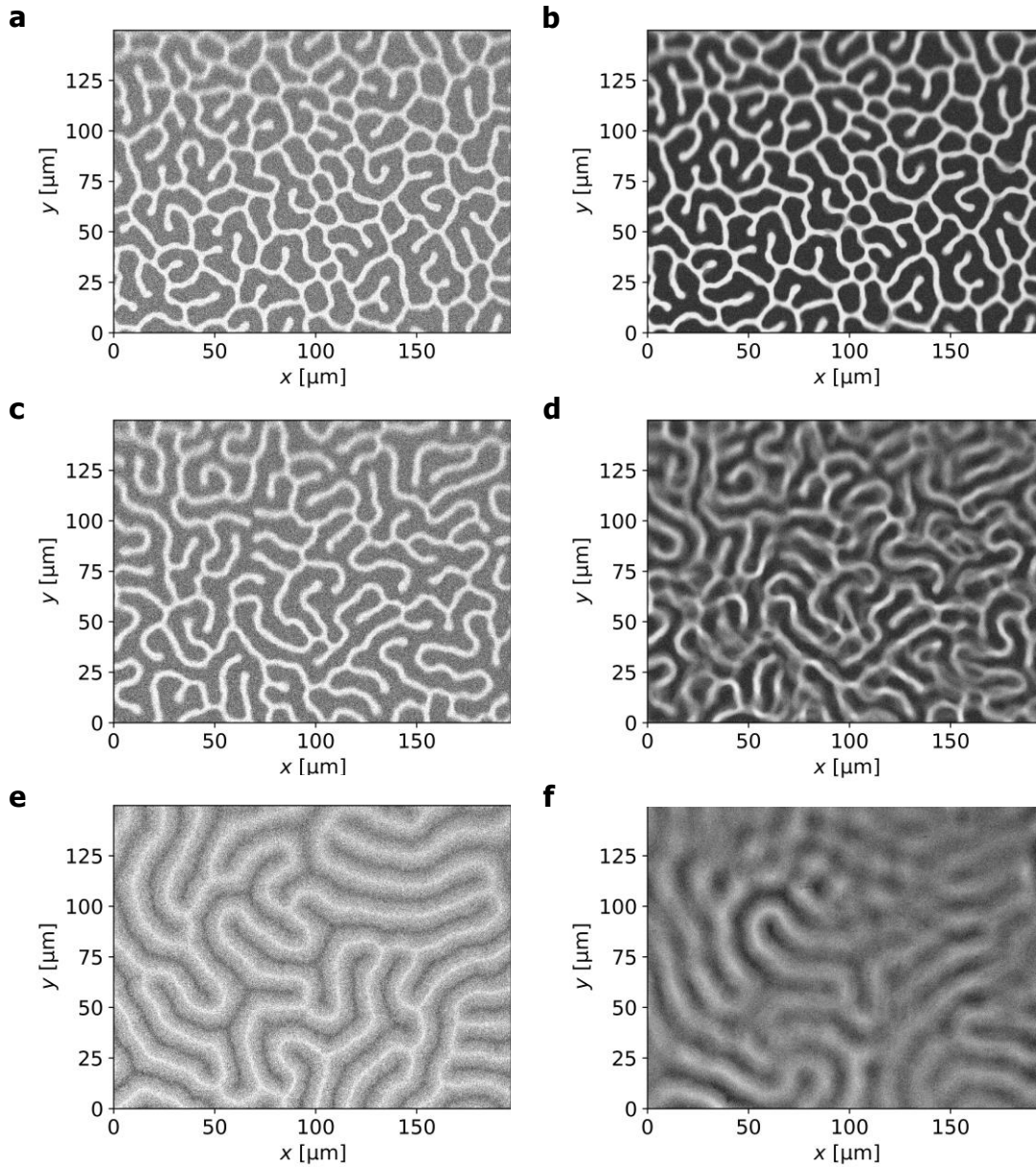


Figure S2. Stripe domains in periodic field excitation. (a) The single frame image (16 frames per second) and (b) average frame image over 15 s of a stripe domain state observed by Kerr microscopy at constant field of $-51 \mu\text{T}$ are almost identical. White/black correspond to magnetization pointing up-/downwards. Generally, contrast is improved by frame averaging due to noise cancellation. In (b), most pixels are very bright/dark representing regions where the magnetization is permanently pointing in one direction while at some positions, the stripes are fluctuating slightly as indicated by intermediate nuances of grey. The comparison of (c) a single frame image and (d) the average image for 15 s under an additionally applied magnetic field oscillation with a frequency of $f = 100 \text{ Hz}$ and peak-to-peak amplitude of $A = 150 \mu\text{T}$ yields that the stripes are moving clearly, but still large parts of the pattern are hardly moving. (e) For an excitation with $f = 100 \text{ Hz}$ and $A = 600 \mu\text{T}$, the expansion and contraction of the stripes due to the field oscillation are so large, that they become visible in the frame image. As the f is larger than the imaging rate, a grey transition regime arises in the image representing the area which changes magnetization direction during the oscillation while thin stripes remain in one direction only. (f) In the average over 15 s corresponding to (e), the stripe structure is only partly recognizable anymore due to the fast motion. However, the non-uniform intensity indicates that several positions keep their magnetization on that timescale.

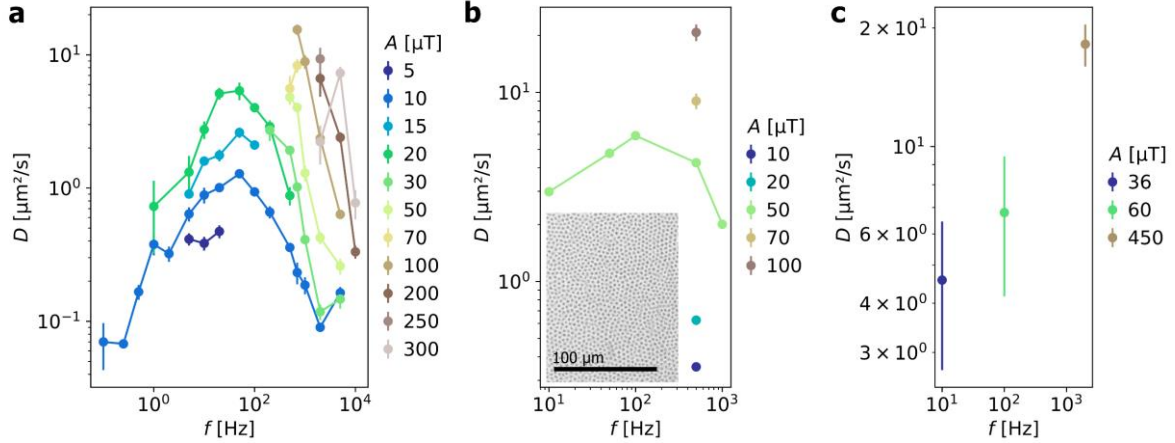


Figure S3. Diffusion constant in alternating magnetic fields on different samples. In analogy to Figure 1a, the diffusion constant D is shown for magnetic field oscillations of frequency f and peak-to-peak amplitude A for two different systems. (a) A Ta(4)/Co₂₀Fe₆₀B₂₀(0.85)/Ta(0.08)/MgO(2)/HfO₂(3) stack exhibiting stronger pinning as the one used in the main text shows qualitatively the same effect of enhanced diffusion due to field oscillations, in particular when increasing A . However, the frequency-dependent peak is shifted to slightly higher f (for similar skyrmion density). The experiments are carried out at $T = 323.0$ K and an offset field of $28 \mu\text{T}$. The diffusion constant for the skyrmions in the system without excitation is $D = (0.07 \pm 0.02) \mu\text{m}^2 \text{s}^{-1}$. (b) A Ta(5)/Co₂₀Fe₆₀B₂₀(0.9)/Ta(0.08)/MgO(2)/HfO₂(3) system hosting high skyrmion densities at 320.0 K and $20 \mu\text{T}$ is used to investigate the effect of field oscillation on dense skyrmion systems. Also there, D is drastically enhanced by the field oscillation with a frequency-peak around $f = 100$ Hz. The inset shows a part of a MOKE image of the used system. (c) Skyrmions in a wire geometry as narrow as 1.8 times the skyrmion diameters in a stack of Ta(5)/Co₂₀Fe₆₀B₂₀(0.95)/Ta(0.09)/MgO(2)/Ta(5) do also show a significant effect of diffusion enhancement. We determine a factor of 97 for the strongest excitation compared to a values of $D = (0.19 \pm 0.03) \mu\text{m}^2 \text{s}^{-1}$ in the static field of $80 \mu\text{T}$.

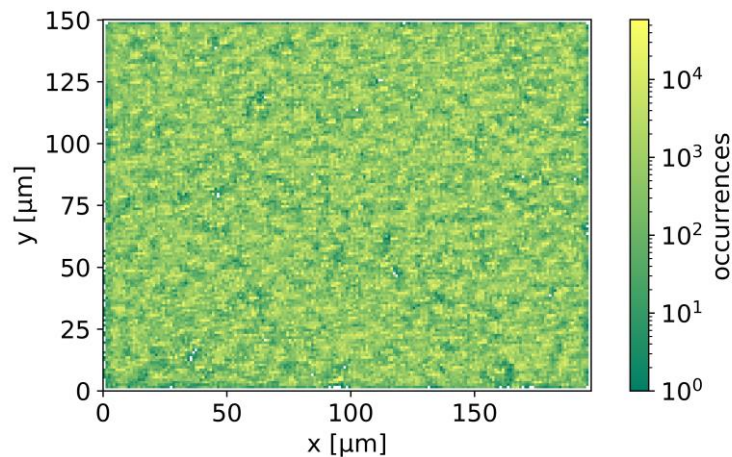


Figure S4. Skyrmion occurrences without excitation. Here, we present the full occurrence map corresponding to Figure 2a with constant offset field of $30 \mu\text{T}$ for the whole measurement duration of 225 minutes.

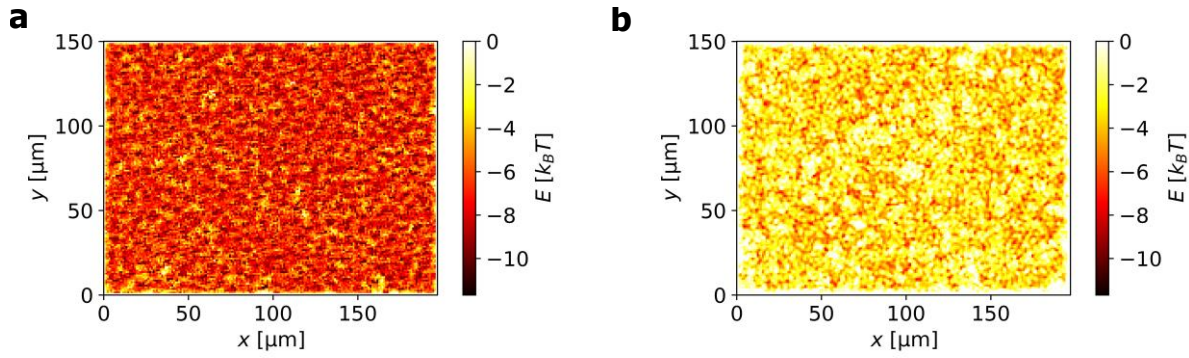


Figure S5. Energy landscapes. Skyrmion pinning energies at (a) constant magnetic field of $30 \mu\text{T}$ and (b) at additional magnetic field oscillation with frequency of 2 kHz and peak-to-peak amplitude $2100 \mu\text{T}$. We calculate the energy landscape from the skyrmion occurrence maps as provided in Figure 2 using the potential of mean force approach $V(x,y) = -k_B T \ln N(x,y)$. For this we use all available statistics instead of using the same number of points for the excited and non-excited case. One problem of this approach is the occurrence of bins with 0 skyrmions over the whole measurement which would lead to an infinite repulsive potential. To prevent this unphysical effect, we set all bins with 0 occurrence to 1 occurrence and calculate the potential normally from there. We see that the energy landscape at static OOP field is significantly deeper than the effective landscape with applied field oscillation. This is another indication that applying an alternating field leads to an effective reduction of pinning.

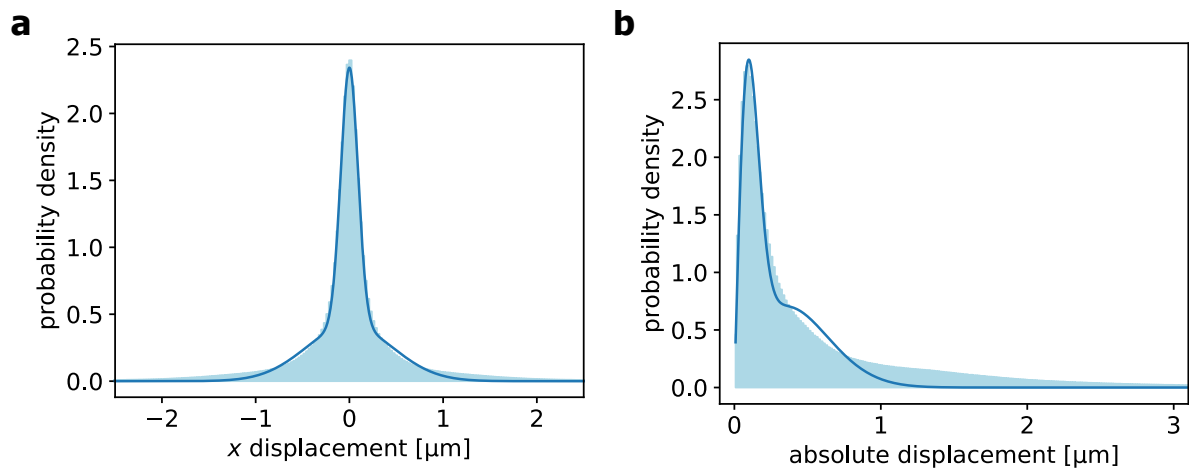


Figure S6. Skyrmion displacements for unexcited case. The (a) x -component and (b) absolute values of the skyrmion displacements after 2 seconds are shown in analogy to Figure 3, but for the unexcited case established in Figure 2a with constant offset field of $30 \mu\text{T}$. The displacement distributions are dominated by small displacements within pinning sites whereas hopping between pinning sites leads to only slightly larger displacements. The fits (dark blue lines) are performed analogous to the ones in Figure 3 in the main text.

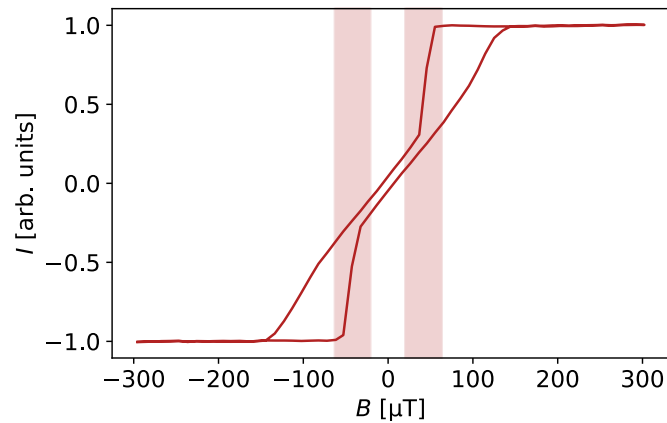


Figure S7. Sample hysteresis. The red line shows the MOKE intensity for the out-of-plane hysteresis loop of B . The red-shaded areas indicate the field range from 21 to 63 μT in which skyrmions are observed.

References

- [1] R. Gruber, J. Zázvorka, M. A. Brems, D. R. Rodrigues, T. Dohi, N. Kerber, B. Seng, M. Vafaei, K. Everschor-Sitte, P. Virnau, M. Kläui, *Nat. Commun.* **2022**, *13*, 3144.
- [2] W. Jiang, X. Zhang, G. Yu, W. Zhang, X. Wang, M. Benjamin Jungfleisch, J. E. Pearson, X. Cheng, O. Heinonen, K. L. Wang, Y. Zhou, A. Hoffmann, S. G. E. te Velthuis, *Nat. Phys.* **2017**, *13*, 162.
- [3] C. Schütte, J. Iwasaki, A. Rosch, N. Nagaosa, *Phys. Rev. B* **2014**, *90*, 174434.
- [4] M. A. Brems, M. Kläui, P. Virnau, *Appl. Phys. Lett.* **2021**, *119*, 132405.

5.2. Additional Results and Experimental Remarks

5.2.1. Suitable System for Skyrmion Diffusion Experiments

Determining the diffusion coefficient D of skyrmions imposes several requirements on the experimental system. First, the system must provide appropriate material parameters to host skyrmions at a suitable density. If the density is too low, only a small number of skyrmions is available, which results in poor statistics for the analysis. Conversely, if the density is too high, skyrmion–skyrmion interactions [70] become increasingly dominant and govern the thermal dynamics [19, 64, 70].

The multilayer stacks used in this work to study skyrmion dynamics (see section 3.3) exhibit a characteristic temperature dependence of their magnetic behavior. Fig. 5.1 shows the hysteresis loops of sample IK120 (labbook database ID 5833) for a range of T .

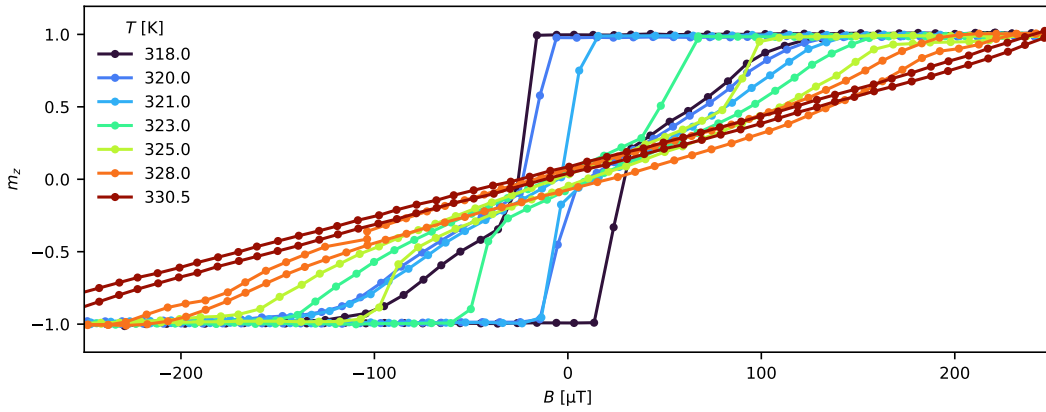


Figure 5.1.: Temperature Dependence of the Hysteresis Loop. Relative OOP magnetization m_z for cycles of the magnetic field B , starting from saturation. The different colors denote loops at different temperature T . The loops are centered and normalized, the shown data points are interpolated as guide to the eye.

At 318 K, the hysteresis loop exhibits a large coercivity and a relatively sharp switching when reversing the field from a saturated state. The loop has a saturation remanence $|m_z(B = 0)| = 1$ and a finite coercivity $B(m_z = 0)$. When approaching saturation in the opposite direction (under opposite OOP fields), the loop flattens out rapidly. In this regime, typically only sparse, isolated skyrmions can exist. Lowering T further by ≈ 5 K, the coercivity increases and the hysteresis reaches a sharp switching behavior [1].

With increasing T , the hysteresis loop flattens towards larger saturation fields $B(|m_z| = 1)$, while both coercivity and remanence decrease until they vanish. At intermediate T (323–328 K), the loop forms two pockets at finite fields while closing around zero field and towards saturation. Such a shape indicates the possibility of

higher skyrmion densities. When the pockets become very narrow, the system favors dense skyrmion lattices, while isolated skyrmions no longer exist and instead expand into stripes. With further increasing T , the skyrmions generally shrink in size and, due to the enhanced thermal energy available, also become more mobile [19, 72]. Eventually, at sufficiently high T , the system undergoes the SRT, preferring IP magnetization alignment and thereby prohibiting OOP skyrmion bubbles.

The measurements reported in section 5.1 [27] were carried out at 319 K (labbook experiment ID 16725). This temperature allows for the existence of sparse skyrmions, thereby minimizing the influence of skyrmion-skyrmion interactions [70] and enabling the measurement of diffusion unaffected by inter-skyrmion effects [19]. A further important requirement is the stability of skyrmions, especially since oscillating magnetic fields of varying amplitude and frequency are applied. A larger stability widens the accessible parameter space for AC excitation, which motivated the choice of this temperature. At lower T , the system is too close to a sharp switching regime, leading to fewer skyrmions and frequent spontaneous annihilations. At higher T , denser systems cause significant skyrmion-skyrmion interactions, while enhanced thermal fluctuations promote annihilations, or stripe formation under oscillating fields.

Another prerequisite for determining D is a sufficient imaging contrast of the skyrmions. Imaging skyrmions can be challenging, even with Kerr microscopy. I typically set the polarizer to $\approx 0.5^\circ$, keep the compensator in its middle position, and adjust the analyzer to maximize contrast [129]. With these settings, the multilayer stacks usually provide adequate visibility. A transparent capping layer such as HfO_2 – as introduced by Maria-Andromachi Syskaki and used in IK120 (labbook database ID 5833) – enhances the contrast significantly compared to commonly used metallic caps such as Ta [19, 64, 112]. Nonetheless, detection becomes difficult when skyrmions move rapidly.

Fig. 5.2 shows Kerr microscopy snapshots from Supplementary Video 2 of section 5.1 [27]. The frames, recorded at 16 fps, are taken consecutively at $t = 18.75$ s. The images reveal a strong contrast of the OOP magnetization of skyrmions. However, rapidly moving skyrmions (two examples are indicated by red and blue arrows) exhibit blurred contrast, complicating their detection. Importantly, these fast-moving skyrmions contribute significantly to the average MSD and thus to D , making their reliable detection and trajectory linking essential for a robust diffusion analysis.

Since single skyrmions become nearly unresolvable within individual frames, this video effectively marks the upper limit of diffusivity D that can still be analyzed in the experiment. In this regard, the experiments reported in section 5.1 [27] are – so far – primarily limited by the ability to resolve and reliably track the diffusing skyrmions, rather than by their intrinsic stability. Nevertheless, stability remains a crucial factor. In an earlier implementation of the experiment, we performed similar measurements on the comparable multilayer stack FAB1077 (labbook database ID 5672). This sample exhibits stronger pinning as well as a more pronounced T -dependence of the hysteresis.

On the one hand, the stronger pinning generally reduces D , causing the skyrmions

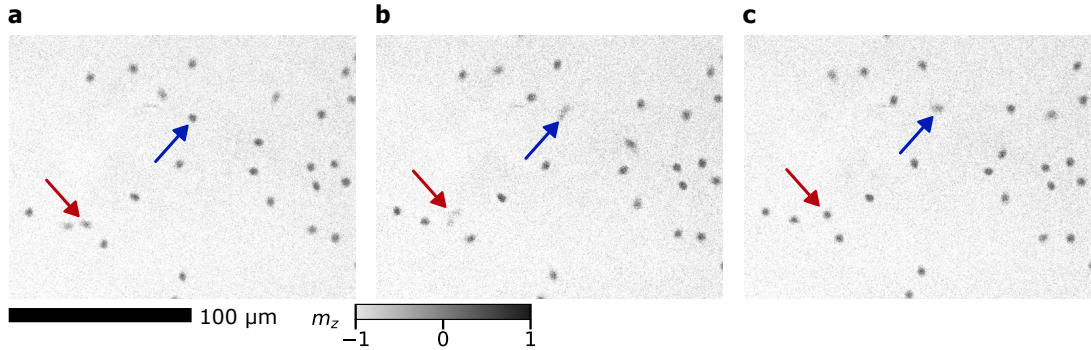


Figure 5.2.: Kerr Snapshots of Diffusing Skyrmions. Kerr microscopy snapshots at (a) $t = 18.6875$ s, (b) the subsequent frame, and (c) the second subsequent frame from Supplementary Video 2 of section 5.1 [27]. The recording rate is 16 fps. The Kerr microscope provides sufficient contrast to resolve the OOP magnetization of skyrmions. However, rapidly moving skyrmions – as the two examples indicated by the red and blue arrows – appear blurred, which complicates detection and analysis.

to move more slowly. This can be advantageous, as it allows a larger margin for diffusion enhancement before reaching the resolution limit. However, it also restricts skyrmions to nucleate and persist primarily at the strongest pinning centers. These centers represent only a few discrete points in the 2D energy landscape but dominate the statistics, which biases the analysis. Moreover, I observed an increased tendency of strongly pinned skyrmions to elongate into stripes rather than to depin. On the other hand, the stronger T -dependence of the magnetic properties reduces skyrmion stability as the system is energetically closer to the SRT and stripe domain phases. As a consequence, skyrmions in FAB1077 annihilate or form stripes more readily when exposed to oscillating fields. Furthermore, the nucleation of skyrmions in comparable configurations proved challenging – in fact, it was impossible to nucleate them at temperatures only 0.6 K lower than optimal. This limitation was the primary reason for restarting the experiment on a different sample. The diffusion characterization of this stack is reported in the Supporting Information as Fig. S3 in section 5.1.1 [27]. In addition, the experiment is subject to naturally occurring temperature fluctuations in the laboratory environment. The presence of a person near the Kerr microscope typically increases the sample temperature by approximately 0.5 K, whereas air currents caused by rapid movement near the setup can reduce the temperature by a similar amount. Even though T can be adjusted and controlled precisely, this requires continuous monitoring and often entails waiting periods until the sample temperature has stabilized again.

Experimental Note

The experiments described here and in section 5.1 [27] were conducted prior to the installation of the laminar flow box enclosing the entire Kerr microscope. The laminar flow box provides independent temperature control, thereby stabilizing the environment of the microscope and the sample, and significantly facilitating the maintenance of reproducible measurement conditions.

Another sample that I tested for diffusion experiments under oscillating fields is MAS763 (labbook database ID 3197). At 292.5 K, this sample hosts sparse, isolated skyrmions. Fig. 5.3a shows D as a function of the oscillation frequency f and amplitude A , in analogy to Fig. 1 in section 5.1 [27]. However, the skyrmions in MAS763 are highly sensitive to the applied field. This sensitivity can be beneficial, as it requires only small field amplitudes – and thus lower power – to enhance diffusion through oscillations. At the same time, it renders the system much more susceptible to distortions caused by field gradients. Despite aligning the OOP and IP coils perpendicularly and positioning the sample above the center of the OOP coil, the system is clearly exposed to a gradient, as illustrated in Fig. 5.3b. When oscillating fields are applied, the skyrmion density increases towards the top left corner of the image, where skyrmions expand into stripes, while the bottom right corner remains nearly empty. This strong density variation likely explains why D does not exhibit a peak with increasing f , but rather decreases monotonically. Overall, this system yields inconclusive results but underscores the importance of carefully selecting an appropriate sample for diffusion experiments, with homogeneous skyrmions of sufficient stability.

When increasing the temperature to 320.5 K, skyrmions appear in a denser arrangement. In this regime, the diffusivity D exhibits a clear peak in the frequency scan and generally increases with higher A , as shown in Fig. 5.4. The corresponding data points are also included in Figure S3 of the Supporting Information in section 5.1.1 [27]. However, since the skyrmions form a dense lattice-like structure, skyrmion-skyrmion interactions [70] become significant. Field oscillations thereby enhance skyrmion annihilation rates (see also chapter 8). The number of skyrmions remaining after 30 s, $N_{\text{sk}}(t = 30 \text{ s})$, is indicated as a colored ring around the diffusion data points. At higher A , more skyrmions annihilate. Since annihilation events alter both the skyrmion size and their effective spacing, they directly affect the measured diffusivity. The contributions of annihilation dynamics and field-driven diffusion can therefore not be disentangled.

Interestingly, although measured in the same run as the sparse-skyrmion results in Fig. 5.3 (labbook experiment ID 16725), the field gradient plays only a minor role for the dense skyrmion system at elevated T . Fig. 5.4b–c shows Kerr microscopy snapshots for $f = 500 \text{ Hz}$ with $A = 30 \mu\text{T}$ and $A = 300 \mu\text{T}$, respectively. Only for the larger amplitude does a gradient become visible in the magnetic structures.

Another crucial aspect when probing skyrmion diffusivity is the long-term stability of the sample properties, even under constant T and applied field. During the ex-

5. 300-Times-Increased Diffusive Skyrmion Dynamics and Effective Pinning Reduction by Periodic Field Excitation

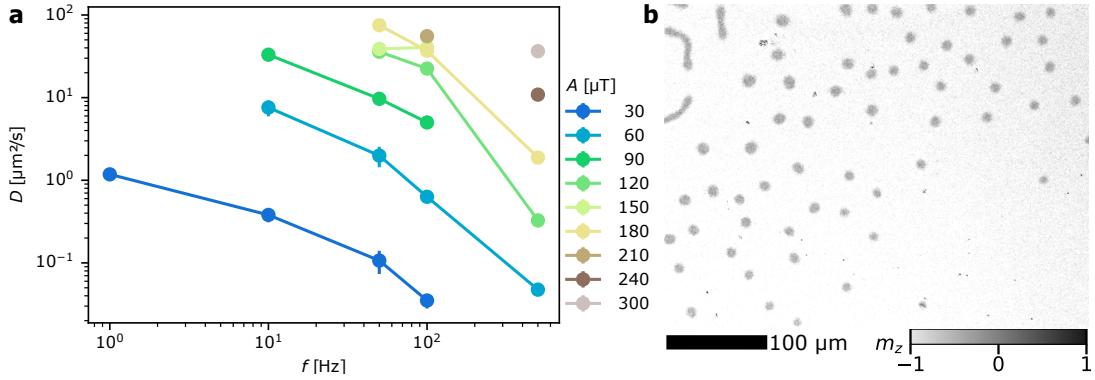


Figure 5.3.: Diffusion of Sparse Skyrmions in MAS763. (a) Diffusion coefficient D of sparse skyrmions exposed to oscillating magnetic fields of frequency f and amplitude A (peak-to-peak). For increasing f , D does not show a peak but decreases monotonously. Data points and error bars represent the mean and standard error of the mean from three independent measurements. (b) Kerr microscope snapshot of the sparse skyrmions in an oscillating field of $f = 100 \text{ Hz}$ and $A = 150 \mu\text{T}$ after $t = 30 \text{ s}$. A clear gradient is visible, with skyrmions becoming larger and denser towards the top left, where they expand into stripes, while the bottom right remains almost empty.

periments for section 5.1 [27], Tobias Sparmann and I recorded almost all data in a single continuous run over 48 h. While maintaining the sample at 320 K, we observed irreversible changes in the magnetic multilayer stack, indicating sample aging. This aging led to systematic shifts of D in Fig. 1 of section 5.1 [27]: at frequencies in the kilohertz range, field oscillations are too rapid to directly affect D , yet the diffusion curves recorded later in the run consistently showed lower values. We attribute this trend to gradual, irreversible material changes.

Similar aging effects have been observed in earlier experiments. For instance, in section 4.1 [27], a sample several years old required higher T for skyrmion nucleation. Likewise, the sample IK120, tested again in 2024, showed strongly altered skyrmion characteristics and could only host skyrmions above 330 K (labbook database ID 5833). The aging is most likely due to atom interdiffusion at the interfaces, changing the anisotropy and thus altering the magnetic behavior [138]. That such aging effects could be detected even within a two-day run highlights the sensitivity of our experiments: probing the entire parameter space of skyrmion stability makes even small variations in material properties measurable. Conversely, this sensitivity provides precise insights into the stability range of skyrmions. In particular, the applied OOP offset field and oscillation amplitude critically define skyrmion stability, as demonstrated in Fig. 1b-c of section 5.1 [27]. There, skyrmions are found to exist only within a $42 \mu\text{T}$ field window and to be particularly stable across a narrower $26 \mu\text{T}$ range. Over experimental timescales of several hours, the background field at the sample position can drift by a few μT due to laboratory devices being switched on or off or remanence in microscope components. During the 48 h run, I observed fluc-

5. 300-Times-Increased Diffusive Skyrmion Dynamics and Effective Pinning Reduction by Periodic Field Excitation

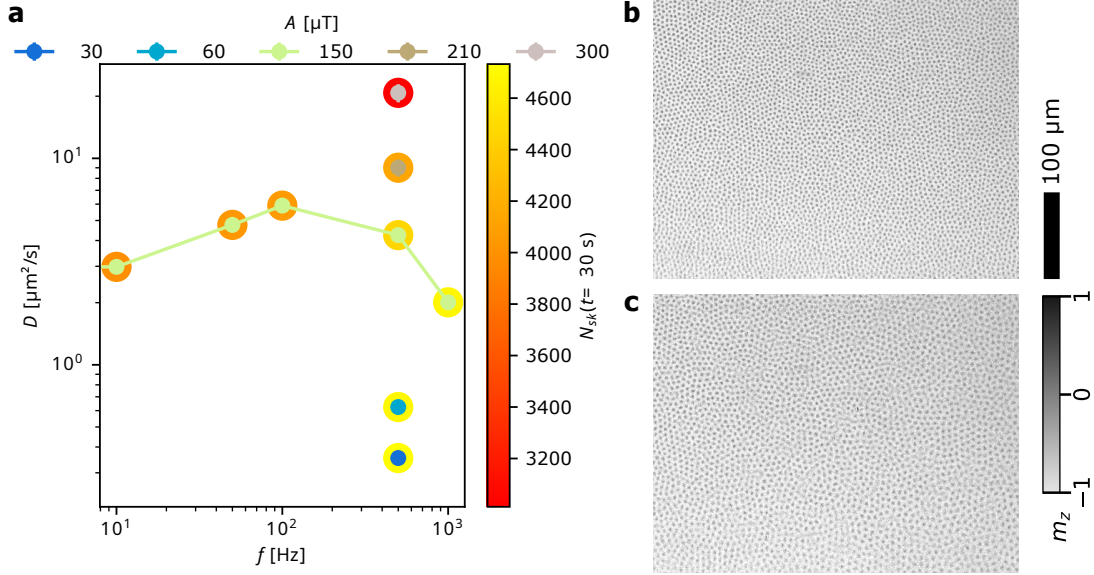


Figure 5.4.: Diffusion of Dense Skyrmions in MAS763. (a) Diffusion coefficient D of densely packed skyrmions exposed to oscillating magnetic fields of frequency f and amplitude A (peak-to-peak). Data points and error bars represent the mean and standard error of the mean from three independent measurements and are also shown in Figure S3b of section 5.1.1 [27]. Colored rings around the data points denote the number of skyrmions N_{sk} remaining after $t = 30$ s. (b–c) Kerr microscopy snapshots of skyrmion lattices in an oscillating field of $f = 500$ Hz with amplitudes $A = 30$ μT (b) and $A = 300$ μT (c) after 30 s. Only in (c) does the field gradient observed in Fig. 5.3 become visible, but of minor impact.

tuations of ± 10 μT in the background field. Nevertheless, by exploiting the precisely known stability criteria, these drifts can be compensated quickly and with remarkable reproducibility to within better than 1 μT .

5.2.2. Data Analysis for Diffusion Determination

Once a suitable skyrmion system and arrangement is established and recorded, the skyrmions must be detected and their occurrences linked to trajectories in order to extract the diffusion coefficient. For the experiments presented here, I exclusively used *trackpy* [131] for skyrmion tracking. Fig. 5.5a–b shows snapshots at $t = 10$ s from Supporting Videos 1–2 of section 5.1 [27], respectively.

In addition to the Kerr microscopy snapshots, I display the trajectories over the previous 5 s and annotate the detected *mass*, defined as the integrated intensity of the detected feature. Note that the parameter called *mass* in the output by *trackpy* is not to be confused with the mass connected to the skyrmion inertia [141]. In the unexcited case (Fig. 5.5a), skyrmions are both smaller and slower compared to the strongly excited case (Fig. 5.5b).

5. 300-Times-Increased Diffusive Skyrmion Dynamics and Effective Pinning Reduction by Periodic Field Excitation

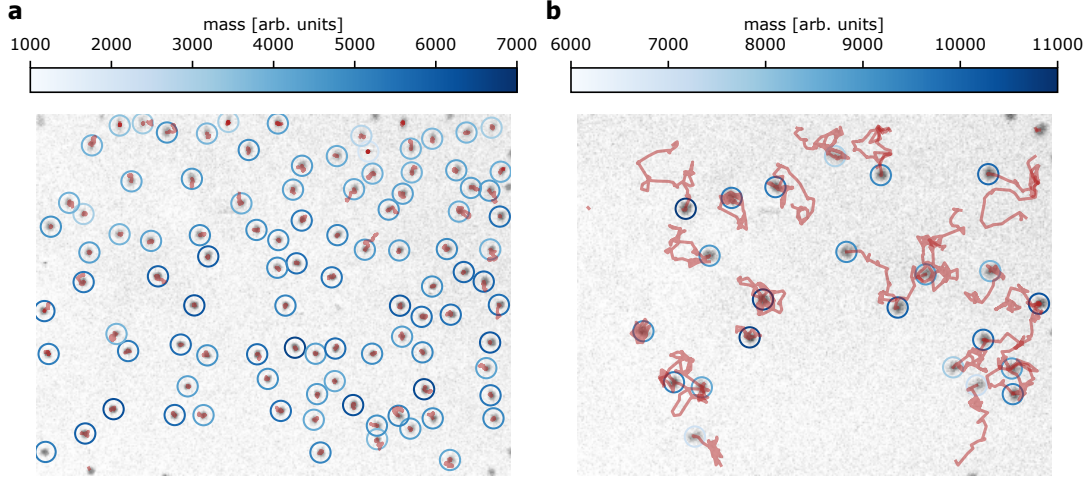


Figure 5.5.: Detection of Diffusing Skyrmions. (a) Kerr microscopy snapshot from Supporting Video 1 of section 5.1 [27] after 10 s without field oscillation. The grayscale contrast represents the OOP magnetization of the skyrmions. The blue circles mark the detected skyrmions in the snapshot, with the circle color denoting the detected *mass*, i.e., the integral of the fitted feature. Red lines indicate skyrmion trajectories over the previous 5 s. (b) Kerr microscopy snapshot from Supporting Video 2 of section 5.1 [27] after 10 s with field oscillation of $A = 2100 \mu\text{T}$ at 2 kHz. Analogous to (a), trajectories and *mass* are shown. Under oscillating fields, the skyrmions move faster and appear larger.

This different appearance of the skyrmions – despite identical temperature and offset field – requires particular consideration for the tracking algorithm described in section 3.2. Reliable and robust detection of skyrmions is a key prerequisite to determine D , as discussed in section 5.2.1. In Fig. 5.6, I present the tracking parameters used for *trackpy* [131] to analyze the experiments in section 5.1 [27].

By default, I use $diameter = 27$, $separation = 15$, and $minmass = 4000$. The parameters $diameter$ and $separation$ are usually kept at their default values and only slightly adjusted depending on skyrmion density and image contrast. The most influential parameter is $minmass$. Since skyrmions appear in varying sizes – as the size fluctuates around the constant offset field – the integrated intensity also varies significantly. In addition, the contrast can change, either due to the specific background subtraction applied or because fast skyrmion motion smears out the Kerr image contrast, especially when D is large. Consequently, $minmass$ must be chosen such that all skyrmions are reliably detected, while background noise and surface defects are excluded. In rare cases, I additionally filter by the *signal* value of the detection to exclude sharp intensity changes from scratches on the sample surface, which otherwise appear as very large *signal* values.

5. 300-Times-Increased Diffusive Skyrmion Dynamics and Effective Pinning Reduction by Periodic Field Excitation

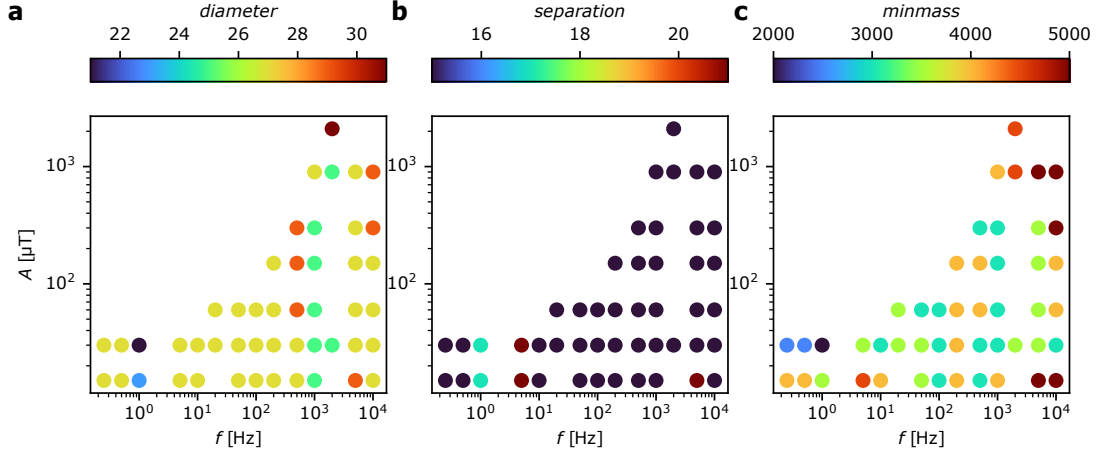


Figure 5.6.: Parameter Variation for Detection of Diffusing Skyrmions. Parameters (a) *diameter*, (b) *separation*, and (c) *minmass* used for detecting skyrmions in section 5.1 [27] with *trackpy* [131].

Experimental Note

Over the past years, a machine-learning based approach has been developed in our group to detect skyrmions, specifically in Kerr microscopy videos [133]. The trained *UNET* model can detect skyrmions efficiently and precisely without requiring explicit parameter choices. However, at the time of this study, the *UNET* could not reliably handle the varying contrast induced by fast skyrmion diffusion. For linking skyrmion occurrences to trajectories, *trackpy* [131, 132] thus remained the state-of-the-art method.

Once the skyrmions are detected and their trajectories linked, the MSD can be directly calculated according to Eq. 1.51. In Fig. 5.7, I present the MSD – including the number of skyrmions present (N_{sk}) and the number contributing to the MSD (N_{msd}) – for three different amplitudes A of the oscillating field at $f = 1$ kHz.

In the conventional definition following Eq. 1.51, the MSD is evaluated with respect to a fixed starting time t_0 . Consequently, only skyrmion trajectories that are already present at t_0 and remain observable at a later time t contribute to $\text{MSD}(t)$. Skyrmions that leave the field of view or trajectories that cannot be continuously linked are excluded, thereby reducing the number of contributing skyrmions N_{msd} . Since especially fast-moving skyrmions are prone to being not captured in this analysis, such restrictions can lead to a systematic underestimation of the diffusion coefficient D , particularly at longer timescales.

In the experiments considered here, the MSD exhibits a linear and stable behavior up to at least 20 s. Therefore, I also perform the fit of D within this time window. To enhance statistical robustness, however, I employ a sliding-window approach: instead of fixing the starting time t_0 , every video frame is treated as a new starting point. and I consider the average over all combinations. Accordingly, a skyrmion that remains observable for $k + 1$ consecutive frames contributes

5. 300-Times-Increased Diffusive Skyrmion Dynamics and Effective Pinning Reduction by Periodic Field Excitation

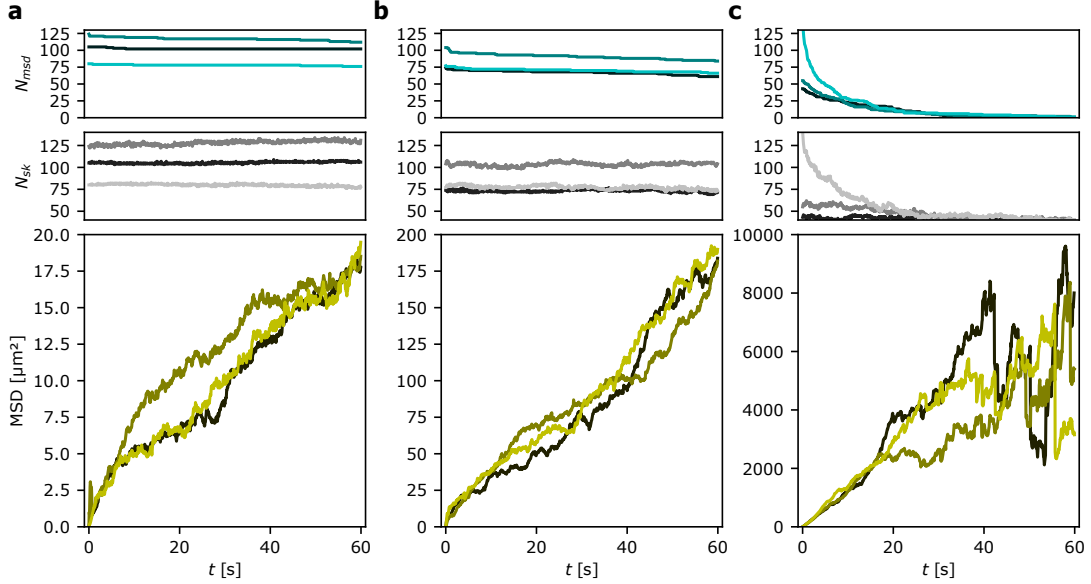


Figure 5.7.: MSD for Varying AC Field Amplitude. (a) MSD as a function of time t relative to $t_0 = 0$ for skyrmions in an oscillating field of $A = 60 \mu\text{T}$ at $f = 1 \text{ kHz}$. The number of skyrmions N_{sk} present in the frame can vary as skyrmions leave or enter the field of view. The number contributing to the MSD, N_{msd} , decreases over time since only trajectories starting at $t_0 = 0$ are included and exiting skyrmions are not replaced. Light, medium, and dark colors represent three independent skyrmion measurements. Analogously, (b) and (c) show N_{msd} , N_{sk} , and the MSD for skyrmions at $A = 300 \mu\text{T}$ and $A = 900 \mu\text{T}$, respectively. For larger A , the MSD increases more rapidly, and the slope determines the diffusion coefficient D . Due to the enhanced dynamics, trajectories are more frequently cut and annihilations occur more often, reducing both N_{msd} and N_{sk} significantly.

- for k steps starting at frame 0,
- for $k - 1$ steps starting at frame 1,
- for $k - 2$ steps starting at frame 2,
- ...
- for 1 step starting at frame k ,

where one step corresponds to the time between two frames, here 0.0625 s. This method significantly improves the statistics of the MSD, as each trajectory is considered multiple times, always with respect to different starting points. The resulting MSD is thus obtained as a function of the time delay τ relative to the starting times. This approach particularly increases N_{msd} for small τ . For τ comparable to or exceeding the recording length, only skyrmions present from the beginning contribute. Fig. 5.8 presents the corresponding results to Fig. 5.7, but obtained with the sliding-window method, which is also employed in the article in section 5.1 [27].

5. 300-Times-Increased Diffusive Skyrmion Dynamics and Effective Pinning Reduction by Periodic Field Excitation

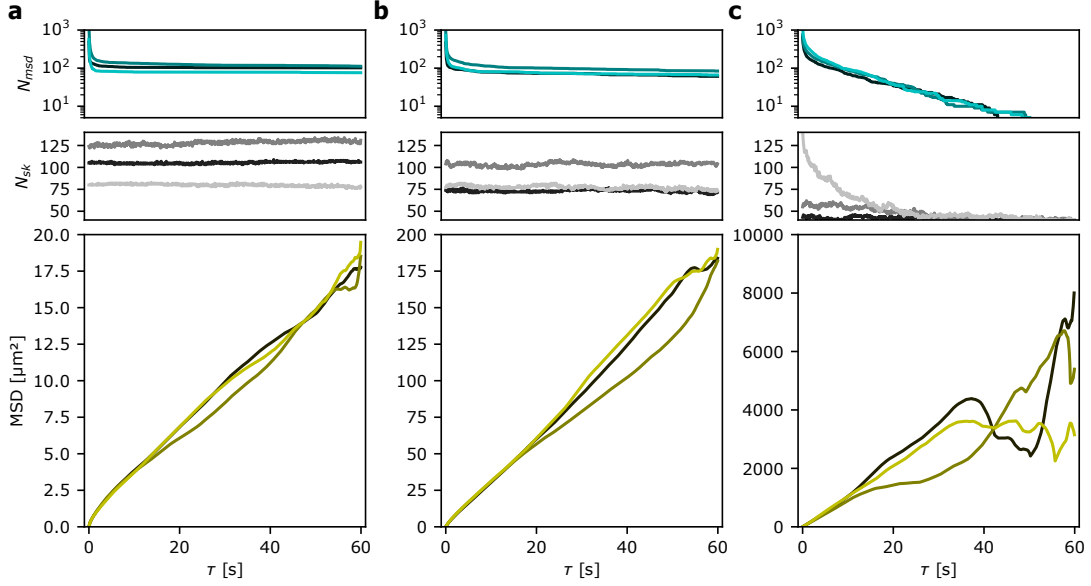


Figure 5.8.: MSD with Sliding-Window Analysis. MSD as a function of delay time τ , number of tracked skyrmions N_{sk} , and number of skyrmions contributing to the MSD for oscillating magnetic fields at $f = 1 \text{ kHz}$ and (a) $A = 60 \mu\text{T}$, (b) $A = 300 \mu\text{T}$, and (c) $A = 900 \mu\text{T}$. Data are evaluated with the sliding-window method, which enhances statistics particularly for small τ . Light, medium, and dark colors denote three independent measurements.

Quantitatively, the methods with and without window sliding yield results for D that are in good agreement. Nevertheless, the sliding-window approach provides substantially improved statistics. As discussed above, broken trajectories due to skyrmions entering or leaving the field of view, or due to mismatched linking, can bias the results. In particular, strongly pinned skyrmions are continuously present and reliably tracked; when they are then counted repeatedly in the sliding-window analysis, D may be systematically underestimated.

Alternatively, avoiding the sliding-window method and instead selecting a fixed starting time t_0 allows one to directly compare $\text{MSD}_{[t_0]}(\tau)$, i.e., the MSD as a function of τ for different, fixed starting times t_0 . This approach can reveal how the MSD evolves over time and permits extraction of the temporal evolution of D , as illustrated in Fig. 5.9. However, one has to be careful that fluctuations in D can also occur for statistical reasons.

5. 300-Times-Increased Diffusive Skyrmion Dynamics and Effective Pinning Reduction by Periodic Field Excitation

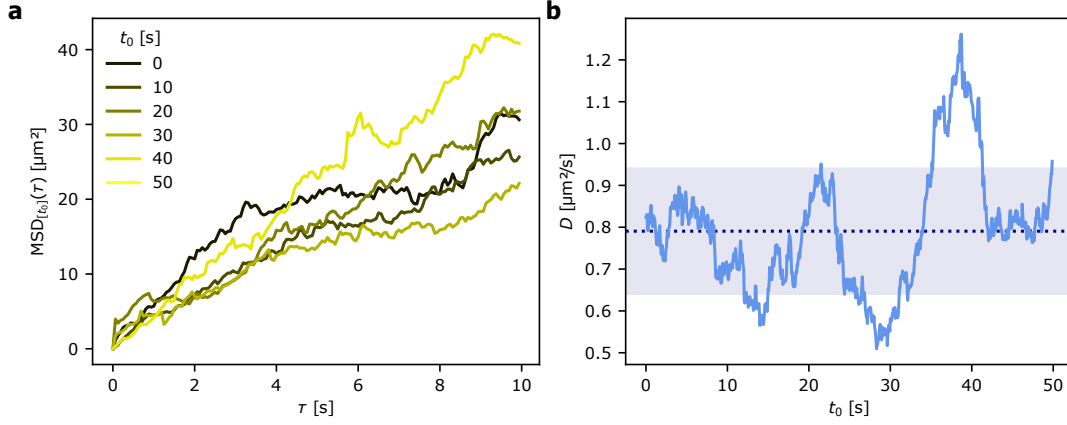


Figure 5.9.: Time Series of MSD and Diffusion Coefficient. (a) $\text{MSD}_{[t_0]}(\tau)$ for time delays τ at different fixed starting times t_0 . (b) Corresponding diffusion coefficients D obtained from fits over $\tau < 10$ s. The dashed line and shaded area indicate the mean value and standard deviation of D across all t_0 .

5.2.3. Setup Characterization for Field Oscillations

To apply oscillating magnetic fields in the experiments, I use an *Agilent A33250A* waveform generator, which can operate up to 80 MHz. The generator drives the electromagnetic OOP coil by applying an oscillating voltage. The effective magnetic field generated by the coil is, however, determined by the current I flowing through it. Since the coil represents an inductive load, it does not follow Ohm's law and must be characterized separately [142].

For this purpose, I include an Ohmic resistor R of 1Ω in series with the coil. Using an oscilloscope, I measure the voltage U across R , which provides a direct measure of I (see Fig. 5.10a). Applying AC voltages of fixed amplitude but varying frequency, I record the resulting U , from which I is determined. The time axis is rescaled such that signals of different frequencies can be displayed on the same axis. By normalizing $I(f)$ to the current at low frequency ($f = 1$ Hz), I obtain the transmission coefficient $T(f)$ shown in Fig. 5.10b. The transmission decreases sharply above 100 Hz due to the inductive response of the coil counteracting field modulation. Since the input is purely sinusoidal, only the amplitude of the transmitted signal is reduced, while its waveform remains sinusoidal [142], allowing to obtain a constant generated field amplitude even for higher frequencies by adjusting the used power.

To calibrate the coil field, I place a Hall probe at the sample position directly above the coil. The waveform generator is set to deliver a constant output. As the generator cannot supply true DC voltages, I mimic constant signals by applying oscillations of amplitude $100 \mu\text{V}$ superimposed on offset voltages up to 100 mV. The measured fields B as a function of U are shown in Fig. 5.11, together with a linear fit yielding the conversion factor $(3.0 \pm 0.1) \mu\text{T mV}^{-1}$. The calibration depends on the output load setting of the generator. Since the coil resistance is 3Ω , I also set the generator

5. 300-Times-Increased Diffusive Skyrmion Dynamics and Effective Pinning Reduction by Periodic Field Excitation

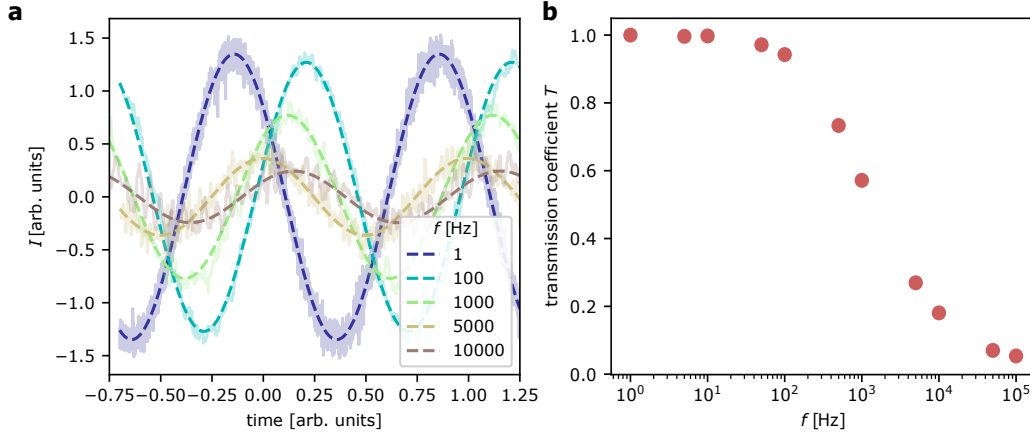


Figure 5.10.: Transmission of AC Currents in the Field Coil. (a) Voltage U across the Ohmic resistor R for different frequencies f of an AC input voltage of fixed amplitude. The time axis is normalized to show all signals on the same periodicity for direct comparison. The transmitted current I decreases with increasing f . Thin, semi-transparent lines indicate measured I (smoothed by a rolling mean over 10 data points for visibility); dashed lines show sinusoidal fits used to extract amplitudes. (b) Transmission coefficient $T = I(f)/I(f = 1 \text{ Hz})$, which decreases strongly for $f > 100 \text{ Hz}$.

output load to 3Ω .

In the experiments, I correct the applied amplitude by a factor $1/T(f)$ to achieve the desired oscillation amplitude A . For example, at $T(1 \text{ kHz}) = 0.57$, reaching $A = 100 \mu\text{T}$ requires applying an effective amplitude of $175.4 \mu\text{T}$, corresponding to an output voltage of 58.5 mV .

Initially, I attempted to use the waveform generator at frequencies up to the MHz range to approach the skyrmion breathing mode in the GHz regime [143]. However, above approximately 5 kHz , the transmitted current deviates from a clean sinusoidal shape, and the generator alone does not provide sufficient power to generate measurable field amplitudes due to the low $T(f)$. In complementary test measurements, oscillating fields up to the GHz range with amplitudes of approximately $25 \mu\text{T}$ were generated using an omega antenna (prepared by Philipp Schwenke, RPTU Kaiserslautern, and tested together). No measurable influence on skyrmion diffusion was observed.

Since the oscillation frequencies at which the diffusion peaks lie in the range of a few to a few hundred hertz in our system, the *Kepeco BOP* power supply integrated into the microscope setup is sufficient. The microscope software provides built-in functionality to generate simple waveforms such as sine and square waves. For quantitative experiments, however, it remains essential to verify the transmitted signal amplitude and shape – analogous to the procedure described above.

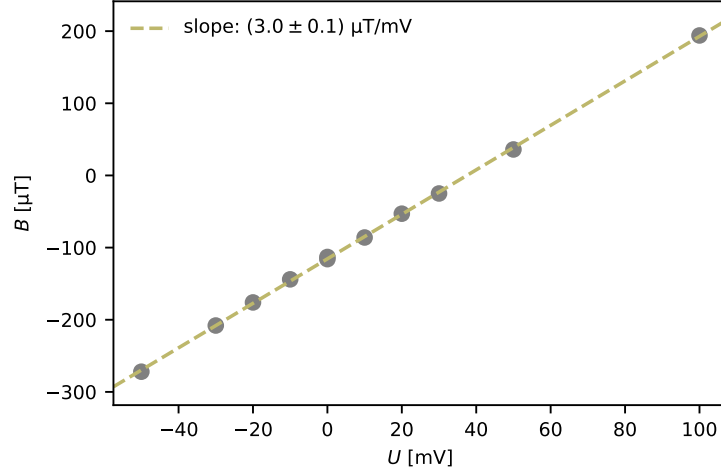


Figure 5.11.: Calibration of Coil Field Strength. Constant voltages U applied by the waveform generator produce constant magnetic fields B , measured with a Hall probe at the sample position. Applying 1 mV (for a generator output load of $3\ \Omega$) corresponds to $B = (3.0 \pm 0.1)\ \mu\text{T}$. Gray points show measured data; the green dashed line is a linear fit.

5.3. Author Contributions

I performed all the experiments at the Kerr microscope. Thereby, Tobias Sparmann kindly assisted me, so we could run long measurements over two full days working in alternating shifts.

I performed the skyrmion detection and trajectory linking using *trackpy* [131]. I also developed the Python code to calculate the MSD and diffusion coefficient. One measurement run was analyzed by Maarten A. Brems and aggregated as shown in Fig. 1 of section 5.1 [27], based on a common idea of the two of us. The code was developed by myself to analyze several measurement runs and to generate the plots shown in section 5.1 [27]. The energy landscape based on skyrmion occurrences was analyzed by me and Jan Rothörl independently. The analysis of the skyrmion displacements was done by Jan Rothörl, with me providing the data and plotting the final result. The argument that the enhanced diffusion cannot simply be explained by the size-dependence of the diffusion coefficient was developed by Maarten A. Brems.

The magnetic multilayer samples were deposited by Iryna Kononenko, Fabian Kammerbauer and Maria-Andromachi Syskaki. The optimization for the material composition was primarily done by Fabian Kammerbauer and Maria-Andromachi Syskaki. Oded Farago helped with the interpretation of the results regarding diffusion in pinning landscapes. Peter Virnau and Mathias Kläui supervised and guided this work. Peter Virnau and Mathias Kläui contributed as PhD supervisors and principal investigators in our skyrmion research group and provided advice in regular discussions.

6. Conclusion – Thermal Skyrmion Diffusion in a Non-Flat Energy Landscape

6.1. Summary

In summary, I investigated the thermal dynamics of isolated skyrmions in CoFeB thin films using Kerr microscopy.

In the presence of a non-flat energy landscape [64], material inhomogeneities induce spatial modulations of the magnetic parameters. These inhomogeneities give rise to position-dependent variations of the skyrmion energy, thereby creating pinning sites that are energetically more favorable than their surroundings. From the occurrence probability density, I reconstructed the effective potential landscape. Our analysis reveals that skyrmions are predominantly pinned at their boundary, such that the pinning strength depends on the skyrmion size [64].

The skyrmion size can be tuned efficiently by the applied magnetic field [19, 64, 117]. When oscillating magnetic fields are applied, the skyrmion size undergoes periodic modulation, which effectively exposes the skyrmions to a time-dependent energy landscape. This external driving assists skyrmions in escaping pinning sites and thereby enhances their diffusion. The diffusion coefficient exhibits pronounced peaks at frequencies ranging from a few to several hundred hertz, depending on the system parameters. In general, larger oscillation amplitudes further enhance diffusion, but at the same time destabilize skyrmions, leading to an increased probability of annihilation [27].

6.2. Challenges

Experimentally, reconstructing non-flat energy landscapes is relatively well established. However, extracting detailed pinning characteristics and predicting the corresponding skyrmion behavior [64, 144] remain challenging. Acquiring a robust energy landscape, in which a significant portion of the field of view is sampled, typically requires several hours of measurement and thus yields a landscape for only a single skyrmion size. On the one hand, mapping the landscape for all possible skyrmion sizes is practically not feasible. On the other hand, pinning effects are not fully captured by position probabilities alone, since boundary pinning dominates. Determining which sections of the boundary remain inaccessible, even across multiple size-dependent landscapes, is nontrivial. Significant further work is required

to extract boundary pinning from such data, for instance by correlating boundary occurrences [145], which in turn necessitates sufficient spatial resolution. Depending on the level of detail required, however, a simplified treatment of skyrmions as rigid particles is often sufficient.

Maintaining stable measurement conditions constitutes another major challenge. Skyrmions are sensitive to OOP magnetic field variations on the order of only a few microtesla – smaller than the Earth’s magnetic field and typical stray fields from neighboring equipment. Such fields must therefore be carefully monitored. Since magnetic fields from distant sources are largely homogeneous across the microscope region, they can be measured effectively with a three-dimensional Fluxgate sensor, which provides nanotesla sensitivity and millisecond time resolution [146]. Owing to its centimeter-scale dimensions, the Fluxgate sensor cannot measure directly at the sample position, but this limitation is acceptable for homogeneous background fields. Detecting and compensating remanence fields from within the microscope itself is more difficult. Because the samples are significantly more sensitive to OOP fields (microtesla relevant) than to IP fields (millitesla relevant), the OOP component is critical. Variations in the size, homogeneity, and stability range of the skyrmions reflect the effective OOP field and can thus serve as indirect monitors of stability, although continuous attention is required. Temperature stability, by contrast, is easier to maintain at the necessary level of about (0.3 ± 0.2) K combining the laminar flow box and the Peltier element. In addition, long-term stability is affected by aging processes in the multilayer stacks, such as annealing or intermixing at the interfaces, which irreversibly alter the magnetic parameters.

Maintaining constant measurement conditions therefore requires not only careful control of directly adjustable parameters such as magnetic field and temperature, but also consideration of uncontrollable influences such as sample aging.

A further challenge in diffusivity measurements is temporal resolution. Exposure times must be long enough to ensure sufficient magnetic contrast, yet short enough to resolve the skyrmion motion – a balance that is especially critical when diffusion is fast.

Experimental Note

In 2024, a new camera was installed on the Kerr microscope. In samples with transparent HfO₂ capping, Grisca Beneke succeeded in recording skyrmion dynamics at frame rates up to 500 fps.

Alternatively, moving intensity averages of consecutive frames and advanced processing techniques such as coherent correlation imaging provide powerful means to improve the effective temporal resolution.

On the simulation side, the central challenge remains modeling non-rigid skyrmion structures on large scales. Micromagnetic simulations can capture flexible skyrmion structures in non-uniform magnetic parameter landscapes [64], but they are computationally demanding and limited to systems extending only from nanometers to a

few micrometers. Since the skyrmions studied here are micrometer-sized and measured in millimeter-scale samples, such approaches are currently impractical. Instead, molecular dynamics simulations treating skyrmions as particles provide an efficient framework [70, 71]. Up to now, the model developed by our collaborators in the group of Prof. Peter Virnau has treated skyrmions as rigid point particles. Extending this model to incorporate non-rigid boundary effects represents an important step toward more realistic and predictive simulations.

6.3. Outlook

Thermal diffusion of magnetic skyrmions constitutes a powerful two-dimensional model system for addressing open questions in fundamental physics.

Modeling oscillating magnetic fields as flashing potentials can refine our understanding of the mechanisms underlying enhanced diffusion and effective pinning reduction. A central open question is whether this mechanism can drive skyrmions to diffuse faster than they would in a flat, pinning-free landscape. Since the oscillating field represents a permanent external drive, it is expected to induce non-equilibrium effects that remain largely unexplored. Another unresolved question is whether oscillating fields – by shifting skyrmion dynamics from local hopping to long-range quasi-free diffusion – enhance the effective Magnus force, thereby enabling the investigation of odd diffusivity effects [147].

It also remains to be clarified to what extent other driving mechanisms yield comparable effects. Experiments by Tobias Sparmann and Leonie Dany have demonstrated that alternating currents can induce similar enhancements. Additional proposals include non-symmetric surface acoustic waves [148], as well as pulsed local heating or stray fields.

For the study of fundamental aspects of two-dimensional physics, enhanced skyrmion diffusion – particularly with potential non-equilibrium features and Magnus force contributions – offers a highly attractive platform. For skyrmion-based spintronic devices, however, the central issue is not diffusion itself but rather depinning mechanisms under external driving. Efficient depinning is essential for device operation, and proposed driving schemes must therefore be tested across a broader range of skyrmion systems and materials. While CoFeB thin films are ideally suited for laboratory studies – with room-temperature skyrmions observable optically and magnetic properties readily accessible – technological applications demand nanoscale operation together with significantly stricter thermal and magnetic stability. Identifying materials and systems that simultaneously fulfill these requirements remains a major open challenge.

On the technical side, the extraction of skyrmion energy landscapes is already well established [64, 71]. Advanced processing techniques such as coherent correlation imaging [145] promise substantial improvements in efficiency and spatial resolution, making them particularly valuable for system characterization in view of future device applications.

Part III.

**Formation & Phase Behavior of 2D
Skyrmion Lattices**

7. Overview

Publication Information


The following article is published as part of the following preprint:

The 2026 Skyrmionics Roadmap

Sabri Koraltan, Claas Abert, Manfred Albrecht, Maria Azhar, Christian Back, H el ene B ea, Max T. Birch, Stefan Bl ugel, Olivier Boule, Felix B uttner, Ping Che, Vincent Cros, Emily Darwin, Louise Desplat, Claire Donnelly, Haifeng Du, Karin Everschor-Sitte, Amalio Fern andez-Pacheco, Simone Finizio, Giovanni Finocchio, Markus Garst, Raphael Gruber, Dirk Grundler, Satoru Hayami, Thorsten Hesjedal, Axel Hoffmann, Aleř Hrabec, Hans Josef Hug, Hariom Jani, Jagannath Jena, Wanjun Jiang, Javier Junquera, Kosuke Karube, Lisa-Marie Kern, Joo-Von Kim, Mathias Kl aui, Hidekazu Kurebayashi, Kai Litzius, Yizhou Liu, Martin Lonsky, Christopher H. Marrows, Jan Masell, Stefan Mathias, Yuriy Mokrousov, Stuart S. P. Parkin, Bastian Pfau, Paolo G. Radaelli, Florin Radu, Ramamoorthy Ramesh, Nicolas Reyren, Stanislas Rohart, Shinichiro Seki, Ivan I. Smalyukh, Sopheak Sorn, Daniel Steil, Dieter Suess, Mykola Tasinkevych, Yoshinori Tokura, Riccardo Tomasello, Victor Ukleev, Hyunsoo Yang, Fehmi Sami Yasin, Xiuzhen Yu, Chenhui Zhang, Shilei Zhang, Le Zhao & Sebastian Wintz

arXiv **2601**, 16575 (2026).

DOI: [10.48550/arXiv.2601.16575](https://doi.org/10.48550/arXiv.2601.16575)

Copyright Information:  CC BY 4.0 Creative Commons Attribution 4.0 International License

Editorial Note: The version shown here is adapted to only show the contribution "2D Skyrmion Lattice Phases" by Raphael Gruber and Mathias Kl aui with the respective references. The blue header/footer bars were added for inclusion in this dissertation and are not part of the original publication.

Contributions

I prepared the draft for this article, which was reviewed and proof-read by Mathias Kl aui prior to submission.

Use of large language models is specified in [section C.3](#).

2D Skyrmion Lattice Phases

Raphael Gruber¹, Mathias Kläui^{1,2}

^{1.} Institute of Physics, Johannes Gutenberg-Universität Mainz, Staudingerweg 7, 55128 Mainz, Germany.

^{2.} Center for Quantum Spintronics, Department of Physics, Norwegian University of Science and Technology, 7491 Trondheim, Norway.

Email: klaeui@uni-mainz.de

Introduction

Phases and phase transitions in two dimensions (2D) are fundamentally distinct from those in other dimensions, a feature that has drawn significant scientific interest over decades[1]. While in 3D, the translationally ordered solid phase and the isotropic liquid phase are well-known, the situation is more complex in 2D, where an intermediate hexatic phase with only orientational order can arise[1,2]. The landmark theoretical framework developed by Kosterlitz, Thouless, Halperin, Nelson, and Young (KTHNY theory) predicts that topological defects play a pivotal role in mediating the phase transitions between those 2D phases[2]. In this picture, each site in a 2D lattice with a coordination number $N \neq 6$ constitutes a topological defect. While the solid phase features only tightly bound dislocation pairs (with a fivefold and a sevenfold coordinated site comprising a dislocation), the hexatic phase is characterized by the unbinding of these dislocations. Finally, in the isotropic liquid phase, dislocations further decompose into disclinations (isolated single defects), which then proliferate (Fig. 1a)[2].

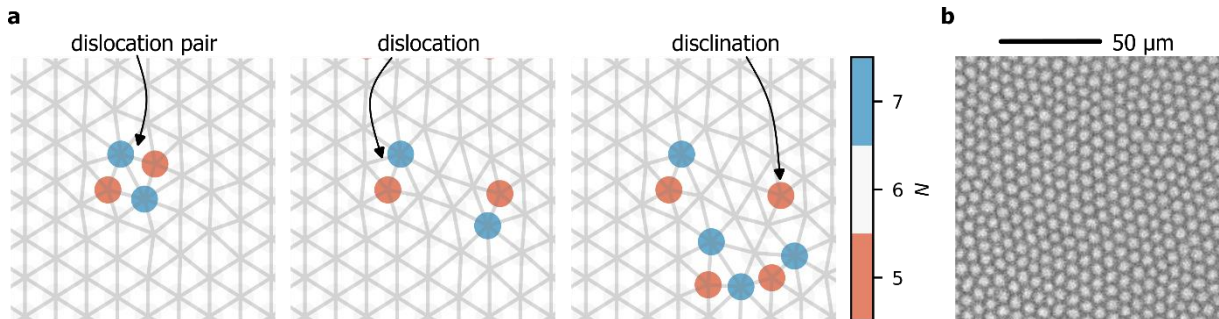


Fig. 1. (a) Schematic of topological lattice defects. Lattice neighbor connections are indicated by the grey lines. The colored dots indicated the number of lattice neighbors (coordination number) N . For slight distortions of an ideal lattice ($N=6$), dislocation pairs of two $N=5$ and $N=7$ defects form. With decreasing order across 2D phase transitions, they unbind into dislocations and disclinations. (b) Kerr microscopy snapshot of a skyrmion lattice in a CoFeB thin film. Black/white contrast corresponds to magnetization pointing up/down.

This sequence of defect-mediated transitions has been directly observed in 2D skyrmion lattices (SkLs), realized in a variety of material platforms including magnetic monolayers (e.g., Fe/Ir(111)), van der Waals magnets (e.g., CrI₃, Fe₃GeTe₂), oxide heterostructures (e.g., Cu₂OSeO₃), and amorphous or polycrystalline thin films (e.g., CoFeB, Fig. 1b)[3–5]. Advances in materials synthesis techniques such as molecular beam epitaxy (MBE) and chemical vapor deposition (CVD) have enabled the engineering of key magnetic parameters—Dzyaloshinskii–Moriya interaction (DMI), anisotropy, and exchange stiffness—allowing precise stabilization of SkLs under ambient and tunable conditions.

As a result, 2D SkL phases have become highly relevant not only for fundamental studies in topological matter and phase transitions, but also for emerging spintronic applications. Their inherent topological stabilization, tunability, and compatibility with thin-film technologies position them as a versatile and promising class of physical systems.

Relevance

At the heart of the relevance of 2D SkLs is their function as an accessible and tunable platform to investigate topological phase transitions and defect-mediated dynamics in two dimensions. Unlike colloidal or superconducting vortex lattices, SkLs allow exceptional control over parameters such as lattice spacing, interaction potential, and both skyrmion as well as defect mobility[3,4,6]—making them uniquely suited to experimentally realize and manipulate the scenarios described by KTHNY theory[7].

In thin CoFeB films, for example, the skyrmion size and mobility can be modulated in situ via the applied magnetic field[6]. In Cu_2OSeO_3 , the interaction potential among skyrmions is similarly field-dependent, enabling fine control over lattice rigidity[3]. More generally, both temperature and external magnetic field govern SkL properties such as density and spacing, allowing the phase space of 2D transitions to be thoroughly explored[5,8] and enabling tuning of the dynamics[4,6].

While nanoscale skyrmions are most relevant for device applications, micrometer-sized skyrmions offer distinct advantages for fundamental studies: they are optically detectable in real time and real space, permitting direct visualization of phase transitions and defect dynamics[4,5]. Kerr microscopy of SkLs in CoFeB thin films has confirmed the emergence of dislocations and disclinations consistent with KTHNY theory, and enabled the tracking of defect trajectories, revealing that dislocations—acting as higher-order quasiparticles—exhibit diffusion coefficients orders of magnitude larger than the skyrmions forming the underlying lattice[4].

Importantly, SkLs can extend KTHNY physics beyond equilibrium. Due to the chiral nature of skyrmions, they experience a transverse Magnus force, making them ideal for studying topological defect dynamics under non-conservative forces—a largely unexplored frontier[4,9]. Furthermore, dynamic perturbations such as magnetic field oscillations or different parameter sweeps can drive SkLs out of equilibrium[4,6], facilitating studies of, e.g., shock waves, lattice phonons, and dissipative phase transitions.

The system's versatility is further expanded by external control techniques. Electric gating and local irradiation can dynamically manipulate magnetic properties and even pin individual skyrmions to predetermined lattice sites, enabling artificial SkLs with engineered defect structures or novel phases[9,10].

Beyond fundamental insights, these properties translate into technological potential. For example, deliberately introducing and manipulating dislocations may provide new modes of low-power information transport[4]. If a dislocation hops between two metastable configurations and this distortion can be electrically detected (e.g., via industrially established devices like magnetic tunnel junctions), it could serve as a logic state. Similarly, the nonlinear, history-dependent responses of SkLs to external fields position them as candidates for reservoir computing, where dynamic complexity is an asset[11]. Key observables include order parameters, elastic constants, noise spectra, and even thermally driven stochasticity, the latter enabling explorations of Brownian computing paradigms[11].

Challenges

Despite significant advances, several key challenges must be addressed to fully realize the promise of 2D SkLs.

First, spatial or time resolution are currently limiting factors. In many systems, skyrmions are only tens of nanometers or less in diameter, requiring high-resolution techniques such as Lorentz transmission electron microscopy (TEM), scanning tunneling microscopy (STM) or magnetic force microscopy (MFM)[3]. These methods, however, offer limited time resolution, complicating the study of dynamics. By contrast, systems such as CoFeB with micrometer-scale skyrmions allow time-resolved optical imaging[4] but suffer from pinning effects due to inhomogeneities and roughness in the film[8,9]. Even with optimized growth conditions, such imperfections are unavoidable in real materials and hinder the formation of perfect SkLs[4].

Second, device integration remains a formidable challenge. For SkLs to be functional in practical architectures, they must be stable over large areas, reproducible, and compatible with CMOS technologies[11]. Precise control over skyrmion generation, annihilation, and manipulation within a lattice is essential, yet more complex than for isolated skyrmions due to collective behavior. Skyrmion-skyrmion interactions and the elastic properties of the lattice can restrict the motion of individual skyrmions[4], necessitating new schemes for local and reversible control—e.g., via tailored current pulses, localized heating, or strain fields—without destabilizing the lattice.

Third, readout and interfacing strategies must be refined. Detection techniques such as tunnel magnetoresistance (TMR) and manipulation by current-induced spin-transfer torque (STT) need to be combined with maintained skyrmion integrity, while providing robust signal contrast and low-power manipulation. Similarly, scalable, in situ, and ideally non-invasive methods for imaging SkLs—especially in buried interfaces and ambient conditions—remain a key requirement.

Finally, from a theoretical standpoint, accurate modeling of SkLs in realistic environments must incorporate disorder, thermal noise, complex interfacial couplings, and non-equilibrium dynamics[12]. Multiscale modeling frameworks that bridge atomistic simulations with micromagnetic and continuum approaches are essential to capture both local defect behavior and long-range lattice dynamics.

Conclusion

In summary, 2D skyrmion lattice phases present an exciting frontier at the convergence of topological statistical physics, materials science, and spintronic device engineering. They not only offer an exceptional platform for studying fundamental aspects of 2D phase transitions and defect dynamics, but also hold promise for applications in reconfigurable, energy-efficient information processing. As we look toward 2026 and beyond, coordinated progress in materials development, experimental methodology, and multiscale modeling will be crucial to unlocking the full potential of SkLs in both scientific discovery and technological innovation.

References

- [1] J.M. Kosterlitz, D.J. Thouless, Ordering, metastability and phase transitions in two-dimensional systems, *J. Phys. C: Solid State Phys.* 6 (1973) 1181–1203. <https://doi.org/10.1088/0022-3719/6/7/010>.
- [2] D.R. Nelson, B.I. Halperin, Dislocation-mediated melting in two dimensions, *Phys. Rev. B* 19 (1979) 2457–2484. <https://doi.org/10.1103/PhysRevB.19.2457>.
- [3] P. Huang, T. Schönenberger, M. Cantoni, L. Heinen, A. Magrez, A. Rosch, F. Carbone, H.M. Rønnow, Melting of a skyrmion lattice to a skyrmion liquid via a hexatic phase, *Nat. Nanotechnol.* 15 (2020) 761–767. <https://doi.org/10.1038/s41565-020-0716-3>.
- [4] R. Gruber, J. Rothörl, S.M. Fröhlich, M.A. Brems, F. Kammerbauer, M.-A. Syskaki, E.M. Jefremovas, S. Krishnia, A. Sudbø, P. Virnau, M. Kläui, Imaging Topological Defect Dynamics Mediating 2D Skyrmion Lattice Melting, (2025). <https://doi.org/10.48550/arXiv.2501.13151>.
- [5] J. Zázvorka, F. Dittrich, Y. Ge, N. Kerber, K. Raab, T. Winkler, K. Litzius, M. Veis, P. Virnau, M. Kläui, Skyrmion Lattice Phases in Thin Film Multilayer, *Adv. Func. Mater.* 30 (2020) 2004037. <https://doi.org/10.1002/adfm.202004037>.
- [6] R. Gruber, M.A. Brems, J. Rothörl, T. Sparmann, M. Schmitt, I. Kononenko, F. Kammerbauer, M.-A. Syskaki, O. Farago, P. Virnau, M. Kläui, 300-Times-Increased Diffusive Skyrmion Dynamics and Effective Pinning Reduction by Periodic Field Excitation, *Adv. Mater.* 35 (2023) 2208922. <https://doi.org/10.1002/adma.202208922>.
- [7] M. Kläui, Freezing and melting skyrmions in 2D, *Nat. Nanotechnol.* 15 (2020) 726–727. <https://doi.org/10.1038/s41565-020-0726-1>.
- [8] R. Gruber, J. Zázvorka, M.A. Brems, D.R. Rodrigues, T. Dohi, N. Kerber, B. Seng, M. Vafaei, K. Everschor-Sitte, P. Virnau, M. Kläui, Skyrmion pinning energetics in thin film systems, *Nat. Commun.* 13 (2022) 3144. <https://doi.org/10.1038/s41467-022-30743-4>.
- [9] C. Reichhardt, C.J.O. Reichhardt, M.V. Milošević, Statics and dynamics of skyrmions interacting with disorder and nanostructures, *Rev. Mod. Phys.* 94 (2022) 035005. <https://doi.org/10.1103/RevModPhys.94.035005>.
- [10] L.-M. Kern, B. Pfau, V. Deinhart, M. Schneider, C. Klose, K. Gerlinger, S. Wittrock, D. Engel, I. Will, C.M. Günther, R. Liefferink, J.H. Mentink, S. Wintz, M. Weigand, M.-J. Huang, R. Battistelli, D. Metternich, F. Büttner, K. Höflich, S. Eisebitt, Deterministic Generation and Guided Motion of Magnetic Skyrmions by Focused He⁺-Ion Irradiation, *Nano Lett.* 22 (2022) 4028–4035. <https://doi.org/10.1021/acs.nanolett.2c00670>.
- [11] O. Lee, R. Msiska, M.A. Brems, M. Kläui, H. Kurebayashi, K. Everschor-Sitte, Perspective on unconventional computing using magnetic skyrmions, *Appl. Phys. Lett.* 122 (2023) 260501. <https://doi.org/10.1063/5.0148469>.
- [12] M.A. Brems, T. Sparmann, S.M. Fröhlich, L.-C. Dany, J. Rothörl, F. Kammerbauer, E.M. Jefremovas, O. Farago, M. Kläui, P. Virnau, Realizing Quantitative Quasiparticle Modeling of Skyrmion Dynamics in Arbitrary Potentials, *Phys. Rev. Lett.* 134 (2025) 046701. <https://doi.org/10.1103/PhysRevLett.134.046701>.

8. Skyrmion Lattice Domain Formation in a Non-Flat Energy Landscape

8.1. Published Article

Publication Information


The following article is published in *Communications Physics*:

Skyrmion Lattice Domain Formation in a Non-Flat Energy Landscape

Raphael Gruber, Simon M. Fröhlich, Jan Rothörl, Maarten A. Brems, Tobias Sparmann, Fabian Kammerbauer, Maria-Andromachi Syskaki, Elizabeth M. Jefremovas, Sachin Krishnia, Asle Sudbø, Peter Virnau & Mathias Kläui

Communications Physics **9**, 29 (2026).

DOI: [10.1038/s42005-025-02462-x](https://doi.org/10.1038/s42005-025-02462-x)


Copyright Information:  CC BY 4.0 Creative Commons Attribution 4.0 International License

Editorial Note: The blue header/footer bars were added for inclusion in this dissertation and are not part of the original publication.

Contributions

The author contributions for this project and article are described in detail in section 8.3.

Experimental Note

Documentation of my experiments used for this article are available for lab members on *eLabFTW* ( labbook database ID [7506](#)).

<https://doi.org/10.1038/s42005-025-02462-x>

Skyrmion lattice domain formation in a non-flat energy landscape

Check for updates

Raphael Gruber¹, Simon M. Fröhlich¹, Jan Rothörl¹, Maarten A. Brems¹, Tobias Sparmann¹, Fabian Kammerbauer¹, Maria-Andromachi Syskaki^{1,2}, Elizabeth M. Jefremovas¹, Sachin Krishnia¹, Asle Sudbø³, Peter Virnau¹ & Mathias Kläui^{1,3} ✉

Magnetic skyrmions are chiral spin structures with non-trivial topology that comprise two-dimensional quasi-particles and are promising information carriers for data storage and processing devices. Skyrmion lattices in magnetic thin films exhibit Kosterlitz–Thouless–Halperin–Nelson–Young (KTHNY) phase transitions and have garnered significant interest for studying emergent 2D phase behavior. In experimental skyrmion lattices, the main factor limiting the quasi-long-range order in thin films has been the non-flat energy landscape – often referred to as pinning effects. We demonstrate direct control of the skyrmion lattice order by effectively tuning the energy landscape employing magnetic field oscillations. By quantifying lattice order and dynamics, we explore how domain boundaries form and evolve due to pinning effects in Kerr microscopy experiments and in Brownian dynamics simulations, offering a pathway to control and study emergent skyrmion lattice properties and 2D phase behavior.

Two-dimensional (2D) lattices encompass a unique nature of ordering phenomena^{1–5}, qualitatively different from 3D or other dimensions. Specifically, the transition between the solid phase—where translational quasi-long-range order (QLRO) is present—and the isotropic liquid phase can be marked by the emergence of an intermediate hexatic phase^{3,4}. This hexatic phase possesses only orientational, but no translational QLRO and is described within the framework of the Kosterlitz–Thouless–Halperin–Nelson–Young (KTHNY) theory^{1–5}.

Magnetic skyrmions—chiral spin textures that exhibit quasi-particle properties due to their topologically non-trivial spin structure^{6–8}—are an ideal platform for exploring the fundamental physics of ordering in 2D^{9–13}. In thin magnetic films with layer thicknesses of around 1 nm, skyrmion sizes can range from nanometers to a few micrometers⁸. This size range, combined with the uniformity of their texture across the film thickness, makes those skyrmions ideal 2D quasi-particles¹². In Ta/CoFeB/MgO multilayer stacks, the repulsive interaction potential^{14–17} enables skyrmion arrangements of high densities to form ordered hexagonal lattices at room temperature^{10,12,16}. Thereby, the thermal excitation of spins is sufficient to cause Brownian motion of the quasi-particle skyrmions^{18–20}. The skyrmion dynamics is even tunable on the fly²¹ and the individual skyrmions can be tracked with high resolution imaging by Kerr microscopy in real-time and -space^{18–20}. Therefore, their versatility in order to induce and observe the dynamics associated with the KTHNY phase transitions¹⁰ is a key advantage

of skyrmions over previously studied colloidal^{22,23} or superconducting vortex^{24,25} systems.

However, achieving QLRO for skyrmion lattices in continuous thin films is challenging because of the underlying non-flat energy landscape^{10–12,26}. The roughness of the energy landscape arises from non-uniform magnetic properties^{20,27} due to non-uniform interfaces or locally varying crystallinity within the material stack^{20,27–31}. The material inhomogeneities cause preferred positions for the skyrmions – so-called pinning sites. The term *pinning* is often used to describe the general roughness of the energy landscape. It is however important to note that the overall non-flat landscape may feature both attractive and repulsive positions^{20,27–31} of varying strengths as a continuous variation of the energy of a skyrmion across the sample. In the energy landscape of thin films, skyrmions are typically pinned at their delineating domain wall, which makes pinning effects dependent on the skyrmion size²⁰ and effectively tunable by magnetic field oscillations²¹. While theoretical predictions allow for the existence of QLRO in skyrmion lattices with weak pinning, stronger pinning suppresses ordering transitions entirely^{27,32,33}. Experimental investigations have revealed that the non-flat energy landscape significantly impacts skyrmion lattice formation^{11,12}, resulting in polycrystalline lattice domains, which are separated by domain boundaries (DB). Hence, QLRO is maintained only on a local scale within a domain, but broken by the DBs^{11,12}. Overcoming the non-flat energy is therefore the key challenge to achieve single-crystal

¹Institute of Physics, Johannes Gutenberg-Universität Mainz, Mainz, Germany. ²Singulus Technologies AG, Kahl am Main, Germany. ³Center for Quantum Spintronics, Department of Physics, Norwegian University of Science and Technology, Trondheim, Norway. ✉ e-mail: klaeui@uni-mainz.de

skyrmion lattices and to study emergent 2D phases and phase transitions on large scales.

In this article, we enhance the size of polycrystalline skyrmion lattice domains by exploiting the effective reduction of pinning due to magnetic field oscillations²¹. We study the interplay between the non-flat energy landscape and the lattice order. Specifically, we show that skyrmions, which stay pinned due to the effects of the non-flat energy landscape, cause domain boundaries between the lattice domains and support our experimental findings with Brownian dynamics simulations. Since enhancing lattice domain sizes towards true QLRO is the main challenge to observe true 2D phase behavior of skyrmions in thin films^{10–12}, our results pave the way to experimentally explore the statics and dynamics of 2D phases and phase transitions in 2D skyrmion lattices.

Results and discussion

Field oscillations assist lattice ordering

We use a Ta(5 nm)/Co₂₀Fe₆₀B₂₀(0.9 nm)/Ta(0.08 nm)/MgO(2 nm)/HfO₂(3 nm) magnetic multilayer stack to nucleate densely packed skyrmions and establish magnetic out-of-plane (OOP) contrast in real space at 16 frames per second using Kerr microscopy (see Methods section for details). After nucleation, the field of view of 200 × 150 μm² contains between 4000 and 5000 skyrmions. Using the *trackpy* Python package³⁴, we detect the skyrmions and calculate the local order parameter

$$\psi_6(\mathbf{r}_j) = \frac{1}{N_{nn}} \sum_{k=1}^{N_{nn}} e^{-i6\theta_{jk}}$$

applying a Voronoi tessellation³⁵ to determine the nearest lattice neighbors. Here, \mathbf{r}_j denotes the position of a particle with N_{nn} nearest neighbors at \mathbf{r}_k , and θ_{jk} represents the angle of the connecting vector $\mathbf{r}_k - \mathbf{r}_j$ relative to a fixed arbitrary axis³. The phase of the complex value defines the local orientation $\alpha = \arg(\psi_6)/6$ of the lattice.

Figure 1a shows the positions of the skyrmions as nucleated ($t_0 = 0$ s), with their local orientations α color-coded. The schematics next to the color bar illustrates examples of different α , where the lattice orientation is highlighted by the differently aligned crystal axes depicted as gray lines. Note that the hexagonal lattice is six-fold symmetric – i.e., the color bar is cyclic with $\alpha = -30^\circ$ being equivalent to $\alpha = 30^\circ$. Figure 1b shows the same skyrmion lattice, but after waiting for $t_1 = 60$ s while an oscillating field of $A = 180$ μT peak-to-peak amplitude at a frequency $f = 100$ Hz is applied. Both at t_0 and t_1 , we find a multi-domain structure with regions of equivalent orientation α , which we identify as lattice domains. Between those lattice domains, α changes abruptly, forming a domain boundary (DB) which breaks QLRO. The inset shows the polar Kerr microscopy snapshot of the corresponding region, where every white dot represents one skyrmion. During the waiting time of 60 s, we find a significant increase of the lattice domain size.

To quantify the lattice domain size, we calculate the orientational correlation function

$$G_6(r = |\mathbf{r}_j - \mathbf{r}_k|) = \langle \psi_6^*(\mathbf{r}_j) \psi_6(\mathbf{r}_k) \rangle \propto \exp(-r/\xi_6)$$

as spatial quantifier of orientational order. In the absence of QLRO, G_6 decays exponentially with a correlation length ξ_6 , which provides a measure for the lattice domain size^{3,4,10}. While the lattice domains also grow slightly at constant applied field, the field oscillations significantly enhance the ordering effect. In Fig. 1c, we demonstrate that introducing field oscillations ($f = 100$ Hz) can significantly enhance both the orientational order $\langle |\psi_6| \rangle$ and the domain size measured by ξ_6 . As field oscillations effectively reduce pinning²¹, skyrmions are enabled to rearrange into larger lattice domains. Similar driving mechanisms have already been reported to lead to depinning and lattice formation of superconducting vortices³⁶. In principle, alternative driving mechanisms like current-induced motion^{26,37}, local heating³⁸ or surface acoustic waves³⁹ have also been shown to assist skyrmion depinning and therefore provide potential alternatives to stabilize skyrmion lattice

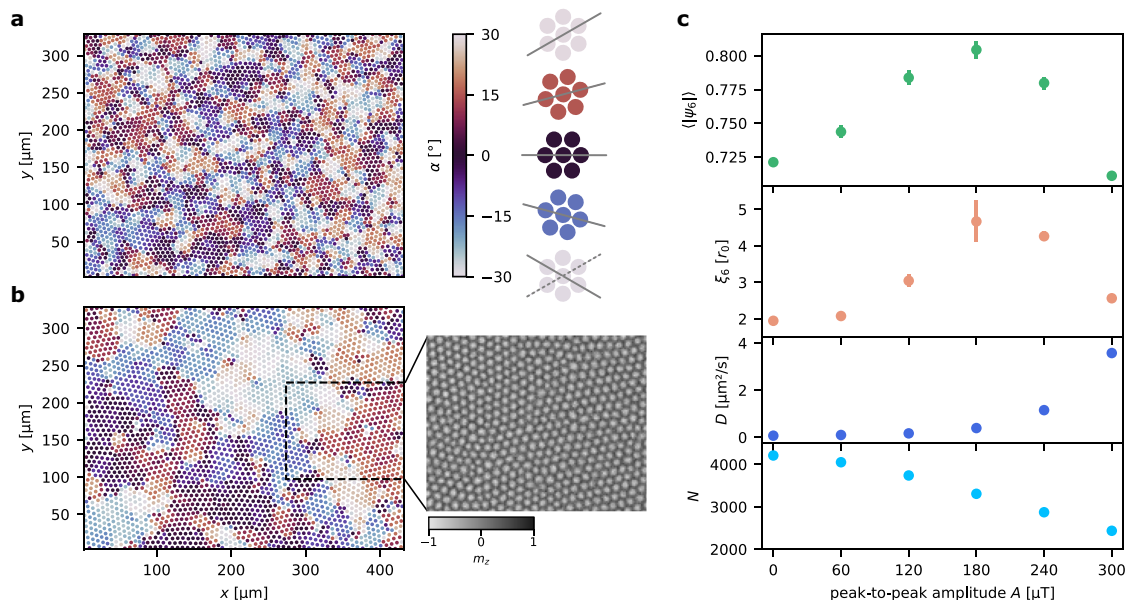


Fig. 1 | Skyrmion lattice domain growth in oscillating fields. **a** Skyrmion positions colored by the lattice orientation α directly after nucleation. The orientation α (illustrated as gray line in color-bar label) is determined by the neighbor positions and is 6-fold symmetric. **b** After 60 s in an oscillating magnetic field (180 μT peak-to-peak at 100 Hz), the lattice domains have grown significantly. The insets show the corresponding Kerr microscopy image with greyscale representing the OOP-component m_z of the magnetization. **c** Influence of the field oscillation amplitude on local order parameter ψ_6 , orientational correlation length ξ_6 , skyrmion diffusion

coefficient D and number of skyrmions N . Data points and error bars denote average and standard deviation, respectively, of 10 s window (160 snapshots between 50 and 60 s after nucleation), averaged for three independent measurements each. As a trade-off of effectively reduced pinning and increased random diffusion, ψ_6 and ξ_6 (as measures of the order and lattice domain size, respectively) peak around $A = 180$ μT. Generally, increased oscillation amplitudes enhance the diffusion D and reduce the number of skyrmions N .

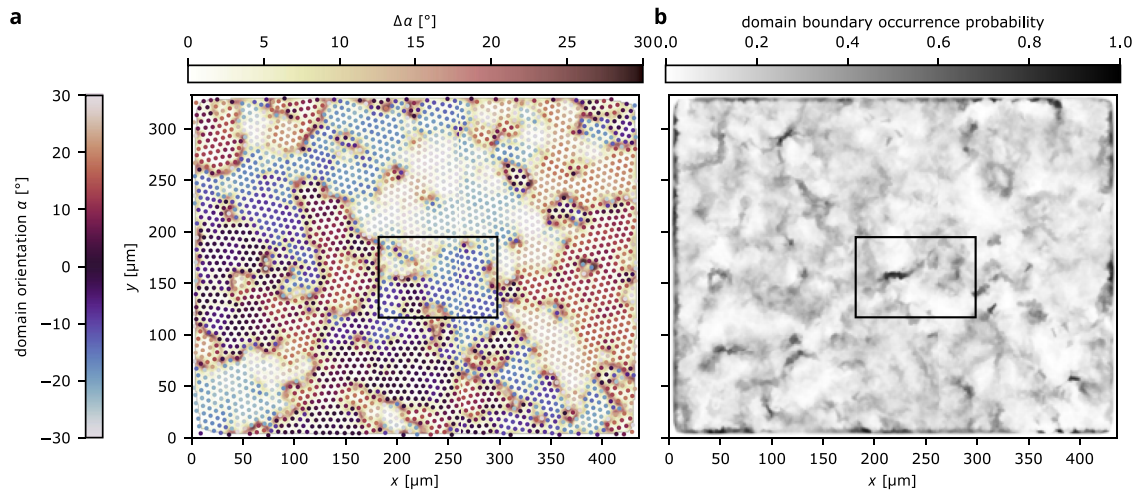


Fig. 2 | Lattice domain boundary analysis. **a** The scattered dots mark the skyrmion positions and local orientation α as in Fig. 1b. The background colormap visualizes the absolute change $\Delta\alpha$ in orientation between neighboring skyrmions as an interpolated map, which highlights the positions of the domain boundaries. The black

rectangle serves as reference marker for the following analysis. **b** Considering every $\Delta\alpha > 10^\circ$ as a DB, the grayscale map yields a probability map of hosting a DB during the 1000 frames of the 62.5 ms video of lattice formation.

order – either separately or even in combined approaches. Here, we use magnetic field oscillations as they act isotropic and since we can apply the excitation on the fly within the relevant field range and time scale. In contrast, additional patterning or devices are necessary for the other techniques.

During the driving by the oscillating field, the system is expected to exhibit non-equilibrium properties. Unlike for superconducting vortices however, the skyrmion order persists even when the driving mechanism (i.e., the field oscillations causing the depinning) is switched off. That is, after switching off the driving by the oscillating field, an equilibrium lattice with significantly enhanced order remains. However, there is a threshold for this mechanism: at large amplitudes (here, $A > 180 \mu\text{T}$), the increased diffusivity—similar to an elevated effective temperature—appears sufficient to counteract lattice stability, leading to a decreased order again. We further show that the diffusion coefficient D of the skyrmions increases monotonously with A . At the same time, larger amplitudes cause increasing annihilation events and decrease the number of present skyrmions N (Fig. 1c). The time evolution of all shown parameters as well as the correlation function G_6 are shown in Supplementary Fig. 1. Additionally, we characterize the effect in a similar scan of varying amplitude at $f = 500 \text{ Hz}$ as well as in a frequency scan at fixed amplitude in Supplementary Fig. 2. Here, we use the frequency of 100 Hz as it leads to a maximum enhancement of the skyrmion diffusion in this system.

Annihilations are a result of skyrmions being destabilized in the field oscillation. This effect has previously been observed for isolated skyrmions²¹. In a dense lattice, it becomes pronounced already for smaller amplitudes A due to the strong skyrmion-skyrmion interactions present¹⁴. Therefore, especially skyrmions in “overpopulated” regions tend to annihilate. Note that the packing fraction—i.e., the area occupied by skyrmions—is predominantly set by the magnetic hysteresis. Therefore, skyrmion annihilations do typically not lead to a reduction of the packing fraction but to an increased size of the remaining skyrmions. Consequently, annihilations may solve space conflicts of individual skyrmions in “overpopulated” regions, which can facilitate the ordering process—provided the overall skyrmion density remains sufficient to stabilize an ordered lattice, as seen here. If too many skyrmions annihilate, the remaining skyrmions expand into stripes.

We note that despite the effective reduction of pinning effects due to the oscillating field²¹, remaining effects of the non-flat energy landscape are still present²⁰. As pinning effects have been shown to play an important role for breaking QLRO^{11,12,27,40}, we now analyze the role of the non-flat energy landscape during the lattice formation. This effective energy landscape

could previously be determined directly from the occurrence probability of the skyrmions as a result of the spatially inhomogeneous skyrmion-material interaction^{20,26}. However, in dense systems such as in a skyrmion lattice, skyrmion-skyrmion interactions between the particles themselves play an important role^{14,16}. Those interactions also affect the occurrence distribution of skyrmions as illustrated in Supplementary Fig. 3, for instance when a skyrmion is confined by its lattice neighbors. Hence, the effects of the skyrmion-skyrmion interaction and the pinning potential cannot be decoupled, and a direct determination of the energy landscape remains inaccessible in this regime. Instead, we access the effect of pinning indirectly through the resulting lattice properties in the following.

Pinning effects confine lattice domains geometrically

As the non-flat energy landscape hampers QLRO and instead favors a “polycrystalline” structure with multiple domains, we first analyze the occurrence of lattice domains and domain boundaries. The orientation α is uniform within a lattice domain but changes at a DB. Therefore, we determine the orientation change $\Delta\alpha$ between neighboring skyrmions. We assign to every connection between nearest neighbors in the skyrmion lattice the absolute value of the change in orientation and interpolate these values onto the pixel grid. We show the determined $\Delta\alpha$ as background in Fig. 2a. For visualization, we overlay the corresponding orientation data from Fig. 1b as scattered dots, so that the orientation change $\Delta\alpha$ between the lattice domains (i.e., clusters of similar color) becomes clearly visible. The existence of a DB, however, is independent of the exact value of $\Delta\alpha$ – as long as it exceeds the typical fluctuations of a few degrees within a domain. Thus, we define all orientation changes $\Delta\alpha$ above a threshold of 10° as DB.

In Fig. 2b, we present the probability of hosting a DB for each pixel within 62.5 s (1000 frames) after nucleation. The domains fluctuate, rearrange, and grow from t_0 to t_1 (snapshots in Fig. 1a, b, respectively). Despite the fluctuations due to the diffusive dynamics, the DB occurrence probability map in Fig. 2b reveals significant spatial variations: some regions consistently host DBs, while others remain firmly inside lattice domains—suggesting an effective pinning of DBs.

To examine the ordering details on a local scale, we now zoom into the area marked by a black rectangle in Fig. 2. For this region of interest, we recall in Fig. 3a–c both the skyrmion positions (from Fig. 2a) and the DB occurrence probability map (from Fig. 2b), for reference. We color the occurring skyrmions by their local lattice orientation α (Fig. 3a), local order parameter $|\psi_6|$ (Fig. 3b) and number of lattice neighbors (Fig. 3c), respectively. The small red dots mark where the absolute orientation change $\Delta\alpha$

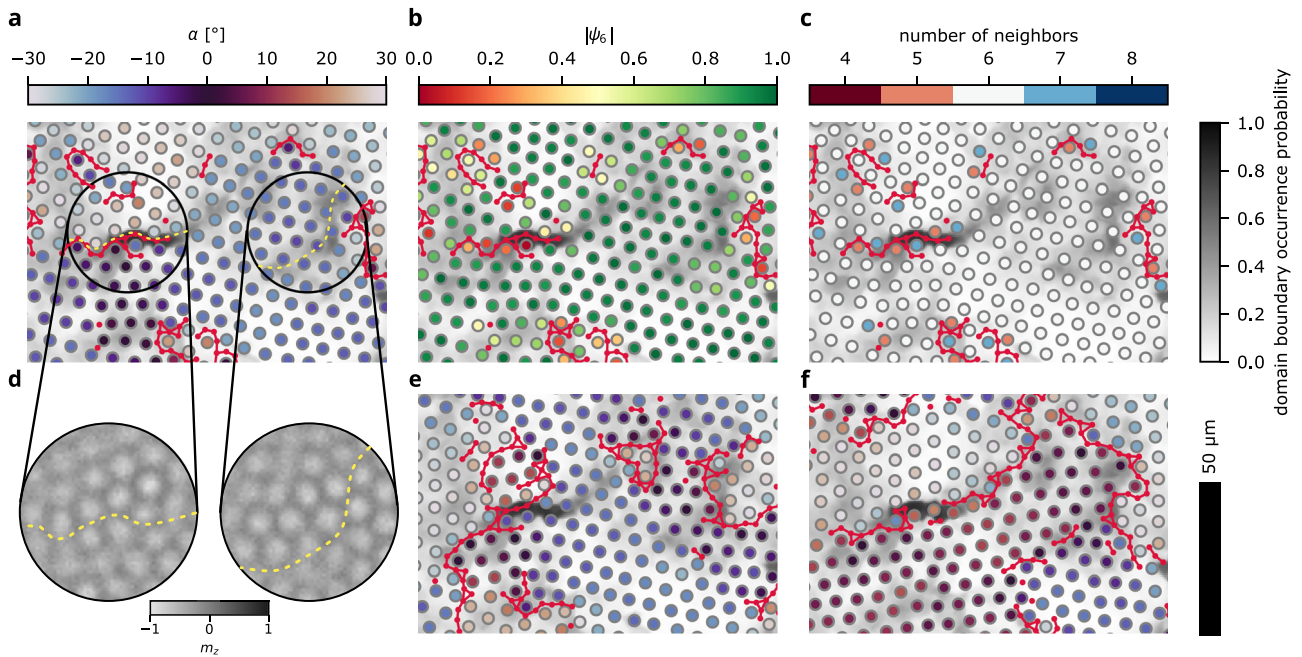


Fig. 3 | Pinning effects induce lattice domain boundaries. Onto the DB occurrence probability of the rectangle as greyscale background, we superimpose the **a** local orientation, **b** $|\psi_6|$ and **c** number of lattice neighbors for every skyrmion as dots using the data from Fig. 2a for a more detailed visualization. Red dots denote the occurrences of $\Delta\alpha > 10^\circ$ between neighboring skyrmions and the red lines mark the corresponding domain boundaries. As the orientation changes along such boundaries, the local order $|\psi_6|$ is reduced and lines of topological defects occur. **d** Average Kerr contrast for three different Kerr videos of 1 min length in the marked circular areas. The yellow dashed line serves as marker to map positions of high domain wall

occurrence probability from (a). Despite the three different nucleations, we find significant average contrast due to skyrmions at the positions where we have found high probability of a DB, thus indicating pinning effects. Contrarily, different configurations arise elsewhere as seen by the blurred contrast. **e, f** Plotting local orientation α of the two different nucleations (snapshots 60 s after nucleation) as colored dots onto the grayscale map of $\Delta\alpha$ from (a–c), we find again that domain boundaries of $\Delta\alpha > 10^\circ$ (red lines) overlap with the DB occurrence probability from before, corroborating that pinning plays an important role for the occurrence of domain boundaries.

between two skyrmions exceeds 10° , contributing to a DB. Neighboring red dots are further connected by red lines to illustrate the DB contour. The marked red boundaries align well with positions where α changes in Fig. 3a, validating our DB identification. Since the orientational order is disrupted locally along a DB, we see in Fig. 3b that the corresponding local order parameter $|\psi_6|$ is reduced at these positions. This disruption also gives rise to topological defects, characterized by the number of lattice neighbors differing from the perfect order with six neighbors.

Next we probe the reproducibility of the skyrmion boundary formation. Since skyrmion pinning effects are a local material property, they are independent of the specific skyrmion configuration resulting from a nucleation event. Therefore, we compare the skyrmion occurrences in the same area but from different nucleations to analyze the DB pinning effect. Firstly, we investigate the circular areas marked in Fig. 3a, where the DB occurrence probability is particularly high. In Fig. 3d, we average the Kerr intensity for these circles across three videos, each capturing the first 62.5 s (1000 frames) of a newly nucleated skyrmion lattice. Despite averaging over three nucleations (with respective independent lattice domain formations) and long observation times relative to the diffusion timescale, we observe significant contrast. This contrast indicates that skyrmions recur at identical positions over time and across re-nucleations. For reference, we add (to Fig. 3d) a dashed yellow contour along which the DB occurrence probability in Fig. 3a is particularly high. These regions of high DB occurrence probability align well with the recurring skyrmions. In contrast, the intensity is more diffuse in areas further away from the primary DB positions, suggesting more fluctuations there. Therefore, we conclude that pinning effects play a crucial role in the formation of DBs within the skyrmion lattice, which inhibit QLRO and favor a polycrystalline multi-domain arrangement.

To further support this conclusion, we analyze snapshots showing the local orientation α (scattered dots) and DBs (red) from the second and third

nucleation in Fig. 3e, f, respectively. In both cases, we plot the DB occurrence probability map from the first nucleation as the background (i.e., from Fig. 2b) for reference. The DBs identified in these additional snapshots frequently align with those from the first nucleation. As these DBs recur at identical positions across different nucleations, our observations confirm that the pinning of individual skyrmions effectively pins DBs within the lattice. As a result, pinned DBs suppress domain rearrangement towards QLRO, instead acting as geometric confinement for lattice domains.

To understand our experimental findings, we perform corresponding Brownian dynamics Thiele model simulations to elucidate the role of the non-flat energy landscape for the formation of lattice domains and DBs.

Simulation results

We simulate skyrmion lattices within the Thiele model using a typical repulsive skyrmion interaction potential^{10,14} (see Methods). The simulations are conducted at a fixed density of 1.25, which places the system deep within the solid phase in the absence of an external potential landscape^{10,17}.

First, we use an experimentally derived skyrmion energy landscape²⁰ as the potential energy input (Supplementary Fig. 4), varying only the depth of the potential landscape while keeping the skyrmion density constant. As shown in Fig. 4a, introducing a non-flat energy landscape results in a multi-domain skyrmion lattice. Pinning reduces the average local order ψ_6 , the orientational correlation length ξ_6 and the diffusion coefficient D (Fig. 4a). As the depth of the potential landscape decreases, all three quantities— ψ_6 , ξ_6 and D —increase, consistent with the experimental observations. However, beyond a certain point, further increases in lattice order lead to a decrease in D , as the system favors preserving order over maximizing diffusivity. In the experiment, these opposing effects cannot be disentangled, as field oscillations primarily enhance diffusivity²¹.

In Fig. 4b, we show that strong pinning results in small domains extending over only a few particles, while weaker pinning allows for

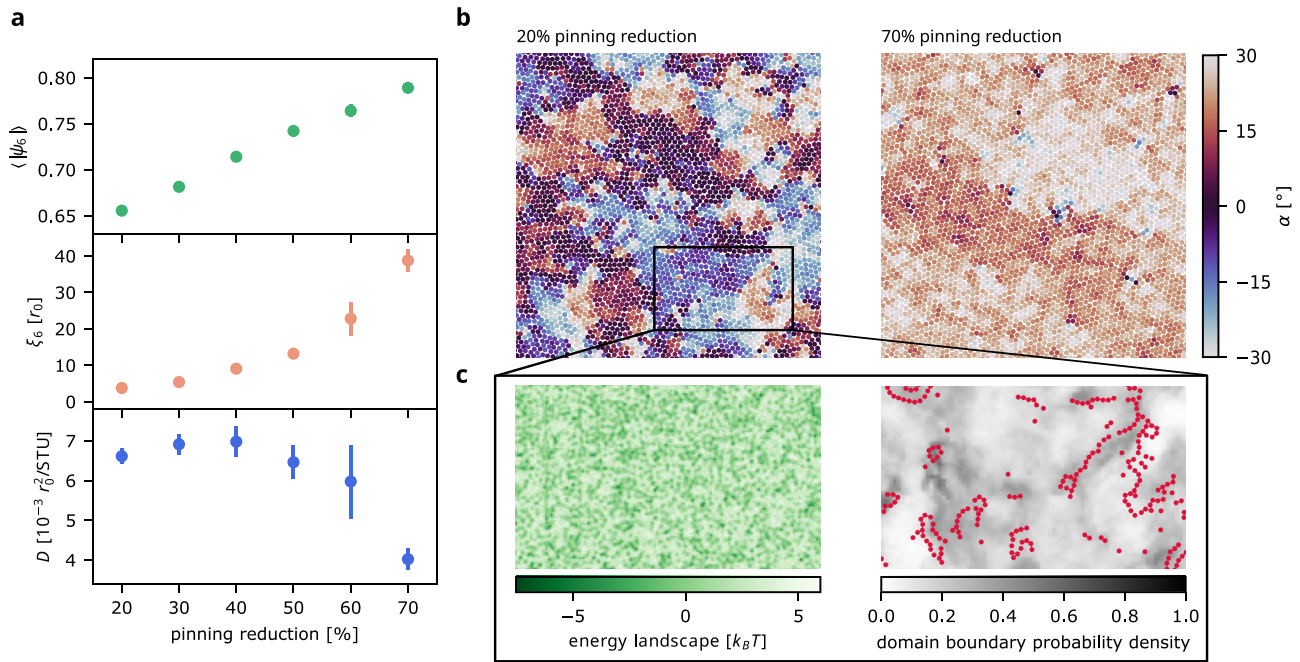
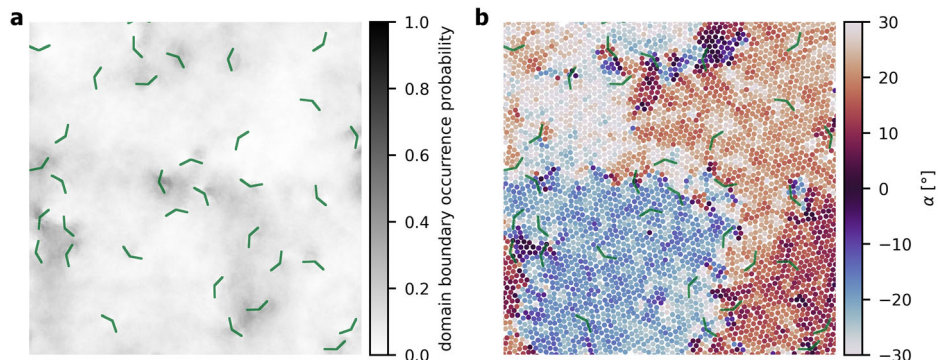


Fig. 4 | Pinning leads to multi-domain states. **a** We use an experimentally determined energy landscape in a Brownian dynamics simulation of 5300 particles at density 1.25, which is deep in the solid phase in the absence of a potential. The pinning leads to reduced local orientational order ψ_6 , smaller correlation length ξ_6 , and suppressed diffusivity. D is given in terms of the nearest neighbor distance r_0 and the simulation time unit STU. When the pinning is reduced in the simulation, ψ_6 , ξ_6 , and D increase. For increasing order, D decreases again to preserve lattice order. Data points and error bars denote average and standard deviation, respectively, of the last

200 writeouts, averaged for four independent simulation runs each. **b** Local lattice orientation α for individual skyrmions (dots) at differently strong pinning. While stronger pinning with only 20% reduction of the energy landscape leads to polycrystalline lattice multi-domain state, reducing pinning by 70% results in an almost uniform α . **c** For the rectangle highlighted in **(b)**, we show the experimental energy landscape (left) and the occurring domain boundaries (right). The grayscale background is the domain boundary occurrence probability throughout the 800 writeouts in 80 STU. The red markers denote the domain boundaries identified in **(b)**.

Fig. 5 | Artificially designed pinning of lattice domain boundaries. **a** In a simulation of 5000 particles at density 1.25, we introduce 40 randomly spread angle-shaped patterns (green) with an energy $-7.5 k_B T$ with respect to the flat background potential. Throughout a simulation run, the domain boundary probability map remains inhomogeneous with regions of high occurrence probability around and between the angle patterns. **b** Snapshot of the local lattice orientation α per skyrmions after 100 STU. Distinct domains of different α form. The orientation changes in regions, where also the overall domain boundary occurrence probability is high. While some of the angle patterns (green) mark domain boundaries, others are located within a lattice domain.



increasingly uniform lattice orientation α . For a selected region of interest (Fig. 4c), we present the experimental energy landscape used in the simulation and the associated DBs. The landscape consists of energy variations on the scale of the skyrmion diameter, forming randomly distributed pinning sites separated by energy barriers of varying height on the order of few $k_B T$. By analyzing 80 simulation time units (STU) of an equilibration, we demonstrate that this heterogeneous energy landscape leads to a highly inhomogeneous probability for domain boundary occurrence. Some DBs appear to remain persistently pinned by the landscape.

To further understand the mechanism of DB pinning, we next introduce designed synthetic energy landscapes into the simulation. In Fig. 5, we

employ a landscape composed of randomly distributed angle-shaped pinning features. Each feature spans three skyrmion spacings in both directions and has a depth of $-7.5 k_B T$ relative to the flat background. The opening angle is set to 135° , which is deliberately chosen to be incommensurate with the hexagonal lattice. The background of Fig. 5a shows the DB occurrence probability over 80 STU, revealing a clearly inhomogeneous distribution. This minimal pattern suffices to create distinct lattice domains and to effectively pin DBs.

Figure 5b shows a snapshot of the local lattice orientation α per skyrmion after 80 STU. At several locations, α changes sharply at the angle-shaped pinning sites, which mark and anchor DBs. However, these angles can also be located within a single domain, merely inducing local distortions.

While domain configurations fluctuate, DBs tend to connect the angular pinning features, though the specific features involved vary over time.

To explore the influence of different pinning geometries, we compare several synthetic patterns. In the case of linear pinning features (Supplementary Fig. 5), domain fragmentation along the pinning lines is unfavorable, as the lines are commensurate with the lattice. Instead, the lines tend to stabilize the interior of a domain and confine DBs to the interstitial regions. Conversely, a landscape consisting of overlapping sinusoidal lines (Supplementary Fig. 6)—which are incommensurate with the hexagonal lattice—favors domain fragmentation. Since the sinusoidal lines are curved, a single domain covering the sine is unfavorable. Instead, breaking of the domains is induced. However, the continuous curvature does not anchor one fixed DB but instead causes small domains and DBs in its vicinity.

In the experimental system, the material's energy landscape is random in nature^{21,26} and likely incommensurate with the hexagonal skyrmion lattice, as shown in Fig. 3d. Additionally, the observed pinning features predominantly exhibit a local character, resembled by the angle-shaped patterns used in the simulation (Fig. 5).

Conclusions

The non-flat skyrmion energy landscape in magnetic thin films has been known to be the key inhibitor of quasi-long-range order (QLRO) of skyrmion lattices^{11,12}. In this work, we demonstrate how skyrmion pinning effects in a non-flat energy landscape cause the local stabilization of lattice domain boundaries. The effectively pinned domain boundaries delineate and confine the polycrystalline lattice domains, breaking QLRO. As we can effectively tune the energy landscape and reduce pinning effects by magnetic field oscillations²¹, we can significantly increase the size of the lattice domains, leading to enhanced average local order. We therefore provide a key enabler to access intrinsic properties and dynamics of skyrmion lattices¹⁰ and their fundamental 2D phase behavior—within the limit of domains as well as towards single crystals of true QLRO in the future. The oscillating fields furthermore allow us to study both equilibrium and non-equilibrium phase behavior. Different mechanisms like current-induced motion^{26,37}, local heating³⁸ or surface acoustic waves³⁹ may also depin³⁶ and increase lattice domains in an alternative or additional approach. We reproduce our experimental results by quasi-particle simulations and we show that local modifications of the energy landscape^{41,42} in order to deterministically pin single skyrmions at their ideal lattice sites pose an option to stabilize artificial lattices on larger scales—in a reverse engineering approach to access lattice properties beyond the current observations in systems with a natural energy landscape.

Methods

Magnetic multilayer material

The magnetic thin film stack is deposited using DC/RF magnetron sputtering in a *Singulus Rotaris* system under a base pressure of 3×10^{-8} mbar. We use a stack composition of Ta(5 nm)/Co₂₀Fe₆₀B₂₀(0.9 nm)/Ta(0.08 nm)/MgO(2 nm)/HfO₂(3 nm) (with layer thicknesses in nanometers, accurate to within 0.01 nm). The perpendicular magnetic anisotropy (PMA, at the Co₂₀Fe₆₀B₂₀/MgO interface) and the interfacial Dzyaloshinskii-Moriya interaction (DMI, primarily at the Ta/Co₂₀Fe₆₀B₂₀ interface)^{43,44} are key ingredients for the stabilization of magnetic skyrmions in our thin film. Thereby, the dusting layer of Ta(0.08 nm) optimizes the material for low pinning and skyrmion lattice formation by fine-tuning the balance between DMI and PMA^{18,45}. The non-trivial topology of our magnetic skyrmion structures is confirmed by driving skyrmions using spin-orbit-torques as well as by micromagnetic simulations^{18–20,46}. We show the magnetic hysteresis curve for an out-of-plane (OOP) field cycle loop in Supplementary Fig. 7.

Experimental setup

To image magnetic skyrmions in the multilayer compound, we operate a commercially available Kerr microscope manufactured by *evico magnetics GmbH* in polar mode, resulting in grayscale contrast of the OOP

magnetization. With a blue LED light source and a CCD camera, we reach a resolution of 200–400 nm and 62.5 ms (16 fps) in real-time and -space. We control and monitor the sample temperature with a Peltier element and a Pt100 with a precision of 0.1 K, respectively^{18,20}. Enclosing the entire microscope in a thermally stabilized flow box further improves temperature stability. Electromagnetic coils provide independent magnetic fields in in-plane(IP) and OOP direction. The OOP field coil is custom-made to allow field control with sub- μ T precision to ensure stable measurement conditions for the skyrmion system.

While a magnetic OOP offset field is required to stabilize skyrmions, a saturating IP field pulse is used to nucleate skyrmions while keeping the temperature constant. We control the density of the nucleated skyrmions by the OOP offset and IP pulsed field^{20,47,48}. Under the varying oscillating fields described in the main text, we take videos of 62.5 s length (1000 frames) and detect skyrmions by the *trackpy* Python package³⁴, which is based on 2D Gaussian kernel fitting. Due to the skyrmions being a collective spin ensemble spanning over many pixels, the detection works with sub-pixel precision²⁰. Except for the geometric patterned confinements, the magnetic film exceeds the field of view by more than one order of magnitude and is therefore considered as continuous, where we neglect boundary effects.

Lattice order and diffusion analysis

From the detected skyrmion positions, we apply a Voronoi tessellation³⁵ to determine lattice neighbors. From the Voronoi grid, we determine the complex local order parameter ψ_6 for every skyrmion. The local lattice orientation directly follows as $\alpha = \arg(\psi_6)/6^{12}$. We then calculate the orientational correlation function G_6 as a function of distance r for every frame¹⁰. As no quasi-long-range order (QLRO) is present due to multi-domain structures³², we determine the decay of the correlation function as an exponential $\propto \exp(-r/\xi_6)$ with a correlation length ξ_6^{34} , which we use as a measure for the lattice domain size. As an additional result of the Voronoi tessellation, we directly gain information about topological lattice defects¹²: every skyrmion with a number of lattice neighbors N_{nn} different from 6 (which is the case in a purely hexagonal lattice structure) is a topological defect.

To evaluate the diffusivity of the skyrmions, we use *trackpy*³⁴ to link the skyrmion coordinates \mathbf{r} from the single frames at time t to trajectories. We then calculate the mean squared displacement

$$\text{MSD}(t) = \langle [\mathbf{r}(t) - \mathbf{r}(t_0)]^2 \rangle = 2dDt$$

with respect to a start time t_0 by averaging over all skyrmion trajectories as indicated by the angled brackets^{18,21}. Since the MSD is related to the diffusion coefficient D via the time t and the system dimensionality $d = 2$, we extract D as a linear fit over a 1 s interval. The accessible fit region is limited in the experiment as it required reliable trajectory linking over the full fit window. We can use any time t_0 as starting time to evaluate the time evolution of the diffusion coefficient¹⁰.

The occurrence probability p of skyrmions at low skyrmion densities can furthermore be used to determine the energy landscape. Following a well-established procedure^{20,26}, we determine the energy landscape in units of $k_B T$ as $-\ln(p)$. The sample used for the lattice measurements features only high skyrmion densities at the measurement temperature. Reducing temperature allows also lower densities, but increases the skyrmion size (which is relevant for the energy landscape) and suppresses the relevant thermal skyrmion diffusion. Since sparse (and thermally diffusing) skyrmions are required in this procedure to minimize contributions from skyrmion-skyrmion interactions, we use a different, similar sample (Ta(5 nm)/Co₂₀Fe₆₀B₂₀(0.9 nm)/Ta(0.09 nm)/MgO(2 nm)/Ta(5 nm) measured at 316 K) to obtain a realistic energy landscape for the simulations.

Brownian dynamics simulation

We use Brownian dynamics simulations in the Thiele model⁴⁹ to simulate thermally diffusing skyrmions. Sets $\{\mathbf{r}\}$ of skyrmions at positions \mathbf{r} positions

with velocity \mathbf{v} , the damping γ (effective skyrmion damping for Brownian Dynamics simulation, not the Gilbert damping) and satisfy the equation of motion^{14,26}

$$-\gamma\mathbf{v} - G_{\text{rel}}\gamma\mathbf{e}_z \times \mathbf{v} + \mathbf{F}_{\text{therm}} + \mathbf{F}_{\text{SkSk}}(\{\mathbf{r}\}) + \mathbf{F}_{\text{pin}}(\mathbf{r}) = 0$$

while using $\gamma = 1$ in simulation units. Since the relative Magnus force strength G_{rel} is negligible in our system, we do not consider the term in the simulations. The dynamics is influenced by several forces \mathbf{F} : the thermal white noise $\mathbf{F}_{\text{therm}}$ (fulfilling the fluctuation-dissipation), skyrmion-skyrmion interactions \mathbf{F}_{SkSk} , and pinning forces \mathbf{F}_{pin} originating from a non-flat energy landscape. Based on previous experiments^{10,14}, we use a skyrmion-skyrmion interaction potential $V(r) = r^{-8}$ with a cutoff distance of 3 simulation units. While theoretical studies⁵⁰⁻⁵⁴ have shown the possibility to adjust the original Thiele equation by adding a mass term, we can confidently estimate the inertia of the skyrmion to be negligible in our system using previous determinations of mass⁵⁵ and damping²⁶.

The equation of motions are integrated using a Heun algorithm and periodic boundary conditions. Writeouts are performed every 10,000 simulation time steps, which corresponds to every 0.1 simulation time units (STU). The lattices are typically equilibrated after 20 STU (thus, 200 writeouts). The density of the skyrmions is determined as number of particles per squared simulation length unit. The system is initialized as a square lattice.

Data availability

The data that support the findings of this study are available on Zenodo⁵⁶ under <https://doi.org/10.5281/zenodo.17406183>.

Code availability

The computer code used for analyzing the experimental results as well as for generating and analyzing simulation data of this study is available from the corresponding author upon reasonable request.

Received: 1 August 2025; Accepted: 5 December 2025;

Published online: 19 December 2025

References

- Kosterlitz, J. M. & Thouless, D. J. Long range order and metastability in two dimensional solids and superfluids. (Application of dislocation theory). *J. Phys. C* **5**, L124 (1972).
- Kosterlitz, J. M. & Thouless, D. J. Ordering, metastability and phase transitions in two-dimensional systems. *J. Phys. C* **6**, 1181–1203 (1973).
- Halperin, B. I. & Nelson, D. R. Theory of two-dimensional melting. *Phys. Rev. Lett.* **41**, 121–124 (1978).
- Nelson, D. R. & Halperin, B. I. Dislocation-mediated melting in two dimensions. *Phys. Rev. B* **19**, 2457–2484 (1979).
- Young, A. P. Melting and the vector Coulomb gas in two dimensions. *Phys. Rev. B* **19**, 1855–1866 (1979).
- Bogdanov, A. & Hubert, A. Thermodynamically stable magnetic vortex states in magnetic crystals. *J. Magn. Magn. Mater.* **138**, 255–269 (1994).
- Mühlbauer, S. et al. Skyrmion lattice in a chiral magnet. *Science* **323**, 915–919 (2009).
- Jiang, W. et al. Skyrmions in magnetic multilayers. *Phys. Rep.* **704**, 1–49 (2017).
- Huang, P. et al. Melting of a skyrmion lattice to a skyrmion liquid via a hexatic phase. *Nat. Nanotechnol.* **15**, 761–767 (2020).
- Gruber, R. et al. Real-time observation of topological defect dynamics mediating two-dimensional skyrmion lattice melting. *Nat. Nanotechnol.* **20**, 1405–1411 (2025).
- Meisenheimer, P. et al. Ordering of room-temperature magnetic skyrmions in a polar van der Waals magnet. *Nat. Commun.* **14**, 3744 (2023).
- Zázvorka, J. et al. Skyrmion lattice phases in thin film multilayer. *Adv. Func. Mater.* **30**, 2004037 (2020).
- Seshadri, R. & Westervelt, R. M. Statistical mechanics of magnetic bubble arrays. II. Observations of two-dimensional melting. *Phys. Rev. B* **46**, 5150–5161 (1992).
- Ge, Y. et al. Constructing coarse-grained skyrmion potentials from experimental data with Iterative Boltzmann Inversion. *Commun. Phys.* **6**, 1–6 (2023).
- Lin, S.-Z., Reichhardt, C., Batista, C. D. & Saxena, A. Particle model for skyrmions in metallic chiral magnets: dynamics, pinning, and creep. *Phys. Rev. B* **87**, 214419 (2013).
- Jefremovas, E. M. et al. The role of magnetic dipolar interactions in skyrmion lattices. *Newton* **1**, 100036 (2025).
- Kapfer, S. C. & Krauth, W. Two-dimensional melting: from liquid-hexatic coexistence to continuous transitions. *Phys. Rev. Lett.* **114**, 035702 (2015).
- Zázvorka, J. et al. Thermal skyrmion diffusion used in a reshuffler device. *Nat. Nanotechnol.* **14**, 658–661 (2019).
- Kerber, N. et al. Anisotropic skyrmion diffusion controlled by magnetic-field-induced symmetry breaking. *Phys. Rev. Appl.* **15**, 044029 (2021).
- Gruber, R. et al. Skyrmion pinning energetics in thin film systems. *Nat. Commun.* **13**, 3144 (2022).
- Gruber, R. et al. 300-times-increased diffusive skyrmion dynamics and effective pinning reduction by periodic field excitation. *Adv. Mater.* **35**, 2208922 (2023).
- Zahn, K., Lenke, R. & Maret, G. Two-stage melting of paramagnetic colloidal crystals in two dimensions. *Phys. Rev. Lett.* **82**, 2721–2724 (1999).
- Zahn, K. & Maret, G. Dynamic criteria for melting in two dimensions. *Phys. Rev. Lett.* **85**, 3656–3659 (2000).
- Guillamón, I. et al. Direct observation of melting in a two-dimensional superconducting vortex lattice. *Nat. Phys.* **5**, 651–655 (2009).
- Roy, I. et al. Melting of the vortex lattice through intermediate hexatic fluid in an α -MoGe thin film. *Phys. Rev. Lett.* **122**, 047001 (2019).
- Brems, M. A. et al. Realizing quantitative quasiparticle modeling of skyrmion dynamics in arbitrary potentials. *Phys. Rev. Lett.* **134**, 046701 (2025).
- Reichhardt, C., Reichhardt, C. J. O. & Milošević, M. V. Statics and dynamics of skyrmions interacting with disorder and nanostructures. *Rev. Mod. Phys.* **94**, 035005 (2022).
- Iwasaki, J., Mochizuki, M. & Nagaosa, N. Universal current-velocity relation of skyrmion motion in chiral magnets. *Nat. Commun.* **4**, 1463 (2013).
- Liu, Y.-H. & Li, Y.-Q. A mechanism to pin skyrmions in chiral magnets. *J. Phys.* **25**, 076005 (2013).
- Navau, C., Del-Valle, N. & Sanchez, A. Interaction of isolated skyrmions with point and linear defects. *J. Magn. Magn. Mater.* **465**, 709–715 (2018).
- Lima Fernandes, I., Bouaziz, J., Blügel, S. & Lounis, S. Universality of defect-skyrmion interaction profiles. *Nat. Commun.* **9**, 4395 (2018).
- Deuschländer, S., Horn, T., Löwen, H., Maret, G. & Keim, P. Two-dimensional melting under quenched disorder. *Phys. Rev. Lett.* **111**, 098301 (2013).
- Nelson, D. R. Reentrant melting in solid films with quenched random impurities. *Phys. Rev. B* **27**, 2902–2914 (1983).
- Allan, D. B., Caswell, T., Keim, N. C., van der Wel, C. M. & Verweij, R. W. soft-matter/trackpy: v0.6.4. *Zenodo* <https://doi.org/10.5281/zenodo.12708864> (2024).
- Finney, J. L. & Bernal, J. D. Random packings and the structure of simple liquids. I. The geometry of random close packing. *Proc. R. Soc. A* **319**, 479–493 (1997).
- Koshelev, A. E. & Vinokur, V. M. Dynamic melting of the vortex lattice. *Phys. Rev. Lett.* **73**, 3580–3583 (1994).

37. Woo, S. et al. Observation of room-temperature magnetic skyrmions and their current-driven dynamics in ultrathin metallic ferromagnets. *Nat. Mater.* **15**, 501–506 (2016).
 38. Kern, L.-M. et al. Tailoring optical excitation to control magnetic skyrmion nucleation. *Phys. Rev. B* **106**, 054435 (2022).
 39. Schwenke, P. et al. Ratchet motion of magnetic skyrmions driven by surface acoustic sawtooth waves. *Phys. Rev. B* **112**, 214409 (2025).
 40. Reichhardt, C., Ray, D. & Reichhardt, C. J. O. Collective transport properties of driven skyrmions with random disorder. *Phys. Rev. Lett.* **114**, 217202 (2015).
 41. Kern, L.-M. et al. Deterministic generation and guided motion of magnetic skyrmions by focused He⁺-ion irradiation. *Nano Lett.* **22**, 4028–4035 (2022).
 42. Riddiford, L. J., Brock, J. A., Murawska, K., Hrabec, A. & Heyderman, L. J. Grayscale control of local magnetic properties with direct-write laser annealing. *Proc. SPIE PC13119, Spintronics XVII*, Vol. PC1311915 (SPIE, 2024).
 43. Dzyaloshinsky, I. A thermodynamic theory of “weak” ferromagnetism of antiferromagnetics. *J. Phys. Chem. Solids* **4**, 241–255 (1958).
 44. Moriya, T. Anisotropic superexchange interaction and weak ferromagnetism. *Phys. Rev.* **120**, 91–98 (1960).
 45. Bhatnagar-Schöffmann, T. et al. Controlling interface anisotropy in CoFeB/MgO/HfO₂ using dusting layers and magneto-ionic gating. *Appl. Phys. Lett.* **122**, 042402 (2023).
 46. Rodrigues, D. R., Abanov, A., Sinova, J. & Everschor-Sitte, K. Effective description of domain wall strings. *Phys. Rev. B* **97**, 134414 (2018).
 47. Zeissler, K. et al. Diameter-independent skyrmion Hall angle observed in chiral magnetic multilayers. *Nat. Commun.* **11**, 428 (2020).
 48. Zivieri, R. et al. Configurational entropy of magnetic skyrmions as an ideal gas. *Phys. Rev. B* **99**, 174440 (2019).
 49. Thiele, A. A. Steady-state motion of magnetic domains. *Phys. Rev. Lett.* **30**, 230–233 (1972).
 50. Psaroudaki, C & Loss, D. Skyrmions driven by intrinsic magnons. *Phys. Rev. Lett.* **120**, 237203 (2018).
 51. Reyes-Osorio, F. & Nikolić, B. K. Anisotropic mass of a magnetic skyrmion due to its interaction with conduction electrons: a Schwinger–Keldysh field theory approach. *J. Phys. Soc. Jpn.* **93**, 094707 (2024).
 52. Psaroudaki, C., Hoffman, S., Klinovaja, J. & Loss, D. Quantum Dynamics of Skyrmions in Chiral Magnets. *Phys. Rev. X* **7**, 041045 (2017).
 53. Pavlis, A. & Psaroudaki, C. Curvature-induced skyrmion mass. *Phys. Rev. Res.* **2**, 032058(R) (2020).
 54. Wu, X. & Tchemyshyov, O. How a skyrmion can appear both massive and massless. *SciPost Phys.* **12**, 159 (2022).
 55. Büttner, F. et al. Dynamics and inertia of skyrmionic spin structures. *Nat. Phys.* **11**, 225–228 (2015).
 56. Gruber, R. et al. Source data - skyrmion lattice domain formation in a non-flat energy landscape. Data Set. *Zenodo* <https://doi.org/10.5281/zenodo.17406183> (2025).
- 101070290, project “NIMFEIA”) and under the Marie Skłodowska-Curie grant agreements No. 860060 (“MagnEfi”) and No. 101119608 (“TOPO-COM”). The authors gratefully acknowledge the computing time granted on the supercomputer MOGON II and III at Johannes Gutenberg University Mainz as part of NHR South-West. M.A.B. was supported by a doctoral scholarship of the Studienstiftung des deutschen Volkes. E.M.J. acknowledges the Alexander von Humboldt Postdoctoral Fellowship. A.S. and M.K. acknowledge support from the Norwegian Research Council through Grant No. 262633, Center of Excellence on Quantum Spintronics (QuSpin).

Author contributions

R.G. performed the Kerr microscopy measurements and experimental data analysis with the help of T.S. J.R. and S.M.F. conducted the MD simulations with the help of M.A.B.; R.G., S.M.F. and M.A.B. analyzed the simulation data. F.K. and M.A.S. optimized and fabricated the multilayer stack. R.G. prepared the manuscript with the help of J.R., M.A.B., E.M.J. and S.K.; A.S., P.V. and M.K. guided and supervised the work. All authors have commented on the manuscript.

Funding

Open Access funding enabled and organized by Projekt DEAL.

Competing interests

The authors declare no competing interests.

Additional information

Supplementary information The online version contains supplementary material available at <https://doi.org/10.1038/s42005-025-02462-x>.

Correspondence and requests for materials should be addressed to Mathias Kläui.

Peer review information *Communications Physics* thanks the anonymous reviewers for their contribution to the peer review of this work. A peer review file is available.

Reprints and permissions information is available at <http://www.nature.com/reprints>

Publisher's note Springer Nature remains neutral with regard to jurisdictional claims in published maps and institutional affiliations.

Open Access This article is licensed under a Creative Commons Attribution 4.0 International License, which permits use, sharing, adaptation, distribution and reproduction in any medium or format, as long as you give appropriate credit to the original author(s) and the source, provide a link to the Creative Commons licence, and indicate if changes were made. The images or other third party material in this article are included in the article's Creative Commons licence, unless indicated otherwise in a credit line to the material. If material is not included in the article's Creative Commons licence and your intended use is not permitted by statutory regulation or exceeds the permitted use, you will need to obtain permission directly from the copyright holder. To view a copy of this licence, visit <http://creativecommons.org/licenses/by/4.0/>.

© The Author(s) 2025

Acknowledgements

This work was funded by the Deutsche Forschungsgemeinschaft (DFG, German Research Foundation) - SPP 2137 (project #403502522), TRR 173 Spin+X (projects A01, A12 and B02). The authors acknowledge funding from TopDyn. This project has received funding from the European Research Council (ERC) under the European Union's Horizon 2020 research and innovation program (Grant No. 856538, project “3D MAGiC” and Grant No.

8.1.1. Supplementary Information


Publication Information

The following supplementary information is published with the article in *Communications Physics*:

Skyrmion Lattice Domain Formation in a Non-Flat Energy Landscape

Raphael Gruber, Simon M. Fröhlich, Jan Rothörl, Maarten A. Brems, Tobias Sparmann, Fabian Kammerbauer, Maria-Andromachi Syskaki, Elizabeth M. Jefremovas, Sachin Krishnia, Asle Sudbø, Peter Virnau & Mathias Kläui
Communications Physics **9**, 29 (2025).

DOI: [10.1038/s42005-025-02462-x](https://doi.org/10.1038/s42005-025-02462-x)


Copyright Information:  CC BY 4.0 Creative Commons Attribution 4.0 International License

Editorial Note: The blue header/footer bars were added for inclusion in this dissertation and are not part of the original publication.

Contributions

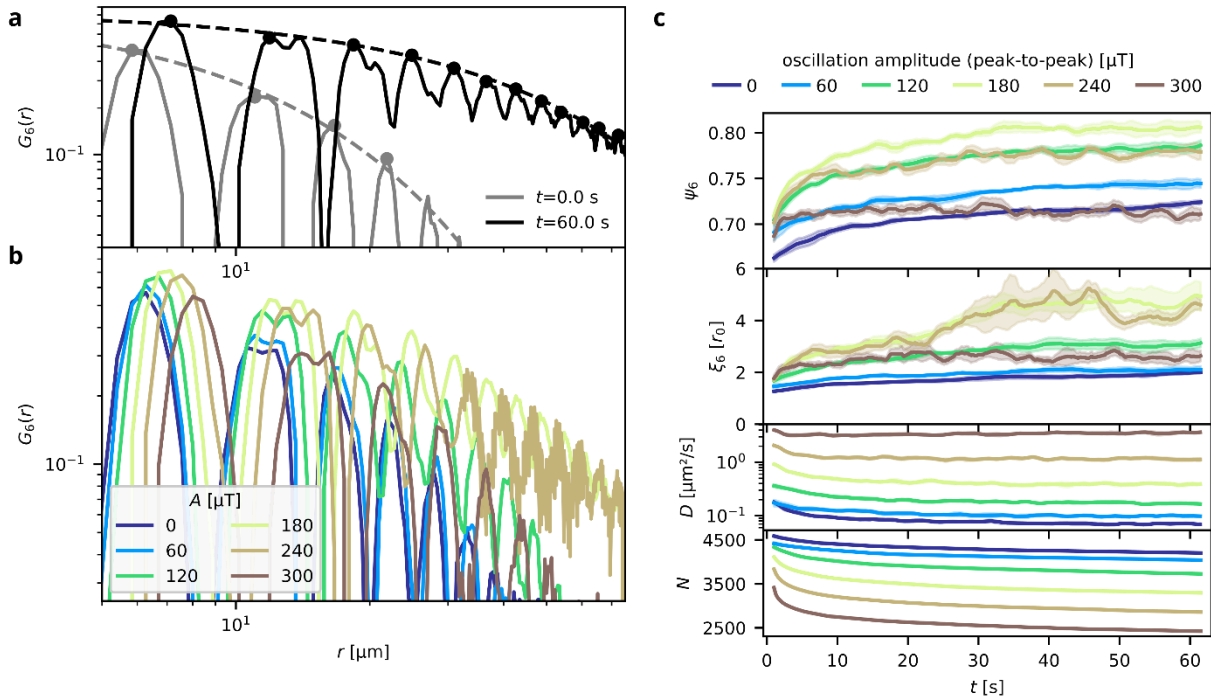
The author contributions for this project and article are described in detail in section 8.3.

Experimental Note

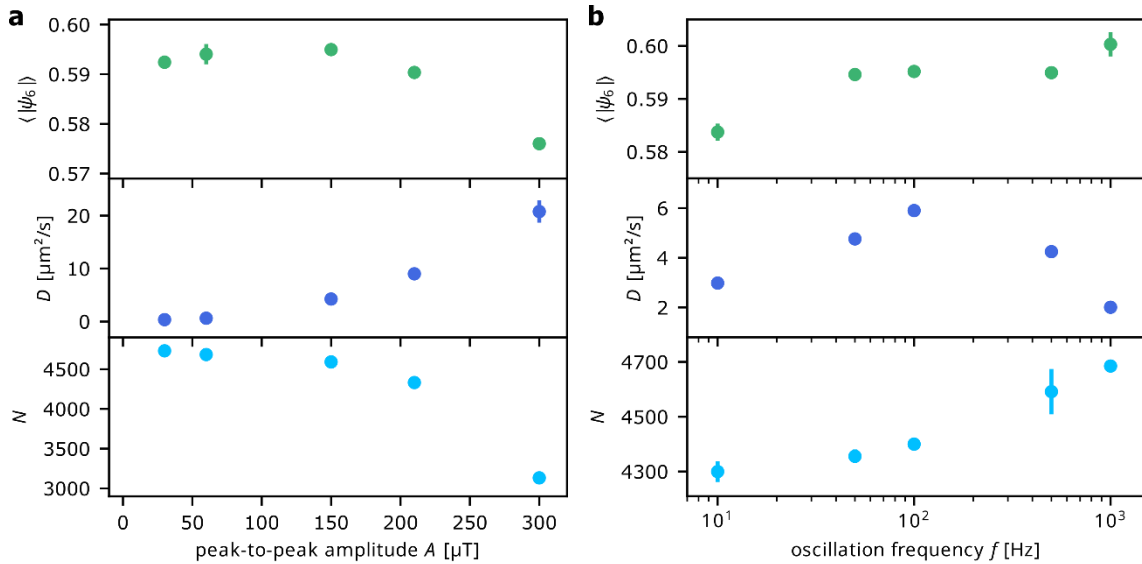
Documentation of my experiments used for this article are available for lab members on *eLabFTW* ( labbook database ID [7506](#)).

Skyrmion Lattice Domain Formation in a Non-Flat Energy Landscape

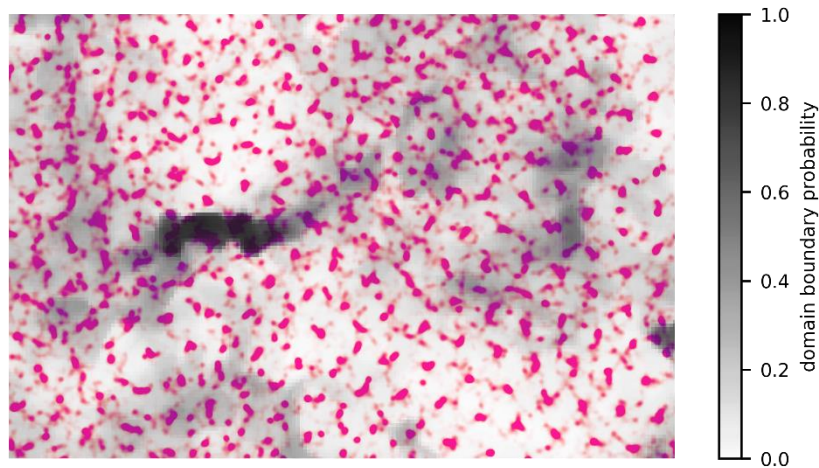
Supplementary Information



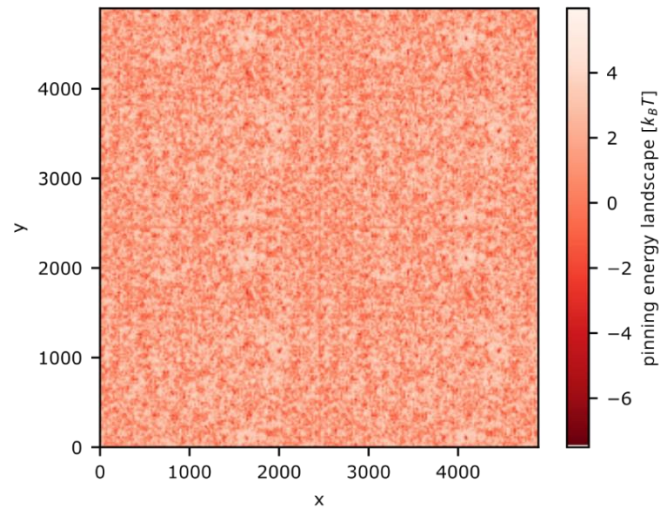
Supplementary Fig. 1. Skyrmion Lattice Evolution in Magnetic Field Oscillations. **a)** Orientational correlation function G_6 as a function of distance r at $t=0$ s and $t=60$ s after nucleation for lattice stabilization at $A=180$ μT (corresponding to Fig. 1d-e, respectively). The dashed lines represent the exponential fit of the correlation length ξ_6 through the marked dots. **b)** G_6 at $t=60$ s for all used amplitudes A , averaged over the three measurements. As described in the main text, G_6 decays slowest, signaling maximum order, around $A=180-240$ μT . Due to the enhanced skyrmion annihilation for increasing A , the nearest neighbor spacing also increases. **c)** Time evolution of the parameters shown in Fig. 1f-i starting right after nucleation. Lines represent the mean over three different nucleations (as rolling average over 2 s); the shaded area visualizes the corresponding standard error of the mean.



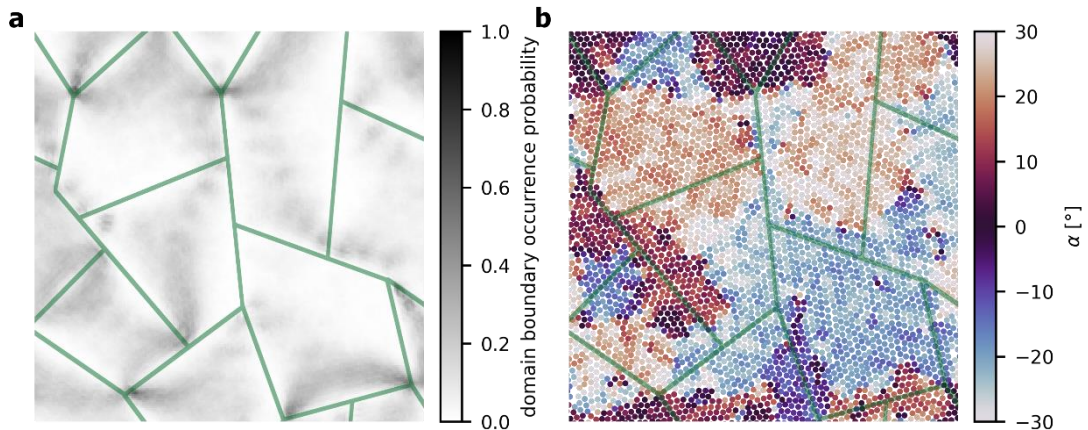
Supplementary Fig. 2. Amplitude and Field Scan of Magnetic Field Oscillations. **a)** Average local order parameter $\langle |\psi_6| \rangle$, diffusion coefficient D , and number of skyrmions N for varying oscillation amplitude A at fixed frequency f of 500 Hz. Data points and error bars denote average and standard deviation, respectively, of 4 s starting 4 s after nucleation, averaged for four independent measurements each. The average order is lower than in Fig 1 as the lattice is less dense and recorded for shorter times, i.e. evaluated faster after nucleation. Otherwise, the behavior is equivalent. **b)** Similarly, $\langle |\psi_6| \rangle$, D , and N for a fixed amplitude of 150 μT at varying frequency. D shows a peak around 100 Hz marking the maximal effect on the lattice dynamics and being the basis for choosing $f=100$ Hz for the further investigation in the main text. At low frequencies, the skyrmion spin structures have more time to react to the imposed field changes and are therefore increasingly destabilized, leading to lower N , but also reduced $\langle |\psi_6| \rangle$. For higher frequencies, $\langle |\psi_6| \rangle$ is only little affected.



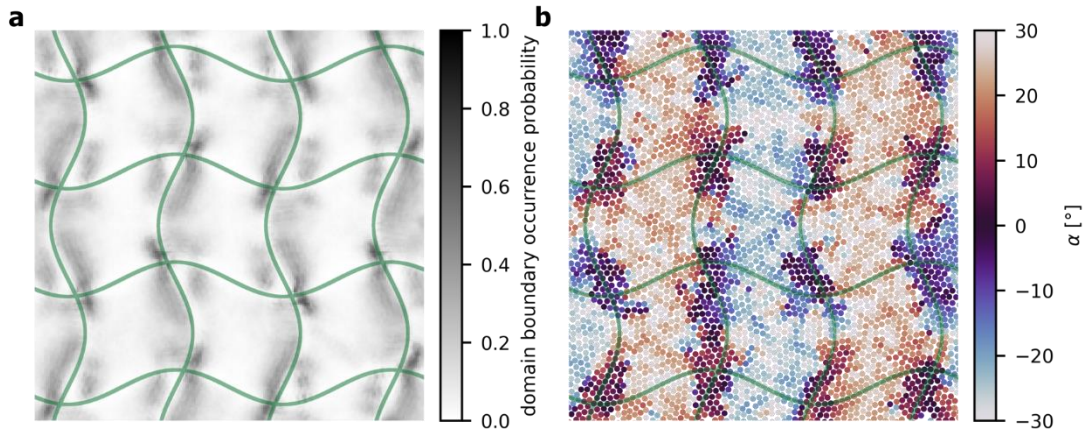
Supplementary Fig. 3. Skyrmion Occurrence Map. Every scattered pink dot represents the position of a skyrmion during three lattice formation videos of 62.5 s length. The grayscale background recalls the domain boundary occurrence probability from Fig. 3a. A regular pattern of frequent skyrmion occurrences forms not only due to pinning sites but also due to skyrmions being confined between their neighbors. Since the occurrences are therefore dominated by both skyrmion-material and skyrmion-skyrmion interactions, the occurrence map remains inconclusive with respect to the pinning potential and does not allow the direct determination of the energy landscape.



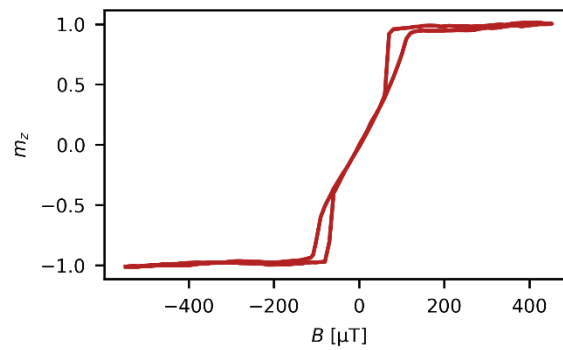
Supplementary Fig. 4. Skyrmion Energy Landscape. From the occurrence probability of sparse skyrmions, we extract the skyrmion energy landscape. We fill up the unsampled pixels with noise. The roughness of the energy landscape determines the strength of present pinning. In order to provide a large enough energy landscape to fit >5000 skyrmions while keeping the relation between pinning site distance and skyrmion distance constant, the energy landscape is repeated periodically to fill the whole space.



Supplementary Fig. 5. Skyrmion pinning along straight-line-shaped pinning landscape. **a)** The green straight lines pin skyrmions with an energy of $-7.5 k_B T$ with respect to the flat background potential. Over a simulation run of 100 STU with 5300 skyrmions at a density of 1.25, lattice domains and boundaries form and have an occurrence probability as shown by the grayscale background. Since straight lines are commensurate with the hexagonal lattice, they anchor the inside of a lattice domain and render domain boundaries unfavorable. Instead, the domain boundaries form between the lines of different orientation. **b)** Snapshot of the lattice orientation α per particle after 100 STU, showing how the lattice domains are anchored along the lines while domain boundaries form in between.



Supplementary Fig. 6. Skyrmion pinning along sinusoidal-line-shaped pinning landscape. **a)** The green sinusoidal lines pin skyrmions with an energy of $-7.5 k_B T$ with respect to the flat background potential. Over a simulation run of 100 STU with 5300 skyrmions at a density of 1.25, lattice domains with domain boundaries form in the vicinity of the sine. Here, the continuous curvature of the sine favors frequent breaking of lattice domains. **b)** Snapshot of the lattice orientation α per particle after 100 STU, showing how the lattice domains break along the sinusoidal lines.



Supplementary Fig. 7. Hysteresis Curve. Relative out-of-plane (OOP) magnetization m_z for OOP field cycle. Note the small saturation field of less than 200 μT .

8.2. Additional Results and Experimental Remarks

8.2.1. Establishing Skyrmion Lattice Order in Experiments

A central challenge in studying 2D skyrmion lattices in CoFeB-based thin films lies in fabricating samples that are both magnetically and structurally optimized. On one hand, the sample must exhibit a suitable balance between PMA and DMI to support skyrmion formation at high packing fractions, as required for ordered lattice phases [100]. On the other hand, the energy landscape must be sufficiently smooth to avoid pinning-induced disruption of QLRO. However, thermal fluctuations that enable skyrmion motion and lattice reconfiguration must remain below a critical threshold. Beyond this threshold, the system favors entropy maximization, and lattice order becomes thermodynamically unfavorable.

The multilayer stacks of composition Ta/CoFeB/Ta/MgO/Ta (or capped with HfO₂) – which are typically used in our group for thermal dynamics studies of skyrmions (see section 3.3) – demonstrate high skyrmion packing fractions near the SRT, as illustrated by the hysteresis loop in Supplementary Fig. 5 in section 8.1. The magnetic properties can be tuned such that skyrmions and skyrmion lattices occur within a temperature range of 295 K to 340 K, which is accessible using the integrated Peltier element, through careful adjustment of sputtering parameters and layer thicknesses [19, 35]. However, approaching the SRT, OOP magnetic structures become increasingly unstable [27, 41]. Even though the multilayer deposition is relatively smooth for our sample, Fig. 8.1 shows that close to the SRT, the magnetic behavior can be markedly different for the regions on a large sample piece of 5 cm lateral extension.

A significant remaining fabrication challenge is to control the energy landscape smoothness, which depends on the homogeneity of individual layers and interfaces. At present, only two magnetic multilayer stacks – FAB435 (labbook database ID 2167) and MAS763 (labbook database ID 3197) – provide sufficient structural and magnetic quality to enable the experiments presented in this thesis.

The results presented in section 8.1 establish a reproducible and systematic procedure to stabilize skyrmion lattices (labbook experiment ID 9498). The method is repeatedly applied across several equivalent runs and under different experimental conditions (e.g., field oscillation amplitude) to ensure statistical robustness. While this approach does not aim at optimizing individual lattice snapshots with maximal order – discussed further in chapter 10 – it provides critical insight into the underlying mechanisms of skyrmion lattice formation and stabilization.

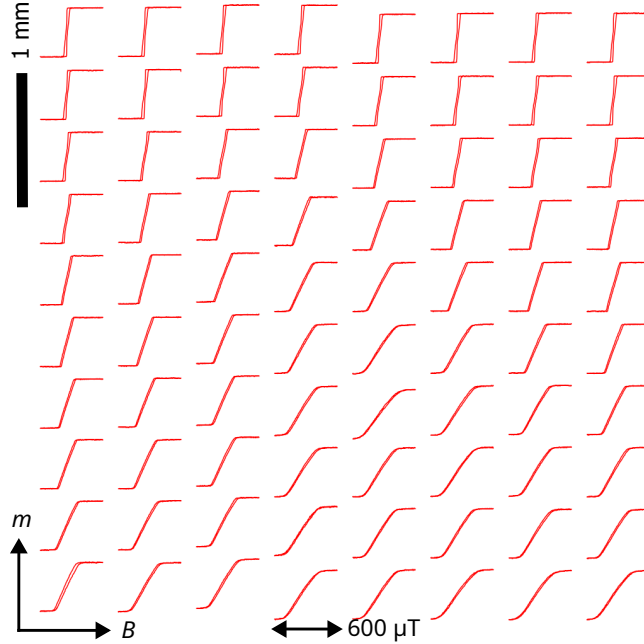


Figure 8.1.: Hysteresis Map. Hysteresis loops of the OOP magnetization m_z over OOP field cycles B of $300 \mu\text{T}$. Each loop corresponds to a measurement location on a $5 \text{ mm} \times 5 \text{ mm}$ sample. The measurements are taken at 295 K , which is approximately at the SRT. A gradient in hysteresis shape is visible across the sample surface. While the top left corner shows hysteresis loops suitable for skyrmion lattices, the bottom right corner is already in the IP phase.

8.2.2. Skyrmion Lattice Statistics

Given that a skyrmion lattice is inherently a many-body system, statistical analysis offers a powerful approach to extract structural and dynamical information. Here, I compare two skyrmion lattices – (I) and (II) – formed at different packing fractions and imaged via Kerr microscopy, as shown in Fig. 8.2. These lattices are similar to the ones discussed in section 8.1, but measured in the very similar FAB435 stack (labbook database ID 2167).

The skyrmion size is not fixed but varies slightly across the lattice. I quantify the skyrmion size using the radius of gyration r returned by the *trackpy* package [132]. While r does not correspond to the actual skyrmion radius, it provides a consistent measure for comparative purposes. As shown in Fig. 8.3a, r varies systematically with the skyrmion’s coordination number N .

Skyrmions at $N = 5$ sites are typically smaller, whereas those at $N = 7$ sites are larger than the mean. This behavior reflects their quasi-particle nature: unlike hard-sphere particles, skyrmions adapt their shape and size depending on magnetic boundary conditions. Particularly close to the SRT, the magnetic field precisely dictates the ratio of up- and down-magnetized domains. At high packing fractions, the skyrmions

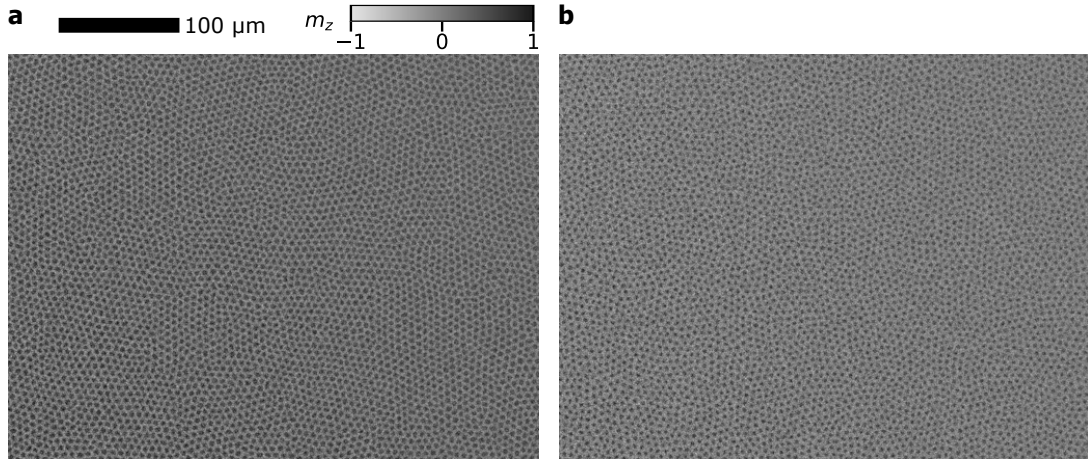


Figure 8.2.: Kerr Microscopy Snapshots of Skyrmion Lattices. (a) Kerr microscopy image of a dense skyrmion lattice at 332 K and 60 μT . Each bright spot corresponds to a single skyrmion. (b) Under 125 μT , the skyrmions shrink and the lattice becomes more dilute.

tend to expand, filling the available area. A 5-fold defect is therefore more tightly confined due to fewer neighbors. In contrast, the neighbors of a 7-defect form a larger shell, allowing for more spatial freedom, leading to larger r (see Fig. 2.2). This effect is more pronounced in the denser lattice (I); in the more dilute configuration (II), the size differences are reduced as the skyrmion size is generally reduced.

Inter-skyrmion distances d also vary with N , following the same trends: 5-defects are more tightly packed, resulting in shorter d , while 7-defects show increased spacing. When defects of different N are adjacent, such as in 5-7 pairs, the opposing effects partially cancel, yielding distances similar to regular $N = 6$ pairings.

Linking the detected skyrmions over time allows us to quantify displacements between consecutive frames (62.5 ms). Skyrmions that maintain their N exhibit relatively uniform displacements. In contrast, transitions in N are associated with larger displacements. These transitions correspond to the creation or annihilation of topological defects. As illustrated in Fig. 2.1 defect formation requires spatial displacement of particles, which is observed here statistically across the lattice.

8.2.3. Related Works in Different Systems

Our findings have interesting similarities to studies on periodically driven systems and 2D phase transitions in both skyrmion and non-skyrmion contexts.

Driving mechanisms have long been employed to facilitate lattice ordering. In superconducting vortex systems, both static and oscillatory currents were used to depin vortices and enable transitions into more ordered states [149–153]. Our approach of applying oscillating magnetic fields draws on these principles, adapted for skyrmions.

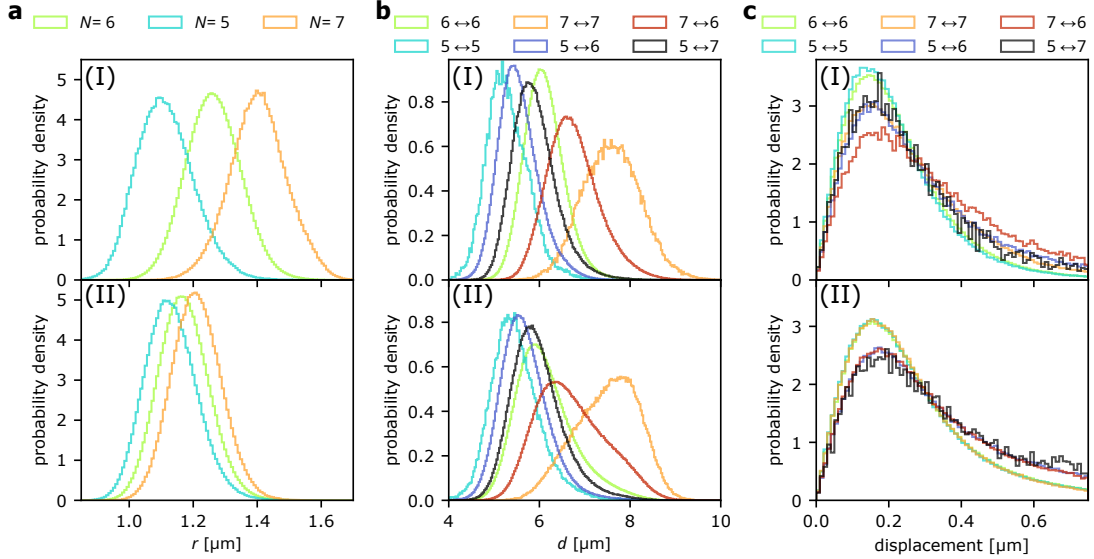


Figure 8.3.: Skyrmion Lattice Statistics. (a) Distribution of skyrmion radii r (radius of gyration) by coordination number N . (b) Inter-skyrmion distances d between neighbors with different N . E.g., $5 \leftrightarrow 6$ refers to distances between neighboring $N = 5$ and $N = 6$ skyrmions. (c) Skyrmion displacements within 62.5 ms, segmented by neighbor transitions. Top: dense lattice (I); bottom: dilute lattice (II). All histograms are normalized to probability densities. Statistics accumulated over 62.5 s for both lattices.

Similarly, colloidal lattices have been driven into QLRO phases using periodic magnetic excitations [124]. Additionally, colloidal systems with tunable particle sizes were explored by exploiting temperature-dependent hydrodynamic radii [154], although this introduces a coupling to temperature that differs from the skyrmion case. Earlier magnetic bubble experiments also employed oscillating OOP fields to form ordered lattices [155]. While these systems have similarity to ours in multilayer structure and methodology, their bubble sizes and spacings differ significantly.

Recent research on skyrmions has shown increasing interest in periodic driving. In our prior work (section 5.1), we demonstrated enhanced skyrmion diffusion under oscillating magnetic fields. In a similar CoFeB-based multilayer system, a similar effect was shown [156]. There, however, the hopping motion of the skyrmions was explicitly shown to follow the expansion and contraction of the skyrmion via a stripe appearance. Also, magnetic field oscillations assist a slight diffusion of skyrmions in FeGe [157].

8.3. Author Contributions

I performed all the experiments at the Kerr microscope on my own – except the measurement of the experimental energy landscape used in the simulations, these were measured by Tobias Sparmann. The wafer MOKE hysteresis map was measured by Fabian Kammerbauer.

The majority of the data analysis shown here was done by me and I also developed the used Python code. I specifically performed the skyrmion detection using *trackpy* [132], calculated the Voronoi tessellation, neighbor connections, local order parameter and correlation functions. I also introduced the orientation gradient to identify domain boundaries. I was provided with existing code for the analysis of ψ_6 and G_6 by Jan Rothörl. I used this code as basis to rewrite the analysis from scratch to optimize robustness, efficiency. Jan and Simon also developed their code further and we used the two independent code sets to validate our results. Particularly, Simon and Jan always calculated ψ_6 independently for the simulation data.

The simulations in this project were all conducted by Simon M. Fröhlich with the support of Jan Rothörl and Maarten A. Brems. Jan Rothörl and Simon M. Fröhlich also developed their analysis code further and we used the two independent code sets to validate our results. Particularly, Simon and Jan always calculated ψ_6 independently for the simulation data.

The magnetic multilayer sample was deposited by Maria-Andromachi Syskaki. However, I also used samples grown by Fabian Kammerbauer and patterned by Elizabeth M. Jefremovas while encountering the reported effect and while gathering data to design the final experiment.

Sachin Krishnia and Elizabeth M. Jefremovas helped me in developing the experiment, the data interpretation and writing the article with frequent discussions in their function as postdoctoral researchers.

Asle Sudbø, Peter Virnau and Mathias Kläui supervised and guided this work. Particularly, Asle Sudbø had the idea to analyze domain boundary occurrences. Peter Virnau and Mathias Kläui contributed as PhD supervisors and principal investigators in our skyrmion research group and provided advice in regular discussions.

9. Skyrmion Lattice Order Controlled by Confinement Geometry

9.1. Published Article

Publication Information

The following article is published in *Applied Physics Letters*:

Skyrmion Lattice Order Controlled by Confinement Geometry

Raphael Gruber, Jan Rothörl, Simon M. Fröhlich, Maarten A. Brems, Fabian Kammerbauer, Maria-Andromachi Syskaki, Elizabeth M. Jefremovas, Sachin Krishnia, Asle Sudbø, Peter Virnau & Mathias Kläui

Applied Physics Letters **127**, 212403 (2025).

DOI: [10.1063/5.0299901](https://doi.org/10.1063/5.0299901)


Copyright Information: Reprinted in this thesis with permission of AIP Publishing. This article may be downloaded for personal use only. Any other use requires prior permission of the author and AIP Publishing. This article appeared in *Appl. Phys. Lett.* **127**, 212403 (2025) and may be found at <https://doi.org/10.1063/5.0299901>.

Editorial Note: The blue header/footer bars were added for inclusion in this dissertation and are not part of the original publication.

Contributions

The author contributions for this project and article are described in detail in section 9.3.

Experimental Note

Documentation of my experiments used for this article are available for lab members on *eLabFTW* ( labbook database ID [7507](#)).

RESEARCH ARTICLE | NOVEMBER 24 2025

Skyrmion lattice order controlled by confinement geometry

Raphael Gruber ; Jan Rothörl ; Simon M. Fröhlich ; Maarten A. Brems ; Fabian Kammerbauer ; Maria-Andromachi Syskaki ; Elizabeth M. Jefremovas ; Sachin Krishna ; Asle Sudbø ; Peter Virnau ; Mathias Kläui

Check for updates

Appl. Phys. Lett. 127, 212403 (2025)

<https://doi.org/10.1063/5.0299901>

**Articles You May Be Interested In**

Driven by Brownian motion Cox–Ingersoll–Ross and squared Bessel processes: Interaction and phase transition

Physics of Fluids (January 2025)

The new effect of oscillations of the total angular momentum vector of viscous fluid

Physics of Fluids (August 2022)

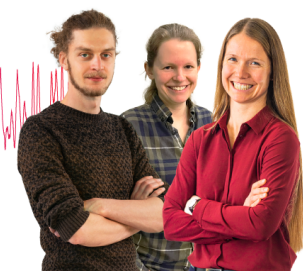
Webinar From Noise to Knowledge

May 13th – Register now



Zurich
Instruments

Universität
Konstanz



Skyrmion lattice order controlled by confinement geometry

Cite as: Appl. Phys. Lett. **127**, 212403 (2025); doi: [10.1063/5.0299901](https://doi.org/10.1063/5.0299901)

Submitted: 29 August 2025 · Accepted: 1 November 2025 ·

Published Online: 24 November 2025



View Online



Export Citation



CrossMark

Raphael Gruber,¹ Jan Rothörl,¹ Simon M. Fröhlich,¹ Maarten A. Brems,¹ Fabian Kammerbauer,¹ Maria-Andromachi Syskaki,^{1,2} Elizabeth M. Jefremovas,¹ Sachin Krishna,¹ Asle Sudbø,³ Peter Virnau,¹ and Mathias Kläui^{1,5,a)}

AFFILIATIONS

¹Institute of Physics, Johannes Gutenberg-Universität Mainz, Staudingerweg 7, 55128 Mainz, Germany

²Singulus Technologies AG, Hanauer Landstraße 103, 63796 Kahl am Main, Germany

³Center for Quantum Spintronics, Department of Physics, Norwegian University of Science and Technology, 7491 Trondheim, Norway

^{a)}Author to whom correspondence should be addressed: klaeui@uni-mainz.de

ABSTRACT

Magnetic skyrmions forming two-dimensional (2D) lattices provide a versatile platform for investigating phase transitions predicted by Kosterlitz–Thouless–Halperin–Nelson–Young theory. While 2D melting in skyrmion systems has been demonstrated, achieving controlled ordering in skyrmion lattices remains challenging due to pinning effects from a non-uniform energy landscape, which often results in polycrystalline structures. Skyrmions in thin films, however, offer thermal diffusion with high tunability and can be directly imaged via Kerr microscopy, enabling real-time observation of their dynamics. To regulate lattice order in such flexible systems, we introduce geometric confinements of varying shapes. Combining Kerr microscopy experiments with Thiele model simulations, we demonstrate that confinement geometry critically influences lattice order. Specifically, hexagonal confinements commensurate with the skyrmion lattice stabilize monodomain hexagonal ordering, while incommensurate geometries induce domain formation and reduce overall order. Understanding these boundary-driven effects is essential for advancing the study of 2D phase behavior and for the design of skyrmion-based spintronic applications, ranging from memory devices to unconventional computing architectures.

Published under an exclusive license by AIP Publishing. <https://doi.org/10.1063/5.0299901>

Magnetic skyrmions are topologically non-trivial chiral spin textures that exhibit quasi-particle behavior.^{1–3} Their small size, stability, and dynamic properties make them highly promising for energy-efficient spintronic applications ranging from data storage⁴ to sensing⁵ and unconventional computing—where so far single skyrmions have been used.^{6–9} For enhanced complexity, however, arrangements of multiple skyrmions can be envisaged.¹⁰ Beyond their technological significance for data processing, systems of dense skyrmion arrangements give rise to intriguing phenomena such as skyrmion drag.¹¹ Even denser lattice arrangements of skyrmions provide an ideal platform for exploring fundamental two-dimensional (2D) ordering phenomena^{12–15} as quasi-long-range order (QLRO) can arise.^{12–16}

Skyrmion quasi-particles can exhibit thermally activated Brownian dynamics^{17–19} and offer on-the-fly tunability of both their size and their diffusivity.^{18,20–22} This versatility allows us to investigate lattice phenomena beyond current observations and is a key advantage of skyrmions over other 2D systems like colloids or superconducting

vortices. In particular, the tunability can be exploited to drive and observe 2D phase transitions¹⁵ as described in Kosterlitz–Thouless–Halperin–Nelson–Young (KTHNY) theory.^{23–27} These 2D phase transitions differ fundamentally from behavior in other dimensions, particularly from 3D. In particular, the KTHNY theory describes the existence of a hexatic phase with only orientational QLRO between the solid phase (with translational QLRO) and the isotropic liquid (no QLRO).^{25–27} Eventually, these ordered lattices can even allow data transport by exploiting shock waves or the dynamics of topological lattice defects, which can move orders of magnitude faster than skyrmions.^{15,16} Consequently, 2D phase transitions have attracted significant fundamental research interest for decades, both in theory and in experiments.^{12,15,23–29}

In experimental skyrmion lattices, the key challenge in realizing QLRO is the underlying non-uniform energy landscape caused by material inhomogeneities.^{13–15,30} The non-flat energy landscape describes a continuously varying potential with attractive as well as

repulsive sites^{18,31}—often commonly referred to as pinning effects. It causes quenched disorder, topological lattice defects, and polycrystallinity, together breaking the QLRO of the lattice.^{13,30} The local order is quantified by the orientational order parameter

$$\psi_6(\mathbf{r}_j) = \frac{1}{n} \sum_{k=1}^n e^{-i6\theta_{jk}} \quad (1)$$

for every skyrmion j at position \mathbf{r}_j and with n nearest neighbors at positions \mathbf{r}_k ($k = 1 \dots n$); where θ_{jk} denotes the angle between the horizontal axis (arbitrarily chosen) and the vector $\mathbf{r}_k - \mathbf{r}_j$ connecting the neighbor pair j and k .²⁵ The Euler angle of the complex value of ψ_6 directly determines the local orientation $\alpha(\mathbf{r}_j) = \arg[\psi_6(\mathbf{r}_j)]/6$ of the lattice for every skyrmion. Regions of similar orientation α form a lattice domain. In a polycrystalline lattice, multiple lattice domains exist with different orientations of each domain. The domains are separated by boundaries at which α changes abruptly. These domain boundaries have been shown to be effectively pinned due to a non-flat energy landscape.³⁰ Thus, the lattice domains and their orientation appear pinned by the sample-specific energy landscape, imposing uncontrolled boundary conditions that are likely to be incommensurate with the ideal hexagonal skyrmion lattice.

To overcome this limitation, in this work, we artificially tune the boundary conditions by confining the skyrmion lattices inside different geometrical shapes. We find that commensurate shapes enhance the lattice order compared to an unconfined lattice, while the order is suppressed by incommensurate shapes. The results are consistent for Kerr microscopy experiments as well as Thiele model simulations.^{31–33}

We stabilize a polycrystalline skyrmion lattice close to room temperature (335 K) in a Ta(5 nm)/Co₂₀Fe₆₀B₂₀(0.9 nm)/Ta(0.07 nm)/MgO(2 nm)/Ta(5 nm) magnetic thin film multilayer stack with various confinement patterns (see the [supplementary material](#) with Fig. S1 for details). The skyrmions are imaged in real-time (16 fps) and -space by using a commercially available Kerr microscope by *evico magnetics GmbH* using the polar magneto-optical Kerr effect. In Fig. 1(a), we show a Kerr image of a skyrmion lattice in a hexagonal confinement. We use the *trackpy*³⁴ Python package to track the skyrmions and a Voronoi tessellation³⁵ to determine the lattice neighbors as well as the local order. After nucleation, the lattice evolves in time. In Fig. 1(b), we color the local lattice orientation α for different snapshots of one video. While several small lattice domains are present in the beginning, the whole lattice aligns with the hexagonal confinement within minutes. The growth of the lattice domains is accelerated by an oscillating magnetic out-of-plane (OOP) field.²⁰ The hexagonal confinement is commensurate with the hexagonal skyrmion lattice structure and therefore allows stabilization of QLRO on this finite length scale.¹⁵

As a comparison, in Fig. 1(c), we present skyrmion lattices confined in different, incommensurate geometric shapes. All confinements are patterned on the same sample piece and have nominally the same area as the hexagon. Furthermore, all shapes are regular, except for the heptagon, which is a hexagon with an additional kink. In all geometries, the lattice locally aligns with the confinement edges and is therefore frustrated for the incommensurate shapes. Consequently, distinct lattice orientations are anchored at the boundary and enforce the occurrence of domain boundaries between each other.³⁰ While for the pentagon, every corner induces only a slight distortion, in total causing

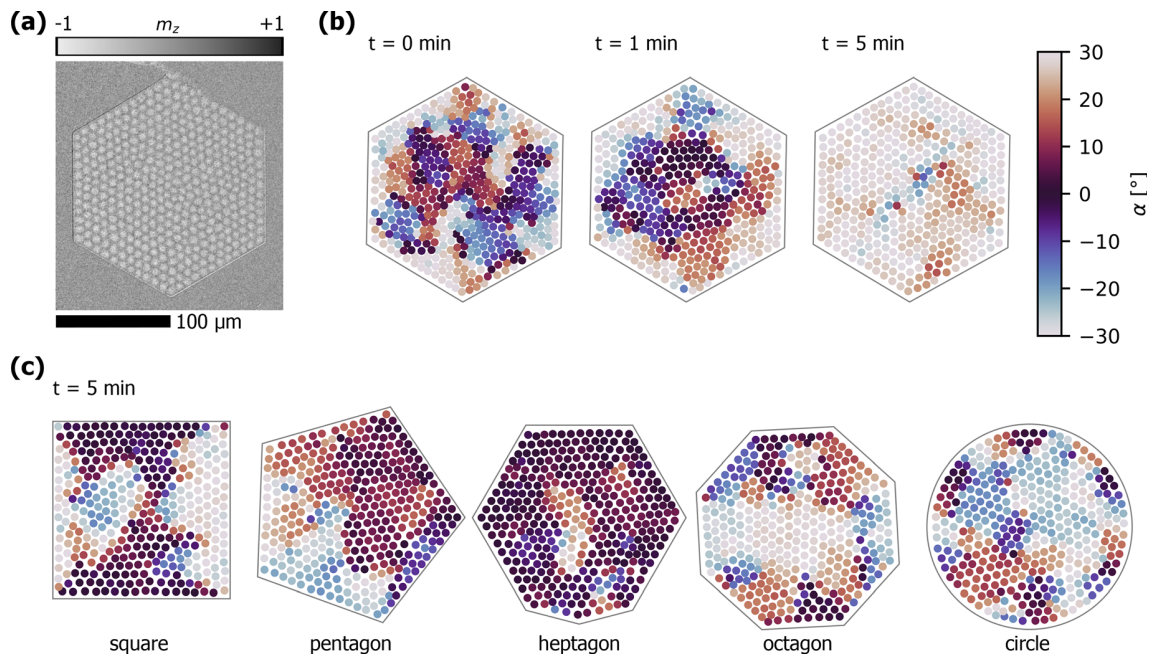


FIG. 1. (a) Polar Kerr microscopy image of a skyrmion lattice in a hexagonal confinement. (b) After nucleation, the skyrmion lattice arranges into hexagonal order on time scales of minutes within the commensurate hexagonal confinement, illustrated by the color-coded lattice orientation α per skyrmion for $t = 0, 1, 5$ min after nucleation. Due to the sixfold symmetry of the hexagonal lattice, the color map of α is cyclic. (c) In different geometries, the incommensurate edges anchor different lattice domains, suppressing hexagonal order even after $t = 5$ min.

one domain boundary through the center, the many orientations around the octagon and the circle lead to much smaller areas of similar orientation. The distortions caused by the subtle irregularity of the heptagon can range from only slight misalignment of the outermost 2–3 skyrmion layers to even significant distortions far inside the lattice. In principle, a regular triangle would also be commensurate with the hexagonal lattice and therefore expected to enhance lattice order. However, edge effects may play a role in comparison to the hexagonal shape, as the distances of every skyrmion to the edges are distributed differently.

To compare the lattice order in the different confinements quantitatively, we calculate the average local order $\Psi_6 = \langle |\psi_6| \rangle$ as well as $\chi_6 = |\langle \psi_6 \rangle|$ in Fig. 2. For both parameters, higher values indicate better ordering. We furthermore compare the results to videos of a continuous sample of millimeter extension, where no confinements are patterned and around 3500 skyrmions are nucleated in the field of view. We find that the ordering is enhanced in the commensurate hexagon and suppressed for the incommensurate shapes. Thereby, χ_6 reveals more drastic differences as it globally averages over α , thus providing more long-range information but being significantly affected by changes of α that occur, for instance, at domain boundaries.

Correspondingly, the fraction of skyrmions being a topological lattice defect (i.e., $n \neq 6$ lattice neighbors) increases for reduced ordering. The topological defects emerge not only as an intrinsic property of 2D lattices mediating their phase behavior^{23–27} but also at domain boundaries or pinning sites. Even though a similar amount of $N = 510 \pm 20$ skyrmions is created per nucleation (at $t = 0$) in every geometry, we notice a clear difference in the annihilation rate for the different shapes: Skyrmion annihilation is less pronounced for the hexagon being commensurate with the hexagonal lattice, resulting in around $N = 395 \pm 5$ skyrmions remaining at $t = 5$ min, which is particularly close to the centered hexagonal number 401. In the incommensurate shapes, however, the different lattice domains and domain boundaries cause space conflicts, which lead to skyrmion annihilations and result in only $N = 365 \pm 15$ at $t = 5$ min. In the continuous reference area, $N = 2620 \pm 15$ skyrmions are left after 5 min, all of them are included to calculate the plotted order parameters. The time evolution of all shown parameters is presented in Fig. S2 in the [supplementary material](#).

Our results demonstrate that confinement geometries play a critical role in stabilizing lattice order. By carefully designing the boundary conditions, however, the degree of order in skyrmion lattices can be effectively controlled—while the finite size itself has been shown to only have a minor effect on the 2D phase behavior.¹⁵ To understand the commensurability effect, we next perform Thiele model simulations^{31–33} using confinements of different geometries.

In the simulations, we employ a purely repulsive interaction potential of the form r^{-8} , which has been demonstrated to describe our experimental skyrmion system well^{15,30,36} (see the [supplementary material](#) with Fig. S3 for details). We find that the simulated particles align with the edges of the confinements as in the experiment and anchor differently oriented domains. We show examples of snapshots for every shape in Fig. 3(a). The extent of the single domains varies between the 1000 snapshots of three different equilibration sequences of the system. However, the average ordering (reflected by Ψ_6 , χ_6 , and the fraction of lattice defects) is consistent as presented in Fig. 3(b). Especially, we reproduce the experimental result that the lattice order

is suppressed in geometric confinements that are incommensurate. The error bars (calculated as standard error of the mean from the three equilibration sequences) are only visible for the incommensurate geometries, as different lattice domains are forced to coexist but vary in extent and distribution from snapshot to snapshot. For example, the distortion induced in the heptagon affects the eight outermost skyrmion layers in Fig. 3(a). However, in some equilibration sequences, it may only affect two to three layers but can—in analogy to the experiment—even reach the center of the geometry in other sequences, depending on the specific configuration. In contrast, the distribution of domains in the experiment is additionally influenced by the energy landscape, which yields certain preferences for domain orientations and domain boundaries.³⁰

In conclusion, we demonstrate in both Kerr microscopy experiments and molecular dynamics simulations that the order of a confined magnetic skyrmion lattice can be tuned as it strongly depends on the confinement geometry. While a hexagonal confinement is commensurate with the hexagonal skyrmion lattice structure and stabilizes the lattice order, incommensurate geometries suppress order, and differently oriented lattice domains form along the edges. In magnetic thin films,

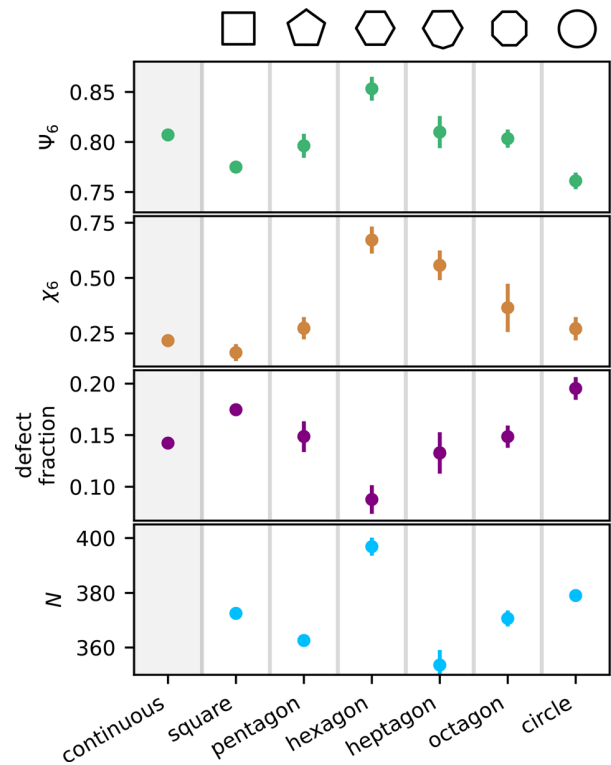


FIG. 2. Order parameters Ψ_6 and χ_6 , the fraction of lattice defects, and the number of skyrmions N compared for different confinement geometries and a lattice in an unpatterned, continuous film ($N > 3000$) for reference. Data points are the average values from the last minute ($4 \text{ min} < t < 5 \text{ min}$) of three independent videos. While the commensurate hexagonal confinement enhances the lattice order, incommensurate geometries suppress order with respect to the continuous case. From the mean values of the three different nucleations, we calculate the standard error of the mean as the error bar.

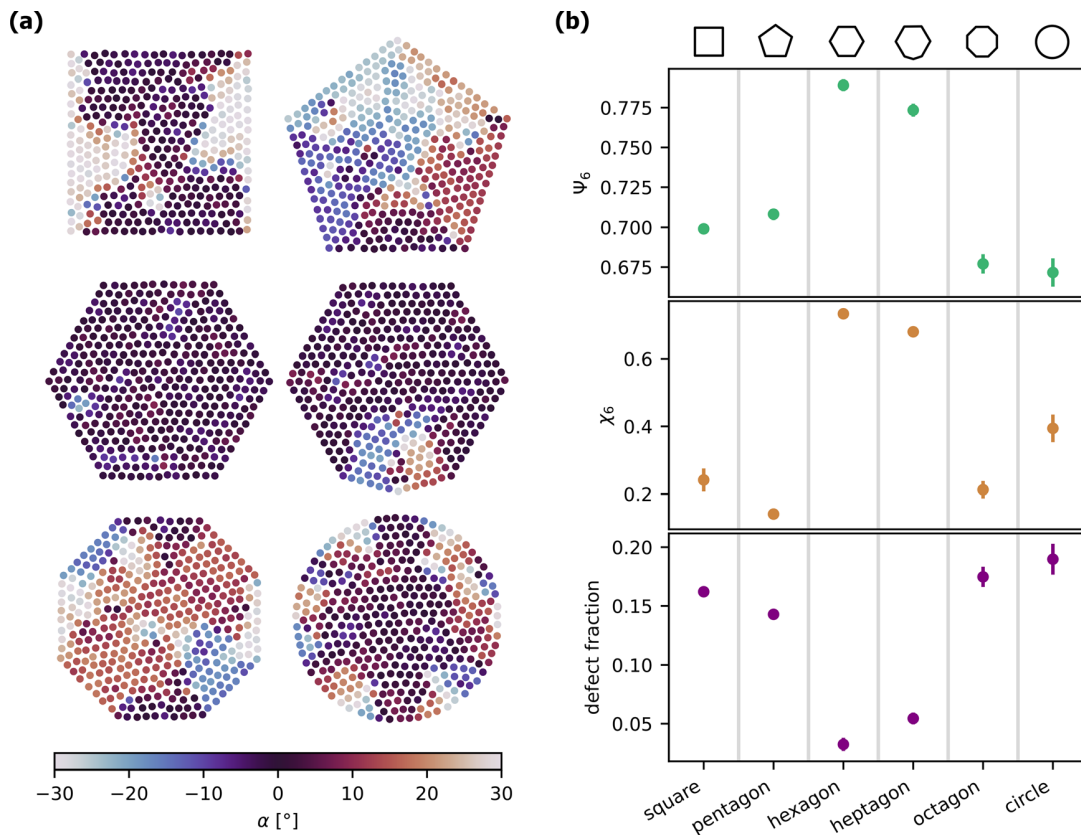


FIG. 3. (a) Local orientation α for simulated skyrmion lattices ($N = 400$) in confinement, reproducing the alignment of lattice domains with the confinement edges and leading to multidomain states in incommensurate geometries. (b) The ordering parameters Ψ_6 and χ_6 as well as the fraction of lattice defects behave similar to the experiment: the lattice order is significantly enhanced in the commensurate hexagon and the closely related heptagon. Data points are averages over 3×1000 snapshots, where the error bar is calculated as the standard error of the mean from the three independent datasets.

lattice domains are typically pinned in a similar way by the non-flat energy landscape.³⁰ Therefore, understanding these boundary effects is key to studying 2D phase behavior with skyrmions on larger scales. Magnetic skyrmions are of special interest for investigating 2D phase behavior as their real-time accessibility in Kerr microscopy can allow one to investigate key open questions like the dynamics of topological defects¹⁵ and their interaction potential—even in the presence of a Magnus force. Understanding and controlling the dynamics of densely packed skyrmions in a confined geometry^{6,7,19} also plays a key role for realizing low-power non-conventional computing applications.^{5–7}

See the [supplementary material](#) for a detailed description of the experimental and simulation setups.

This work was funded by the Deutsche Forschungsgemeinschaft (DFG, German Research Foundation)—SPP 2137 (Project No. 403502522) and TRR 173/2 Spin+X (projects A01, A12, and B02). The authors acknowledge funding from TopDyn. This project has received funding from the European Research Council (ERC) under the European Union’s Horizon 2020 research and innovation program (Grant No. 856538, project “3D MAGiC”) and under the Marie Skłodowska-Curie Grant Agreement Nos. 860060 (“MagnEfi”) and

101119608 (“TOPOCOM”). The authors gratefully acknowledge the computing time granted on the supercomputer MOGON II and III at Johannes Gutenberg University Mainz as part of NHR South-West. M.A.B. was supported by a doctoral scholarship of the Studienstiftung des deutschen Volkes. E.M.J. acknowledges the Alexander von Humboldt Postdoctoral Fellowship. A.S. and M.K. acknowledge support from the Norwegian Research Council (Grant No. 262633), Center of Excellence on Quantum Spintronics (QuSpin). A.S. also acknowledges support from Norwegian Research Council (Grant No. 323766).

AUTHOR DECLARATIONS

Conflict of Interest

The authors have no conflicts to disclose.

Author Contributions

Raphael Gruber: Conceptualization (lead); Data curation (lead); Formal analysis (lead); Investigation (lead); Methodology (lead); Software (lead); Validation (lead); Visualization (lead); Writing – original draft (lead). **Jan Rothörl:** Formal analysis (equal); Investigation (equal); Methodology (equal); Software (equal); Visualization (equal).

Simon M. Fröhlich: Formal analysis (equal); Investigation (equal); Software (equal). **Maarten A. Brems:** Conceptualization (equal); Methodology (equal); Software (supporting); Validation (supporting). **Fabian Kammerbauer:** Resources (lead). **Maria-Andromachi Syskaki:** Resources (supporting). **Elizabeth M. Jefremovas:** Conceptualization (equal); Resources (lead); Validation (supporting); Writing – review & editing (equal). **Sachin Krishnia:** Conceptualization (equal); Supervision (equal); Writing – review & editing (equal). **Asle Sudbo:** Conceptualization (equal); Methodology (equal); Supervision (equal). **Peter Virnau:** Conceptualization (equal); Funding acquisition (equal); Methodology (equal); Supervision (equal). **Mathias Kläui:** Conceptualization (lead); Funding acquisition (lead); Project administration (lead); Supervision (lead); Writing – review & editing (lead).

DATA AVAILABILITY

The data that support the findings of this study are openly available in Zenodo at <https://doi.org/10.5281/zenodo.17406257>, Ref. 37.

REFERENCES

- 1A. Bogdanov and A. Hubert, “Thermodynamically stable magnetic vortex states in magnetic crystals,” *J. Magn. Magn. Mater.* **138**(3), 255–269 (1994).
- 2S. Mühlbauer, B. Binz, F. Jonietz, C. Pfleiderer, A. Rosch, A. Neubauer, R. Georgii, and P. Böni, “Skyrmion lattice in a chiral magnet,” *Science* **323**(5916), 915–919 (2009).
- 3K. Everschor-Sitte, J. Masell, R. M. Reeve, and M. Kläui, “Perspective: Magnetic skyrmions—Overview of recent progress in an active research field,” *J. Appl. Phys.* **124**(24), 240901 (2018).
- 4A. Fert, V. Cros, and J. Sampaio, “Skyrmions on the track,” *Nat. Nanotechnol.* **8**(3), 152–156 (2013).
- 5K. Leutner, T. B. Winkler, R. Gruber, R. Frömter, J. Güttinger, H. Fangohr, and M. Kläui, “Skyrmion automation and readout in confined counter-sensor device geometries,” *Phys. Rev. Appl.* **20**(6), 064021 (2023).
- 6K. Raab, M. A. Brems, G. Beneke, T. Dohi, J. Rothörl, F. Kammerbauer, J. H. Mentink, and M. Kläui, “Brownian reservoir computing realized using geometrically confined skyrmion dynamics,” *Nat. Commun.* **13**(1), 6982 (2022).
- 7G. Beneke, T. B. Winkler, K. Raab, M. A. Brems, F. Kammerbauer, P. Gerhards, K. Knobloch, S. Krishnia, J. H. Mentink, and M. Kläui, “Gesture recognition with Brownian reservoir computing using geometrically confined skyrmion dynamics,” *Nat. Commun.* **15**(1), 8103 (2024).
- 8O. Lee, R. Msiska, M. A. Brems, M. Kläui, H. Kurebayashi, and K. Everschor-Sitte, “Perspective on unconventional computing using magnetic skyrmions,” *Appl. Phys. Lett.* **122**(26), 260501 (2023).
- 9M. A. Brems, M. Kläui, and P. Virnau, “Circuits and excitations to enable Brownian token-based computing with skyrmions,” *Appl. Phys. Lett.* **119**(13), 132405 (2021).
- 10T. B. Winkler, J. Rothörl, M. A. Brems, G. Beneke, H. Fangohr, and M. Kläui, “Coarse-graining collective skyrmion dynamics in confined geometries,” *Appl. Phys. Lett.* **124**(2), 022403 (2024).
- 11C. Reichhardt, “Dynamics and nonmonotonic drag for individually driven skyrmions,” *Phys. Rev. B* **104**(6), 064441 (2021).
- 12P. Huang, T. Schönenberger, M. Cantoni, L. Heinen, A. Magrez, A. Rosch, F. Carbone, and H. M. Rønnow, “Melting of a skyrmion lattice to a skyrmion liquid via a hexatic phase,” *Nat. Nanotechnol.* **15**(9), 761–767 (2020).
- 13J. Zázvorka, F. Dittrich, Y. Ge, N. Kerber, K. Raab, T. Winkler, K. Litzius, M. Veis, P. Virnau, and M. Kläui, “Skyrmion lattice phases in thin film multilayer,” *Adv. Func. Mater.* **30**(46), 2004037 (2020).
- 14P. Meisenheimer, H. Zhang, D. Raftrey, X. Chen, Y.-T. Shao, Y.-T. Chan, R. Yalisove, R. Chen, J. Yao, M. C. Scott, W. Wu, D. A. Muller, P. Fischer, R. J. Birgeneau, and R. Ramesh, “Ordering of room-temperature magnetic skyrmions in a polar van der Waals magnet,” *Nat. Commun.* **14**(1), 3744 (2023).
- 15R. Gruber, J. Rothörl, S. M. Fröhlich, M. A. Brems, F. Kammerbauer, M.-A. Syskaki, E. M. Jefremovas, S. Krishnia, A. Sudbø, P. Virnau, and M. Kläui, “Real-time observation of topological defect dynamics mediating two-dimensional skyrmion lattice melting,” *Nat. Nanotechnol.* **20**(10), 1405–1411 (2025).
- 16C. Reichhardt, C. J. O. Reichhardt, and M. V. Milošević, “Statics and dynamics of skyrmions interacting with disorder and nanostructures,” *Rev. Mod. Phys.* **94**(3), 035005 (2022).
- 17J. Zázvorka, F. Jakobs, D. Heinze, N. Keil, S. Kromin, S. Jaiswal, K. Litzius, G. Jakob, P. Virnau, D. Pinna, K. Everschor-Sitte, L. Rózsa, A. Donges, U. Nowak, and M. Kläui, “Thermal skyrmion diffusion used in a reshuffler device,” *Nat. Nanotechnol.* **14**(7), 658–661 (2019).
- 18R. Gruber, J. Zázvorka, M. A. Brems, D. R. Rodrigues, T. Dohi, N. Kerber, B. Seng, M. Vafaee, K. Everschor-Sitte, P. Virnau, and M. Kläui, “Skyrmion pinning energetics in thin film systems,” *Nat. Commun.* **13**(1), 3144 (2022).
- 19C. Song, N. Kerber, J. Rothörl, Y. Ge, K. Raab, B. Seng, M. A. Brems, F. Dittrich, R. M. Reeve, J. Wang, Q. Liu, P. Virnau, and M. Kläui, “Commensurability between element symmetry and the number of skyrmions governing skyrmion diffusion in confined geometries,” *Adv. Func. Mater.* **31**(19), 2010739 (2021).
- 20R. Gruber, M. A. Brems, J. Rothörl, T. Sparmann, M. Schmitt, I. Kononenko, F. Kammerbauer, M.-A. Syskaki, O. Farago, P. Virnau, and M. Kläui, “300-Times-increased diffusive skyrmion dynamics and effective pinning reduction by periodic field excitation,” *Adv. Mater.* **35**(17), 2208922 (2023).
- 21N. Kerber, M. Weissenhofer, K. Raab, K. Litzius, J. Zázvorka, U. Nowak, and M. Kläui, “Anisotropic skyrmion diffusion controlled by magnetic-field-induced symmetry breaking,” *Phys. Rev. Appl.* **15**(4), 044029 (2021).
- 22F. Rucker, A. Bezvershenko, D. Mettus, A. Bauer, M. Garst, A. Rosch, and C. Pfleiderer, “Shaking and pushing skyrmions: Formation of a non-equilibrium phase with zero critical current,” *arXiv:2504.01133* (2025).
- 23J. M. Kosterlitz and D. J. Thouless, “Long range order and metastability in two dimensional solids and superfluids. (Application of dislocation theory),” *J. Phys. C: Solid State Phys.* **5**(11), L124 (1972).
- 24J. M. Kosterlitz and D. J. Thouless, “Ordering, metastability and phase transitions in two-dimensional systems,” *J. Phys. C: Solid State Phys.* **6**(7), 1181–1203 (1973).
- 25B. I. Halperin and D. R. Nelson, “Theory of two-dimensional melting,” *Phys. Rev. Lett.* **41**(2), 121–124 (1978).
- 26D. R. Nelson and B. I. Halperin, “Dislocation-mediated melting in two dimensions,” *Phys. Rev. B* **19**(5), 2457–2484 (1979).
- 27A. P. Young, “Melting and the vector Coulomb gas in two dimensions,” *Phys. Rev. B* **19**(4), 1855–1866 (1979).
- 28S. C. Kapfer and W. Krauth, “Two-dimensional melting: From liquid-hexatic coexistence to continuous transitions,” *Phys. Rev. Lett.* **114**(3), 035702 (2015).
- 29K. Zahn, R. Lenke, and G. Maret, “Two-stage melting of paramagnetic colloidal crystals in two dimensions,” *Phys. Rev. Lett.* **82**(13), 2721–2724 (1999).
- 30R. Gruber, J. Rothörl, S. M. Fröhlich, M. A. Brems, T. Sparmann, F. Kammerbauer, M.-A. Syskaki, E. M. Jefremovas, S. Krishnia, A. Sudbø, P. Virnau, and M. Kläui, “Skyrmion lattice domain formation in a non-flat energy landscape,” *arXiv:2508.12988* (2025).
- 31M. A. Brems, T. Sparmann, S. M. Fröhlich, L.-C. Dany, J. Rothörl, F. Kammerbauer, E. M. Jefremovas, O. Farago, M. Kläui, and P. Virnau, “Realizing Quantitative Quasiparticle Modeling of Skyrmion Dynamics in Arbitrary Potentials,” *Phys. Rev. Lett.* **134**(4), 046701 (2025).
- 32A. A. Thiele, “Steady-State Motion of Magnetic Domains,” *Phys. Rev. Lett.* **30**(6), 230–233 (1973).
- 33J. A. Anderson, J. Glaser, and S. C. Glotzer, “HOOMD-blue: A Python package for high-performance molecular dynamics and hard particle Monte Carlo simulations,” *Comput. Mater. Sci.* **173**, 109363 (2020).
- 34D. B. Allan, T. Caswell, N. C. Keim, C. M. van der Wel, and R. W. Verweij, “soft-matter/trackpy: V 0.6.4,” (2024).
- 35J. L. Finney and J. D. Bernal, “Random packings and the structure of simple liquids. I. The geometry of random close packing,” *Proc. R. Soc. A* **319**(1539), 479–493 (1997).
- 36Y. Ge, J. Rothörl, M. A. Brems, N. Kerber, R. Gruber, T. Dohi, M. Kläui, and P. Virnau, “Constructing coarse-grained skyrmion potentials from experimental data with Iterative Boltzmann Inversion,” *Commun. Phys.* **6**(1), 1–6 (2023).
- 37R. Gruber, J. Rothörl, S. M. Fröhlich, M. A. Brems, F. Kammerbauer, M.-A. Syskaki, E. M. Jefremovas, S. Krishnia, A. Sudbø, P. Virnau, and M. Kläui (2025). “Source data - Skyrmion lattice order controlled by confinement geometry,” Zenodo. <https://doi.org/10.5281/zenodo.17406257>

9.1.1. Supplementary Material

Publication Information

The following supplementary material is published with the article in *Applied Physics Letters*:

Skyrmion Lattice Order Controlled by Confinement Geometry

Raphael Gruber, Jan Rothörl, Simon M. Fröhlich, Maarten A. Brems, Fabian Kammerbauer, Maria-Andromachi Syskaki, Elizabeth M. Jefremovas, Sachin Krishnia, Asle Sudbø, Peter Virnau & Mathias Kläui
Applied Physics Letters **127**, 212403 (2025).

DOI: [10.1063/5.0299901](https://doi.org/10.1063/5.0299901)

Copyright Information: Reprinted in this thesis with permission of AIP Publishing. This article may be downloaded for personal use only. Any other use requires prior permission of the author and AIP Publishing. This article appeared in *Appl. Phys. Lett.* **127**, 212403 (2025) and may be found at <https://doi.org/10.1063/5.0299901>.

Editorial Note: The blue header/footer bars were added for inclusion in this dissertation and are not part of the original publication.

Contributions

The author contributions for this project and article are described in detail in section 9.3.

Experimental Note

Documentation of my experiments used for this article are available for lab members on *eLabFTW* (📖 labbook database ID [7507](#)).

Skyrmion Lattice Order Controlled by Confinement Geometry

Supplementary Material

Raphael Gruber¹, Jan Rothörl¹, Simon M. Fröhlich¹, Maarten A. Brems¹, Fabian Kammerbauer¹, Maria-Andromachi Syskaki^{1,2}, Elizabeth M. Jefremovas¹, Sachin Krishnia¹, Asle Sudbø³, Peter Virnau¹, Mathias Kläui^{1,3*}

1. Institute of Physics, Johannes Gutenberg-Universität Mainz, Staudingerweg 7, 55128 Mainz, Germany.
2. Singulus Technologies AG, Hanauer Landstraße 103, 63796 Kahl am Main, Germany.
3. Center for Quantum Spintronics, Department of Physics, Norwegian University of Science and Technology, 7491 Trondheim, Norway.

*Email: klaeui@uni-mainz.de

Magnetic Multilayer Material

The Ta(5 nm)/Co₂₀Fe₆₀B₂₀(0.9 nm)/Ta(0.07 nm)/MgO(2 nm)/Ta(5 nm) multilayer stack is deposited using DC/RF magnetron sputtering in a *Singulus Rotaris* system under a base pressure of 3×10^{-8} mbar. The layer thickness is accurate to within 0.01 nm. The geometric confinements are patterned by electron beam lithography (EBL), followed by Argon ion etching. The continuous film reference measurements are performed on the same sample in a region of millimeter lateral dimension.

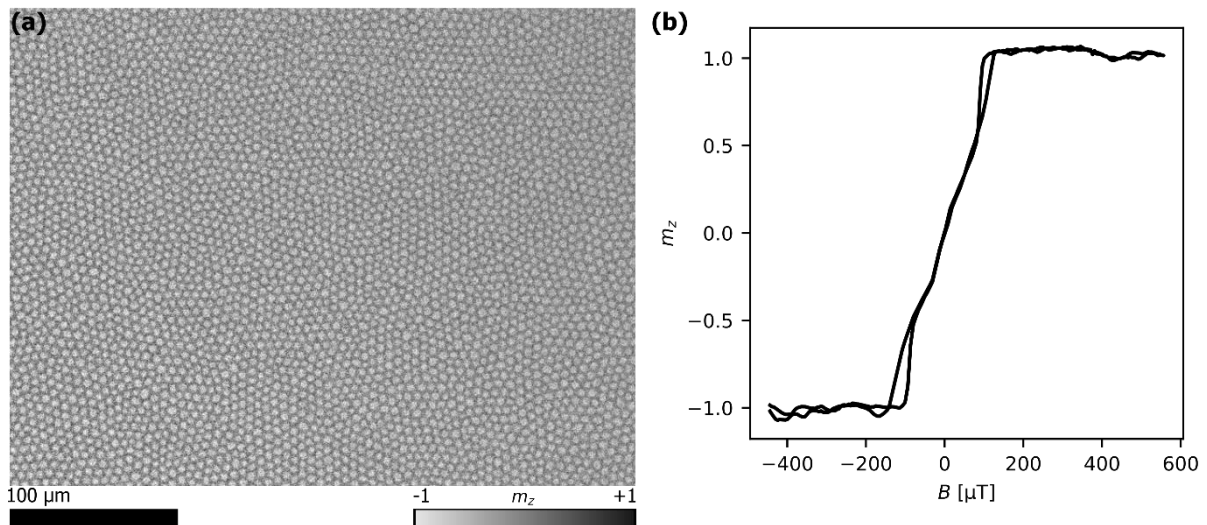


Fig. S1. Skyrmion Lattice and Hysteresis Curve. (a) Skyrmion lattice in the continuous film (millimeter extension) imaged by Kerr microscopy. The grayscale contrast denotes the out-of-plane (OOP) magnetization. (b) Relative OOP magnetization m_z for an OOP field cycle measured by Kerr microscopy at 333 K. Note the small saturation field of less than 200 μT .

The interfacial Dzyaloshinskii-Moriya interaction (DMI)^{1,2} arises primarily at the Ta/Co₂₀Fe₆₀B₂₀ interface, while the Co₂₀Fe₆₀B₂₀/MgO interface induces perpendicular magnetic anisotropy (PMA). We use a dusting layer of Ta(0.07) to balance DMI and PMA^{3,4}, thereby stabilizing skyrmions and optimizing the energy landscape for skyrmion lattice formation and dynamics. Skyrmions are stable in the continuous film as shown in Fig. S1a. For the patterned structures, the stack is physically removed to provide geometric confinement.

We provide the out-of-plane (OOP) hysteresis loop in Fig. S1b of the Supplementary Material to characterize the magnetic properties of the multilayer stack. Using spin-orbit torque-driven skyrmion motion and micromagnetic simulations, we confirm the non-trivial topology of the magnetic bubbles in our experiment^{3,5-7}.

Skyrmion Imaging and Order Analysis

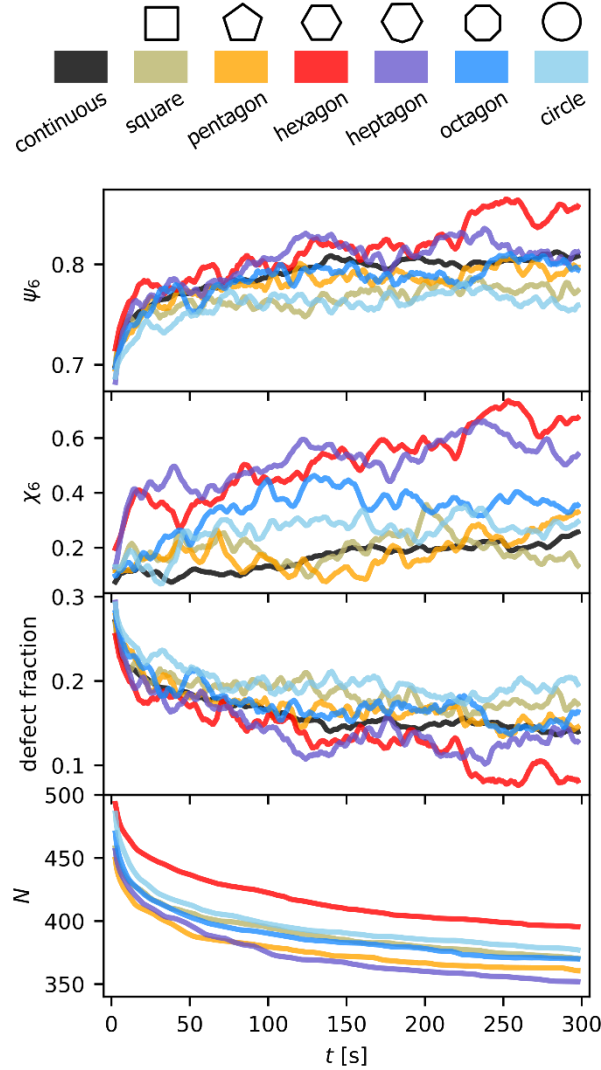


Fig. S2: Typical time evolution of the order parameters ψ_6 and χ_6 , the fraction of lattice defects and the number of skyrmions N in the different confinements. For better visibility, only the rolling mean over 5 s is shown.

We establish magnetic contrast by magneto-optical Kerr effect in polar mode using a commercially available Kerr microscope manufactured by *evico magnetics GmbH* with a blue LED light source. We acquire Kerr images and videos (16 frames per second; 62.5 ms exposure time) with a CCD camera yielding gray-scale contrast at a field of view of $200 \times 150 \mu\text{m}^2$. We can control the magnetic field in in-plane (IP) and out-of-plane (OOP) direction separately by perpendicularly aligned electromagnetic coils. The OOP field coil is custom-made and allows for field control with a

precision better than $1 \mu\text{T}$. The fields are calibrated using a Hall probe and corrected for background fields by the offset of hysteresis loops^{8,9}. A Peltier element on top of the coil allows for temperature control with a precision better than 0.1 K ^{3,6}. The thin film sample is placed directly on top of the Peltier element and temperature is monitored by a Pt100 sensor directly next to the sample. The whole setup is within a thermally stabilized flow box to improve stability of the operating conditions.

Skyrmions are nucleated by applying a large IP field pulse^{5,10,11} while keeping the OOP field constant at its set value. The resulting skyrmions are a stable OOP domain state when the IP field is switched off again. We control the density and size of the skyrmions by the applied OOP field at a constant temperature^{6,12,13}. We accelerate the formation of lattice order by reducing effective pinning with OOP field oscillations. We compare this formation process for several nucleations in videos capturing the 5 min after nucleation.

We use the 2D Gaussian kernel fitting within the *trackpy* Python package¹⁴ to detect skyrmion positions in every frame. In the continuous reference area, the magnetic film extent of several millimeters exceeds the field of view significantly and is therefore considered as continuous, where we neglect boundary effects. We use a Voronoi tessellation¹⁵ in every frame to extract nearest neighbor connections and the complex local order parameter ψ_6 for every skyrmion, where $\alpha = \arg(\psi_6)/6$ determines the local lattice orientation¹⁶. Every skyrmion with more or less than six nearest neighbors is a topological lattice defect^{17,18}.

Thiele Model Simulations of Skyrmion Lattices

To simulate the thermal dynamics of skyrmions in a lattice configuration, we perform computer simulations. Since the experimental skyrmions are of micrometer size in a system spanning hundreds of micrometers, the skyrmions and especially their dynamics are not accessible in micromagnetic or atomistic simulations. Instead, we use a coarse-grained approach using the Thiele model¹⁹. The corresponding equation of motion reads^{20,21}

$$-\gamma \mathbf{v} - G_{\text{rel}} \gamma \mathbf{e}_z \times \mathbf{v} + \mathbf{F}_{\text{therm}} + \mathbf{F}_{\text{SkSk}}(\{\mathbf{r}\}) + \mathbf{F}_{\text{SkBnd}}(\mathbf{r}) = 0 \quad (\text{S1})$$

with the set $\{\mathbf{r}\}$ of skyrmion positions \mathbf{r} , the skyrmion velocity \mathbf{v} , the total damping γ (in the context of a Brownian Dynamics simulation, not the Gilbert damping) and the relative Magnus force strength G_{rel} (as tangent of the skyrmion Hall angle). We use $\gamma=1$ in simulation units. As G_{rel} is negligible in our system and furthermore only influences the lattice dynamics but not the static ordering, it is neglected here. The thermal Gaussian white noise $\mathbf{F}_{\text{therm}}$ fulfils the fluctuation-dissipation theorem at a simulation unit temperature of $k_{\text{B}}T=1$. \mathbf{F}_{SkSk} and $\mathbf{F}_{\text{SkBnd}}$ represent the repulsive skyrmion-skyrmion and skyrmion-boundary interaction. For the skyrmion-skyrmion interaction, a $V(r)=r^{-8}$ is used (cutoff distance of 1.8 simulation units²²), which has been demonstrated to match the experimental system^{8,20}. This skyrmion interaction potential has previously been determined in a very similar material stack by using Iterative Boltzmann Inversion (IBI)²⁰ without assuming any general form of the potential. The exact potential form used in this manuscript was however not determined from the conducted measurements presented here but in a less dense skyrmion liquid, as high density lattices generally lead to artefacts in the IBI²⁰. In general, the skyrmion-skyrmion interaction in this system can be well described by both exponential and power-law forms since the potential within the cutoff radius is sufficiently steep. Choosing the power-law potential has the advantage that this form is widely studied in theory and allows comparison to previous works^{8,20,22}. For the skyrmion-boundary interaction, we use a fully repulsive Lennard-Jones potential

$$V_{\text{LJ}}(r) = 4\epsilon \left[\left(\frac{\sigma}{r}\right)^{12} - \left(\frac{\sigma}{r}\right)^6 + \frac{1}{4} \right] \quad (\text{S2})$$

with $r_{\text{cut}}=2^{1/6}$ and $\varepsilon=\sigma=1$. We simulate systems of different skyrmion densities (see Fig. S3) by varying the spacing between skyrmions and set the density ρ as the number of skyrmions per squared simulation unit length. With an Euler algorithm

$$\mathbf{r}(t + \Delta t) = \mathbf{r}(t) + \mathbf{v}(t)\Delta t \quad (\text{S3})$$

applying a time step of $\Delta t=10^{-4}$ in the *HOOMD-blue* software package²³, we determine the equation of motion.

The system is initialized with a square lattice and equilibrated for 10^6 steps before running for 10^7 steps with the trajectory saved every 10^4 steps. Three independent equilibrations runs lead to 3×1000 saved position arrays (of all the 400 skyrmions) for every geometry.

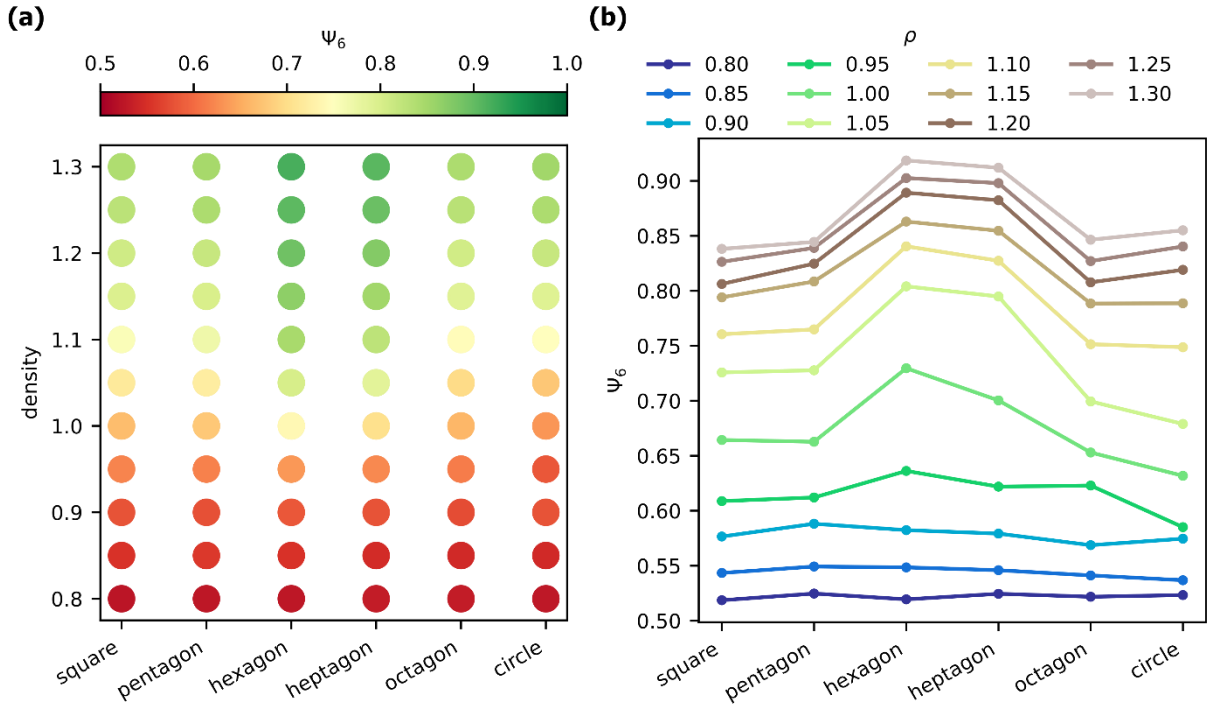


Fig. S3. Average local order Ψ_6 for Thiele model simulations of 400 skyrmions at different density ρ and for different confinement geometries. **(a)** The resulting average value of Ψ_6 is presented as color-code for the different densities and confinement geometries. **(b)** The identical average values of Ψ_6 are now alternatively plotted for the different shapes (lines as guide to eye) where the color of the individual lines denotes the density ρ .

References

- ¹ I. Dzyaloshinsky, "A thermodynamic theory of 'weak' ferromagnetism of antiferromagnetics," *J. Phys. Chem. Solids* **4**(4), 241–255 (1958).
- ² T. Moriya, "Anisotropic Superexchange Interaction and Weak Ferromagnetism," *Phys. Rev.* **120**(1), 91–98 (1960).
- ³ J. Zázvorka, F. Jakobs, D. Heinze, N. Keil, S. Kromin, S. Jaiswal, K. Litzius, G. Jakob, P. Virnau, D. Pinna, K. Everschor-Sitte, L. Rózsa, A. Donges, U. Nowak, and M. Kläui, "Thermal skyrmion diffusion used in a reshuffler device," *Nat. Nanotechnol.* **14**(7), 658–661 (2019).
- ⁴ T. Bhatnagar-Schöffmann, A. Kovács, R. Pachat, D. Ourdani, A. Lamperti, M.-A. Syskaki, T. da Câmara Santa Clara Gomes, Y. Roussigné, S. Ono, J. Langer, M. Cherif, R.E. Dunin-Borkowski, P. Schöffmann, D. Ravelosona, M. Belmeguenai, A. Solognac, and L. Herrera Diez, "Controlling interface anisotropy in CoFeB/MgO/HfO₂ using dusting layers and magneto-ionic gating," *Appl. Phys. Lett.* **122**(4), 042402 (2023).
- ⁵ N. Kerber, M. Weißenhofer, K. Raab, K. Litzius, J. Zázvorka, U. Nowak, and M. Kläui, "Anisotropic Skyrmion Diffusion Controlled by Magnetic-Field-Induced Symmetry Breaking," *Phys. Rev. Applied* **15**(4), 044029 (2021).
- ⁶ R. Gruber, J. Zázvorka, M.A. Brems, D.R. Rodrigues, T. Dohi, N. Kerber, B. Seng, M. Vafaei, K. Everschor-Sitte, P. Virnau, and M. Kläui, "Skyrmion pinning energetics in thin film systems," *Nat. Commun.* **13**(1), 3144 (2022).
- ⁷ D.R. Rodrigues, A. Abanov, J. Sinova, and K. Everschor-Sitte, "Effective description of domain wall strings," *Phys. Rev. B* **97**(13), 134414 (2018).
- ⁸ R. Gruber, J. Rothörl, S.M. Fröhlich, M.A. Brems, F. Kammerbauer, M.-A. Syskaki, E.M. Jefremovas, S. Krishnia, A. Sudbø, P. Virnau, and M. Kläui, "Real-time observation of topological defect dynamics mediating two-dimensional skyrmion lattice melting," *Nat. Nanotechnol.* **20**(10), 1405–1411 (2025).
- ⁹ R. Gruber, M.A. Brems, J. Rothörl, T. Sparmann, M. Schmitt, I. Kononenko, F. Kammerbauer, M.-A. Syskaki, O. Farago, P. Virnau, and M. Kläui, "300-Times-Increased Diffusive Skyrmion Dynamics and Effective Pinning Reduction by Periodic Field Excitation," *Adv. Mater.* **35**(17), 2208922 (2023).
- ¹⁰ K. Leutner, T.B. Winkler, R. Gruber, R. Frömter, J. Güttinger, H. Fangohr, and M. Kläui, "Skyrmion automotion and readout in confined counter-sensor device geometries," *Phys. Rev. Appl.* **20**(6), 064021 (2023).
- ¹¹ E.M. Jefremovas, K. Leutner, M.G. Fischer, J. Marqués-Marchán, T.B. Winkler, A. Asenjo, J. Sinova, R. Frömter, and M. Kläui, "The role of magnetic dipolar interactions in skyrmion lattices," *Newton* **1**(2), (2025).
- ¹² K. Zeissler, S. Finizio, C. Barton, A.J. Huxtable, J. Massey, J. Raabe, A.V. Sadovnikov, S.A. Nikitov, R. Brearton, T. Hesjedal, G. van der Laan, M.C. Rosamond, E.H. Linfield, G. Burnell, and C.H. Marrows, "Diameter-independent skyrmion Hall angle observed in chiral magnetic multilayers," *Nat. Commun.* **11**(1), 428 (2020).
- ¹³ R. Zivieri, R. Tomasello, O. Chubykalo-Fesenko, V. Tiberkevich, M. Carpentieri, and G. Finocchio, "Configurational entropy of magnetic skyrmions as an ideal gas," *Phys. Rev. B* **99**(17), 174440 (2019).
- ¹⁴ D.B. Allan, T. Caswell, N.C. Keim, C.M. van der Wel, and R.W. Verweij, "soft-matter/trackpy: v0.6.4," (2024).
- ¹⁵ J.L. Finney, and J.D. Bernal, "Random packings and the structure of simple liquids. I. The geometry of random close packing," *Proc. R. Soc. A* **319**(1539), 479–493 (1997).
- ¹⁶ J. Zázvorka, F. Dittrich, Y. Ge, N. Kerber, K. Raab, T. Winkler, K. Litzius, M. Veis, P. Virnau, and M. Kläui, "Skyrmion Lattice Phases in Thin Film Multilayer," *Adv. Func. Mater.* **30**(46), 2004037 (2020).
- ¹⁷ J.M. Kosterlitz, and D.J. Thouless, "Long range order and metastability in two dimensional solids and superfluids. (Application of dislocation theory)," *J. Phys. C: Solid State Phys.* **5**(11), L124 (1972).
- ¹⁸ J.M. Kosterlitz, and D.J. Thouless, "Ordering, metastability and phase transitions in two-dimensional systems," *J. Phys. C: Solid State Phys.* **6**(7), 1181–1203 (1973).
- ¹⁹ A.A. Thiele, "Steady-State Motion of Magnetic Domains," *Phys. Rev. Lett.* **30**(6), 230–233 (1972).

- ²⁰ Y. Ge, J. Rothörl, M.A. Brems, N. Kerber, R. Gruber, T. Dohi, M. Kläui, and P. Virnau, “Constructing coarse-grained skyrmion potentials from experimental data with Iterative Boltzmann Inversion,” *Commun. Phys.* **6**(1), 1–6 (2023).
- ²¹ M.A. Brems, T. Sparmann, S.M. Fröhlich, L.-C. Dany, J. Rothörl, F. Kammerbauer, E.M. Jefremovas, O. Farago, M. Kläui, and P. Virnau, “Realizing Quantitative Quasiparticle Modeling of Skyrmion Dynamics in Arbitrary Potentials,” *Phys. Rev. Lett.* **134**(4), 046701 (2025).
- ²² S.C. Kapfer, and W. Krauth, “Two-Dimensional Melting: From Liquid-Hexatic Coexistence to Continuous Transitions,” *Phys. Rev. Lett.* **114**(3), 035702 (2015).
- ²³ J.A. Anderson, J. Glaser, and S.C. Glotzer, “HOOMD-blue: A Python package for high-performance molecular dynamics and hard particle Monte Carlo simulations,” *Comput. Mater. Sci.* **173**, 109363 (2020).

9.2. Additional Results and Experimental Remarks

9.2.1. Map of Confinement Geometries

The sample FAB435p (labbook database ID 2168), used for the experiments presented in section 9.1 and section 10.1, contains a wide range of confinement geometries patterned via EBL. An overview of the labeled structures is shown in Fig. 9.1.

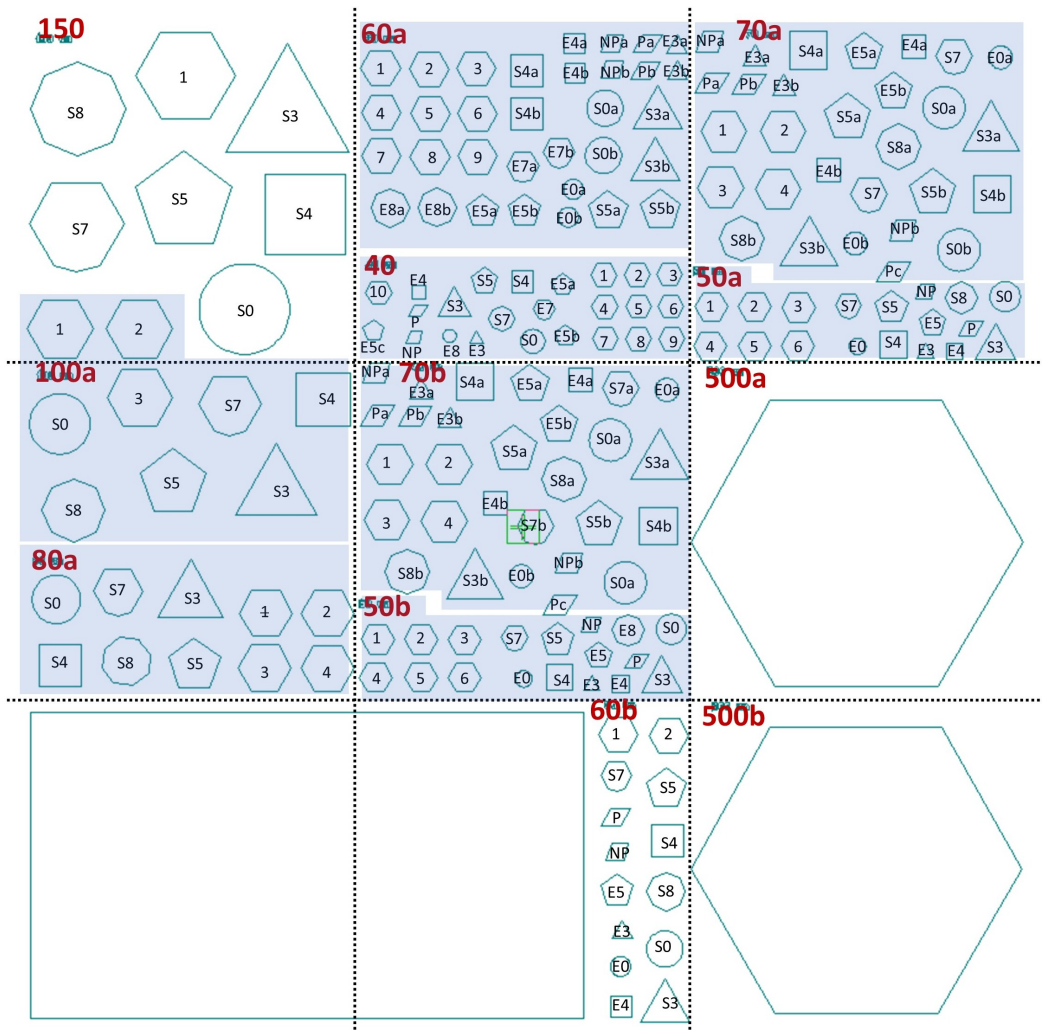


Figure 9.1.: Pattern Map of Sample FAB435p. Map of the geometric confinement patterns on sample FAB435p (labbook database ID 2168). The turquoise layout reflects the underlying EBL design created by Elizabeth M. Jefremovas. The red and black labels, as well as the blue-shaded areas serve to better distinguish the different geometries in this visualization.

The pattern set includes regular geometries such as triangles ("3"), squares ("4"), pentagons ("5"), hexagons ("6" or unlabeled), octagons ("8"), and circles ("0"), as well as irregular or less conventional shapes, including heptagons ("7"), symmetric parallelograms ("P"), and non-symmetric trapezoids ("NP"). The abbreviations in parentheses correspond to the labels used to distinguish between the different confinement types. The irregular heptagon ("7") is derived from a regular hexagon, with one edge modified by a kink offset of 15° . Each geometry is realized in multiple sizes. Notably, hexagons with an edge length of $100\ \mu\text{m}$ are labeled "100". Geometries of equal *area* to this reference hexagon are labeled "100S", while those sharing the same *edge length* are denoted "100E". To uniquely identify multiple instances of the same geometry, an additional alphanumeric suffix (e.g., "a2") is appended. For example, "100S4a2" refers to a square ("4") with the same area as the $100\ \mu\text{m}$ hexagon ("100S"), assigned to subgroup "a" and representing its second instance. The precise confinement geometry employed in each measurement is documented in the corresponding *eLabFTW* [158] labbook entry.

Not all confinement instances are equally effective in supporting skyrmion lattice formation. Strong pinning centers or edge roughness frequently suppress lattice ordering. Among all tested structures, the hexagonal confinement labeled "100a2" consistently produced the most well-ordered skyrmion lattices. In contrast, triangular confinements of comparable area – which, in principle, are also commensurate with a hexagonal lattice – exhibit defects such as surface scratches that hinder the formation of ordered configurations. Fig. 9.2 shows the best lattice order I have managed to stabilize in the triangular confinement.

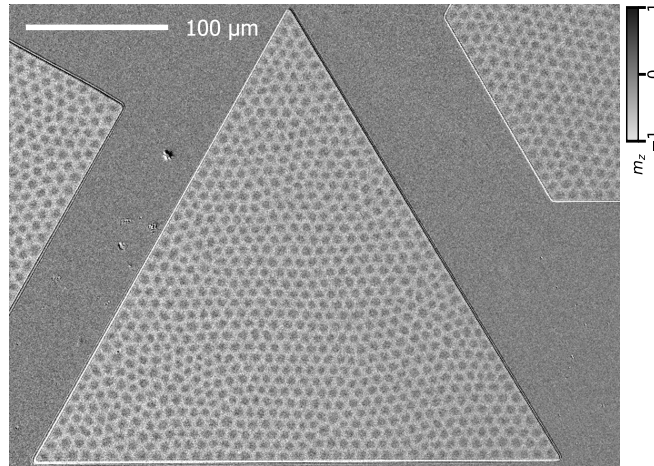


Figure 9.2.: Skyrmion Lattice in Triangular Confinement. The triangular confinement has the same area as the hexagon with $100\ \mu\text{m}$ edge length and is also commensurate with the hexagonal lattice. However, I have never reached equally good lattice order in the triangular confinement. This skyrmion lattice is the best ordered I have managed in the triangle with $\Psi_6 = 0.83$, compared to regular observations of $\Psi_6 > 0.9$ in the hexagonal structures.

9.2.2. Stabilizing Skyrmions in Confinement

To nucleate skyrmion lattices within confinement geometries, I apply both OOP and IP magnetic fields, as outlined in section 1.2.3. However, the optimal OOP field for achieving a well-ordered lattice often differs from the field strength that maximizes the overall skyrmion population – i.e., the condition favorable for nucleating a dense skyrmion ensemble. Additionally, the effect of geometric confinement on the magnetic behavior plays a significant role in stabilizing skyrmions [159].

Generally, elevated temperatures are required to stabilize skyrmion configurations within confinement such that they resemble those found in extended (unconfined) regions. This temperature dependence becomes increasingly relevant as the lateral dimensions of the confinement are reduced [160, 161].

All measurements discussed in chapter 9 are performed on the same physical sample piece and at a constant temperature of 333.5 K (■ labbook experiment ID 7155). At this scale, the confinement geometries are sufficiently large such that the intrinsic magnetic properties of the material remain largely unaffected – at the same temperature, the behavior of the skyrmion lattices is equivalent to that in the continuous film.

In contrast, for smaller confinements, a moderate increase in temperature – typically a few kelvin – is necessary to achieve a comparable level of skyrmion stability and ordering. For example, I have successfully stabilized skyrmion lattices in smaller hexagonal confinements with an edge length of only 80 μm (■ labbook experiment ID 7886). There, lattice configurations of comparable quality to those in the 100 μm hexagon can be achieved, but only at elevated temperatures of approximately 338 K. Representative images of these lattices are shown in Fig. 9.3.

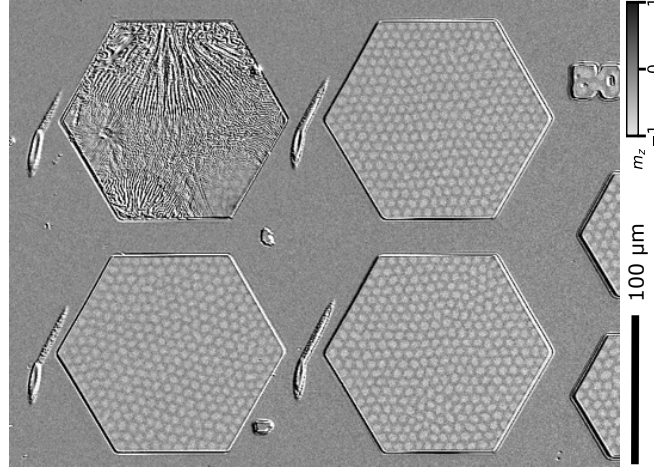


Figure 9.3.: Skyrmion Lattices in a Smaller Hexagon. The four hexagons with $80\ \mu\text{m}$ edge length labeled 80a 1-4 according to Fig. 9.1 host well-ordered skyrmion lattices at 338 K with values of Ψ_6 up to 0.90. The grayscale contrast represents a measure for the OOP magnetization. The first hexagon is still covered by a resist, which was not washed away during development of the pattern.

Due to the smaller confinement area, fewer skyrmions are present in the system, and the boundaries exert a stronger relative influence on the overall lattice configuration. As a result, it is somewhat easier to achieve a high degree of lattice order than in the $100\ \mu\text{m}$ case. However, the significantly reduced number of skyrmions (approximately 330 instead of 400) leads to poorer statistical reliability in the computation of correlation functions. In particular, the statistics at intermediate length scales – around 10 nearest neighbor distances – are notably suppressed. This range is critical for determining 2D phase behavior; therefore, the larger hexagonal confinement provides more robust and informative insights. Furthermore, smaller systems are generally more susceptible to boundary effects, as discussed in section 10.1.1.

9.2.3. Treatment of Skyrmions Along the System Edge

Skyrmions located along the system boundary define the geometric limits of the lattice and play a critical role when the lattice is subject to confinement. These edge skyrmions typically possess fewer than six nearest neighbors, which is reflected in a locally reduced order parameter. Consequently, I exclude them from the order analysis and do not classify them as topological defects.

To isolate skyrmions within the confined region from the outset, I apply a masking procedure to each frame of the Kerr microscopy video sequences. This masking sets all pixels outside the confinement geometry to a constant intensity value. Careful masking also ensures that intensity discontinuities at the system boundary – caused by topographic features of the pattern or residual background drift following image subtraction – are effectively suppressed. If not masked, these sharp gradients

frequently lead to false detections or obscure true skyrmion signatures. Fig. 9.4 compares a raw Kerr image with its corresponding masked version to illustrate the effectiveness of the procedure.

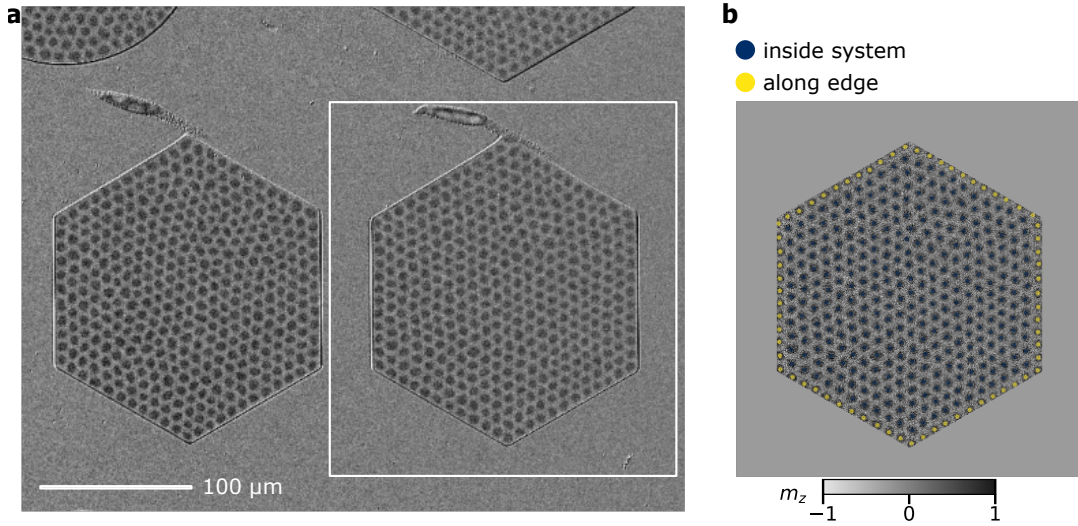


Figure 9.4.: Confinement Masking and Edge Detection. (a) Skyrmion lattices in two neighboring hexagonal structures. The grayscale contrast represents a measure for the OOP magnetization (b) For the skyrmion detection, the relevant image part (here: white box in (a)) is first masked with uniform gray color to cover the confinement edge and the region outside. Depending on the angles between neighboring skyrmions, particles along the edge (yellow) and inside the system (blue) can be distinguished.

To identify which skyrmions reside along the edge, I first detect all skyrmions and compute their local environment using a Voronoi tessellation [162]. This tessellation provides information on neighbor connectivity and allows determination of angles between adjacent neighbor bonds. At the system edge, the lack of a complete hexagonal neighborhood typically results in at least one unusually large angular separation between neighboring skyrmions. I label a skyrmion as an edge skyrmion if it exhibits at least one inter-neighbor angle exceeding 100° . Empirically, this threshold offers a reliable compromise: smaller angles can occur in the lattice interior and may lead to false positives, whereas higher thresholds risk overlooking genuine edge cases, particularly where skyrmions are misaligned with the confinement boundary.

Although this angular criterion provides a good initial estimate, it is not fully robust. Therefore, I impose an additional constraint: a skyrmion is only confirmed as being at the edge if it has at least two neighbors that are also preliminarily identified as edge skyrmions. This second condition improves the stability of edge labeling by enforcing spatial continuity along the system boundary.

Fig. 9.4b visualizes the outcome of this classification, where yellow and blue dots indicate skyrmions that are and are not identified as edge particles, respectively, thereby demonstrating the effectiveness and robustness of the combined detection

method.

9.3. Author Contributions

I performed all the experiments at the Kerr microscope on my own. The majority of the data analysis shown here was done by me and I also developed the used Python code. I specifically performed the skyrmion detection using *trackpy* [132], calculated the Voronoi tessellation, neighbor connections, local order parameter and correlation functions. I also introduced the orientation gradient to identify domain boundaries. I was provided with existing code for the analysis of ψ_6 and G_6 by Jan Rothörl. I used this code as basis to rewrite the analysis from scratch to optimize robustness, efficiency. Jan Rothörl and Simon M. Fröhlich also developed their code further and we used the two independent code sets to validate our results. Particularly, Simon and Jan always calculated ψ_6 independently for the simulation data.

The simulations in this project were all conducted by Jan Rothörl with the support of Simon M. Fröhlich and Maarten A. Brems. Jan Rothörl and Simon M. Fröhlich also developed their analysis code further and we used the two independent code sets to validate our results. Particularly, Simon and Jan always calculated ψ_6 independently for the simulation data.

The magnetic multilayer sample was deposited by Fabian Kammerbauer, the patterning of the geometric confinements was done by Elizabeth M. Jefremovas. However, I also used samples grown by Maria-Andromachi Syskaki while encountering the reported effect and while gathering data to design the final experiment.

Sachin Krishnia and Elizabeth M. Jefremovas especially helped me in developing the experiment, the data interpretation and writing the article during frequent discussions in their function as postdoctoral researchers.

Asle Sudbø, Peter Virnau and Mathias Kläui supervised and guided this work. Peter Virnau and Mathias Kläui contributed as PhD supervisors and principal investigators in our skyrmion research group and provided advice in regular discussions.

10. Real-Time Observation of Topological Defect Dynamics Mediating 2D Skyrmion Lattice Melting

10.1. Published Article

Publication Information


The following article is published in *Nature Nanotechnology*:

Real-Time Observation of Topological Defect Dynamics Mediating 2D Skyrmion Lattice Melting

Raphael Gruber, Jan Rothörl, Simon M. Fröhlich, Maarten A. Brems, Fabian Kammerbauer, Maria-Andromachi Syskaki, Elizabeth M. Jefremovas, Sachin Krishnia, Asle Sudbø, Peter Virnau & Mathias Kläui

Nature Nanotechnology **20**, 1405-1411 (2025).

DOI: [10.1038/s41565-025-01977-2](https://doi.org/10.1038/s41565-025-01977-2)


Copyright Information:  CC BY 4.0 Creative Commons Attribution 4.0 International License

Editorial Note: The blue header/footer bars were added for inclusion in this dissertation and are not part of the original publication.

Contributions

The author contributions for this project and article are described in detail in section 10.3.

Experimental Note

Documentation of my experiments used for this article are available for lab members on *eLabFTW* ( labbook database ID [5832](#)).



Real-time observation of topological defect dynamics mediating two-dimensional skyrmion lattice melting

Received: 19 December 2024

Accepted: 17 June 2025

Published online: 04 August 2025

Check for updates

Raphael Gruber¹, Jan Rothörl¹, Simon M. Fröhlich¹, Maarten A. Brems¹, Fabian Kammerbauer¹, Maria-Andromachi Syskaki^{1,2}, Elizabeth M. Jefremovas¹, Sachin Krishnia¹, Asle Sudbø³, Peter Virnau¹ & Mathias Kläui^{1,3} ✉

Topological defects are the key feature mediating two-dimensional phase transitions. However, both resolution and tunability have been lacking to access the dynamics of these transitions in the various two-dimensional systems explored. Skyrmions in magnetic thin films are two-dimensional, topologically non-trivial quasi-particles that provide rich dynamics as well as tunability as an essential ingredient for the control of their phase behaviour. With dynamic Kerr microscopy, we directly capture the melting of a confined two-dimensional magnetic skyrmion lattice in a Ta/CoFeB/Ta/MgO/Ta magnetic multilayer system with high resolution in real time and real space. By the applied magnetic field, we tune the skyrmion size and effective temperature on the fly to drive the two-step melting through an intermediate hexatic regime between the solid lattice and the isotropic liquid. We quantify the characteristic occurrence of topological defects mediating the transitions and reveal the dynamics of the lattice dislocations. The full real-time and real-space imaging reveals the diffusion coefficient of dislocations, which is two orders of magnitude higher than that of skyrmions.

Magnetic skyrmions are topologically non-trivial chiral spin structures exhibiting quasi-particle behaviour^{1–3}. Besides being ideal candidates for low-power applications in data storage and processing^{4–13}, skyrmions hosted in nanometre-thin films³ are a flexible model system for studying two-dimensional (2D) system properties^{14–16}, particularly 2D phase transitions.

The Kosterlitz–Thouless–Halperin–Nelson–Young (KTHNY) theory^{17–21} describes 2D melting from a solid with translational quasi-long-range order (QLRO) to a disordered, isotropic liquid in two steps via an intermediate hexatic phase with orientational QLRO only. The two KTHNY phase transitions are associated with the unbinding and proliferation of pairs of topological defects of the lattice and have been observed in several systems and experiments, including

colloids^{22,23}, superconducting vortices^{24,25} and skyrmions^{14,26,27}. However, in all these previous experimental investigations, resolution^{14,15,24,25} or tunability^{15,22,23,27} of the system have been insufficient to drive the system through phase transitions and elucidate the dynamics of melting, including the defect evolution in real time and real space.

Skyrmions in Ta/CoFeB/Ta/MgO magnetic thin films form 2D lattices with their purely repulsive interaction potentials^{28–30}, exhibiting rich Brownian dynamics^{7,31,32} and providing the required tunability of size and diffusivity^{7,32–34} to control transitions on the fly. Additionally, in Kerr microscopy, their dynamics is directly accessible in real time and real space, which is challenging in many other techniques^{14,15}. However, pinning effects in the form of a non-flat-energy landscape in the magnetic multilayers have hampered the formation of QLRO

¹Institute of Physics, Johannes Gutenberg-Universität Mainz, Mainz, Germany. ²Singulus Technologies AG, Kahl am Main, Germany. ³Center for Quantum Spintronics, Department of Physics, Norwegian University of Science and Technology, Trondheim, Norway. ✉e-mail: klaui@uni-mainz.de

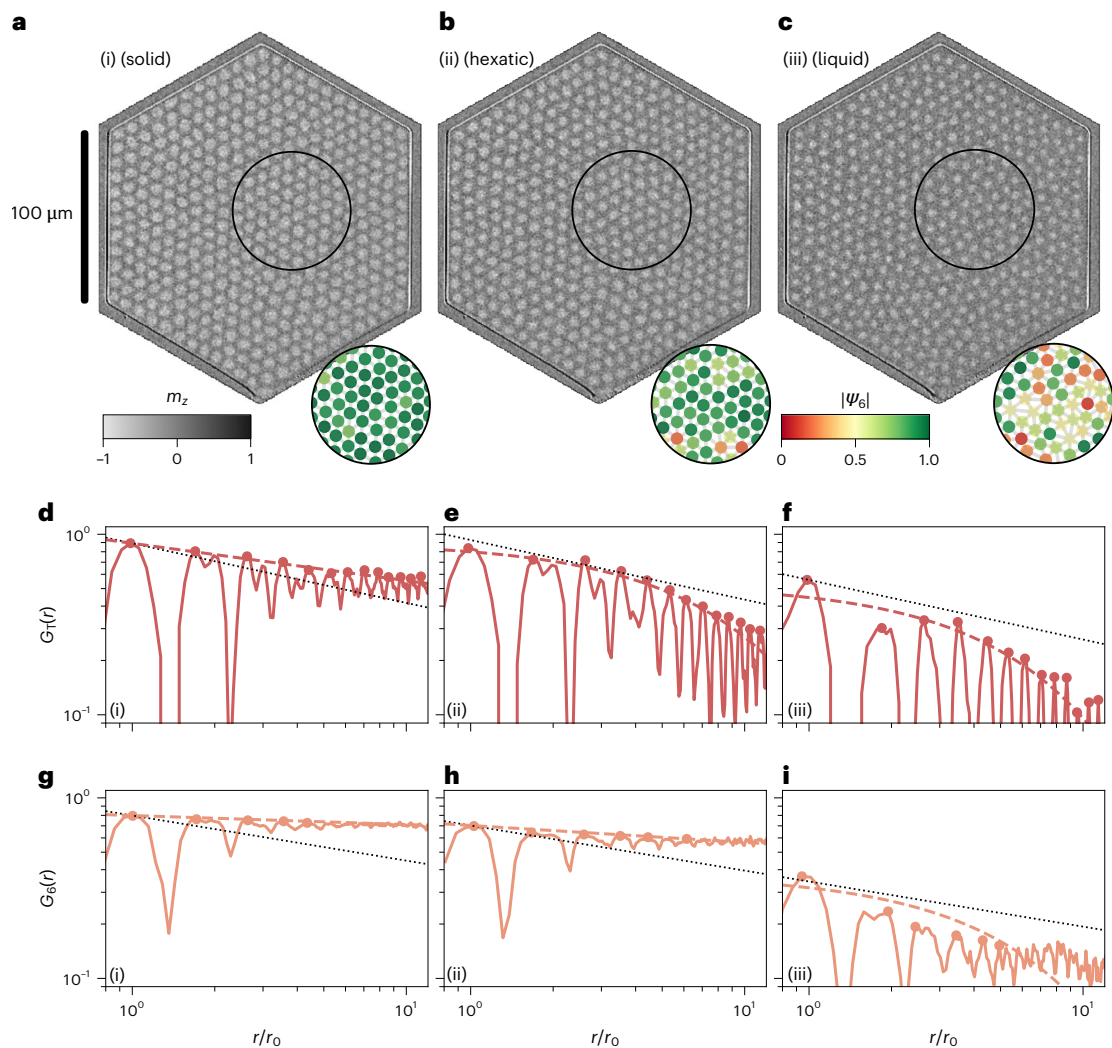


Fig. 1 | Skyrmion lattices with different order. **a–c**, Kerr microscopy images of 401 skyrmions comprising lattices in hexagonal geometric confinement: snapshots (i)–(iii) at 60 μT (**a**), 84 μT (**b**) and 114 μT (**c**); grayscale contrast represents the OOP magnetization m_z . The insets visualize the local order parameter $|\psi_6|$ per skyrmion in the black circle. **d–f**, Translational correlation functions $G_T(r)$ as a function of distance r in units of nearest-neighbour distances r_0 . The dashed line represents the power-law (**d**) and exponential (**e** and **f**) envelope fits for snapshots (i)–(iii), and the dots are fitted points. The dotted

black line is the power law with the critical exponent $\eta_T = 1/3$ for reference. Although the data in **d** decay algebraically with an exponent smaller than 1/3, the data in **e** and **f** decay exponentially. **g–i**, Analogous orientational correlation functions $G_6(r)$ as a function of distance r/r_0 (solid orange line), envelope fit (dashed line) and fitted points (dotted line) for snapshots (i)–(iii). The dotted black line represents the power law with critical exponent $\eta_6 = 1/4$. Although the data in **g** and **h** exhibit power-law behaviour with η_6 smaller than 1/4, the data in **i** yields a faster decay.

of skyrmion lattices^{15,16,26,35,36}. Therefore, for sufficiently low pinning, the structural disorder may be small enough to allow for translational order and enhancing the phase space of the hexatic phase^{26,35}, enabling better feasibility to study the phases and transitions.

In this study, we exploit the on-the-fly tunability of our 2D skyrmion lattice to melt the system to disorder in a two-step process using two independent methods: (1) by shrinking the skyrmions and reducing the packing fraction and (2) by increasing the skyrmions' diffusivity corresponding to an effective temperature. We stabilize the skyrmion lattice in a low-pinning Ta/CoFeB/Ta/MgO magnetic thin-film stack^{7,33,34} at 333.5 K using hexagonal geometric confinement providing commensurate boundary conditions³⁷ for the lattice formation, and we identify the two-step melting by spatial and time correlation functions. With high-resolution Kerr microscopy in real time and real space, we capture the topological defect dynamics and find that the diffusion coefficient of dislocations is two orders of magnitude larger than that of skyrmions. Therefore, the rich dynamics of the system yields powerful insights into the formation and dissociation of topological defects, which is the key feature mediating the

melting transitions in two dimensions—but has so far been experimentally inaccessible.

Two-step skyrmion lattice melting

We stabilize a skyrmion lattice in a hexagonal geometric confinement of 100- μm edge length in a Ta(5 nm)/Co₂₀Fe₆₀B₂₀(0.9 nm)/Ta(0.07 nm)/MgO(2 nm)/Ta(5 nm) stack. We observe the skyrmions in real time and real space with Kerr microscopy⁷ (Supplementary Video 1)³⁸. In Fig. 1a–c, we show Kerr microscopy snapshots (i)–(iii) at different magnetic out-of-plane (OOP) field, which controls the skyrmion size^{33,39,40} and, thus, the packing fraction.

We determine the local order parameter ψ_6 (Fig. 1a–c, insets) and calculate the translational (Fig. 1d–f) and orientational (Fig. 1g–i) correlation functions to analyse the ordering. We fit the correlation functions $G_T(r)$ and $G_6(r)$ with a power-law decay, yielding exponents η_T and η_6 , respectively. Furthermore, we perform an exponential fit to determine the corresponding correlation lengths ξ_T and ξ_6 (Methods). Despite our finite system, we use the terms solid, hexatic and liquid measured in analogy to the KTHNY theory to distinguish between the different regimes.

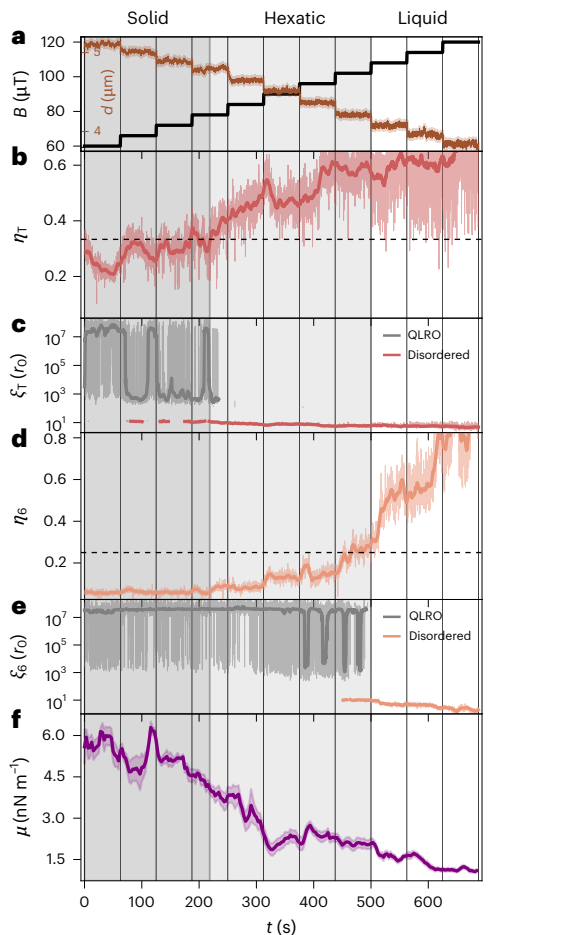


Fig. 2 | Time-resolved quantification of the melting. **a**, The applied magnetic field B (black) is increased stepwise, directly causing the skyrmion diameter d (brown, average and standard deviation) to decrease. The vertical black lines delimit the intervals of constant OOP fields in all panels. **b**, Exponent η_T of G_T and rolling mean over 6.25 s. The dashed horizontal line marks the critical exponent of $1/3$. **c**, Correlation length ξ_T of G_T and rolling median over 6.25 s. ξ_T is well beyond the system size in the critical (QLRO) regime (grey) and within the system size in the disordered regime (red). **d**, Exponent η_6 of G_6 and rolling mean over 6.25 s. The dashed horizontal line marks the critical exponent of $1/4$. **e**, Correlation length ξ_6 of G_6 and rolling median over 6.25 s for the QLRO (grey) and disordered (orange) regimes. The dark-grey, light-grey and white backgrounds represent the solid, hexatic and liquid regimes, respectively. **f**, Shear modulus μ of the skyrmion lattice determined from fitting the local lattice deformations on a logarithmic scale. Fit (solid line) and standard deviation of the fit (shaded area) are shown for sliding window averages over 6.25 s (100 frames).

For the densely packed skyrmions in snapshot (i), the translational correlation $G_T(r)$ decays algebraically with an exponent η_T smaller than $1/3$. The orientational correlation $G_6(r)$ is almost constant. Hence, the system exhibits translational and orientational orders, which we identify as solid. For snapshot (ii), $G_T(r)$ decays exponentially, whereas $G_6(r)$ is still decaying algebraically with an exponent η_6 smaller than $1/4$. Thus, the translational order has vanished, whereas the orientational order persists; we identify this as hexatic. In snapshot (iii), both $G_T(r)$ and $G_6(r)$ decay faster with the critical exponent; therefore, we classify this unordered state as liquid.

Finite-size effects occurring for the correlation functions, such as deviations for larger distances and the unclear exponential behaviour for snapshot (iii) (Fig. 1i) are described in Supplementary Note 1 and Supplementary Fig. 1. Furthermore, in the Thiele model simulations, we see that hexagonal confinements indeed stabilize ordering, particularly

for smaller systems and with commensurability (Supplementary Note 2 with Supplementary Fig. 2). Regarding the qualitative processes and critical exponents, however, neither simulations nor experiments appear to be affected noticeably by finite-size effects. Therefore, we use the confinement for lattice stabilization and preventing local pinning centres from macroscopically hampering the lattice order^{15,16,26}. Therefore, we reveal intrinsic effects and dynamics during a two-step melting expected from the KTHNY theory.

In contrast to other systems in which 2D phases have been observed^{14,15,22}, our system is highly flexible in the sense that we can tune the skyrmions' size^{31,33} and mobility³⁴ on the fly by the OOP magnetic field, in addition to the thermal Brownian-like diffusion⁷. Together with direct real-time observation in Kerr microscopy, this allows for a full real-time and real-space analysis of the dynamics associated with 2D phase transitions and critical phenomena, which have not been revealed in other systems. In the following, we perform the time-resolved quantitative analysis of the observed melting.

Real-time quantification of the melting

To capture the full melting process, we stepwise increase the magnetic field to shrink the skyrmions and, thus, reduce their packing fraction. We observe the evolution of lattice order—disorder emerging from the field steps and fluctuations in the intervals of constant field—to fully capture the melting dynamics in a quasi-equilibrium process (Methods). In Fig. 2a, we visualize the OOP field (black) and the corresponding skyrmion diameter (brown). The black vertical lines represent the times at which the field changes in all panels. Since the shrinking skyrmions have effectively more space available, the number of accessible microstates and, thus, the configurational entropy increase, which we exploit to drive the system to disorder.

Figure 2b shows the time evolution of η_T ; the black dotted line marks its critical value of $1/3$. We find that initially, the exponent is below the critical value, signalling translational QLRO, which we identify as the solid regime. After 70 s, the exponent starts fluctuating around the critical value. At around 225 s, after further shrinking steps, η_T permanently exceeds $1/3$. However, the power-law exponent is only well defined in the critical, ordered phase delimited by the critical exponent ($\eta_T = 1/3$), where the decay becomes solely exponential. Figure 2c shows the corresponding correlation length ξ_T . Note that ξ_T must be determined differently for the critical (QLRO) and disordered regimes (Fig. 2c). In the solid regime, we accordingly observe ξ_T being orders of magnitude beyond the system size—effectively corresponding to divergence as predicted by the KTHNY theory^{18,19}, highlighting the quality of the power-law fit. Reaching the critical exponent, the correlation length drops below the system size. Hence, the solid character given by translational QLRO has vanished.

Analogously, we plot η_6 and the associated correlation length ξ_6 (Fig. 2d,e, respectively). We see that η_6 starts well below its critical value of $1/4$ (black dots) in the solid, meaning G_6 is almost constant (in contrast to G_T). At the point where the translational order vanishes, however, the orientational order persists as η_6 still stays below its critical value of $1/4$, which we identify as hexatic. In the hexatic regime, the exponent η_6 grows significantly until reaching $1/4$ eventually, denoting the transition to a liquid. It fluctuates around the critical value after around 450 s and permanently exceeds it after 490 s. We visualize the three determined regimes by the grey shading in Fig. 2.

Since we drive the melting by shrinking the skyrmions with the applied magnetic field, we additionally present the respective data based on the applied magnetic field (Extended Data Fig. 1)—as both time average and time-dependent orientational correlation $G_6(\tau)$ for every field interval, showing good agreement with theory²³.

To further underline the robustness of our analysis, we go beyond the entropy-mediated melting due to skyrmion shrinking and exploit the tunability of our system further to provide a second, independent approach to drive the system across disordering transitions. By

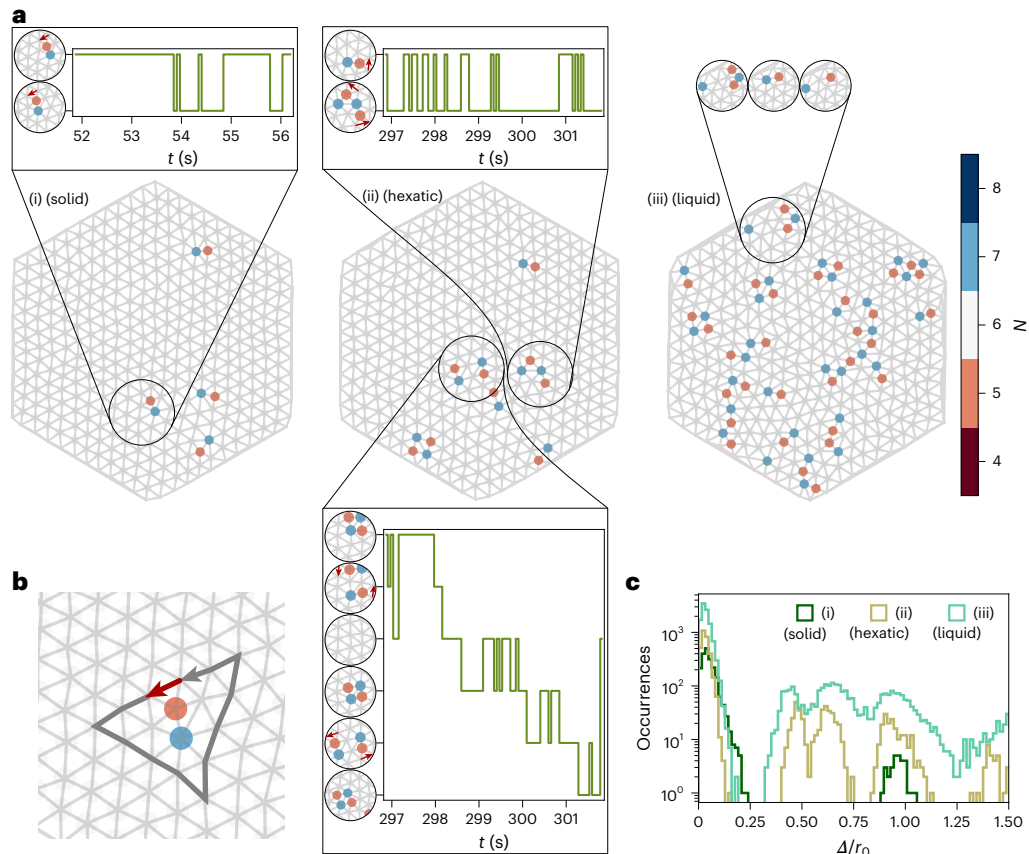


Fig. 3 | Fluctuations of topological defects. **a**, Lattice defects of snapshots (i)–(iii), coloured by the number of lattice neighbours N . Snapshots (i)–(iii) from Fig. 1a–c are used, which correspond to the images of melting shown in Fig. 2 at $t_{(i)} = 50.0$ s, $t_{(ii)} = 301.6$ s and $t_{(iii)} = 576.3$ s, respectively. The grey net shows the nearest-neighbour connections between the experimental skyrmions. The insets show how defect configurations can change between discrete states, and the attached green step plots visualize the fluctuations between those states in

measurement time t . Example Burgers vectors are drawn as red arrows.

b, Four lattice vectors (grey) along each crystal direction would yield a closed path in a perfect lattice. However, to surround a dislocation counterclockwise, an additional lattice vector (red) is missing; it is identified as the Burgers vector.

c, Histogram of dislocation displacements Δ within 62.5 ms (one frame) compared for snapshots (i)–(iii) (using the statistics of 31 s).

magnetic OOP-field oscillations, we increase the diffusivity³⁴ (that is, the effective temperature of the system; Supplementary Video 2)³⁸ and, therefore, induce melting (Extended Data Fig. 2). The results are consistent for the two approaches; however, in the case of field oscillations present, we expect the emergence of non-equilibrium properties due to the permanent driving of the skyrmion size.

Finally, we can even probe the shear modulus μ (refs. 41,42) by analysing local lattice deformations as the characteristic behaviour associated with melting transitions is also exhibited by elastic constants. In Fig. 2f, we show that μ is approximately constant in the solid. When translational QLRO vanishes, μ decreases significantly. However, μ is not vanishing since we must assume linear elasticity in our analysis, which becomes less applicable when reducing the packing fraction. Yet, qualitatively, the resulting shear modulus clearly supports our conclusions. In Extended Data Fig. 3, we present example shear components and their energies.

Hence, we demonstrate that we can drive a finite lattice from solid order to a liquid via the hexatic regime, particularly image the melting process directly with high time resolution. This allows us to access the dynamics of every skyrmion quasi-particle. With the full information of the individual skyrmion trajectories, we can uniquely identify the topological lattice defects and probe their dynamics, which is typically not accessible. The topological defects are the key feature of 2D melting, as described in the KTHNY theory. Therefore, we need to quantify the occurrence and dynamics of those lattice defects to fully understand the transitions.

Topological defects dynamics

The formation and dissociation of topological defects is the key feature of 2D melting in the KTHNY theory. Our system allows us to observe the defect dynamics, gaining insights into the melting process in a unique way. The thermally activated diffusion of skyrmions induces rich dynamics including lattice fluctuations and defect formations on sub-second timescales and dynamic imaging allows us to unambiguously identify the topological defects (Supplementary Video 3). Due to the time resolution of 62.5 ms, we can further analyse the dynamics of the topological defects. In particular, we can tune the dynamics of both skyrmions and defects by the applied magnetic field. We note that previous observations of 2D phase transitions lack sufficient resolution^{14,24} or tunability of order and its fluctuations^{15,22,23,27} to explicitly investigate the defect dynamics.

In Fig. 3a, we present the topological defect map for the previously defined snapshots (i)–(iii). In the dense-packed (solid) snapshot (i), only four dislocations exist. We identify those dislocations as a consequence of the incommensurate number of skyrmions (Supplementary Note 3 and Supplementary Fig. 3), combined with the underlying energy landscape of the sample^{32,33}. These dislocations remain stable and may only hop between the nearest-neighbour sites. An example of such a fluctuating dislocation is shown in the clipped inset connected to the black circle (Fig. 3a). The dislocation fluctuates back and forth between two discrete states. The discrete states are represented on the vertical axis in the black boxes in Fig. 3a, where the green line shows the temporal fluctuation between the states in measurement time t . We

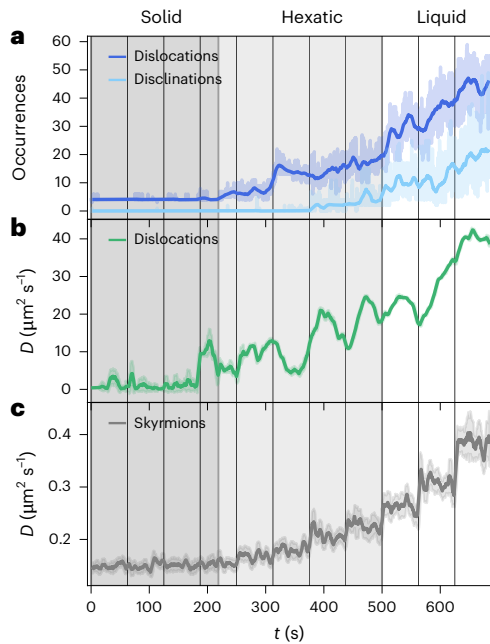


Fig. 4 | Time-resolved defect dynamics. **a**, Number of dislocations and disclinations observed during the melting for each frame (shaded) and a rolling mean over 6.25 s (100 frames). **b, c**, The diffusion coefficient D of the dislocations (**b**) is up to two orders of magnitude larger than the one for skyrmions (**c**). The solid lines represent the mean of the diffusion constant fit for a sliding window of 6.25 s (100 frames); the shaded area denotes the corresponding standard deviation. The dark-grey, light-grey and white backgrounds represent the predetermined solid, hexatic and liquid regimes, respectively.

see that the Burgers vector (red arrows in the insets) associated with the dislocation is preserved when the dislocation hops. An example construction of the Burgers vector is shown in Fig. 3b. In addition to the four dislocations present in the solid, dislocation pairs can form spontaneously and annihilate again within a short time. The dislocation pairs are the characteristic clusters in the solid phase and have opposite Burgers vectors, which cancel out to zero.

In the 5-s time window around the hexatic snapshot (ii), new defects appear and exhibit more dynamics, also indicated in Fig. 3a. In the corresponding inset, the fluctuations between the identified states are showcased as a step function. The top inset shows how a dislocation can rearrange into two dislocations. Indeed, the total Burgers vector is conserved during the rearrangement. Furthermore, the second (bottom) inset for snapshot (ii) reveals how a dislocation pair can be created and annihilated, split up, merge and, therefore, move. These local fluctuations result in at least the six presented states. Note that during the fluctuation, the total Burgers vector is always zero. However, the opposing vectors can change direction as the dislocation pair can split into either two horizontally or two vertically oriented dislocations. By the controlled manipulation of the energy landscape^{43,44}, such fluctuations could, in principle, become deterministic and, thus, transport information rapidly with very low power in specially designed devices. By tailoring the boundary conditions and comparing the skyrmion lattices in distorted hexagons, even topological defect dynamics under shear⁴⁵ could be experimentally explored. The defect interaction potential, however, remains an open question as our limited system size does not provide sufficient statistics.

In the disordered liquid snapshot (iii), the created and constantly rearranging defects form a complex pattern consisting of several defect clusters. The clusters still span dislocations and square dislocation pairs, but also isolated defects, linear defect chains and more complex configurations. The corresponding inset in Fig. 3a shows an example of how a dislocation can split into two disclinations or rearrange into

an isolated defect plus a chain of three defects as a key feature of the liquid regime. Since dislocations and clusters, in general, can rearrange, split and merge in many ways and, therefore, increasingly interact with neighbouring clusters, the number of observed states as well as their dynamics increases drastically. Eventually, the complexity does not allow us anymore to determine specific states and their fluctuations in time within a clipped region only.

This becomes more apparent when we investigate the dynamics of defect pairs. To this purpose, we match all defects into pairs of one $N=5$ and $N=7$ defect (Methods). We consider the nearest-neighbour matches as dislocations (otherwise, disclinations) and link their occurrences to trajectories using trackpy⁴⁶. We provide a detailed visualization of the pair matching in Supplementary Fig. 3, including a more generalized defect clustering in good agreement with previous simulation results⁴⁷. Figure 3c shows the histograms of the found dislocation displacements Δ within 62.5 ms for snapshots (i)–(iii) by using statistics of a total of 31 s around each snapshot. We find that in the solid regime (snapshot (i)), the defects are stable and may only rarely hop by a nearest-neighbour connection r_0 . In the hexatic regime (snapshot (ii)), nearest-neighbour hopping becomes more frequent and displacements different from r_0 occur. The inset of snapshot (ii) (Fig. 3a) may serve as an illustration. The splitting of one dislocation into two causes a displacement of $r_0/2$ due to the associated reorientation, whereas dislocation pairs changing between two horizontal and two vertical pairs contribute with displacements of $\sqrt{r_0}/2$ each. In the liquid regime (snapshot (iii)), an almost continuous distribution of displacements for the identified dislocations arises due to the complex rearrangements and interactions of defect clusters, signalling the unbinding of topological defects.

Our full real-time and real-space analysis allows us to ascertain the quantitative evolution of dislocations and disclinations (Fig. 4a). We find that the occurrence of dislocations (beyond the ones existing initially due to incommensurability and a vacancy) starts as predicted by theory at the transition from solid to hexatic. The occurrence of disclinations starts at the transition from the hexatic to liquid regime, also in good agreement with the KTHNY theory.

Finally, the identification of dislocations as topological quasi-particles throughout the melting process allows us to investigate their dynamics. From the mean squared displacement (MSD) of the dislocations (Supplementary Video 4), we fit the diffusion coefficient D (Methods), as shown in Fig. 4b. We find that for the dislocations, D is almost constant in the solid regime and increases drastically when transitioning from solid to hexatic due to dislocation unbinding. Within the hexatic regime, D continues to increase slightly as fluctuations increase. When entering the liquid regime, D starts increasing drastically again due to complex defect rearrangements. For comparison, we also determine the diffusion coefficient of skyrmions (Fig. 4c). For skyrmions, D increases continuously during melting; however, it does not change its behaviour qualitatively at the found transitions, highlighting the key role of topological defects in mediating melting. As the underlying mechanism, we see that the increasing skyrmion diffusivity due to a reduced packing fraction enables the formation and rearrangement of topological defects, which drastically speeds up the dislocation dynamics. During melting, D for the dislocations becomes up to two orders of magnitude larger than for the skyrmions forming the underlying lattice. This can be explained by the fact that dislocations are second-order (meta-) quasi-particles of the lattice (comprising quasi-particle skyrmions) and can, thus, hop significantly even if skyrmions are only slightly displaced. The fact that the dynamics of topological point defects can exceed the particle dynamics has been previously demonstrated for vacancies and interstitials^{48,49}. Such point defects do not break QLRO and can also occur in our skyrmion lattice. An example of a quadruple vacancy is discussed in Supplementary Note 3. For 2D melting, however, the additional emergence of topological defects and especially the dynamics due to their dissociation is the key ingredient.

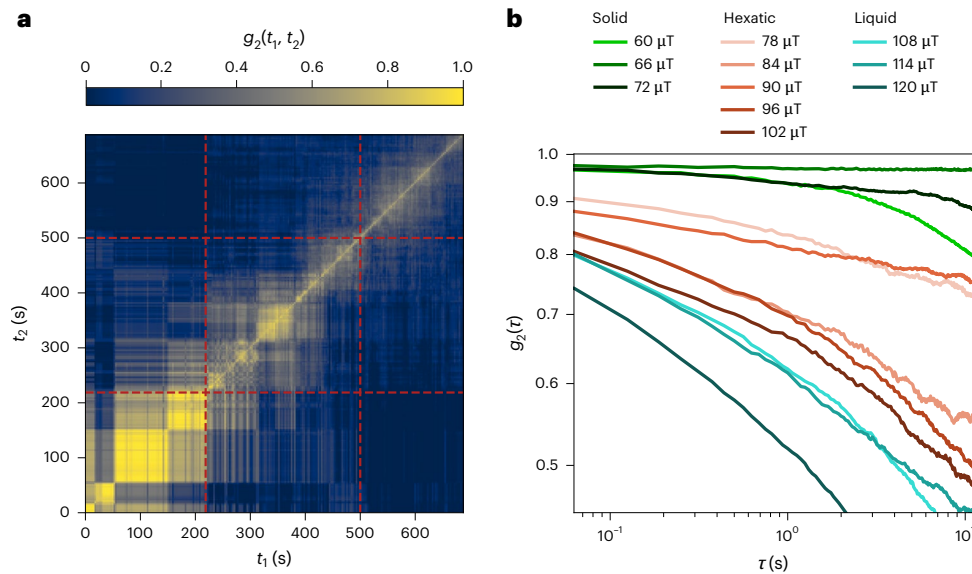


Fig. 5 | Time correlation of defect occurrences. **a**, Two-time correlation map of the Pearson correlation coefficient $g_2(t_1, t_2)$ correlating the defect occurrences of times t_1 and t_2 per skyrmion. The red dashed lines indicate the previously determined transitions from solid to hexatic and hexatic to liquid. The correlation generally decreases over time, with steps at the transitions.

b, One-time correlation function $g_2(\tau)$ as a function of delay $\tau = t_2 - t_1$ for every magnetic-field interval of 62.5-s (1,000-frame) length. For increasing field throughout melting, $g_2(\tau)$ decays faster, corresponding to an enhanced dynamics of topological defects.

Although dislocation identification and tracking work generally well until deep in the hexatic regime, they become increasingly unstable at the onset of the liquid regime (Methods). Therefore, we also provide a different approach to access the defect dynamics by assessing the time correlation g_2 of defect occurrences per skyrmion at times t_1 and t_2 (refs. 50–52) in Fig. 5 (Methods). As g_2 decays increasingly fast throughout melting, we corroborate that the dynamics of defects keeps increasing—also throughout the liquid regime.

Conclusions

In conclusion, we find the on-the-fly tunability of our system to be key to provide two unique and independent methods to controllably drive a 2D skyrmion lattice to disorder via a hexatic regime. We exploit a developed geometric confinement to locally stabilize the lattice, allowing us to capture the full intrinsic dynamics. Due to the rich dynamics and flexibility, real-time and real-space Kerr microscopy yields the necessary insights to understand the 2D melting process. We capture the emergence and dynamics of the characteristic topological defects mediating the phase transitions in the KTHNY theory and quantify the dynamics of the involved dislocations. Therefore, we image the so far unrevealed key mechanism of 2D melting, including a meta-quasi-particle diffusion coefficient of the dislocations that is found to be orders of magnitude higher than skyrmion diffusion. We quantify the correlation functions and shear modulus, which behave in excellent agreement with the KTHNY theory. Thus, our work provides a new approach to access the key dynamics in 2D melting and opens up new possibilities to study the intrinsic phase behaviour, boundary effects and identify the role of topological defects in 2D systems. In the future, the development of material stacks with further reduced pinning effects can even allow the use of skyrmion lattices for experimentally exploring 2D melting in the presence of a significant Magnus force⁵³ as well as for determining the interaction potential of topological defects.

Online content

Any methods, additional references, Nature Portfolio reporting summaries, source data, extended data, supplementary information, acknowledgements, peer review information; details of author contributions and competing interests; and statements of data and code availability are available at <https://doi.org/10.1038/s41565-025-01977-2>.

References

- Bogdanov, A. & Hubert, A. Thermodynamically stable magnetic vortex states in magnetic crystals. *J. Magn. Magn. Mater.* **138**, 255–269 (1994).
- Mühlbauer, S. et al. Skyrmion lattice in a chiral magnet. *Science* **323**, 915–919 (2009).
- Jiang, W. et al. Skyrmions in magnetic multilayers. *Phys. Rep.* **704**, 1–49 (2017).
- Fert, A., Cros, V. & Sampaio, J. Skyrmions on the track. *Nat. Nanotechnol.* **8**, 152–156 (2013).
- Parkin, S. & Yang, S.-H. Memory on the racetrack. *Nat. Nanotechnol.* **10**, 195–198 (2015).
- Everschor-Sitte, K., Masell, J., Reeve, R. M. & Kläui, M. Perspective: magnetic skyrmions—overview of recent progress in an active research field. *J. Appl. Phys.* **124**, 240901 (2018).
- Zázvorka, J. et al. Thermal skyrmion diffusion used in a reshuffler device. *Nat. Nanotechnol.* **14**, 658–661 (2019).
- Raab, K. et al. Brownian reservoir computing realized using geometrically confined skyrmion dynamics. *Nat. Commun.* **13**, 6982 (2022).
- Beneke, G. et al. Gesture recognition with Brownian reservoir computing using geometrically confined skyrmion dynamics. *Nat. Commun.* **15**, 8103 (2024).
- Zhang, X., Ezawa, M. & Zhou, Y. Magnetic skyrmion logic gates: conversion, duplication and merging of skyrmions. *Sci. Rep.* **5**, 9400 (2015).
- Pinna, D. et al. Skyrmion gas manipulation for probabilistic computing. *Phys. Rev. Appl.* **9**, 064018 (2018).
- Lee, O. et al. Perspective on unconventional computing using magnetic skyrmions. *Appl. Phys. Lett.* **122**, 260501 (2023).
- Brems, M. A., Kläui, M. & Virnau, P. Circuits and excitations to enable Brownian token-based computing with skyrmions. *Appl. Phys. Lett.* **119**, 132405 (2021).
- Huang, P. et al. Melting of a skyrmion lattice to a skyrmion liquid via a hexatic phase. *Nat. Nanotechnol.* **15**, 761–767 (2020).
- Meisenheimer, P. et al. Ordering of room-temperature magnetic skyrmions in a polar van der Waals magnet. *Nat. Commun.* **14**, 3744 (2023).

16. Zázvorka, J. et al. Skyrmion lattice phases in thin film multilayer. *Adv. Func. Mater.* **30**, 2004037 (2020).
17. Kosterlitz, J. M. & Thouless, D. J. Long range order and metastability in two dimensional solids and superfluids. (Application of dislocation theory). *J. Phys. C* **5**, L124 (1972).
18. Kosterlitz, J. M. & Thouless, D. J. Ordering, metastability and phase transitions in two-dimensional systems. *J. Phys. C* **6**, 1181–1203 (1973).
19. Halperin, B. I. & Nelson, D. R. Theory of two-dimensional melting. *Phys. Rev. Lett.* **41**, 121–124 (1978).
20. Nelson, D. R. & Halperin, B. I. Dislocation-mediated melting in two dimensions. *Phys. Rev. B* **19**, 2457–2484 (1979).
21. Young, A. P. Melting and the vector Coulomb gas in two dimensions. *Phys. Rev. B* **19**, 1855–1866 (1979).
22. Zahn, K., Lenke, R. & Maret, G. Two-stage melting of paramagnetic colloidal crystals in two dimensions. *Phys. Rev. Lett.* **82**, 2721–2724 (1999).
23. Zahn, K. & Maret, G. Dynamic criteria for melting in two dimensions. *Phys. Rev. Lett.* **85**, 3656–3659 (2000).
24. Guillamón, I. et al. Direct observation of melting in a two-dimensional superconducting vortex lattice. *Nat. Phys.* **5**, 651–655 (2009).
25. Roy, I. et al. Melting of the vortex lattice through intermediate hexatic fluid in an α -MoGe thin film. *Phys. Rev. Lett.* **122**, 047001 (2019).
26. Reichhardt, C., Reichhardt, C. J. O. & Milošević, M. V. Statics and dynamics of skyrmions interacting with disorder and nanostructures. *Rev. Mod. Phys.* **94**, 035005 (2022).
27. Seshadri, R. & Westervelt, R. M. Statistical mechanics of magnetic bubble arrays. II. Observations of two-dimensional melting. *Phys. Rev. B* **46**, 5150–5161 (1992).
28. Kapfer, S. C. & Krauth, W. Two-dimensional melting: from liquid-hexatic coexistence to continuous transitions. *Phys. Rev. Lett.* **114**, 035702 (2015).
29. Ge, Y. et al. Constructing coarse-grained skyrmion potentials from experimental data with iterative Boltzmann inversion. *Commun. Phys.* **6**, 30 (2023).
30. Lin, S.-Z., Reichhardt, C., Batista, C. D. & Saxena, A. Particle model for skyrmions in metallic chiral magnets: dynamics, pinning, and creep. *Phys. Rev. B* **87**, 214419 (2013).
31. Kerber, N. et al. Anisotropic skyrmion diffusion controlled by magnetic-field-induced symmetry breaking. *Phys. Rev. Appl.* **15**, 044029 (2021).
32. Brems, M. A. et al. Realizing quantitative quasiparticle modeling of skyrmion dynamics in arbitrary potentials. *Phys. Rev. Lett.* **134**, 046701 (2025).
33. Gruber, R. et al. Skyrmion pinning energetics in thin film systems. *Nat. Commun.* **13**, 3144 (2022).
34. Gruber, R. et al. 300-times-increased diffusive skyrmion dynamics and effective pinning reduction by periodic field excitation. *Adv. Mater.* **35**, 2208922 (2023).
35. Deuschländer, S., Horn, T., Löwen, H., Maret, G. & Keim, P. Two-dimensional melting under quenched disorder. *Phys. Rev. Lett.* **111**, 098301 (2013).
36. Nelson, D. R. Reentrant melting in solid films with quenched random impurities. *Phys. Rev. B* **27**, 2902–2914 (1983).
37. Song, C. et al. Commensurability between element symmetry and the number of skyrmions governing skyrmion diffusion in confined geometries. *Adv. Func. Mater.* **31**, 2010739 (2021).
38. Gruber, R. et al. Source data—2D skyrmion lattice melting. *Zenodo* <https://doi.org/10.5281/zenodo.15472065> (2025).
39. Zeissler, K. et al. Diameter-independent skyrmion Hall angle observed in chiral magnetic multilayers. *Nat. Commun.* **11**, 428 (2020).
40. Zivieri, R. et al. Configurational entropy of magnetic skyrmions as an ideal gas. *Phys. Rev. B* **99**, 174440 (2019).
41. Schall, P., Weitz, D. A. & Spaepen, F. Structural rearrangements that govern flow in colloidal glasses. *Science* **318**, 1895–1899 (2007).
42. Russell, E. R., Spaepen, F. & Weitz, D. A. Anisotropic elasticity of experimental colloidal Wigner crystals. *Phys. Rev. E* **91**, 032310 (2015).
43. Kern, L.-M. et al. Deterministic generation and guided motion of magnetic skyrmions by focused He⁺-ion irradiation. *Nano Lett.* **22**, 4028–4035 (2022).
44. Riddiford, L. J., Brock, J. A., Murawska, K., Hrabec, A. & Heyderman, L. J. Grayscale control of local magnetic properties with direct-write laser annealing. Preprint at arXiv <https://doi.org/10.48550/arXiv.2401.09314> (2024).
45. Ghimenti, F., Ozawa, M., Biroli, G. & Tarjus, G. Shear-induced phase behavior and topological defects in two-dimensional crystals. *Phys. Rev. B* **109**, 104114 (2024).
46. Allan, D. B., Caswell, T., Keim, N. C., van der Wel, C. M. & Verweij, R. W. soft-matter/trackpy: v0.6.4. *Zenodo* <https://doi.org/10.5281/zenodo.12708864> (2024).
47. Mazars, M. & Salazar, R. Topological defects in the two-dimensional melting. *EPL* **126**, 56002 (2019).
48. Pertsinidis, A. & Ling, X. S. Diffusion of point defects in two-dimensional colloidal crystals. *Nature* **413**, 147–150 (2001).
49. Libál, A., Reichhardt, C. & Reichhardt, C. J. O. Point-defect dynamics in two-dimensional colloidal crystals. *Phys. Rev. E* **75**, 011403 (2007).
50. Lal, J., Abernathy, D., Auvray, L., Diat, O. & Grübel, G. Dynamics and correlations in magnetic colloidal systems studied by X-ray photon correlation spectroscopy. *Eur. Phys. J. E* **4**, 263–271 (2001).
51. Lhermitte, J. R. M., Rogers, M. C., Manet, S. & Sutton, M. Velocity measurement by coherent X-ray heterodyning. *Rev. Sci. Instrum.* **88**, 015112 (2017).
52. Klose, C. et al. Photon correlation spectroscopy with heterodyne mixing based on soft X-ray magnetic circular dichroism. *Phys. Rev. B* **105**, 214425 (2022).
53. Braverman, L., Scheibner, C., VanSaders, B. & Vitelli, V. Topological defects in solids with odd elasticity. *Phys. Rev. Lett.* **127**, 268001 (2021).

Publisher's note Springer Nature remains neutral with regard to jurisdictional claims in published maps and institutional affiliations.

Open Access This article is licensed under a Creative Commons Attribution 4.0 International License, which permits use, sharing, adaptation, distribution and reproduction in any medium or format, as long as you give appropriate credit to the original author(s) and the source, provide a link to the Creative Commons licence, and indicate if changes were made. The images or other third party material in this article are included in the article's Creative Commons licence, unless indicated otherwise in a credit line to the material. If material is not included in the article's Creative Commons licence and your intended use is not permitted by statutory regulation or exceeds the permitted use, you will need to obtain permission directly from the copyright holder. To view a copy of this licence, visit <http://creativecommons.org/licenses/by/4.0/>.

© The Author(s) 2025

Methods

Magnetic multilayer stack

The Ta(5 nm)/Co₂₀Fe₆₀B₂₀(0.9 nm)/Ta(0.07 nm)/MgO(2 nm)/Ta(5 nm) multilayer stack (layer thickness with an accuracy better than 0.01 nm) is deposited by d.c./radio-frequency magnetron sputtering using a Singulus Rotaris machine with a base pressure of 3×10^{-8} mbar. The hexagonal geometric confinement is patterned by electron-beam lithography followed by argon-ion etching.

Interfacial Dzyaloshinskii–Moriya interaction^{54,55} is mainly induced at the Ta/Co₂₀Fe₆₀B₂₀ interface; the Co₂₀Fe₆₀B₂₀/MgO interface causes perpendicular magnetic anisotropy. The Ta(0.08) dusting layer is used to not only balance the perpendicular magnetic anisotropy and Dzyaloshinskii–Moriya interaction^{7,56} to host skyrmions but also to optimize the energy landscape for skyrmion lattice formation and dynamics. We provide the OOP hysteresis loop in Supplementary Note 4 with Supplementary Fig. 4. The non-trivial topology of the observed bubbles is experimentally confirmed by spin-orbit-torque-driven skyrmion motion and supported by micromagnetic simulations^{7,31,33}.

Furthermore, the skyrmion interaction potential has been demonstrated to be purely repulsive in the studied material stack²⁹; in particular, we note that it is of a form in which the KTHNY transitions are predicted to occur²⁸. In contrast, other materials can also lead to attractive skyrmion interaction potentials^{57–59}. Although fundamentally, the existence of a Magnus force is a further unique property of skyrmions, the relative strength of the effect is, however, small in our system. It is roughly proportional to the ratio of the domain-wall width (10–20 nm) to the skyrmion core diameter (few micrometres)^{33,60} and, therefore, negligible in our system, resulting in a maximum skyrmion Hall angle of a few degrees⁶¹. Additionally, the hopping-like skyrmion dynamics in the non-flat-energy landscape is dominated by pinning forces^{7,33,34}, suppressing the Magnus effect. Small skyrmions or (close-to) pinning-free diffusion systems can, however, lead to a sizable Magnus force, which is of special interest as topological defect dynamics in systems with a Magnus force and odd elasticity⁵³ is an open question.

Skyrmion stabilization and imaging

A commercially available evico magnetics Kerr microscope is used to establish magnetic contrast with a resolution of 300 nm in space and 62.5 ms in time, using a blue light-emitting diode light source and a charge-coupled device camera with a field of view of $200 \times 150 \mu\text{m}^2$. Magnetic fields can be applied in both in-plane (IP) and OOP directions. The alignment of coils is optimized by aligning the shift of OOP hysteresis loops with and without an IP field. The OOP magnet is custom made to allow field control with sub-microtesla precision. The sample itself is placed onto a Peltier element directly on top of the coil for temperature control. The temperature is kept constant at 333.5 K and monitored by a Pt100 sensor directly next to the sample to ensure temperature stability better than 0.1 K.

Skyrmions are nucleated by applying an IP-field pulse, which saturates the sample in the IP direction at a constant OOP field. The resulting skyrmion lattice is equilibrated by an oscillating OOP magnetic field at 100 Hz with amplitudes up to 60 μT in addition to the constant OOP-field offset before measuring the obtained configuration.

We have direct and precise control over the skyrmion size via the applied OOP magnetic field^{33,39,40}. The sizes of the individual skyrmions are detected by a machine learning-based pixel-wise classification⁶². Additionally, we can continuously tune the skyrmion diffusivity by sinusoidal OOP-field oscillation in addition to the offset field^{9,34}. In the melting procedure presented in Figs. 1–4, we increase the external OOP-field offset every 62.5 s (corresponding to 1,000 frames) in steps of 6 μT . During each interval of 62.5 s, the field is kept constant to obtain reasonable statistics for every field value. In a constant external field, the skyrmion ensemble is in equilibrium. In the picosecond–nanosecond timescale of the magnetization dynamics, the intrinsic precessional dynamics of magnetization is always damped out on the timescales we

investigate, whereas the thermally activated diffusive skyrmion dynamics takes place on the millisecond–second timescale that we investigate. The skyrmions also react fast (\lesssim milliseconds)³⁴ to field changes and the steps of 6 μT are very small—the system ordering responds to size changes typically faster than 1 s, apart from fluctuations close to the observed transitions. Therefore, we can treat the whole melting process to be in quasi-equilibrium. Accordingly, we have chosen the time intervals and field steps to preserve quasi-equilibrium and ensure stable measurement conditions during the whole melting protocol. However, oscillating fields—which are only used to initialize the skyrmion lattice order here, but which can also be used to destabilize the lattice order (Supplementary Fig. 4)—are expected to introduce non-equilibrium properties as they permanently drive skyrmion size changes.

Quantification of 2D order

The translational order is quantified by the translational correlation function

$$G_T(r = |\mathbf{r}_j - \mathbf{r}_k|) = \langle e^{-i\mathbf{G} \cdot (\mathbf{r}_j - \mathbf{r}_k)} \rangle, \quad (1)$$

averaging the link between two particle positions \mathbf{r}_j and \mathbf{r}_k with respect to a reciprocal lattice vector \mathbf{G} over the distance r . The orientational correlation function

$$G_6(r = |\mathbf{r}_j - \mathbf{r}_k|) = \langle \psi_6^*(\mathbf{r}_j) \psi_6(\mathbf{r}_k) \rangle \quad (2)$$

quantifies the orientational order based on the local orientational order parameter

$$\psi_6(\mathbf{r}_j) = \frac{1}{N} \sum_{k=1}^N e^{-i6\theta_{jk}} \quad (3)$$

of a particle at position \mathbf{r}_j with N nearest neighbours labelled $k = 1$ to N . θ_{jk} denotes the angle of the connecting vector $\mathbf{r}_k - \mathbf{r}_j$ with respect to an arbitrary axis¹⁹.

In a 2D solid, $G_T(r)$ decays algebraically as $\propto r^{-\eta_T}$, signalling QLRO. When the exponent η_T reaches its critical value of 1/3, an exponential decay $\propto \exp(-r/\xi_T)$ with correlation length ξ_T sets in; translational QLRO has disappeared¹⁹. In contrast, $G_6(r)$ is constant in a solid, but shows an algebraic decay $\propto r^{-\eta_6}$ when the translational order vanishes if orientational QLRO persists. Hence, orientational order is still present in what is referred to as the hexatic phase, which is unique to 2D systems^{19,20}. When η_6 reaches its critical value of 1/4, $G_6(r)$ becomes exponential ($\propto \exp(-r/\xi_6)$) with correlation length ξ_6 , resulting in an isotropic liquid. At the transition from exponential to algebraic decay, the respective correlation lengths of both correlation functions diverge, causing the exponential term to vanish in the critical (QLRO) phases¹⁹.

Similar to the correlation functions in space, we calculate the orientational time correlation as

$$G_6(\tau) = \langle \psi_6^*(t) \psi_6(t + \tau) \rangle \quad (4)$$

as a function of time delay τ , which reveals the dynamics for every field interval²³. The angle brackets represent the average over all particles and all starting times t within the interval of constant field. Theory suggests a constant behaviour of $G_6(\tau)$ in the solid phase, algebraic decay in the hexatic phase and exponential decay in the liquid phase²³. The hexatic and liquid phases are separated by a critical exponent $\eta_t = 1/8$. Our results shown in Extended Data Fig. 1 match the theory qualitatively well. The predicted critical value of $\eta_t = 1/8$ for an infinite system is, however, too large to match our scenario. We can attribute the enhanced time correlation in our experiment to the effects of confinement and non-flat-energy landscape.

Any lattice site with the number of nearest neighbours different from $N = 6$ is a topological defect. A dislocation is a pair of defects

Article

with opposite topological charge: one $N=5$ and one $N=7$ defect. In a solid, only a few dislocation pairs occur, which are tightly bound and of opposite orientation. The orientation of a dislocation is specified by the Burgers vector. The Burgers vector is determined as the missing vector when encircling a dislocation counterclockwise with a set of lattice vectors, which would yield a closed path in a perfect lattice. At the transition point separating the solid from the hexatic phase, the dislocation pairs unbind and proliferate. This formation of isolated free dislocations causing the loss of translational QLRO is measurable macroscopically as a vanishing shear modulus μ . At the transition point separating the hexatic from the liquid phase, the dislocations eventually unbind and proliferate into two isolated disclinations^{18,19}.

Data analysis

For the detection of skyrmions from the greyscale video and linking them to trajectories, we use the trackpy package⁴⁶ in Python. The obtained positions are used for every skyrmion to determine the local order parameter ψ_6 and its nearest neighbours applying a Voronoi tessellation, which automatically determines the lattice defects. Skyrmions at the edge of the system are neglected for the analysis of ψ_6 and lattice defects as their position at the edge produces artefacts in the Voronoi tessellation⁶³.

For all skyrmions that are not located at the edge of the system, we determine a value for G_T and G_6 with respect to all other skyrmions. We bin the values of the respective correlation and perform an average in every bin, resulting in the distance-dependent correlation functions $G_T(r)$ and $G_6(r)$ (Fig. 1d–i). The determination of the correlation function works for single-frame images; however, we average the correlation functions of ten consecutive frames (over 0.625 s) to reduce noise significantly. Therefore, all the plots and fits of the correlation functions are performed on the averaged data. To determine the decay of the translational correlation function, we fit $G_T(r)$ with a power-law decay $\propto (r/r_0)^{-\eta_T}$ as a function of distance r in units of the skyrmion lattice constant r_0 . We use the initial power-law fit to determine if the system is translationally ordered (η_T below a critical value of 1/3) or not ($\eta_T > 1/3$). In disorder, however, the exponent η_T is no longer well defined since the decay of G_T is now solely exponential. Therefore, for the disordered cases, we fit the exponential ($\propto \exp(-r/\xi_T)$) instead of the power law. Since the exponential term is technically also present in the ordered critical regime, we also fit an exponential for the occurrences of $\eta_T < 1/3$, but as an additional factor to the power law. We use this additional factor in the fit as confirmation that the correlation length ξ_T becomes infinite in the ordered regime. For the orientational correlation function G_6 , we proceed analogously to determine the exponent η_6 as well as the correlation length ξ_6 . However, the orientational correlation has a different critical value of $\eta_6 = 1/4$, which we use to determine whether the system is orientationally ordered ($\eta_6 < 1/4$) or not ($\eta_6 = 1/4$) and whether we fit the exponential as an additional factor to or instead of the power law, respectively.

In our system, we lack the possibility to apply stress forces to directly measure the elastic moduli. Instead, we analyse the local deformations of the lattice in real space to estimate the shear modulus μ (refs. 41,42,64). As the reference lattice, we use a central skyrmion with six perfectly arranged nearest neighbours at positions $\mathbf{x}_i^{\text{ref}}$ with average lattice spacing. To this reference, we fit a local deformation tensor δ for every skyrmion and its neighbours in the experimental lattice, such that the squared distance

$$d^2 = \sum_i |(\delta \mathbf{x}_i^{\text{ref}}) - \mathbf{x}_i^{\text{exp}}|^2 \quad (5)$$

between experimental lattice positions $\mathbf{x}_i^{\text{exp}}$ and the tweaked reference is minimized. To extract the shear component, we decompose $\delta = \epsilon + R_\alpha$ to a symmetric strain tensor ϵ and an anti-symmetric rotation R_α by an angle α . The diagonal elements of ϵ describe the strain along x and y ,

whereas the off-diagonal element is the shear component. In case of linear elasticity, a shear deformation is associated with a shear energy $E_{\text{shear}} = \frac{1}{2}(2\epsilon_{xy})^2 V \cdot \mu$, where V denotes the volume over which the shearing takes place (area spanned by the nearest neighbours in our case). Assuming a Boltzmann distribution $P(E) \propto \exp(-E/k_B T)$ of the shear energy at temperature T , we fit μ as the slope of

$$\log [P(E)] = -\frac{E_{\text{shear}}}{k_B T} + \text{constant} = \mu \left[\frac{1}{2}(2\epsilon_{xy})^2 \frac{V}{k_B T} \right] + \text{constant} \quad (6)$$

when calculating a histogram over the square bracket as a measure of the logarithm of the shear energy distribution. The procedure requires the assumption of linear elasticity, which becomes less applicable in a less dense system, especially in liquid. Therefore, the shear modulus does not vanish completely during melting. Also, the distribution of shear energies associated with the determined deformations is not perfectly Boltzmann like, as already observed for colloidal systems⁴². Since the dependence is not perfectly linear, we perform a set of fits over different ranges and use the standard deviation as error of the mean value.

The determination of topological defects follows directly from the Voronoi tessellation used for calculating the local ordering. Every skyrmion with a number of nearest neighbours N different from 6, which is not located at the edge of the system, is identified as a lattice defect. Since defects in the solid and hexatic regimes almost only occur pairwise, identifying those pairs as dislocations is trivial. However, transitioning to a liquid, complex clusters of defects evolve. The complex appearance, including the interactions between defect clusters, makes the identification of the formal connection between defects impossible. To analyse the further evolution of defects, we establish a simplified approach of identifying pairs of defects. To every 5-defect i , we assign exactly one 7-defect j and take the distance between the defects as d_{ij} . To establish unique pair connections, we minimize the total square distance

$$d_{\text{tot}}^2 = \sum_{ij} d_{ij}^2 \quad (7)$$

associated with all possible connections ij using the Hungarian method⁶⁵. We identify a determined defect pair as a dislocation if the corresponding d_{ij} is a nearest-neighbour connection; otherwise, we identify the two connected defects as two disclinations. To study the dislocation dynamics, we keep only the centre of mass of all the identified dislocations and link them to trajectories with trackpy⁴⁶. Note that the 5/7-defect pair matching as well as the linking of dislocation trajectories work generally well until deep in the hexatic regime as defects always occur in pairs and do not fully dissociate. At the onset of the liquid regime, however, disclinations and complex defect clusters start occurring and make the formally correct matching and evolution of defect pairs inaccessible. With our approach being purely based on distance minimization, we, therefore, expect a possible systematic error in the quantification of defect dynamics from the onset of the liquid regime, whereas the increased dynamics as a direct consequence of defect fluctuations, rearrangements and dissociation is still reflected.

To evaluate the diffusion coefficient of the skyrmions at different times of the measurement, we determine the MSD as

$$\text{MSD}(t) = \langle [\mathbf{r}(t) - \mathbf{r}(t_0)]^2 \rangle = 2dDt \quad (8)$$

by calculating the square distance of skyrmion position \mathbf{r} at time t relative to the position at the time of initial occurrence t_0 and take the average over all skyrmions. The MSD is further related to the dimensionality d of the system (here $d=2$) and D over t in the case of normal diffusion^{7,31,34}. Since we want to determine D at any time t_0 with reliable statistics, we consider all trajectories present in a 10-s time window

around t_0 and use the time of first occurrence as t_0 . We then fit the first 1 s of the resulting MSD to determine D . For the dislocations, we proceed analogously but use all the trajectories occurring in a time window of 31 s around t_0 to fit D for statistical reasons because there are significantly fewer dislocations than skyrmions.

To correlate defect occurrences of time, for every skyrmion n at time t , we associate a variable

$$u_n(t) = \begin{cases} 1 & \text{(no defect)} \\ 0 & \text{(is defect)} \end{cases} \quad (9)$$

to be correlated. We calculate the Pearson correlation

$$g_2(t_1, t_2) = \frac{\langle (u(t_1) - \mu(t_1))(u(t_2) - \mu(t_2)) \rangle_n}{\sigma(t_1)\sigma(t_2)} = \frac{\langle u(t_1)u(t_2) \rangle_n - \langle u(t_1) \rangle_n \langle u(t_2) \rangle_n}{\sigma(t_1)\sigma(t_2)} \quad (10)$$

for every pair of times t_1 and t_2 by averaging over all skyrmions n (refs. 50–52). Here μ and σ represent the mean and standard deviation of u at the respective time. The corresponding two-time correlation map is shown in Fig. 5a. The correlation decreases over time during the melting and one can observe more rapid changes in the time regions of the previously determined transitions (Fig. 5a, dashed red lines).

By averaging over equal time delays $\tau = t_2 - t_1$, we convert the two-time correlation map to a one-time correlation function $g_2(\tau)$ for every interval of constant magnetic field (as the field is changed stepwise every 62.5 s). Although $g_2(\tau)$ (Fig. 5b) stays almost constant for the fields representing the solid regime, it decays notably and increasingly rapidly throughout the melting process. As the decay of $g_2(\tau)$ is directly related to the dynamics of the underlying feature^{51,52}—that is, the topological defects in this case—this corroborates that the defect dynamics keeps increasing throughout the melting procedure.

Data availability

The data supporting the findings of this study are available within the article and Supplementary Information. These data are also available via Zenodo at <https://doi.org/10.5281/zenodo.15472065> (ref. 38). Source data are provided with this paper.

References

- Dzyaloshinsky, I. A thermodynamic theory of 'weak' ferromagnetism of antiferromagnetics. *J. Phys. Chem. Solids* **4**, 241–255 (1958).
- Moriya, T. Anisotropic superexchange interaction and weak ferromagnetism. *Phys. Rev.* **120**, 91–98 (1960).
- Bhatnagar-Schöffmann, T. et al. Controlling interface anisotropy in CoFeB/MgO/HfO₂ using dusting layers and magneto-ionic gating. *Appl. Phys. Lett.* **122**, 042402 (2023).
- Rózsa, L. et al. Skyrmions with attractive interactions in an ultrathin magnetic film. *Phys. Rev. Lett.* **117**, 157205 (2016).
- Loudon, J. C., Leonov, A. O., Bogdanov, A. N., Hatnean, M. C. & Balakrishnan, G. Direct observation of attractive skyrmions and skyrmion clusters in the cubic helimagnet Cu₂OSeO₃. *Phys. Rev. B* **97**, 134403 (2018).
- Du, H. et al. Interaction of individual skyrmions in a nanostructured cubic chiral magnet. *Phys. Rev. Lett.* **120**, 197203 (2018).
- Jefremovas, E. M. et al. The role of magnetic dipolar interactions in skyrmion lattices. *Newton* **1**, 100036 (2025).
- Litzius, K. et al. Skyrmion Hall effect revealed by direct time-resolved X-ray microscopy. *Nat. Phys.* **13**, 170–175 (2017).
- Labrie-Boulay, I. et al. Machine-learning-based detection of spin structures. *Phys. Rev. Appl.* **21**, 014014 (2024).
- Finney, J. L. & Bernal, J. D. Random packings and the structure of simple liquids. I. The geometry of random close packing. *Proc. R. Soc. A* **319**, 479–493 (1997).
- Falk, M. L. & Langer, J. S. Dynamics of viscoplastic deformation in amorphous solids. *Phys. Rev. E* **57**, 7192–7205 (1998).
- Kuhn, H. W. The Hungarian method for the assignment problem. *Nav. Res. Logist.* **2**, 83–97 (1955).

Acknowledgements

This work was funded by the Deutsche Forschungsgemeinschaft (DFG, German Research Foundation)—SPP 2137 (project no. 403502522) and TRR 173/2 Spin+X (projects A01, A12 and B02). We acknowledge funding from TopDyn. This project has received funding from the European Research Council (ERC) under the European Union's Horizon 2020 research and innovation programme (grant no. 856538, project '3D MAGIC') and under the Marie Skłodowska-Curie grant agreement nos. 860060 ('MagnEFi'), 101119608 ('TOPOCOM') and 101070290 ('NIMFEIA'). We gratefully acknowledge the computing time granted on the MOGON II and III supercomputers at Johannes Gutenberg University Mainz as part of NHR South-West. M.A.B. was supported by a doctoral scholarship of the Studienstiftung des deutschen Volkes. E.M.J. acknowledges the Alexander von Humboldt Postdoctoral Fellowship. A.S. and M.K. acknowledge support from the Norwegian Research Council through grant no. 262633, Center of Excellence on Quantum Spintronics (QuSpin).

Author contributions

R.G. performed the Kerr microscopy measurements and experimental data analysis. J.R., S.M.F. and M.A.B. conducted the MD simulations. R.G., J.R., S.M.F. and M.A.B. analysed the simulation data. F.K., M.-A.S. and E.M.J. optimized and fabricated the multilayer stack. R.G. prepared the paper with help from J.R., M.A.B., S.K. and E.M.J. A.S., P.V. and M.K. guided and supervised the work. All authors commented on the paper.

Funding

Open access funding provided by Johannes Gutenberg-Universität Mainz.

Competing interests

The authors declare no competing interests.

Additional information

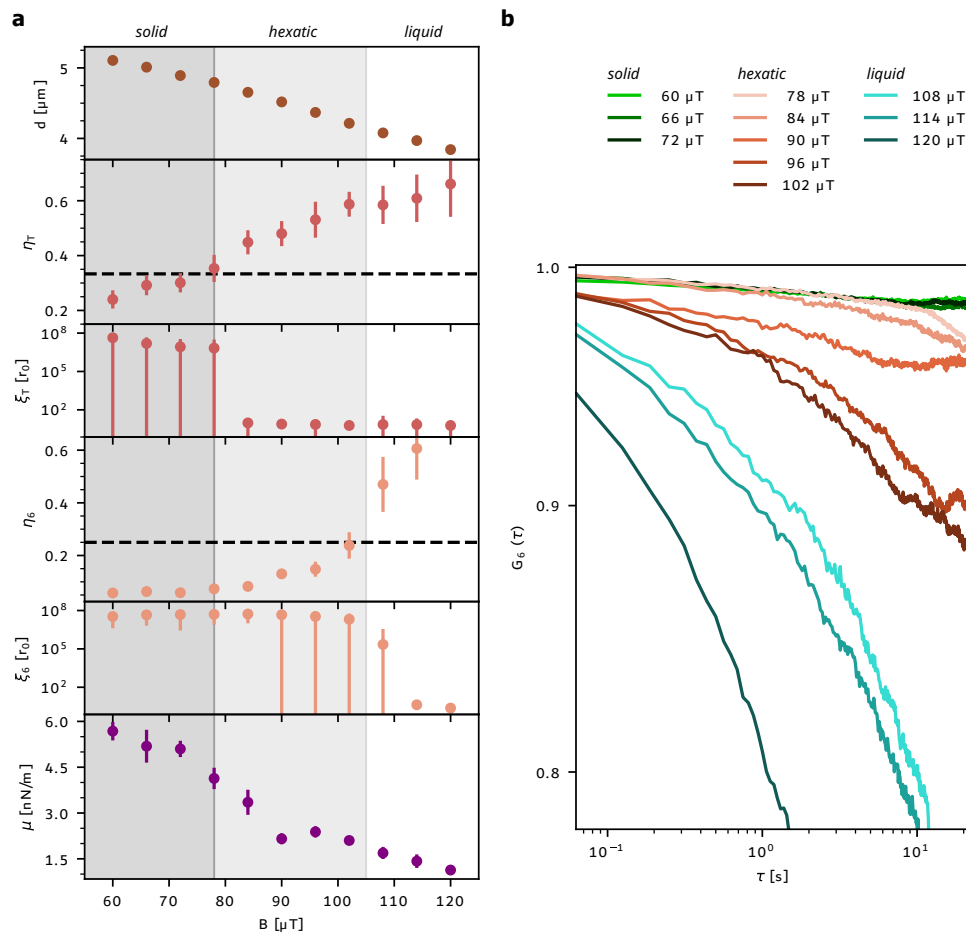
Extended data is available for this paper at <https://doi.org/10.1038/s41565-025-01977-2>.

Supplementary information The online version contains supplementary material available at <https://doi.org/10.1038/s41565-025-01977-2>.

Correspondence and requests for materials should be addressed to Mathias Kläui.

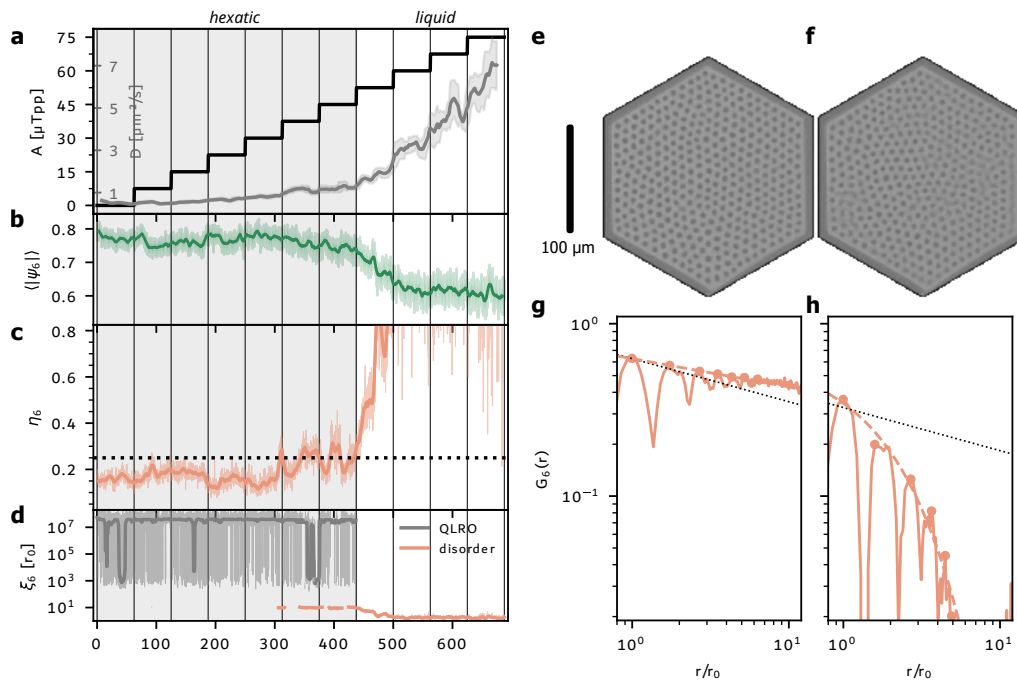
Peer review information *Nature Nanotechnology* thanks the anonymous reviewers for their contribution to the peer review of this work.

Reprints and permissions information is available at www.nature.com/reprints.



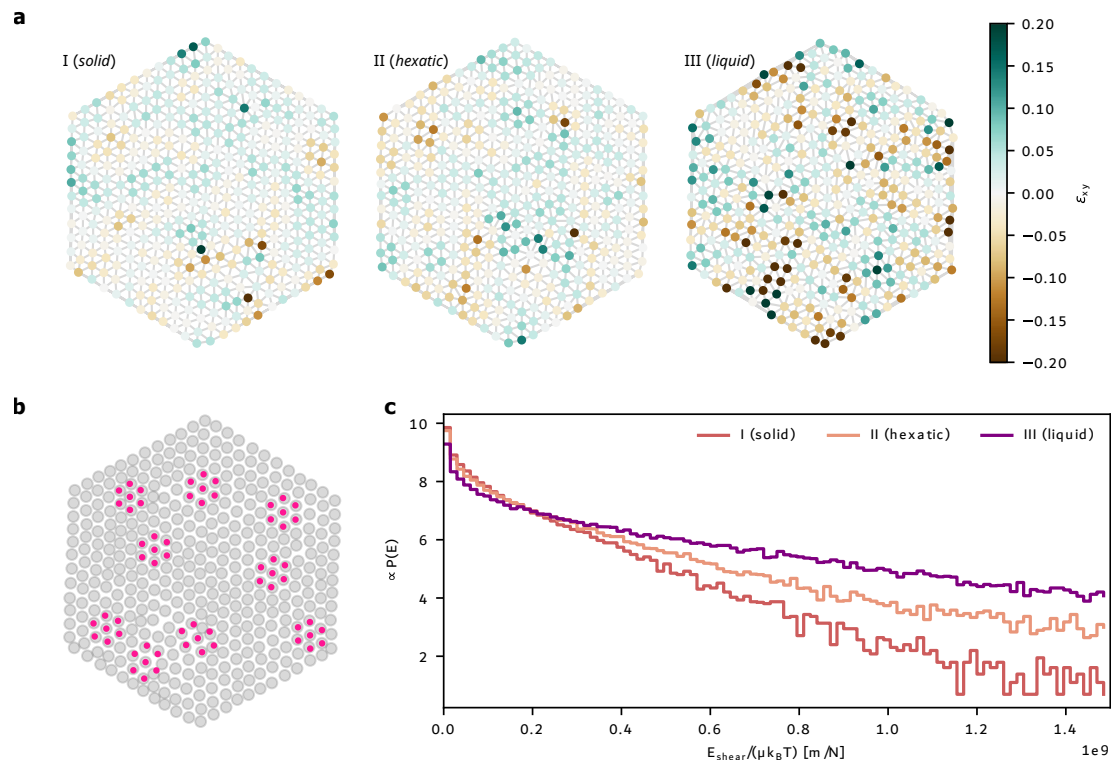
Extended Data Fig. 1 | Quantification of Melting – Dependence on Magnetic Field. **a** Increasing the magnetic field B causes the skyrmion diameter d (mean and negligible standard error of the mean) to shrink. Correspondingly, we plot the time-average over the fluctuations (error bar: standard deviation) of the ordering quantities presented in Fig. 2 for the 62.5 s interval (1000 frames) recorded at every field value: exponent η_T of and correlation length ξ_T of the translational correlation function $G_T(r)$, exponent η_6 of and correlation length ξ_6 of the orientational correlation function $G_\theta(r)$, and shear modulus μ .

b Orientational time correlation function $G_\theta(\tau)$ for every time delay τ (sliding window average) at every field value. We see a clear separation between the correlation in the three different regimes. While $G_\theta(t)$ is almost constant in the solid regime, it decays notably in the hexatic regime and much faster in the liquid, in good agreement with theory. The predicted critical value of $\eta_T=1/8$ for an infinite system is however too large to match our scenario. We can attribute the enhanced time correlation in our experiment to effects of the confinement and the non-flat energy landscape.

**Extended Data Fig. 2 | Lattice Melting by Increasing Skyrmion Diffusivity.**

a The amplitude A (peak-to-peak at 100 Hz) of the oscillating applied field is increased in steps (black) while the offset field is kept constant at $102 \mu\text{T}$. This causes the diffusion coefficient D of the 378 skyrmions to increase (gray, rolling mean and standard deviation). With increasing diffusivity, skyrmions start annihilating. Black vertical lines denote the field steps in all subplots. **b** Average absolute value $\langle |\psi_6| \rangle$ of the local order parameter, for each frame (shaded) and rolling average over 6.25 s (solid line). **c** Exponent η_6 of G_6 and rolling mean over 6.25 s. The dotted horizontal line marks the critical exponent of $1/4$. We

find that tuning the diffusivity, we can drive the η_6 from well below to above the critical value of $1/4$. **d** Correlation length ξ_6 of G_6 and rolling median over 6.25 s (100 frames). **e, f** Kerr images averaged over 5 s at **(e)** $t = 75$ s and **(f)** $t = 575$ s. The smeared-out contrast visualizes the increased diffusivity in **(f)**. **g, h** Orientational correlation functions G_6 for **(e)** and **(f)**, respectively. The black dots represent a power-law decay with the critical exponent of $1/4$. The dashed line is the envelope fit and the dots are the points used for the fit. While in the hexatic case in **(g)**, G_6 decays algebraically, it is now exponential in the liquid case shown in **(h)**.



Extended Data Fig. 3 | Shear Analysis of the Lattice. **a** Shear components ε_{xy} of the determined local lattice deformations for snapshots (i)-(iii) from Fig. 1a-c. During the melting, larger components of the strain tensor become possible and more likely. **b** Visualization of determined local lattice deformation at $t = 0$. The gray circles denote the observed skyrmion positions. The pink dots represent the locally deformed lattice at exemplary sites: For every skyrmion position, a deformation of a local hexagonal lattice (up to the first nearest neighbors) is

fitted to match the neighboring positions best. ε_{xy} is extracted as the asymmetric component of the deformation matrix. **c** Every shear component over the area spanned by the nearest neighbors is associated with a shear energy E_{shear} in units of the shear modulus μ and $k_B T$, which is related to the Boltzmann energy distribution $P(E)$. The slope of the distribution determines the shear modulus μ . The shear energy contributions are shown for the snapshots (i)-(iii) using statistics of 12.5 s.

10.1.1. Supplementary Information


Publication Information

The following Supplementary Information is published with the article in *Nature Nanotechnology*:

Real-Time Observation of Topological Defect Dynamics Mediating 2D Skyrmion Lattice Melting

Raphael Gruber, Jan Rothörl, Simon M. Fröhlich, Maarten A. Brems, Fabian Kammerbauer, Maria-Andromachi Syskaki, Elizabeth M. Jefremovas, Sachin Krishnia, Asle Sudbø, Peter Virnau & Mathias Kläui
Nature Nanotechnology (2025).

DOI: [10.1038/s41565-025-01977-2](https://doi.org/10.1038/s41565-025-01977-2)


Copyright Information:  CC BY 4.0 Creative Commons Attribution 4.0 International License

Editorial Note: The blue header/footer bars were added for inclusion in this dissertation and are not part of the original publication.

Contributions

The author contributions for this project and article are described in detail in section 10.3.

Experimental Note

Documentation of my experiments used for this article are available for lab members on *eLabFTW* ( labbook database ID [5832](#)).



Real-time observation of topological defect dynamics mediating two-dimensional skyrmion lattice melting

In the format provided by the authors and unedited

Content

Supplementary Note 1: Finite Size Effects in the Experiment.....	2
Supplementary Fig. 1.....	3
Supplementary Note 2: Finite Size Effects in Simulations	4
Supplementary Fig. 2.....	6
Supplementary Note 3: Defect Clustering and Defect Pair Matching	7
Supplementary Fig. 3.....	8
Supplementary Note 4: Hysteresis Loop.....	9
Supplementary Fig. 4.....	9
References.....	9

Supplementary Note 1: Finite Size Effects in the Experiment

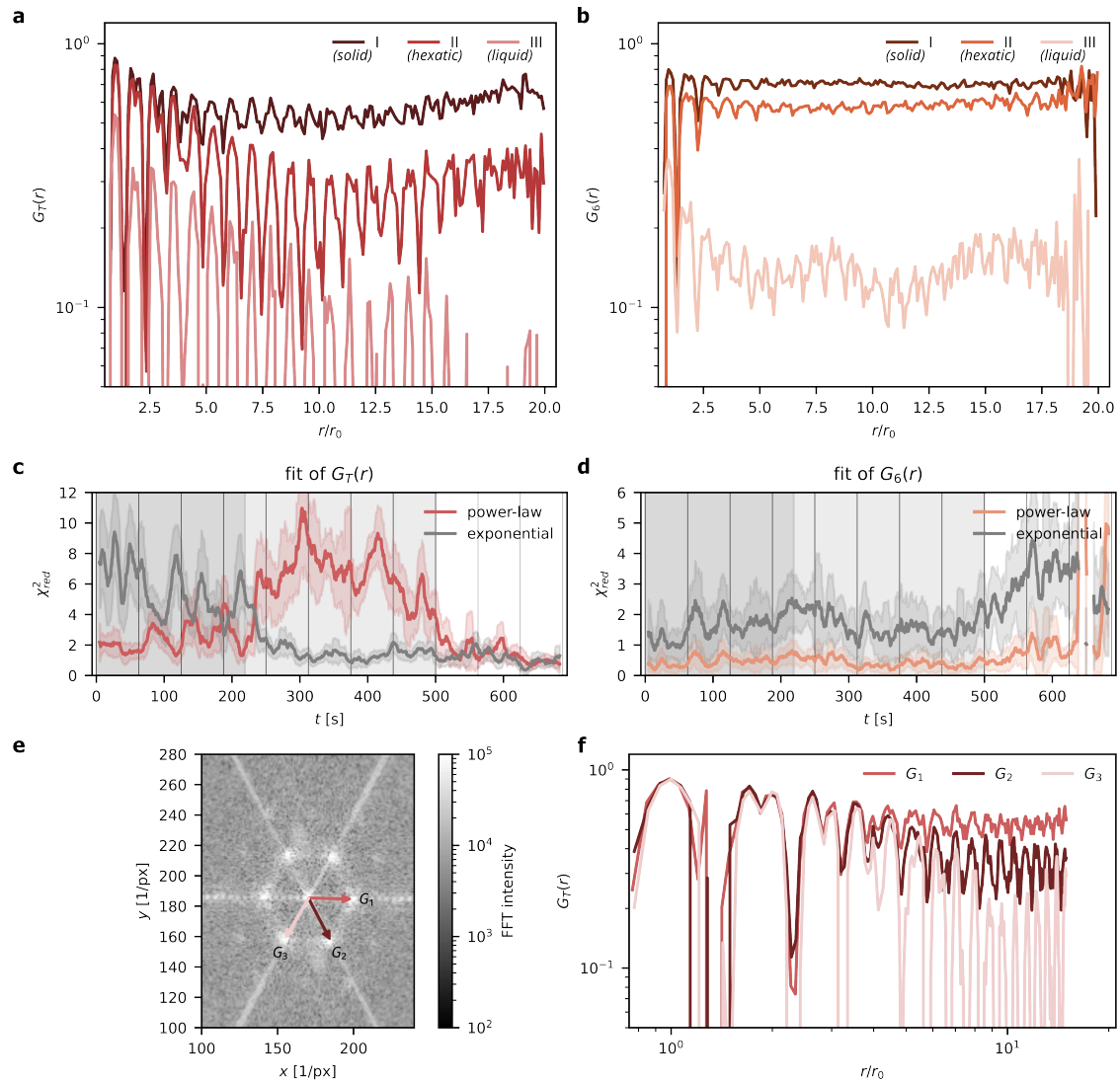
Since the experimentally observed lattice is a finite system, it is expected to exhibit finite size effects. In contrast, measures to classify phases in KTHNY are derived for infinite systems. Therefore, we investigate in the following how our results align with those measures.

Analyzing the behavior of G_T and G_6 at larger distances (Fig. S1a and b, respectively; both for snapshots I-III), we see that the correlation functions can increase with distance due to the lattice stabilization by the boundary, especially for distances beyond ten nearest neighbor distances r_0 . In contrast to Fig. 1, we use a semilogarithmic plot to highlight the larger distances. The effect is stronger for the orientational correlation since the confinement with its commensurate shape provides primarily orientational stabilization. We observe the boundary effect on G_T starting at distances of approximately $12 r_0$; for G_6 , an influence is visible already at $7 r_0$. We therefore use those distances as limits for the fit range when we determine the decay exponents η_T and η_6 , respectively.

According to KTHNY theory, the correlation functions are expected to change their functional behavior qualitatively between power-law and exponential at the critical point determined by the critical exponents. We therefore compare the reduced χ^2 of pure power-law and pure exponential fits during the entire melting procedure. For each distance bin of the correlation functions, we use the mean and standard deviation from the performed average over 10 frames (0.625 s) for the fit. In Fig. S1c, we show that a power-law fit for G_T is indeed more favorable in the predetermined solid regime (dark-gray shading). Entering the hexatic regime (light-gray shading), the exponential becomes more favorable. Hence, the critical value of $1/3$ does not appear to be affected by finite size effects. At $t > 450$ s, the power-law fit yields decreasing values χ^2 and seems to become favorable again; however, this is only because of the small values of G_T deep in disorder, which therefore become increasingly prone to noise and the present boundary effects. For G_6 , χ^2 of the power-law fit is always smaller than of the exponential, thus indicating better description by a power-law behavior for all times. However, due to the boundary effect seen in Fig. S1b, the fit region is strongly limited and yields maximum 7 points; especially, we lack values over larger distances, which are decisive to analyze the functional behavior. In contrast to the critical QLRO regime, we therefore do not find a clear preference for either a power-law or exponential behavior but our results remain inconclusive regarding the exact form. In the experiment presented in Fig. S3h however, we find that G_6 is indeed exponential as soon as the stabilization due to the boundary is overcome; there, with sufficient diffusion.

For the translational correlation, we furthermore notice an anisotropy of the crystal order. Fig. S1e shows the Fourier transform (FFT) of the Kerr microscopy snapshot I. We clearly see discrete peaks (even in higher order) in sixfold symmetry as expected for a hexagonal lattice. The first-order peaks determine the reciprocal hexagonal lattice vectors used for the calculation of G_T . The stripes through the center (in six-fold symmetry) are an artefact caused by the hexagonal shape of the confinement. As a feature of the finite nature of our system, G_T can evolve differently depending on the choice of the lattice vector used. Fig. S1f provides a comparison for the usage of the three lattice vectors in G_T resulting in differently fast decays. The anisotropy is only possible on finite scales and depends on the specific location of lattice defects.

Supplementary Fig. 1



Supplementary Fig. 1. Analysis of Finite Size Effects in the Experiment. **a-b** G_T (a) and G_6 (b) for single-frame snapshots of snapshots I-III (as examples for solid, hexatic, liquid) as presented in Fig. 1, but up to the maximum system distance of $\sim 20r_0$. Note that in contrast to Fig. 1, we show a semilogarithmic plot to highlight the effect of larger distances: Due to the orientational stabilization by the hexagonal confinement, the correlation functions may increase again due to large distances being increasingly affected by boundary effects. **c-d** Reduced χ^2 for fitting a pure power-law (colored) or exponential (gray) to the correlation functions G_T (c) and G_6 (d) throughout the melting over time t . Average and standard deviation over 10 s are drawn. The dark-gray, light-gray and white shading represent the solid, hexatic and liquid phase, respectively. **e** Fourier transformed frame image of snapshot I exhibiting sixfold symmetry and determining the reciprocal lattice vectors G_1 - G_3 (drawn as arrows). The six-fold lines are due to the hexagonal geometry of the system. **f** Due to the finite system size and the specific lattice defect configuration present, the translational correlation function may depend on the choice of lattice direction (G_1 - G_3) as presented here for snapshot I.

Supplementary Note 2: Finite Size Effects in Simulations

To analyze finite size effects and their dependence on the system size, we perform computer simulations in the Thiele model¹ applied to magnetic skyrmions. In the case investigated in this article, the equation of motion reads^{2,3}

$$-\gamma\mathbf{v} - G_{\text{rel}}\gamma\mathbf{e}_z \times \mathbf{v} + \mathbf{F}_{\text{therm}} + \mathbf{F}_{\text{SkSk}}(\{\mathbf{r}\}) + \mathbf{F}_{\text{SkBnd}}(\mathbf{r}) = 0 \quad (\text{S1})$$

where \mathbf{r} is the skyrmion position, \mathbf{v} the skyrmion velocity and $\{\mathbf{r}\}$ indicates the set of all skyrmion positions. γ indicates the damping (in the context of a Molecular Dynamics simulation, not to be confused with the Gilbert damping) and G_{rel} is the relative Magnus force amplitude which is calculated as tangent of the skyrmion Hall angle. In this article, G_{rel} and thereby the Magnus force is set to zero as the Magnus force affects only dynamics of the system but not static properties such as ordering. γ is set to 1 (in simulation units). $\mathbf{F}_{\text{therm}}$ is thermal Gaussian white noise satisfying the fluctuation-dissipation theorem at a temperature of $k_{\text{B}}T=1$ (in simulation units). \mathbf{F}_{SkSk} and $\mathbf{F}_{\text{SkBnd}}$ indicate skyrmion-skyrmion and skyrmion-boundary repulsion. The skyrmion-skyrmion interaction is approximated by a $V(r)=r^{-8}$ potential with a cutoff distance of 1.8 simulation units⁴ and the skyrmion-boundary interaction is using a fully repulsive Lennard-Jones potential

$$V_{\text{LJ}}(r) = 4\varepsilon \left[\left(\frac{\sigma}{r}\right)^{12} - \left(\frac{\sigma}{r}\right)^6 + \frac{1}{4} \right] \quad (\text{S2})$$

with $r_{\text{cut}}=2^{1/6}$ and $\varepsilon=\sigma=1$. Skyrmion interaction potentials for similar materials have previously been extracted using Iterative Boltzmann Inversion (IBI)², where no assumptions on the potential form had been made. The distances and the exact potential form are not directly extracted from the experiment in this case as such high densities generally cause artefacts in the IBI². Instead, the exponent $n=8$ is determined from a slightly less dense skyrmion liquid⁵. Comparing with other measurements in similar material stacks, we have made sure that the exponent changes by less than 1 for size variations two times larger than covered in this investigation – thus not affecting the theoretically predicted phase behavior⁴. In particular, the r^{-8} potential features well-known liquid-hexatic and hexatic-solid phase transitions in continuum⁴. To explain the lattice melting induced by shrinking the skyrmions (i.e., the packing fraction), we simulate the system at different skyrmion densities. Accordingly, we adjust the interaction radius of the skyrmions, but not the form of the potential given by the approximately constant exponent.

Densities ρ in this simplified model are defined as skyrmions per unit length squared in simulation units. The equations of motion were integrated using an Euler algorithm

$$\mathbf{r}(t + \Delta t) = \mathbf{r}(t) + \mathbf{v}(t)\Delta t \quad (\text{S3})$$

with a time step of $\Delta t=10^{-4}$ implemented in the *HOOMD-blue* software package⁶. The system is initialized with either perfect hexagonal order (for commensurate numbers) or hexagonal order with a few particles missing (for non-commensurate numbers) and equilibrated for 10^6 steps before running for 10^7 steps with the trajectory saved every 10^4 steps. Correlation functions are calculated and fitted individually for every saved step. Simulations of non-commensurate numbers are all averaged over at least 10 independent runs with independent initialization. Results of these simulations are presented as the mean over each individual simulation. Commensurate simulations use only one simulation run (except for 11 and 12 skyrmions per edge where we perform 10 runs) as there is only one specific starting condition and for large number a significantly longer computation time is required.

The main approximations of the Thiele model include that skyrmions are described as perfectly circular and of constant size as well as neglecting skyrmion creation and annihilation. These approximations are justified by the small amount of size polydispersity (standard deviation of the

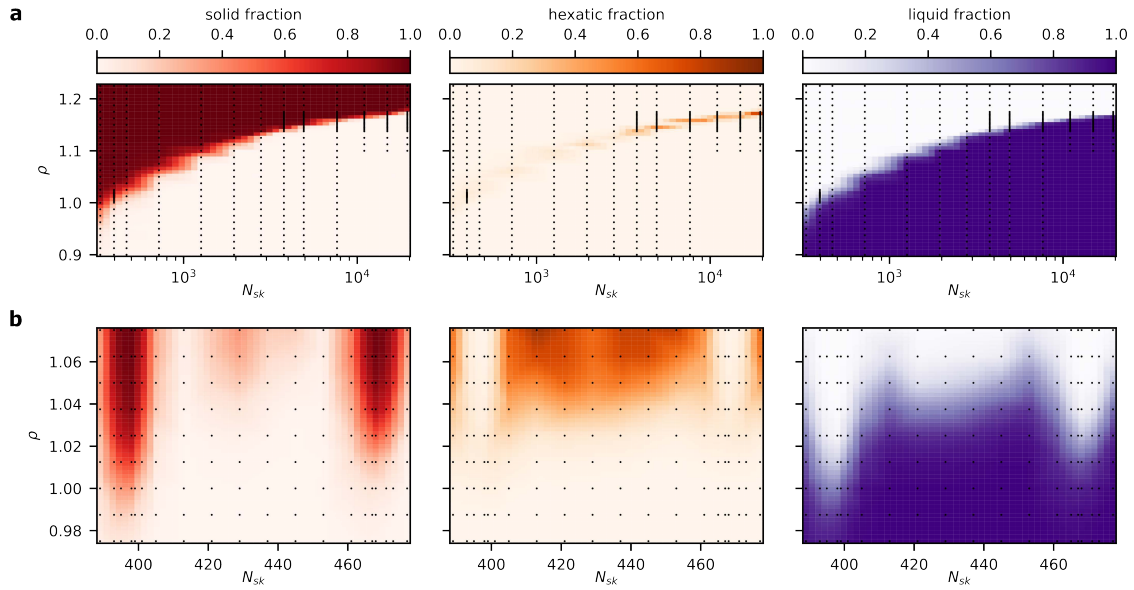
diameter: 11 %) as well as deformations found in the experiments. Also, the system investigated does not feature spontaneous skyrmion creation; skyrmion annihilation is only observed deep in the liquid regime. This makes the Thiele model applicable for a description of the skyrmions used in this article.

In Fig. S2a, we show for computer simulations of a hexagonal system with commensurate numbers of skyrmions (centered hexagonal numbers) that the hexagonal boundary condition stabilizes QLRO in the system. The stabilization becomes stronger for smaller systems, causing QLRO to persist down to lower skyrmion density. We plot the fraction of states observed in the solid, hexatic and liquid regime, respectively. For smaller systems, transition regions between the different regimes at identical parameters also become larger. For larger systems, the influence of the finite size effects decreases, the regimes occur separated and the densities where the system transitions between the regimes approach the values for an infinite system⁴.

In addition to the size scaling of the system, we also investigate how the commensurability of the particle number with respect to the confinement geometry⁷ affects the ordering. Fig. S2b depicts similar simulations for various numbers of skyrmions around and between the commensurate (centered hexagonal) numbers of 397 (11 per edge) and 469 (12 per edge). As incommensurability enforces the existence of dislocations, it strongly suppresses translational QLRO, i.e. the solid regime; in return, the liquid and especially the hexatic regime are widened and enhanced due to quenched disorder^{8,9}. Interestingly, we find a half-commensurate state alternatingly combining 11 and 12 skyrmions per edge, weakly stabilizing QLRO.

The experiments presented in the main text are performed with 401 skyrmions, i.e. slightly off commensurability. Indeed, the system exhibits the three different, well-separated regimes of order and is thus in good agreement with the simulations and KTHNY theory in general. In particular, we observe a relatively wide parameter space for the hexatic regime due to slight incommensurability and low pinning, while still benefitting from sufficient local stabilization due to the geometric confinement.

Supplementary Fig. 2

**Supplementary Fig. 2. Ordering for different numbers of skyrmions in a hexagonal confinement.**

a Ordering regimes in computer simulations of skyrmions in the Thiele model for different particle densities ρ and system sizes using commensurate numbers of skyrmions N_{sk} (centered hexagonal numbers) between 331 (10 skyrmions per edge) and 19441 particles (80 per edge). The black dots represent the parameters at which simulations are performed. The coloring of the parameter space denotes which fractions of the recorded simulations is in the respective regime; for visualization purposes, we show the linear interpolation of the determined fraction over the entire parameter space. The three regimes (solid, hexatic, liquid) exist for all system sizes and QLRO is stabilized by the hexagonal confinement: The smaller the system, the lower the density at which QLRO can still be stabilized; transition regions between different regimes also become larger. The square artefact between simulation parameters are due to the linear interpolation displayed on a logarithmic scale.

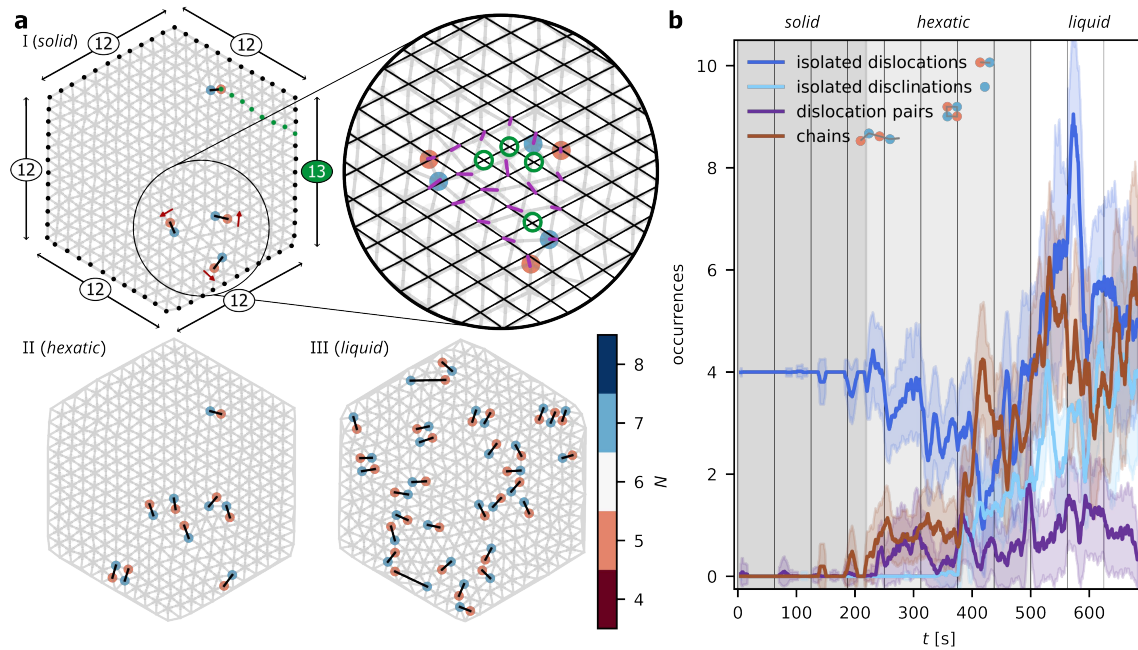
b Analogously, ordering regimes of non-commensurate numbers of skyrmions. Between the commensurate states containing 397 (11 per edge) and 469 skyrmions (12 per edge), translational QLRO and thus the solid regime is strongly suppressed. Instead, the liquid and especially the hexatic regime are enhanced. In between, we find a half-commensurate state (alternating combination of 11 and 12 skyrmions per edge), QLRO is weakly stabilized.

Supplementary Note 3: Defect Clustering and Defect Pair Matching

To detect and classify defect clusters, an approach based on the Voronoi tessellation of the system is used. For each particle with a neighbor number less (greater) than $N=6$, its neighbors are checked and neighboring particles with more (less) than $N=6$ neighbors are considered an associated pair. If no neighbor with an opposing neighbor number defect is found, it is classed as an isolated disclination. Otherwise, all particles within a graph of shared associations are considered part of the same cluster. Clusters consisting of exactly one 5- and one 7-defect are classed as isolated dislocations. Dislocation pairs are defined as consisting of exactly two 5- and two 7-defects where each defect is neighbor to both of the opposing defects. Chains are defined as any cluster consisting of at least 3 particles, which are connected linearly only.

Based on the Voronoi tessellation of the particle positions, particles that do not have exactly 6 neighbors are identified as defects and neighboring opposing defects are combined to clusters. This allows for the identification of different types of defect clusters to compare them to theoretical predictions¹³⁻¹⁶. While theory predicts only dislocation pairs in the solid phase, four stable 5-7-defect pairs (dislocations) are present. As the number of particles (401) is not commensurate with the confinement (closest match would be 397), one dislocation is needed to fit the additional particles. In Fig. S5a, we find that the number of skyrmions along every edge (black dots) is 12 except for the right edge, which contains 13 skyrmions, as indicated by the surrounding arrows labelled with the number of edge skyrmions. The 13th skyrmion causes an additional crystal line (green dots), which ends at one dislocation. Instead of only the four excess skyrmions however, this additional line features eight skyrmions. That is, the other four skyrmions have to be missing elsewhere. Thus, the other three, encircled dislocations comprise a quadruple vacancy and are topologically trivial: their Burger's vectors (red arrows) span all three lattice vectors exactly once and add up to zero. In the inset, we compare the observed skyrmion occurrences inside this vacancy (overall gray Delauney triangulation forming the nearest-neighbor net) to the ideal case in which the surrounding lattice would continue (indicated by black grid). When we match every occurring skyrmion to one ideal lattice site (purple links), indeed four sites (open green circles) stay vacant, confirming the quadruple vacancy. The combination of the observed dislocation (due to the incommensurability) together with the quadruple vacancy as stable initial state is a consequence of the non-flat energy landscape. Consequently, the top dislocation is bound to the right edge and can in the solid regime only move up or down with a fixed distance of eight skyrmions to the edge (see Supplementary Video 3), or later interact with other defects. In the hexatic phase, dislocation pairs as well as chains proliferate, but defects are still bound in opposing pairs. The total number of defects again rises in the liquid phase and dislocations disassociate leading to isolated defects.

Supplementary Fig. 3

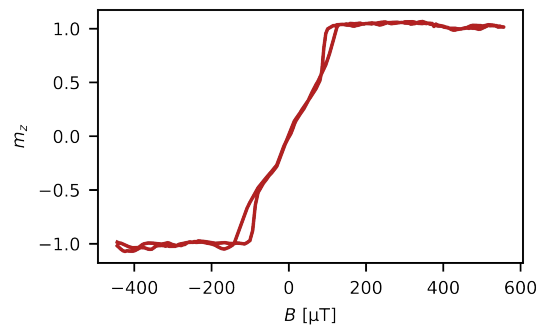


Supplementary Fig. 3. Defect Clustering and Pair Matching. **a** Defect pair matching for snapshots I-III. The black lines represent the connection within a pair. While the matching is trivial in the solid and hexatic regime, the matching in the liquid is not obvious and obtained by distance minimization. In snapshot I, we additionally note that every edge contains 12 skyrmions (black dots and number on arrows), except the right edge with 13 skyrmions. The 13th skyrmion causes the existence of an additional skyrmion row (marked in green), ending at a dislocation. The remaining three encircled dislocations are topologically trivial as their Burger's vectors (red arrows) cancel. They comprise a quadruple vacancy as the lattice has four excess skyrmions (401 instead of 397), but eight are bound to the top dislocation (green dots). The circle inset visualizes the appearance of the fourfold vacancy: if we at the vacancy map in purple every skyrmion to the ideal surrounding lattice (black lines), four sites remain unoccupied (green open circles). **b** Occurrences of more specific clusters of defects occurring during the melting (rolling average and standard deviation over 10 s).

Supplementary Note 4: Hysteresis Loop

We measure the OOP hysteresis loop in terms of the relative OOP magnetization m_z by the total intensity in Kerr microscopy over an OOP field (B) cycle. Note that the saturation field of the loop is below 200 μT , which is of the order of the earth magnetic field. We correct the surrounding magnetic offset field by shifting the hysteresis to be centered around zero. All field values given in the manuscript are corrected for the background field.

Supplementary Fig. 4



Supplementary Fig. 4. Hysteresis Loop. The red line shows the MOKE intensity corresponding to the relative magnetization m_z for a cycle of the OOP magnetic field B .

References

1. Thiele, A. A. Steady-State Motion of Magnetic Domains. *Phys. Rev. Lett.* **30**, 230–233 (1972).
2. Ge, Y. *et al.* Constructing coarse-grained skyrmion potentials from experimental data with Iterative Boltzmann Inversion. *Commun. Phys.* **6**, 1–6 (2023).
3. Brems, M. A. *et al.* Realizing Quantitative Quasiparticle Modeling of Skyrmion Dynamics in Arbitrary Potentials. *Phys. Rev. Lett.* **134**, 046701 (2025).
4. Kapfer, S. C. & Krauth, W. Two-Dimensional Melting: From Liquid-Hexatic Coexistence to Continuous Transitions. *Phys. Rev. Lett.* **114**, 035702 (2015).
5. Rothörl, J. Particle-based computer simulations of magnetic skyrmions. (Johannes Gutenberg-Universität Mainz, Mainz, 2024).
6. Anderson, J. A., Glaser, J. & Glotzer, S. C. HOOMD-blue: A Python package for high-performance molecular dynamics and hard particle Monte Carlo simulations. *Comput. Mater. Sci.* **173**, 109363 (2020).

7. Song, C. *et al.* Commensurability between Element Symmetry and the Number of Skyrmions Governing Skyrmion Diffusion in Confined Geometries. *Adv. Func. Mater.* **31**, 2010739 (2021).
8. Deuschländer, S., Horn, T., Löwen, H., Maret, G. & Keim, P. Two-Dimensional Melting under Quenched Disorder. *Phys. Rev. Lett.* **111**, 098301 (2013).
9. Nelson, D. R. Reentrant melting in solid films with quenched random impurities. *Phys. Rev. B* **27**, 2902–2914 (1983).
10. Zahn, K. & Maret, G. Dynamic Criteria for Melting in Two Dimensions. *Phys. Rev. Lett.* **85**, 3656–3659 (2000).
11. Gruber, R. *et al.* 300-Times-Increased Diffusive Skyrmion Dynamics and Effective Pinning Reduction by Periodic Field Excitation. *Adv. Mater.* **35**, 2208922 (2023).
12. Huang, P. *et al.* Melting of a skyrmion lattice to a skyrmion liquid via a hexatic phase. *Nat. Nanotechnol.* **15**, 761–767 (2020).
13. Kosterlitz, J. M. & Thouless, D. J. Long range order and metastability in two dimensional solids and superfluids. (Application of dislocation theory). *J. Phys. C: Solid State Phys.* **5**, L124 (1972).
14. Kosterlitz, J. M. & Thouless, D. J. Ordering, metastability and phase transitions in two-dimensional systems. *J. Phys. C: Solid State Phys.* **6**, 1181–1203 (1973).
15. Halperin, B. I. & Nelson, D. R. Theory of Two-Dimensional Melting. *Phys. Rev. Lett.* **41**, 121–124 (1978).
16. Nelson, D. R. & Halperin, B. I. Dislocation-mediated melting in two dimensions. *Phys. Rev. B* **19**, 2457–2484 (1979).
17. Lal, J., Abernathy, D., Auvray, L., Diat, O. & Grübel, G. Dynamics and correlations in magnetic colloidal systems studied by X-ray photon correlation spectroscopy. *Eur. Phys. J. E* **4**, 263–271 (2001).
18. Lhermitte, J. R. M., Rogers, M. C., Manet, S. & Sutton, M. Velocity measurement by coherent x-ray heterodyning. *Review of Scientific Instruments* **88**, 015112 (2017).

19. Klose, C. *et al.* Photon correlation spectroscopy with heterodyne mixing based on soft x-ray magnetic circular dichroism. *Phys. Rev. B* **105**, 214425 (2022).
20. Russell, E. R., Spaepen, F. & Weitz, D. A. Anisotropic elasticity of experimental colloidal Wigner crystals. *Phys. Rev. E* **91**, 032310 (2015).

10.2. Additional Results and Experimental Remarks

10.2.1. Optimizing Skyrmion Lattices for 2D Phase Observations

The skyrmion lattices with the highest number density (i.e., skyrmions per area) are not necessarily the best ordered. While the magnetic field can effectively tune the average skyrmion size [64, 117], individual skyrmions exhibit a distribution of sizes due to pinning effects and skyrmion-skyrmion interactions [64]. Moreover, the non-uniform energy landscape interacts with skyrmions of different sizes in distinct ways [64].

To achieve maximal lattice order, the skyrmions should ideally be as uniform in size as possible and minimally influenced by local energy inhomogeneities. In any case, the number of skyrmions decrease over the first seconds to minutes after nucleation due to spontaneous annihilation – even under constant field conditions, as shown in section 8.1. Additional field oscillations have been demonstrated to promote lattice ordering (section 8.1) but also enhance annihilation rates (section 8.1).

Observing a two-step melting process in 2D systems, as discussed in section 10.1, requires high-quality skyrmion lattices exhibiting translational order. This is particularly challenging in the present experimental system, where lattice order typically persists only over a few skyrmion distances. Even at short length scales, translational order is difficult to maintain, as minor distortions readily disrupt it. Whether the skyrmions self-organize accordingly is therefore difficult to control and reproduce.

My approach involves first nucleating a lattice with the highest possible skyrmion density, usually at a temperature increased by 2 to 3 K. Subsequently, I reduced the temperature to the value at which I have previously observed the best lattice quality. By tuning the magnetic field, I increase the skyrmion size [64, 117] and thereby the packing fraction. This denser arrangement forces skyrmions into quasi-lattice positions, improving overall order. In the best observed configuration – as shown, for instance, in section 10.1 – most skyrmions are similar in size (labbook experiment ID 7155). Nonetheless, the standard deviation of the skyrmion diameters of $(0.57 \pm 0.02) \mu\text{m}$ remains relatively large. However, the intrinsic flexibility of skyrmions enables them to locally adjust in size – either by extending or compressing (section 10.1.1) – which helps smoothing out local density variations [163]. This flexibility facilitates the accommodation of vacancies and interstitials with minimal impact on global lattice order (see Fig. 10.3 in the following section 10.2.2).

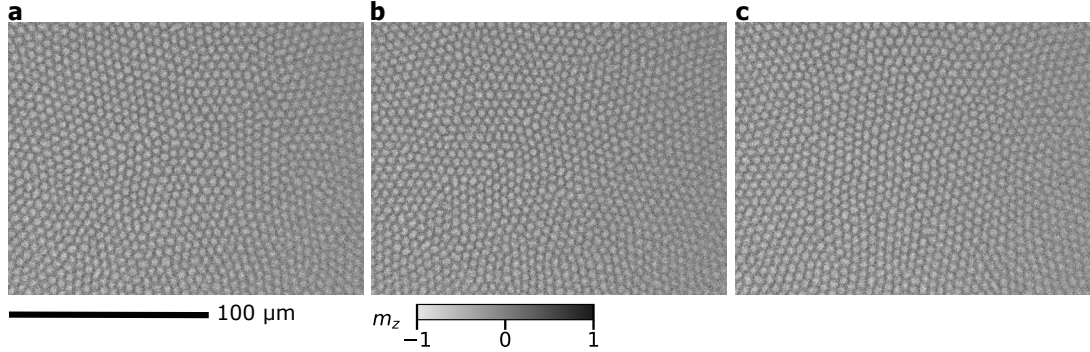


Figure 10.1.: Kerr Images of Skyrmion Lattices. Snapshots from Kerr microscopy experiments on sample FAB435 at 335.0 K and an applied magnetic field of (a) 85 μT ($\Psi_6 = 0.79$), (b) 80 μT ($\Psi_6 = 0.80$), and (c) 75 μT ($\Psi_6 = 0.83$). Images (a)–(b) were acquired approximately 4 min after nucleation; (c) was recorded 2 min after reducing the field from (b) to 75 μT .

An example of skyrmion lattice formation is shown in Fig. 10.1. The lattices in panels (a) and (b) are nucleated under identical conditions using an IP field pulse of 100 mT at an OOP field of 180 μT at 335.0 K. The relatively high field at nucleation leads to the formation of many small skyrmions. Subsequently, reducing the OOP field increased the packing fraction and, correspondingly, improved lattice order. Even though some skyrmions merge and the total number of skyrmions decreases, their shape remains largely symmetric, favoring order. Only when skyrmions elongate into stripe-like configurations, lattice order is compromised. The optimal field for achieving maximum lattice order in this case is (75 ± 2) μT . Despite greater size homogeneity at 80 and 85 μT , order is best at 75 μT . This can be attributed to the fact that the presence of vacancies and interstitials is more easily compensated by size variations, which in turn reinforces lattice fidelity.

After optimizing the OOP field, I apply field oscillations at 100 Hz, which is close to the frequency where the skyrmion diffusion peaks (section 5.1.1) [27]. Increasing the oscillation amplitude assists depinning and enhances the diffusion coefficient, but also contributes to skyrmion destabilization (section 8.1). This depinning is essential to allow skyrmions to rearrange into ideal lattice positions. However, the associated increase in diffusivity acts analogously to an elevated effective temperature, which can destabilize the lattice if excessive.

Large oscillation amplitudes capable of inducing annihilation can therefore reduce lattice order – a behavior comparable to that induced by large static fields. Nevertheless, this effect can be harnessed to regulate local skyrmion density. Because a nucleation can yield regions of locally elevated skyrmion density, strong field oscillations can selectively annihilate or merge skyrmions in these "overpopulated" areas, thereby promoting a more homogeneous lattice configuration [163]. This behavior, however, is highly non-deterministic, as the specific skyrmions that annihilate cannot be predicted with certainty. In section 10.1, I employ amplitudes up to $A = 150$ μT

(peak-to-peak) to induce annihilation in specific regions. However, if annihilation occurred elsewhere, the configuration is typically lost and the procedure has to be restarted (📖 labbook experiment ID 7155). In general, the amplitude A has to be tuned dynamically depending on the current skyrmion configuration. For moderate reconfiguration without inducing annihilation, amplitudes in the range of 80 to 100 μT are suitable.

In summary, there is no universal set of parameters that guarantees maximum lattice order. Notably, I have so far only been able to stabilize a translationally ordered skyrmion lattice once, despite hundreds of attempts. That singular measurement eventually formed the basis for our most successful analysis. The corresponding methods and theoretical context were developed in close collaboration with Prof. Peter Virnau and Prof. Asle Sudbø. It took more than a year to thoroughly analyze, interpret, and validate the results. Even the reproduction attempts provided crucial insights that contributed to our understanding of lattice stabilization under confinement.

10.2.2. Analysis of 2D Phase Behavior

10.2.2.1. Determination of Order

Once the skyrmion lattice is stabilized, tracking and order analysis becomes straightforward. The skyrmions are effectively confined by the surrounding lattice, suppressing diffusive motion and reducing fluctuations. This enhances imaging contrast and facilitates tracking based on single-frame images. Moreover, the skyrmions typically occur at regular distances, which makes the selection of appropriate *diameter* and *separation* parameters in *trackpy* [131, 132] highly effective. In the case of dense lattices, this method often outperforms the *UNET* algorithm [133], which is based on machine-learning.

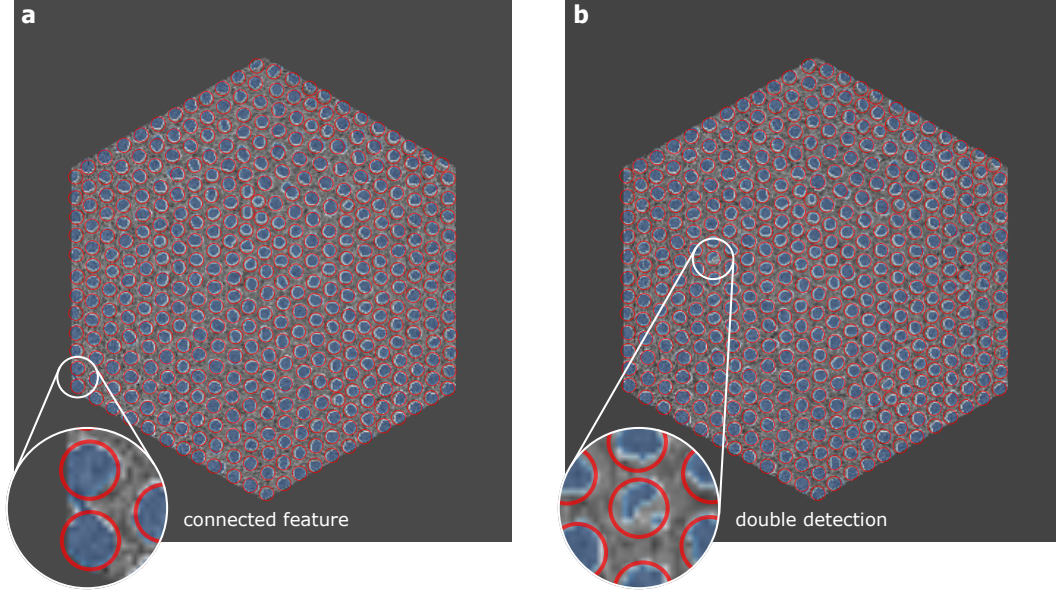


Figure 10.2.: Skyrmion Detection Comparison. (a) Detection of the skyrmions in a masked Kerr microscopy frame (grayscale background). The blue features are the skyrmions labeled by the *UNET*. The red circles mark the detections by *trackpy*. In the prediction by the *UNET*, two features are incorrectly connected and thus counted as one skyrmion. (b) Similarly, in the next frame, a skyrmion is incorrectly detected as two features by the *UNET*.

The performance of *trackpy* is robust within a relatively wide parameter range, typically exceeding 10%, without a noticeable degradation in detection quality. This robustness stems from the dense packing of skyrmions, where nearly every intensity peak corresponds to a real skyrmion, leaving little room for false positives. In contrast, *UNET* – in the versions available so far – often suffers from both false negatives (missed skyrmions) and false positives (merging of adjacent skyrmions into a single labeled feature). The predictions using the *UNET* were run by Kilian Leutner.

Despite these limitations, the *UNET* is very useful for determining skyrmion sizes, as it takes into account the actual extent of labeled features [133, 163], whereas *trackpy* measures the size based on the radius of gyration of a fitted Gaussian kernel [64, 132]. The orientational order of the lattice can be readily determined from the skyrmion positions. The local order parameter ψ_6 (Eq. 2.2) and the orientational correlation function $G_6(r)$ (Eq. 2.3) are computed directly from the Voronoi tessellation [162] of the lattice. These metrics are generally robust, even in the presence of detection errors. For example, a missing skyrmion in the nearest-neighbor shell of skyrmion j , as illustrated in Fig. 10.3, does not affect $\psi_6(\mathbf{r}_j)$ significantly, since the remaining neighbors contribute with nearly ideal 60° angular spacing. However, the missing particle leads to incorrect neighbor connections to second-nearest neighbors in the tessellation, which can affect $\psi_6(\mathbf{r}_j)$ to a limited extent, depending on the angles of the connections between neighbors.

10. Real-Time Observation of Topological Defect Dynamics Mediating 2D Skyrmion Lattice Melting

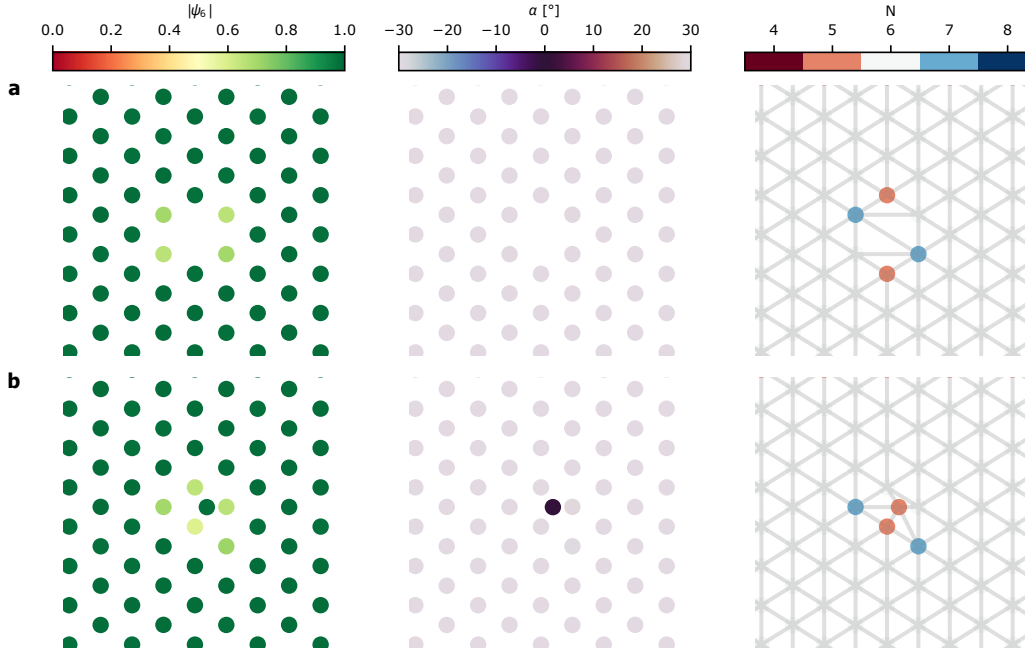


Figure 10.3.: Effect of Vacancies and Interstitials on Lattice Order. Local order parameter ψ_6 , lattice orientation α , and number of neighbors N per skyrmion in the presence of (a) a vacancy and (b) an interstitial. A vacancy induces topological defects ($N \neq 6$), slightly reduces ψ_6 , but does not influence α . An interstitial causes similar effects if symmetrically placed, but can perturb the orientation α if asymmetric. The exact defect configuration depends on the particle placement.

The most critical impact of detection errors arises in diffusion analysis and defect statistics. Missing detections break particle trajectories, reducing the accuracy of the diffusion coefficient D , while spurious detections may lead to incorrect trajectory linking. Moreover, false positives and negatives manifest as interstitials and vacancies, respectively, artificially increasing the number of topological defects [164, 165]. The translational correlation function $G_T(r)$ (Eq. 2.1) is only slightly affected by misdetections. Missing particles reduce G_T marginally, while additional detections primarily influence the correlation between the peaks, which are irrelevant for G_T . However, careful definition of the reciprocal lattice vector \mathbf{G} is essential. One approach is via Fourier transform, identifying the six peaks associated with hexagonal symmetry. However, these peaks are often insufficiently sharp for precise determination of \mathbf{G} . Instead, I construct \mathbf{G} from real-space data using the mean nearest-neighbor distance r_0 and the orientation ϕ of the confinement geometry. For instance, in section 10.1, I use $r_0 = 13.35$ px (equivalent to $8.66 \mu\text{m}$) and $\phi = 88.5^\circ$ relative to the x -axis. The corresponding reciprocal vector has modulus $G = \frac{4\pi}{\sqrt{3}r_0}$ and orienta-

tion $\phi = 90^\circ$ [3].

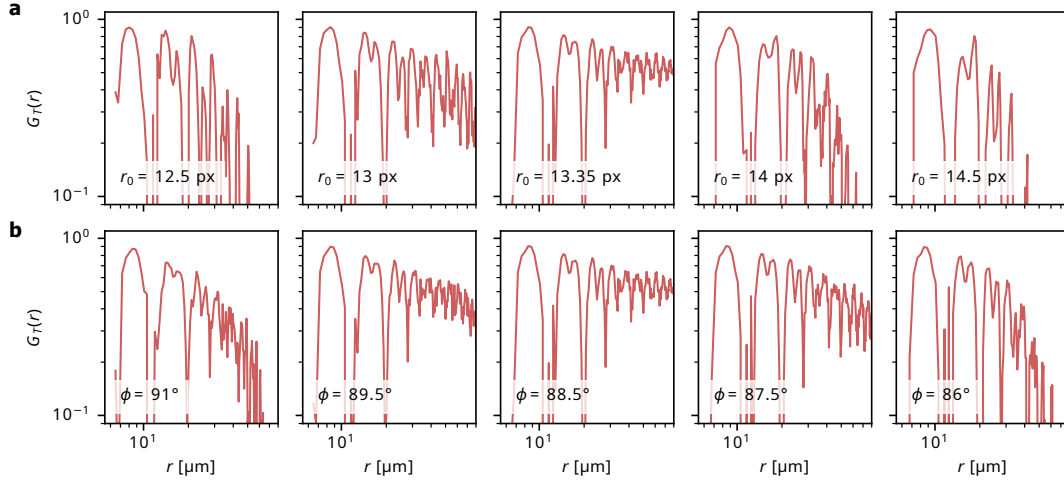


Figure 10.4.: G_T for Variations in the Reciprocal Lattice Vector. Effects of variations in the reciprocal lattice vector \mathbf{G} : (a) changes in r_0 , and (b) changes in ϕ significantly alter $G_T(r)$. The data corresponds to snapshot (i) in section 10.1, with $r_0 = (13.35 \pm 0.05)$ px and $\phi = (88.5 \pm 0.5)^\circ$. Here, 1 px equals $0.65 \mu\text{m}$.

Hence, precise selection of \mathbf{G} is vital for reliable $G_T(r)$. Even small deviations in r_0 or ϕ result in substantial differences in the correlation function. An additional complication in finite lattices is anisotropy. In Supplementary Fig. 1 (section 10.1.1), G_T varies across the three primary lattice directions, despite individual optimization. This reflects a slight anisotropy in the lattice structure, with directional variations in $r_0^{(i)}$ and $\phi^{(i)}$. Specifically, I find:

- $\mathbf{G}^{(1)}$: $r_0^{(1)} = (13.35 \pm 0.05)$ px, $\phi^{(1)} = (88.5 \pm 0.5)^\circ$,
- $\mathbf{G}^{(2)}$: $r_0^{(2)} = (13.35 \pm 0.05)$ px, $\phi^{(2)} = (33.0 \pm 0.5)^\circ$,
- $\mathbf{G}^{(3)}$: $r_0^{(3)} = (13.35 \pm 0.05)$ px, $\phi^{(3)} = (-32.0 \pm 0.5)^\circ$.

Although lattice vectors with non-six-fold symmetry can arise in deformed (e.g., sheared) lattices, the observed anisotropies are only viable on finite scales. On larger scales, they would disrupt QLRO [92].

10. Real-Time Observation of Topological Defect Dynamics Mediating 2D Skyrmion Lattice Melting

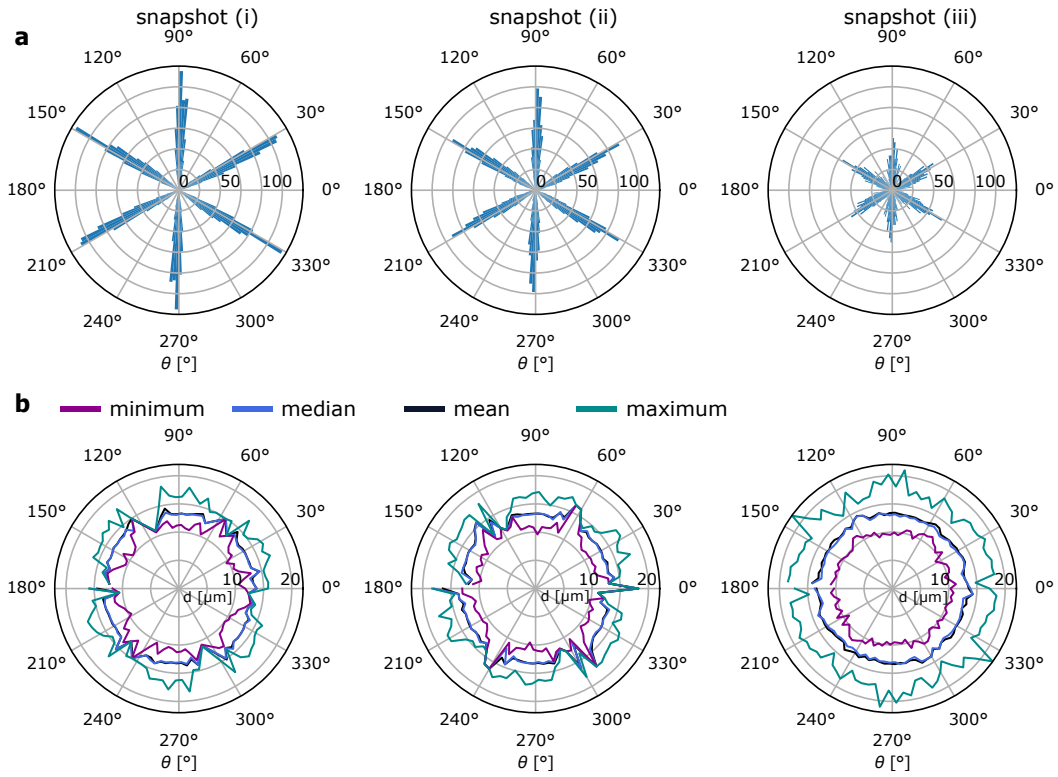


Figure 10.5.: Bond Angles and Lengths of Neighbor Connections. (a) Histogram of bond angle θ between neighboring skyrmions in snapshots (i)–(iii), using 1 s statistics and 2° bins. The angular distribution is initially peaked along lattice directions but becomes more uniform during melting. (b) Distance to nearest neighbors as a function of bond angle θ , using 1 s statistics and 4° bins. Despite lower statistics off the principal directions, a general broadening of bond lengths is observed toward the isotropic liquid state (snapshot iii).

It is not obvious which lattice direction yields the best translational order, so I optimized all three. To guide this, I analyzed bond angle and bond length distributions in Fig. 10.5. While sixfold symmetry is prominent in snapshot (i), this structure vanishes toward the liquid snapshot (iii). However, this analysis alone is insufficient to determine \mathbf{G} or to diagnose topological defects.

10. Real-Time Observation of Topological Defect Dynamics Mediating 2D Skyrmion Lattice Melting

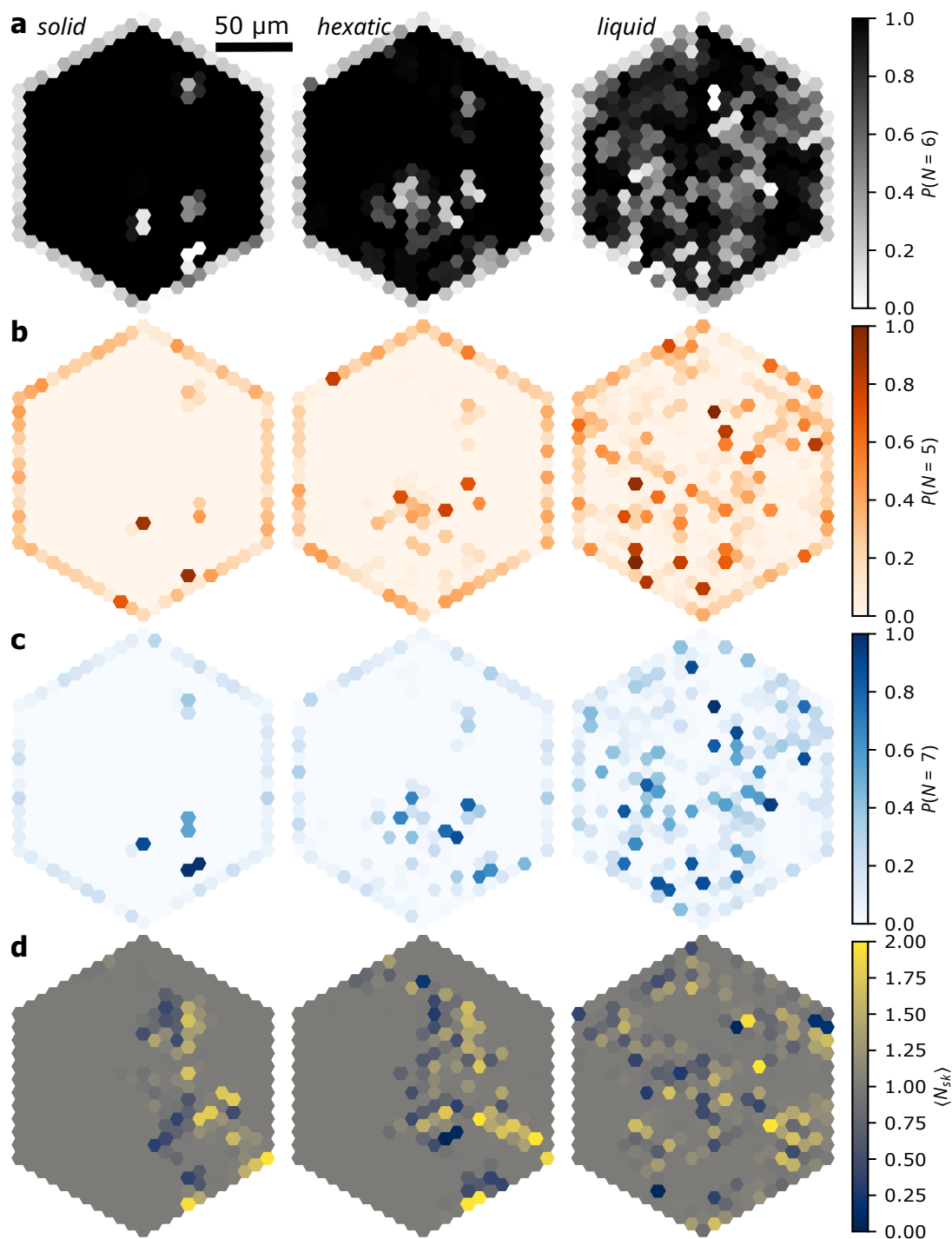


Figure 10.6.: Histogram of Skyrmion & Defect Occurrences. Spatial probability P of observing (a) a skyrmion with $N = 6$ neighbors, (b) a 5-fold defect, (c) a 7-fold defect, and (d) average skyrmion number $\langle N_{sk} \rangle$ per ideal lattice site. Statistics are gathered over 1 min intervals around snapshots (i)–(iii), representing the solid, hexatic, and liquid regimes.

The hexagonal boundary conditions offer another approach for spatially resolved analysis. Given the lattice orientation and a commensurate number of skyrmions N_{sk} , the skyrmion positions are essentially fixed. I therefore bin the sample into hexagonal cells along the ideal lattice sites and analyze the spatial distribution of skyrmions and defects relative to these positions. In this experiment, $N_{sk} = 401$, compared to the ideal centered hexagonal number 397, corresponding to four excess skyrmions. These introduce minor irregularities but do not preclude the analysis. Fig. 10.6 compares spatial defect distributions across the solid, hexatic, and liquid regimes.

10.2.2.2. Measuring Topological Defect Dynamics

A central advance in this study is the quantitative measurement of topological defect dynamics. In addition to imaging the defects with high temporal resolution, I present two complementary approaches for quantifying their dynamics.

The first method is based on tracking the trajectories of dislocations. These trajectories are obtained using *trackpy* [132], following the detection and classification of topological defects as described in section 10.1. From the tracked trajectories, we calculate the MSD and fit an effective diffusion coefficient D , as shown in Fig. 10.7. The MSD, however, exhibits sublinear growth in time t (Fig. 10.7a) – at least on the limited accessible time scale. In principle, the dynamics can be described by a generalized diffusion coefficient K_α , with $\text{MSD}(t) \propto K_\alpha t^\alpha$. However, since trajectory linking is only feasible over relatively short time intervals of a few seconds, the long-time behavior remains inaccessible. Therefore, rather than introducing speculative assumptions about the exact functional form of $\text{MSD}(t)$, we perform a linear fit to extract D for consistency and comparison. This choice allows us to directly compare D between skyrmions and topological defects, as both exhibit qualitatively similar MSD behavior on short time scales. In Fig. 10.7, we compare the time evolution of D obtained using different upper fit limits. As non-linear MSD causes D to depend on the (linear) fit range, the absolute values differ slightly between intervals. However, the trends are qualitatively consistent, corroborating the robustness of the analysis. Specifically, it confirms that dislocation diffusion increases markedly during the melting process. Nevertheless, the influence of the fitting interval must be taken into account when comparing D across different systems.

The second method utilizes a time-resolved boolean series assigned to each skyrmion, indicating whether it is classified as a lattice defect (see section 10.1). The autocorrelation decay of this series provides a quantitative measure of the defect dynamics. This approach is highly versatile and can be adapted to probe the dynamics of various defect types, including dislocations, disclinations, 5-defects, and 7-defects, by appropriately redefining the boolean series.

10. Real-Time Observation of Topological Defect Dynamics Mediating 2D Skyrmion Lattice Melting

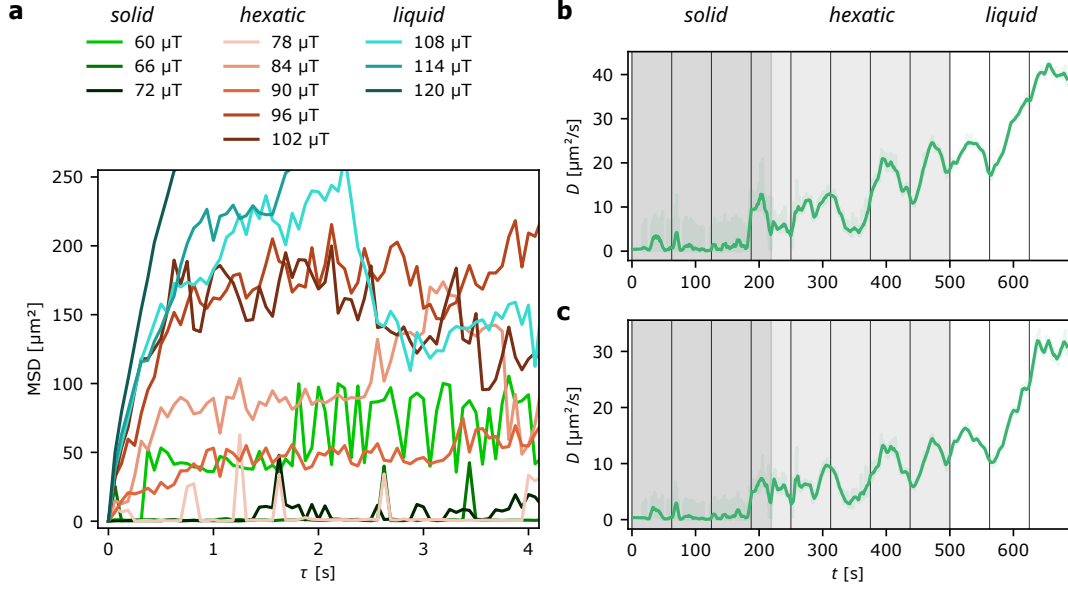


Figure 10.7.: Measuring the Dislocation Diffusion. (a) MSD of the tracked dislocations as a function of time delay τ for each field interval. Since only few dislocations exist, all trajectories within a 31 s window are used to improve statistics. The MSD clearly shows sublinear scaling. (b-c) Diffusion coefficient D fitted over different intervals: (b) 1 s and (c) 2 s. Although absolute values differ, the qualitative evolution of D remains robust. Full time resolution and a rolling mean over 6.25 s are shown.

In Fig. 10.8, I present the one-time correlation function $g_2(\tau)$ for different field intervals. Separate analyses are shown for 5- and 7-defects (Fig. 10.8b), as well as for dislocations and disclinations (Fig. 10.8c).

Across all defect types, $g_2(\tau)$ exhibits progressively faster decay during melting, indicating increasing defect mobility. However, the separated correlation functions offer further insight. While 5- and 7-defects yield nearly identical g_2 profiles, both decay more rapidly than the overall defect correlation. This initially counterintuitive result reflects that individual skyrmions may switch between defect types (e.g., from 5- to 7-defect), while remaining classified as a defect. Thus, the fluctuations in defect *type* are faster than the appearance or disappearance of defects themselves, a behavior also observed qualitatively in section 10.1, and now quantified.

10. Real-Time Observation of Topological Defect Dynamics Mediating 2D Skyrmion Lattice Melting

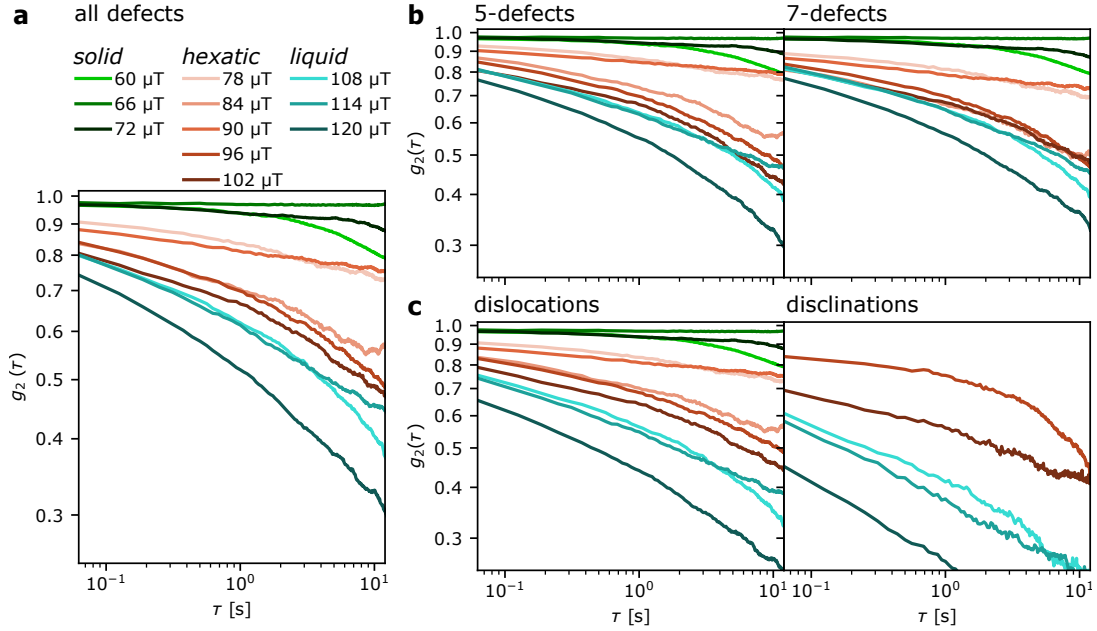


Figure 10.8.: Time-Correlation of Topological Defect Occurrences. (a) Time correlation $g_2(\tau)$ of all defect occurrences per skyrmion, as introduced in section 10.1. Faster decay with time delay τ corresponds to more rapid fluctuations. (b) g_2 evaluated separately for 5-defects and 7-defects. The curves are nearly identical, with 5-defects showing a slightly faster decay. In the hexatic regime, both fluctuate faster than the combined defect signal. (c) g_2 evaluated for dislocations and disclinations. Dislocations and disclinations begin to fluctuate faster in the hexatic regime. In the liquid regime, disclinations fluctuate even faster than dislocations. Note that disclinations are rare or absent in the solid and most of the hexatic regime, which prevents a meaningful evaluation of g_2 in this regime.

Similarly, dislocations and disclinations fluctuate more rapidly than defects in general starting in the hexatic regime. It is important to note that a meaningful evaluation of the correlation function g_2 for disclinations is not possible until deep into the hexatic regime, as the persistence of QLRO suppresses the formation of disclinations, rendering them either absent or exceedingly rare. However, once disclinations begin to emerge in the hexatic regime, their dynamic fluctuations quickly surpass those of dislocations – particularly in the liquid regime.

To validate the results shown in Fig. 5 of section 10.1, I repeat the analysis for a spatial subset comprising only half of the system while declaring the rest as "no defect". This yields deviations of only a few percent, confirming the robustness of the conclusions. Nonetheless, the specific spatial configuration can slightly affect the quantitative results, and this must be taken into account in comparisons.

10.2.2.3. Extraction of Shear and Strain

Elastic constants are directly linked to the two-dimensional phase behavior [91, 92], and thus provide macroscopic insights into the structural transitions of the system. For the analysis of the shear modulus, I quantify the deformation of the nearest-neighbor environment for each skyrmion. Starting from an initially ideal hexagonal shell, I locally fit a deformation tensor to match the experimental lattice configuration around each skyrmion. From this, I extract the corresponding strain tensor, which serves as the basis for calculating the local shear energy. The full procedure is described in detail in section 10.1. Given its non-trivial nature, I aim here to provide a reproducible framework for this analysis, which can serve future experiments.

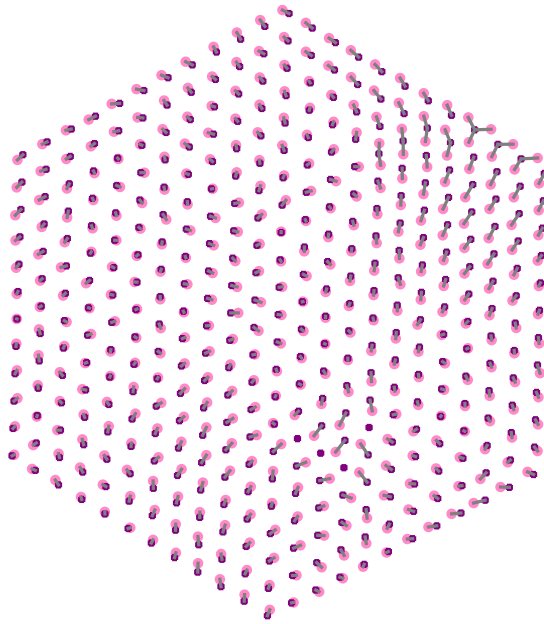


Figure 10.9.: Reference Lattice Fit. The larger pink dots represent the positions of skyrmions in the experiment. The smaller purple dots are fitted reference lattice. The gray lines connect every skyrmion with the closest reference lattice site. The reference lattice is fitted such that the total distance between experimental and reference lattice is minimal. Note that some reference sites are linked several times while other remain unconnected, which happens because of the distortion present in the incommensurate experimental lattice.

Initially, I fit a reference lattice to the most ordered frames of the experimental data, as illustrated in Fig. 10.9. Although this reference lattice is not strictly required for the local determination of the strain tensor or shear modulus – since each skyrmion is treated independently – it provides a useful visualization of the procedure and the global lattice structure. Due to the slightly incommensurate number of skyrmions (401 instead of 397 for a centered hexagonal configuration), local distortions are inevitable. These are reflected in the deviation between the experimental skyrmion positions (pink dots) and the corresponding reference lattice sites (purple plus signs). The gray lines connect each skyrmion to its nearest reference site, and larger displacements typically appear near topological defects – i.e., where lattice lines terminate or are disrupted.

In principle, a displacement field derived from this reference lattice could be used to calculate elastic moduli. However, because of the incommensurability, the mapping from experimental skyrmions to reference sites is non-unique: some reference sites may remain unassigned while others may be linked to multiple skyrmions. This ambiguity renders such a global approach unreliable.

Therefore, I instead rely exclusively on a local analysis: the strain tensor is determined by fitting the deformation tensor in the immediate neighborhood of each skyrmion. Even here, the assignment of reference sites plays a role. Since not all skyrmions have six neighbors, the deformation fit is based only on the best local matches. For example, in the case of a 5-defect, only the five nearest skyrmions are matched to five of the six ideal reference positions, leaving one reference site unused. Similarly, for a 7-defect, only six of the seven neighboring skyrmions are included in the fit. While this procedure may introduce systematic variations, these are expected to be small given the limited number of defects. A more general approach might include next-nearest neighbors or a larger neighborhood in the fitting procedure; however, this becomes increasingly unstable near domain boundaries.

Fig. 10.10 shows the distribution of the calculated shear energies, analogous to the results in section 10.1. The histogram displays the occurrence frequency of shear energy contributions associated with the off-diagonal strain components ϵ_{xy} . On a logarithmic scale, the shear modulus μ manifests as the linear decay slope of this distribution.

Fig. 10.10a reveals the full distribution across all energy values. Clearly, the decay of the probability P with increasing shear energy E_{shear} is not purely exponential. A prominent peak at very low energies (close to zero) is visible, which has also been reported in previous studies [166]. At higher energies, the distribution flattens and displays a noisy background beyond $1.3 \cdot 10^{10} \mu k_B T$. This flattening may result from fitting artifacts, such as imperfect neighbor matching, the assumption of linear elasticity (which breaks down for large deformations), or the truncation of the fitting domain to nearest neighbors only. Nevertheless, such high-energy occurrences are rare and can be considered outliers compared to the well-behaved statistics at low energies.

To obtain a reliable estimate of μ , I restrict the fit range to a well-defined interval of shear energies. Fig. 10.10b focuses on this range for improved clarity. To avoid

10. Real-Time Observation of Topological Defect Dynamics Mediating 2D Skyrmion Lattice Melting

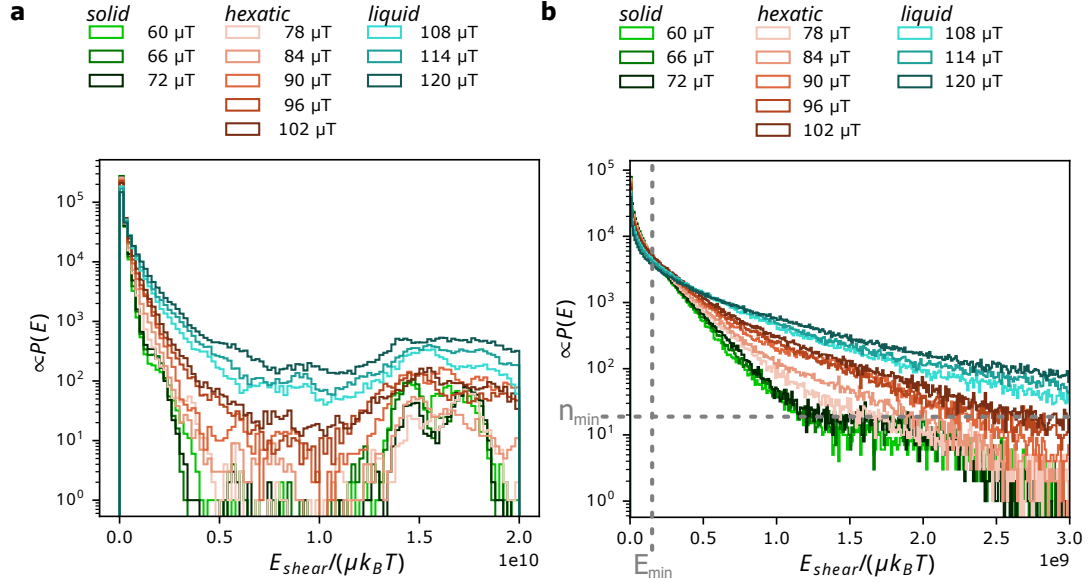


Figure 10.10.: Shear Energy Distribution. (a) Occurrence probability $P(E)$ of the energies corresponding to the determined shearing components. Note that the shear energies E_{shear} depends still on the shear modulus μ and is therefore not a true energy but a measure for the energy. The increasing values for large energies resemble artifacts due to the applied methods and are unphysical. (b) The same distribution on a truncated energy scale yields a close-to linear decay. To determine the slope yielding μ , I apply a low-statistics cutoff n_{min} and a low-energy cutoff E_{min} (here shown schematically only).

bias from the low-energy peak, I introduce a lower cutoff E_{min} ; similarly, to exclude the lacking statistics at high-energy, I apply a statistics cutoff n_{min} , disregarding the distribution after it drops below n_{min} entries. Because both cutoffs are an arbitrary choice, I systematically analyze their influence in Fig. C.2 and Fig. C.3, respectively. Within a broad and stable region – specifically, for $10 < n_{\text{min}} < 20$ (using energy bins of width $1 \cdot 10^8 \mu k_B T$) and $1 < E_{\text{min}} [10^8 \mu k_B T] < 6$ – the extracted values of μ remain consistent. Note that the energy, which I refer to here, contains units of the shear modulus μ due to the procedure and is therefore strictly speaking not an energy, but a measure of the energy. I average the results across this parameter space and report the mean value of μ along with its standard deviation as the associated uncertainty. Although the absolute values of μ remain uncertain, the qualitative trend is robust and in good agreement with predictions from KTHNY theory [97–99]. Finally, the present analysis assumes the shear energy (as one component of the total deformation energy) to follow a Boltzmann distribution. The complementary contribution stems from the isotropic strain energy, associated with the bulk modulus B (see Eq. 2.7). However, unlike the shear component – which scales quadratically with ϵ_{xy} and is associated with a clean exponential in the energy distribution – the isotropic strain energy involves a more complex combination of both bulk and shear

terms. Consequently, it is not possible to directly extract B using this method alone.

10.2.3. Non-Equilibrium Lattice Dynamics

Since our skyrmion lattice can be driven into disorder either by shrinking the skyrmions or by increasing their diffusivity, a combined approach – shrinking the skyrmions while applying an oscillating field – is also feasible. Here, I present a measurement in which the skyrmion lattice is melted to disorder by reducing the packing fraction (via skyrmion size reduction), while an oscillating magnetic field of constant amplitude $A = 60 \mu\text{T}$ and frequency 100 Hz is applied. This oscillating field continuously drives the skyrmion size out of equilibrium [163, 167]. The procedure thus enables the investigation of non-equilibrium phenomena in two-dimensional phase transitions, which remains a vibrant and active area of research.

This experiment is based on the same initial nucleation as used in section 10.1. After the described melting procedure, the lattice is re-stabilized by increasing the skyrmion size (and thus the packing fraction), and field oscillations of varying strength were applied as described in section 10.2.1. As a result, 398 of the initially nucleated 401 skyrmions remained. With the oscillating field ($A = 60 \mu\text{T}$, peak-to-peak, and $f = 100 \text{ Hz}$) permanently activated, I again decreased the skyrmion packing fraction by incrementally increasing the applied magnetic field. The resulting analysis, presented in Fig. 10.11, mirrors the methodology used for the equilibrium melting case discussed earlier.

10. Real-Time Observation of Topological Defect Dynamics Mediating 2D Skyrmion Lattice Melting

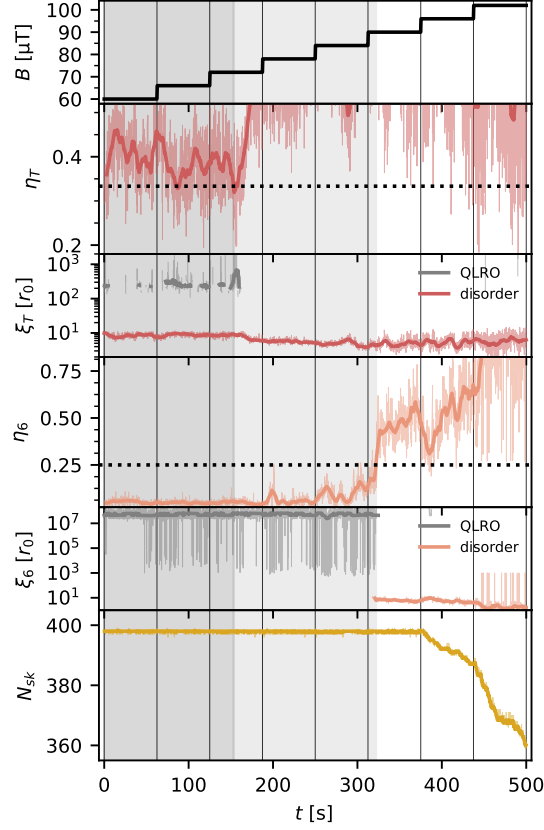


Figure 10.11.: Melting by Skyrmion Shrinking under Field Excitation. The applied magnetic field is increased in steps of $6 \mu\text{T}$ every 62.5 s (corresponding to 1000 frames), leading to a gradual shrinking of the skyrmions. An additional oscillating field ($f = 100 \text{ Hz}$, $A = 60 \mu\text{T}$, peak-to-peak) is permanently active. As the packing fraction is reduced, the exponent η_T of G_T increases – from values near the critical threshold of $1/3$ (indicated by the dashed black line) to values clearly exceeding it. The corresponding correlation length ξ_T spans the system size for QLRO (red) and matches the system size in the disordered regime (gray) separately as the determination method is different for both regimes. Due to the only few points of translational QLRO, intermediate only few values are visible. Similarly, the orientational exponent η_6 of G_6 rises with decreasing skyrmion size, crossing the critical threshold of $1/4$ (dashed black line). The associated correlation length ξ_6 decreases from values well above to approximately the system size. The number of skyrmions N_{sk} remains constant until the liquid regime is reached, where the oscillating field destabilizes skyrmions and leads to their annihilation. Thick lines show a rolling mean over 6.25 s (10 frames); thin lines indicate frame-to-frame fluctuations. Background shading represents the degree of order: white (isotropic liquid), light gray (hexatic regime), and dark gray (fluctuating solid-like states).

Initially, the translational correlation exponent η_T hovers near the critical value of $1/3$. Although it drops below this threshold in a few individual frames, translational order is not well-established – and when present, remains highly unstable. This instability may arise from the additional fluctuations introduced by the oscillating field, the specific skyrmion configuration (see section 10.2.1), or both – ultimately preventing the emergence of robust translational QLRO. Around $t \approx 150$ s, η_T increases significantly above the critical value, indicating that the system is no longer near the onset of a solid lattice state. At this stage, the correlation length ζ_T is comparable to the system size, consistent with the absence of QLRO. In rare frames where $\eta_T < 1/3$ (i.e., translational order exists), the correlation length exceeds the system size but remains around $10^2 r_0$ – much smaller than in the case without excitation – suggesting only marginal translational QLRO.

To further characterize the system, I tracked the number of skyrmions N_{sk} over time. The oscillating field, known to destabilize skyrmions [27], enhances their annihilation during shrinkage, thereby reducing N_{sk} . However, this reduction begins only in the isotropic liquid regime, where QLRO has already vanished. Thus, the method remains suitable for probing two-dimensional melting, even under non-equilibrium conditions arising from the continuous size modulation.

Interestingly, the initial count of $N_{\text{sk}} = 398$ is only one above the commensurate value of 397 for a centered hexagonal lattice, potentially enabling near-ideal ordering. Nonetheless, the system consistently exhibits multiple defects. Moreover, due to the enhanced diffusive dynamics under excitation [27], the defect configurations fluctuate more strongly than in the equilibrium case. Fig. 10.12 visualizes these fluctuating defects across consecutive frames, each displaying a distinct defect landscape.

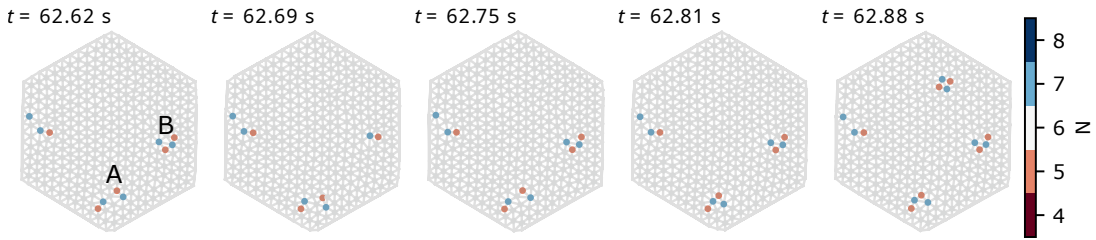


Figure 10.12.: Maps of Fluctuating Lattice Defects under Field Excitation. Gray lines show nearest-neighbor connections between skyrmions at various times t . Colored dots indicate the number of lattice neighbors N . Defect configurations change noticeably from frame to frame – much more than in the absence of field excitation. Labels A and B highlight defects with especially frequent rearrangements.

Fig. 10.12 further illustrates the dynamics of interacting lattice defects. While the configurations at $t = 62.62$ s and $t = 62.81$ s are nearly equivalent, the others are distinct. Notably, the dislocation labeled A shifts downward between these frames. This motion involves a non-trivial rearrangement: the two dislocations labeled B merge into a single dislocation. In contrast, the subsequent shift of A at $t = 62.81$ s occurs without further rearrangement. In the final snapshot, a dislocation pair – frequently observed

under excitation – reappears. These rapid and frequent fluctuations in topological defects suggest that measurements under field excitation could serve as a promising testbed for developing and validating defect interaction potentials.

A particularly intriguing phenomenon emerged during tests of lattice formation in non-flat energy landscapes under oscillating fields: the formation of spiral domains once the oscillation amplitude A exceeds a certain threshold. When the field amplitude is ramped up from an initial skyrmion lattice state, the lattice begins to shake, followed by skyrmion annihilation and eventual merging into spiral structures. As illustrated in Fig. 10.13, these spirals appear to nucleate at pinning centers, recurring at consistent positions upon repeated trials. Their centers remain fixed in space over time. The spirals expand and rotate continuously until the available space is filled. Occasionally, the direction of rotation reverses for short periods. Overall, spirals of both helicities tend to emerge adjacent to one another. The underlying mechanism for this spiral formation is currently under investigation in a project led by Jun.-Prof. Dr. Michael te Vrugt.

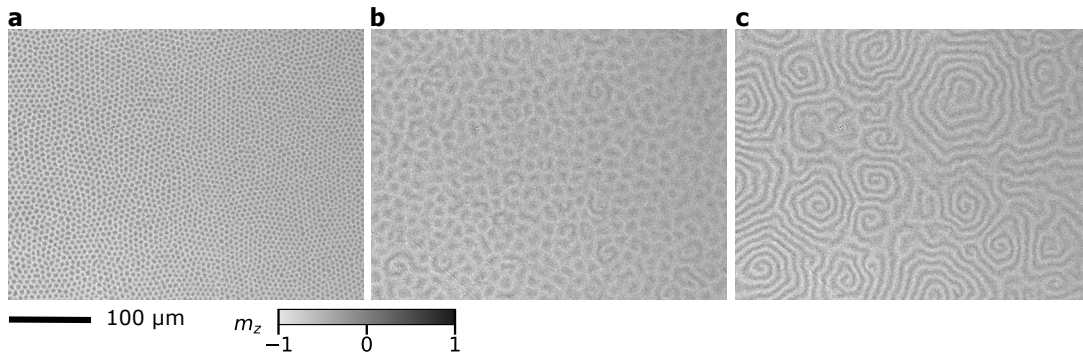


Figure 10.13.: Formation of Spiral Magnetic Domains. (a) Starting from a skyrmion lattice, an OOP field oscillation at $f = 100$ Hz is applied while the amplitude A is gradually increased. Initially, the number of skyrmions decreases slowly, then more drastically. (b) At $A \approx 150 \mu\text{T}$, remaining skyrmions elongate into stripes and rotate around fixed centers, forming spirals. (c) These spirals grow and rotate until the system is filled, with motion eventually suppressed by spatial constraints, here imaged 1 min after start.

10.3. Author Contributions

I performed all the experiments at the Kerr microscope on my own. The majority of the data analysis shown here was done by me and I also developed the used Python code. I specifically performed the skyrmion detection using *trackpy* [132], calculated the Voronoi tessellation, neighbor connections, local order parameter and correlation functions. I was provided with existing code for the analysis of ψ_6 and G_6 by Jan Rothörl. I used this code as basis to rewrite the analysis from scratch to optimize robustness and efficiency.

I performed the analysis of the shear modulus based on existing works [166, 168] as

suggested by Thomas Palberg. Also, I calculated the time correlation of defect occurrences based on my own idea and with the consulting help of Christopher Klose. I also established the identification procedure of topological defects as dislocations and disclinations as well as the method to link dislocation trajectories in order to determine their diffusion coefficient. The detection runs using the *UNET* [133] (using three models applied to one video) was run by Kilian Leutner.

The simulations in this project were all conducted by Jan Rothörl with the support of Simon M. Fröhlich and Maarten A. Brems. Jan Rothörl and Simon M. Fröhlich also developed their analysis code further and we used the two independent code sets to validate our results. Particularly, Simon and Jan always calculated ψ_6 independently for the simulation data. Simon M. Fröhlich established the defect clustering algorithm.

The magnetic multilayer sample was deposited by Fabian Kammerbauer, the patterning of the geometric confinements was done by Elizabeth M. Jefremovas. However, I also used samples grown by Maria-Andromachi Syskaki while encountering the reported effect and while gathering data to design the final experiment.

Sachin Krishnia and Elizabeth M. Jefremovas especially helped me in developing the experiment, the data interpretation and writing the article during frequent discussions in their function as postdoctoral researchers.

Asle Sudbø, Peter Virnau and Mathias Kläui supervised and guided this work. Asle Sudbø helped and guided me to develop analysis methods particularly regarding correlation functions, the occurrence of topological defects and the shear modulus. Peter Virnau and Mathias Kläui contributed as PhD supervisors and principal investigators in our skyrmion research group and provided advice in regular discussions.

11. Conclusion – Formation & Phase Behavior of 2D Skyrmion Lattices

11.1. Summary

In summary, we stabilize skyrmion lattices in CoFeB thin films and observe the lattices in real-time and real-space using Kerr microscopy.

Due to the non-flat energy landscape of the materials, a state containing multiple lattice domains forms. Applying magnetic field oscillations effectively reduces the energy landscape and can be used to drastically enhance the lattice domain size and average local order. However, remaining pinning effects are still present and cause domain boundaries between the remaining lattice domains. We find that those domain boundaries are effectively pinned by features in the energy landscape, which are not commensurate with the hexagonal skyrmion lattice structure. Thus, effectively confining the lattice domains. In artificially patterned confinement geometries, we furthermore find that the confinement geometry influences and controls the lattice order. While a hexagonal confinement, which is commensurate with the hexagonal skyrmion lattice structure, enhances lattice order, other, incommensurate confinement geometries reduce the lattice order.

In a hexagonal confinement, we even manage to stabilize a skyrmion lattice fulfilling translational order, i.e., corresponding to solid order. We melt this lattice to disorder by reducing the skyrmion size and thus the packing fraction on the fly. Alternatively, we can increase the skyrmion diffusivity by magnetic field oscillations to destabilize and melt the lattice. Due to our real-space and real-time imaging method, we can directly identify the emergence and dynamics of topological defects during 2D KTHNY melting, which is challenging in other systems due to lacking tunability of the system or insufficient imaging resolution.

11.2. Challenges

Challenges remain both for experiments and theory. In the experiment, advancing lattice order towards true QLRO or at least longer length scales is a key step in order to use skyrmion lattices in CoFeB thin films for novel insights into 2D phase behavior. Both advances in the material composition and growth optimization but also additional experimental methods in order to stabilize the actual skyrmion lattice can contribute. An experimental technique that could be helpful is to also consider alternating currents, which can induce a shaking effect similar to the magnetic field

oscillations but provide an additional skyrmion depinning mechanism [71]. Another approach could be based on using surface acoustic waves, for instance induced using a piezoelectric substrate [148]. These approaches may then require adjustment of the experimental procedure or material composition to still feature densely-packed skyrmion lattices of at least the known quality in terms of ordering.

Such a larger system with correspondingly better foundation for statistical analyses can finally provide the possibility to extract the interaction potential of topological defects, which is the key experimental challenge regarding the defect interaction potential. However, from the theoretical perspective, it remains an open question how this interaction potential can be determined in an adequate way. Statistics on the inter-defect distances as previously established for the interaction potential between skyrmions [70] may not be sufficient, since the topological defects are non-trivially but formally bound; introducing possible conditions on the position, distance and propagation direction of a defect, that may be of a complex nature and go beyond a radial potential function for describing the defect interaction potential.

Another theoretical challenge is to translate existing scaling laws close to the phase transitions into the experimental parameter space. Theoretical frameworks typically describe melting by an increase in temperature. However, since we drive the transitions in an entropy-mediated way tuning for instance the packing fraction, corresponding scaling laws for instance of the correlation lengths and the Young's modulus [91, 92] can give insight into universality class of the phase transitions.

A further open question is the theoretical description of phase transitions both in non-equilibrium systems as well as under the presence of a Magnus force. Both can or could be realized with skyrmions [163]. Experimentally however, a system showing 2D skyrmion lattice order, exhibiting rich dynamics and tunability over phase transitions, and exhibiting a sizable Magnus force while being observable with sufficient resolution in time and space remains a challenge.

Furthermore, it remains a challenge to extract a second elastic constant to capture the full elastic properties of the observed skyrmion lattices. To do so, an existing framework [166] could be translated to a hexagonal lattice structure. Additionally, experimental means to apply controlled stress to the skyrmion lattice – for instance, by local stray fields [56] – would be helpful to directly determine the elastic constants from the resulting displacement field. The method applying real-space fitting of a strain tensor to particle coordinates [163, 166, 168] requires linear elasticity and does not yield quantitatively reliable values [163].

11.3. Outlook

In the future, skyrmion lattice can be utilized for several novel investigations of 2D phase behavior. In short term, lattices in parallelogram confinements (see section 9.2.1) can be utilized to introduce an artificial shearing to the lattice and study the topological defect dynamics under applied shear. Also, controlled manipulation of the energy landscape [88, 89] can be used to create pinning sites on ideal lattice

positions, which may be used to stabilize a larger-scale skyrmion lattice in CoFeB thin films artificially and extend the capabilities of the system for further lattice investigations – potentially obeying distinct scaling laws [169].

In more advanced projects, skyrmion lattices – with their tunability and possibility to be observed with high resolution in real-time and -space – can give valuable and novel possibilities to determine and study interaction potentials between topological defects. Also, driving mechanism by magnetic or electric fields pave the way to study emergent phase 2D behavior when driving the system out of equilibrium – and to study a non-equilibrium extension of KTHNY theory.

On the longer time scale, skyrmions may eventually be used to study 2D phase behavior under presence of a sizable Magnus force. For this, a system showing 2D skyrmion lattice order and exhibiting a sizable Magnus force, which however keeps the rich dynamics and tunability over phase transitions as well as the possibility to be observed with sufficient resolution in time and space. Besides lattice properties being important for high density data storage and processing applications, even skyrmion lattice defects could theoretically be used for information transport. If topological defects can be reliably controlled to occur and fluctuate between fixed positions, this is possible if the involved skyrmions' positions can be read out efficiently and precisely.

Back Matter

A. Overall Conclusion & Outlook

In conclusion, the investigation of skyrmion dynamics provides valuable insights into both their static and dynamic properties, which are relevant not only for the design of novel spintronic devices but also for the study of fundamental two-dimensional physics.

While the determination of the energy landscape [64] and the enhancement of diffusion [27] have become established techniques, several open questions remain. On the one hand, the microscopic origin of the energy landscape modulation on the atomic scale requires further clarification. Electron microscopy studies of the thin-film layers and their interfaces could provide important insights in this regard. On the other hand, the precise mechanism underlying oscillating-field-enhanced diffusion and the associated effective pinning reduction [27] is still not fully understood. A promising direction is to compare the system to flashing-potential models and to employ measurements with higher temporal resolution as well as coherent correlation imaging [144]. In my view, one of the main remaining questions is which alternative external stimuli – such as electric currents [15], surface acoustic waves [148], or locally applied fields [56] and heating – can induce comparable effects, and which of these are integrable into nanoscale devices with high efficiency. From a fundamental perspective, a central open question is whether such driven systems can achieve faster-than-free diffusion, i.e., exceed the diffusion expected for a given spin structure and temperature in a flat potential. A major milestone would for instance also be the observation of diffusion with a sizable Magnus force and odd diffusivity [147, 170].

The formation of skyrmion lattices constitutes another well-established yet highly intriguing phenomenon. Although the detailed investigation of lattice domain formation in non-flat energy landscapes and under confined geometries is system-specific [171], it nonetheless provides important general insights into the behavior of skyrmions in dense configurations – a factor of high relevance for nanoscale device design, where material imperfections and geometric confinement are unavoidable [172]. The most important finding, however, is the observation of two-dimensional phase behavior and the direct imaging of topological defect dynamics even on finite length scales [173]. The on-the-fly tunability of skyrmion size and diffusivity provides a degree of flexibility not found in other two-dimensional systems and thereby

opens up unique opportunities. A key question for the future is whether lattice order in such tunable and highly dynamic systems can be stabilized over larger scales, thus enabling further studies of two-dimensional phase phenomena with significantly improved statistics. Furthermore, it remains to be explored whether additional key features – such as non-equilibrium effects induced by oscillating fields, artificially stabilized lattices, or the presence of a sizable Magnus force – can be incorporated to broaden the scope of observable phenomena within an extended framework.

B. References

- (1) Coey, J. M. D.,
Magnetism and Magnetic Materials;
Cambridge University Press: Cambridge, 2010,
DOI: [10.1017/CB09780511845000](https://doi.org/10.1017/CB09780511845000).
- (2) Guimarães, A. P.,
Principles of Nanomagnetism;
NanoScience and Technology;
Springer-Verlag: Berlin Heidelberg, 2009,
DOI: [10.1007/978-3-642-01482-6](https://doi.org/10.1007/978-3-642-01482-6).
- (3) Kittel, C.,
Introduction to Solid State Physics, 8th Edition;
Wiley John + Sons: Hoboken, NJ, 2004; 704 pp.
- (4) Grünberg, P.; Schreiber, R.; Pang, Y.; Brodsky, M. B.; Sowers, H.
Physical Review Letters **1986**, 57, 2442–2445,
DOI: [10.1103/PhysRevLett.57.2442](https://doi.org/10.1103/PhysRevLett.57.2442).
- (5) Binash, G.; Grünberg, P.; Saurenbach, F.; Zinn, W.
Physical Review B **1989**, 39, 4828–4830,
DOI: [10.1103/PhysRevB.39.4828](https://doi.org/10.1103/PhysRevB.39.4828).
- (6) Julliere, M.
Physics Letters A **1975**, 54, 225–226,
DOI: [10.1016/0375-9601\(75\)90174-7](https://doi.org/10.1016/0375-9601(75)90174-7).
- (7) Miyazaki, T.; Tezuka, N.
Journal of Magnetism and Magnetic Materials **1995**, 139, L231–L234,
DOI: [10.1016/0304-8853\(95\)90001-2](https://doi.org/10.1016/0304-8853(95)90001-2).
- (8) Parkin, S. S. P.; Kaiser, C.; Panchula, A.; Rice, P. M.; Hughes, B.; Samant, M.;
Yang, S.-H.
Nature Materials **2004**, 3, 862–867,
DOI: [10.1038/nmat1256](https://doi.org/10.1038/nmat1256).
- (9) Hirohata, A.; Yamada, K.; Nakatani, Y.; Prejbeanu, I.-L.; Diény, B.; Pirro, P.;
Hillebrands, B.
Journal of Magnetism and Magnetic Materials **2020**, 509, 166711,
DOI: [10.1016/j.jmmm.2020.166711](https://doi.org/10.1016/j.jmmm.2020.166711).
- (10) Bogdanov, A.; Hubert, A.
Journal of Magnetism and Magnetic Materials **1994**, 138, 255–269,

B. References

- DOI: [10.1016/0304-8853\(94\)90046-9](https://doi.org/10.1016/0304-8853(94)90046-9).
- (11) Rößler, U. K.; Bogdanov, A. N.; Pfeleiderer, C.
Nature **2006**, *442*, 797–801,
DOI: [10.1038/nature05056](https://doi.org/10.1038/nature05056).
- (12) Mühlbauer, S.; Binz, B.; Jonietz, F.; Pfeleiderer, C.; Rosch, A.; Neubauer, A.; Georgii, R.; Böni, P.
Science **2009**, *323*, 915–919,
DOI: [10.1126/science.1166767](https://doi.org/10.1126/science.1166767).
- (13) Romming, N.; Hanneken, C.; Menzel, M.; Bickel, J. E.; Wolter, B.; von Bergmann, K.; Kubetzka, A.; Wiesendanger, R.
Science **2013**, *341*, 636–639,
DOI: [10.1126/science.1240573](https://doi.org/10.1126/science.1240573).
- (14) Woo, S. et al.
Nature Materials **2016**, *15*, 501–506,
DOI: [10.1038/nmat4593](https://doi.org/10.1038/nmat4593).
- (15) Litzius, K. et al.
Nature Physics **2017**, *13*, 170–175,
DOI: [10.1038/nphys4000](https://doi.org/10.1038/nphys4000).
- (16) Yu, X. Z.; Onose, Y.; Kanazawa, N.; Park, J. H.; Han, J. H.; Matsui, Y.; Nagaosa, N.; Tokura, Y.
Nature **2010**, *465*, 901–904,
DOI: [10.1038/nature09124](https://doi.org/10.1038/nature09124).
- (17) Seki, S.; Yu, X. Z.; Ishiwata, S.; Tokura, Y.
Science **2012**, *336*, 198–201,
DOI: [10.1126/science.1214143](https://doi.org/10.1126/science.1214143).
- (18) Yu, X. Z.; Kanazawa, N.; Onose, Y.; Kimoto, K.; Zhang, W. Z.; Ishiwata, S.; Matsui, Y.; Tokura, Y.
Nature Materials **2011**, *10*, 106–109,
DOI: [10.1038/nmat2916](https://doi.org/10.1038/nmat2916).
- (19) Zázvorka, J.; Jakobs, F.; Heinze, D.; Keil, N.; Kromin, S.; Jaiswal, S.; Litzius, K.; Jakob, G.; Virnau, P.; Pinna, D.; Everschor-Sitte, K.; Rózsa, L.; Donges, A.; Nowak, U.; Kläui, M.
Nature Nanotechnology **2019**, *14*, 658–661,
DOI: [10.1038/s41565-019-0436-8](https://doi.org/10.1038/s41565-019-0436-8).
- (20) Fert, A.; Reyren, N.; Cros, V.
Nature Reviews Materials **2017**, *2*, 1–15,
DOI: [10.1038/natrevmats.2017.31](https://doi.org/10.1038/natrevmats.2017.31).
- (21) Tokura, Y.; Kanazawa, N.
Chemical Reviews **2021**, *121*, 2857–2897,
DOI: [10.1021/acs.chemrev.0c00297](https://doi.org/10.1021/acs.chemrev.0c00297).

- (22) Everschor-Sitte, K.; Masell, J.; Reeve, R. M.; Kläui, M.
Journal of Applied Physics **2018**, *124*, 240901,
DOI: [10.1063/1.5048972](https://doi.org/10.1063/1.5048972).
- (23) Reichhardt, C.; Reichhardt, C. J. O.; Milošević, M. V.
Reviews of Modern Physics **2022**, *94*, 035005,
DOI: [10.1103/RevModPhys.94.035005](https://doi.org/10.1103/RevModPhys.94.035005).
- (24) Hubert, A.; Schäfer, R.,
Magnetic Domains: The Analysis of Magnetic Microstructures;
Springer-Verlag: Berlin Heidelberg, 1998,
DOI: [10.1007/978-3-540-85054-0](https://doi.org/10.1007/978-3-540-85054-0).
- (25) Heinze, S.; von Bergmann, K.; Menzel, M.; Brede, J.; Kubetzka, A.; Wiesen-
danger, R.; Bihlmayer, G.; Blügel, S.
Nature Physics **2011**, *7*, 713–718,
DOI: [10.1038/nphys2045](https://doi.org/10.1038/nphys2045).
- (26) Nagaosa, N.; Tokura, Y.
Nature Nanotechnology **2013**, *8*, 899–911,
DOI: [10.1038/nnano.2013.243](https://doi.org/10.1038/nnano.2013.243).
- (27) Gruber, R.; Brems, M. A.; Rothörl, J.; Sparmann, T.; Schmitt, M.; Kononenko,
I.; Kammerbauer, F.; Syskaki, M.-A.; Farago, O.; Virnau, P.; Kläui, M.
Advanced Materials **2023**, *35*, 2208922,
DOI: [10.1002/adma.202208922](https://doi.org/10.1002/adma.202208922).
- (28) Seki, S.; Suzuki, M.; Ishibashi, M.; Takagi, R.; Khanh, N. D.; Shiota, Y.; Shibata,
K.; Koshibae, W.; Tokura, Y.; Ono, T.
Nature Materials **2022**, *21*, 181–187,
DOI: [10.1038/s41563-021-01141-w](https://doi.org/10.1038/s41563-021-01141-w).
- (29) Wolf, D.; Schneider, S.; Rößler, U. K.; Kovács, A.; Schmidt, M.; Dunin-
Borkowski, R. E.; Büchner, B.; Rellinghaus, B.; Lubk, A.
Nature Nanotechnology **2022**, *17*, 250–255,
DOI: [10.1038/s41565-021-01031-x](https://doi.org/10.1038/s41565-021-01031-x).
- (30) Zheng, F.; Rybakov, F. N.; Borisov, A. B.; Song, D.; Wang, S.; Li, Z.-A.; Du, H.;
Kiselev, N. S.; Caron, J.; Kovács, A.; Tian, M.; Zhang, Y.; Blügel, S.; Dunin-
Borkowski, R. E.
Nature Nanotechnology **2018**, *13*, 451–455,
DOI: [10.1038/s41565-018-0093-3](https://doi.org/10.1038/s41565-018-0093-3).
- (31) Grelier, M.; Godel, F.; Vecchiola, A.; Collin, S.; Bouzheouane, K.; Fert, A.; Cros,
V.; Reyren, N.
Nature Communications **2022**, *13*, 6843,
DOI: [10.1038/s41467-022-34370-x](https://doi.org/10.1038/s41467-022-34370-x).
- (32) Gross, R.; Marx, A.,
Festkörperphysik;
De Gruyter Oldenbourg: 2014.

B. References

- (33) Gross, I.; Akhtar, W.; Hrabec, A.; Sampaio, J.; Martínez, L. J.; Chouaieb, S.; Shields, B. J.; Maletinsky, P.; Thiaville, A.; Rohart, S.; Jacques, V. *Physical Review Materials* **2018**, *2*, 024406, DOI: [10.1103/PhysRevMaterials.2.024406](https://doi.org/10.1103/PhysRevMaterials.2.024406).
- (34) Moreno, R.; Evans, R. F. L.; Khmelevskiy, S.; Muñoz, M. C.; Chantrell, R. W.; Chubykalo-Fesenko, O. *Physical Review B* **2016**, *94*, 104433, DOI: [10.1103/PhysRevB.94.104433](https://doi.org/10.1103/PhysRevB.94.104433).
- (35) Jefremovas, E. M.; Leutner, K.; Fischer, M. G.; Marqués-Marchán, J.; Winkler, T. B.; Asenjo, A.; Sinova, J.; Frömter, R.; Kläui, M. *Newton* **2025**, *1*, DOI: [10.1016/j.newton.2025.100036](https://doi.org/10.1016/j.newton.2025.100036).
- (36) Ikeda, S.; Miura, K.; Yamamoto, H.; Mizunuma, K.; Gan, H. D.; Endo, M.; Kanai, S.; Hayakawa, J.; Matsukura, F.; Ohno, H. *Nature Materials* **2010**, *9*, 721–724, DOI: [10.1038/nmat2804](https://doi.org/10.1038/nmat2804).
- (37) Yang, H. X.; Chshiev, M.; Dieny, B.; Lee, J. H.; Manchon, A.; Shin, K. H. *Physical Review B* **2011**, *84*, 054401, DOI: [10.1103/PhysRevB.84.054401](https://doi.org/10.1103/PhysRevB.84.054401).
- (38) Peng, S.; Wang, M.; Yang, H.; Zeng, L.; Nan, J.; Zhou, J.; Zhang, Y.; Hallal, A.; Chshiev, M.; Wang, K. L.; Zhang, Q.; Zhao, W. *Scientific Reports* **2015**, *5*, 18173, DOI: [10.1038/srep18173](https://doi.org/10.1038/srep18173).
- (39) Dieny, B.; Chshiev, M. *Reviews of Modern Physics* **2017**, *89*, 025008, DOI: [10.1103/RevModPhys.89.025008](https://doi.org/10.1103/RevModPhys.89.025008).
- (40) Nakajima, N.; Koide, T.; Shidara, T.; Miyauchi, H.; Fukutani, H.; Fujimori, A.; Iio, K.; Katayama, T.; Nývlt, M.; Suzuki, Y. *Physical Review Letters* **1998**, *81*, 5229–5232, DOI: [10.1103/PhysRevLett.81.5229](https://doi.org/10.1103/PhysRevLett.81.5229).
- (41) Pappas, D. P.; Kämper, K.-P.; Hopster, H. *Physical Review Letters* **1990**, *64*, 3179–3182, DOI: [10.1103/PhysRevLett.64.3179](https://doi.org/10.1103/PhysRevLett.64.3179).
- (42) Callen, H. B.; Callen, E. *Journal of Physics and Chemistry of Solids* **1966**, *27*, 1271–1285, DOI: [10.1016/0022-3697\(66\)90012-6](https://doi.org/10.1016/0022-3697(66)90012-6).
- (43) Rózsa, L.; Atxitia, U.; Nowak, U. *Physical Review B* **2017**, *96*, 094436, DOI: [10.1103/PhysRevB.96.094436](https://doi.org/10.1103/PhysRevB.96.094436).
- (44) Sato, H.; Churemart, P.; Matsukura, F.; Chantrell, R. W.; Ohno, H.; Evans, R. F. L.

- Physical Review B* **2018**, *98*, 214428,
DOI: [10.1103/PhysRevB.98.214428](https://doi.org/10.1103/PhysRevB.98.214428).
- (45) Dzyaloshinsky, I.
Journal of Physics and Chemistry of Solids **1958**, *4*, 241–255,
DOI: [10.1016/0022-3697\(58\)90076-3](https://doi.org/10.1016/0022-3697(58)90076-3).
- (46) Moriya, T.
Physical Review **1960**, *120*, 91–98,
DOI: [10.1103/PhysRev.120.91](https://doi.org/10.1103/PhysRev.120.91).
- (47) Shirane, G.; Cowley, R.; Majkrzak, C.; Sokoloff, J. B.; Pagonis, B.; Perry, C. H.; Ishikawa, Y.
Physical Review B **1983**, *28*, 6251–6255,
DOI: [10.1103/PhysRevB.28.6251](https://doi.org/10.1103/PhysRevB.28.6251).
- (48) Fert, A.; Levy, P. M.
Physical Review Letters **1980**, *44*, 1538–1541,
DOI: [10.1103/PhysRevLett.44.1538](https://doi.org/10.1103/PhysRevLett.44.1538).
- (49) Ma, X.; Yu, G.; Tang, C.; Li, X.; He, C.; Shi, J.; Wang, K. L.; Li, X.
Physical Review Letters **2018**, *120*, 157204,
DOI: [10.1103/PhysRevLett.120.157204](https://doi.org/10.1103/PhysRevLett.120.157204).
- (50) Hasselberg, G.; Yanes, R.; Hinzke, D.; Sessi, P.; Bode, M.; Szunyogh, L.; Nowak, U.
Physical Review B **2015**, *91*, 064402,
DOI: [10.1103/PhysRevB.91.064402](https://doi.org/10.1103/PhysRevB.91.064402).
- (51) Wang, J.; Strungaru, M.; Ruta, S.; Meo, A.; Zhou, Y.; Deák, A.; Szunyogh, L.; Gavriloea, P.-I.; Moreno, R.; Chubykalo-Fesenko, O.; Wu, J.; Xu, Y.; Evans, R. F. L.; Chantrell, R. W.
Physical Review B **2021**, *104*, 054420,
DOI: [10.1103/PhysRevB.104.054420](https://doi.org/10.1103/PhysRevB.104.054420).
- (52) Lemesh, I. et al.
Advanced Materials **2018**, *30*, 1805461,
DOI: [10.1002/adma.201805461](https://doi.org/10.1002/adma.201805461).
- (53) Finazzi, M.; Savoini, M.; Khorsand, A. R.; Tsukamoto, A.; Itoh, A.; Duò, L.; Kirilyuk, A.; Rasing, T.; Ezawa, M.
Physical Review Letters **2013**, *110*, 177205,
DOI: [10.1103/PhysRevLett.110.177205](https://doi.org/10.1103/PhysRevLett.110.177205).
- (54) Je, S.-G.; Vallobra, P.; Srivastava, T.; Rojas-Sánchez, J.-C.; Pham, T. H.; Hehn, M.; Malinowski, G.; Baraduc, C.; Auffret, S.; Gaudin, G.; Mangin, S.; Béa, H.; Boule, O.
Nano Letters **2018**, *18*, 7362–7371,
DOI: [10.1021/acs.nanolett.8b03653](https://doi.org/10.1021/acs.nanolett.8b03653).
- (55) Moreau-Luchaire, C. et al.

- Nature Nanotechnology* **2016**, *11*, 444–448,
DOI: [10.1038/nnano.2015.313](https://doi.org/10.1038/nnano.2015.313).
- (56) Ognev, A. V. et al.
ACS Nano **2020**, *14*, 14960–14970,
DOI: [10.1021/acsnano.0c04748](https://doi.org/10.1021/acsnano.0c04748).
- (57) Leutner, K.; Winkler, T. B.; Gruber, R.; Frömter, R.; Güttinger, J.; Fangohr, H.; Kläui, M.
Physical Review Applied **2023**, *20*, 064021,
DOI: [10.1103/PhysRevApplied.20.064021](https://doi.org/10.1103/PhysRevApplied.20.064021).
- (58) Boulle, O. et al.
Nature Nanotechnology **2016**, *11*, 449–454,
DOI: [10.1038/nnano.2015.315](https://doi.org/10.1038/nnano.2015.315).
- (59) Powalla, L.; Birch, M. T.; Litzius, K.; Wintz, S.; Schulz, F.; Weigand, M.; Scholz, T.; Lotsch, B. V.; Kern, K.; Schütz, G.; Burghard, M.
Nano Letters **2022**, *22*, 9236–9243,
DOI: [10.1021/acs.nanolett.2c01944](https://doi.org/10.1021/acs.nanolett.2c01944).
- (60) Legrand, W.; Maccariello, D.; Reyren, N.; Garcia, K.; Moutafis, C.; Moreau-Luchaire, C.; Collin, S.; Bouzehouane, K.; Cros, V.; Fert, A.
Nano Letters **2017**, *17*, 2703–2712,
DOI: [10.1021/acs.nanolett.7b00649](https://doi.org/10.1021/acs.nanolett.7b00649).
- (61) Büttner, F.; Lemesh, I.; Schneider, M.; Pfau, B.; Günther, C. M.; Hessing, P.; Geilhufe, J.; Caretta, L.; Engel, D.; Krüger, B.; Viefhaus, J.; Eisebitt, S.; Beach, G. S. D.
Nature Nanotechnology **2017**, *12*, 1040–1044,
DOI: [10.1038/nnano.2017.178](https://doi.org/10.1038/nnano.2017.178).
- (62) Jiang, W.; Upadhyaya, P.; Zhang, W.; Yu, G.; Jungfleisch, M. B.; Fradin, F. Y.; Pearson, J. E.; Tserkovnyak, Y.; Wang, K. L.; Heinonen, O.; te Velthuis, S. G. E.; Hoffmann, A.
Science **2015**, *349*, 283–286,
DOI: [10.1126/science.aaa1442](https://doi.org/10.1126/science.aaa1442).
- (63) Kerber, N.; Weißenhofer, M.; Raab, K.; Litzius, K.; Zázvorka, J.; Nowak, U.; Kläui, M.
Physical Review Applied **2021**, *15*, 044029,
DOI: [10.1103/PhysRevApplied.15.044029](https://doi.org/10.1103/PhysRevApplied.15.044029).
- (64) Gruber, R.; Zázvorka, J.; Brems, M. A.; Rodrigues, D. R.; Dohi, T.; Kerber, N.; Seng, B.; Vafaei, M.; Everschor-Sitte, K.; Virnau, P.; Kläui, M.
Nature Communications **2022**, *13*, 3144,
DOI: [10.1038/s41467-022-30743-4](https://doi.org/10.1038/s41467-022-30743-4).
- (65) Stöhr, J.; Siegmann, H. C.,
Magnetism: From Fundamentals to Nanoscale Dynamics;
Solid-State Sciences;

- Springer: Berlin, Heidelberg, 2006,
DOI: [10.1007/978-3-540-30283-4](https://doi.org/10.1007/978-3-540-30283-4).
- (66) Vansteenkiste, A.; Leliaert, J.; Dvornik, M.; Helsen, M.; Garcia-Sanchez, F.; Van Waeyenberge, B.
AIP Advances **2014**, *4*, 107133,
DOI: [10.1063/1.4899186](https://doi.org/10.1063/1.4899186).
- (67) Abert, C.; Exl, L.; Selke, G.; Drews, A.; Schrefl, T.
Journal of Magnetism and Magnetic Materials **2013**, *326*, 176–185,
DOI: [10.1016/j.jmmm.2012.08.041](https://doi.org/10.1016/j.jmmm.2012.08.041).
- (68) Thiele, A. A.
Phys. Rev. Lett. **1972**, *30*, 230–233.
- (69) Lin, S.-Z.; Reichhardt, C.; Batista, C. D.; Saxena, A.
Physical Review B **2013**, *87*, 214419,
DOI: [10.1103/PhysRevB.87.214419](https://doi.org/10.1103/PhysRevB.87.214419).
- (70) Ge, Y.; Rothörl, J.; Brems, M. A.; Kerber, N.; Gruber, R.; Dohi, T.; Kläui, M.; Virnau, P.
Communications Physics **2023**, *6*, 1–6,
DOI: [10.1038/s42005-023-01145-9](https://doi.org/10.1038/s42005-023-01145-9).
- (71) Brems, M. A.; Sparmann, T.; Fröhlich, S. M.; Dany, L.-C.; Rothörl, J.; Kammerbauer, F.; Jefremovas, E. M.; Farago, O.; Kläui, M.; Virnau, P.
Physical Review Letters **2025**, *134*, 046701,
DOI: [10.1103/PhysRevLett.134.046701](https://doi.org/10.1103/PhysRevLett.134.046701).
- (72) Schütte, C.; Iwasaki, J.; Rosch, A.; Nagaosa, N.
Physical Review B **2014**, *90*, 174434,
DOI: [10.1103/PhysRevB.90.174434](https://doi.org/10.1103/PhysRevB.90.174434).
- (73) Loudon, J. C.; Leonov, A. O.; Bogdanov, A. N.; Hatnean, M. C.; Balakrishnan, G.
Physical Review B **2018**, *97*, 134403,
DOI: [10.1103/PhysRevB.97.134403](https://doi.org/10.1103/PhysRevB.97.134403).
- (74) Rózsa, L.; Deák, A.; Simon, E.; Yanes, R.; Udvardi, L.; Szunyogh, L.; Nowak, U.
Physical Review Letters **2016**, *117*, 157205,
DOI: [10.1103/PhysRevLett.117.157205](https://doi.org/10.1103/PhysRevLett.117.157205).
- (75) Du, H.; Zhao, X.; Rybakov, F. N.; Borisov, A. B.; Wang, S.; Tang, J.; Jin, C.; Wang, C.; Wei, W.; Kiselev, N. S.; Zhang, Y.; Che, R.; Blügel, S.; Tian, M.
Physical Review Letters **2018**, *120*, 197203,
DOI: [10.1103/PhysRevLett.120.197203](https://doi.org/10.1103/PhysRevLett.120.197203).
- (76) Lima Fernandes, I.; Bouaziz, J.; Blügel, S.; Lounis, S.
Nature Communications **2018**, *9*, 4395,
DOI: [10.1038/s41467-018-06827-5](https://doi.org/10.1038/s41467-018-06827-5).

B. References

- (77) Arjana, I. G.; Lima Fernandes, I.; Chico, J.; Lounis, S.
Scientific Reports **2020**, *10*, 14655,
DOI: [10.1038/s41598-020-71232-2](https://doi.org/10.1038/s41598-020-71232-2).
- (78) Choi, H. C.; Lin, S.-Z.; Zhu, J.-X.
Physical Review B **2016**, *93*, 115112,
DOI: [10.1103/PhysRevB.93.115112](https://doi.org/10.1103/PhysRevB.93.115112).
- (79) Müller, J.; Rosch, A.
Physical Review B **2015**, *91*, 054410,
DOI: [10.1103/PhysRevB.91.054410](https://doi.org/10.1103/PhysRevB.91.054410).
- (80) Navau, C.; Del-Valle, N.; Sanchez, A.
Journal of Magnetism and Magnetic Materials **2018**, *465*, 709–715,
DOI: [10.1016/j.jmmm.2018.06.044](https://doi.org/10.1016/j.jmmm.2018.06.044).
- (81) Iwasaki, J.; Mochizuki, M.; Nagaosa, N.
Nature Communications **2013**, *4*, 1463,
DOI: [10.1038/ncomms2442](https://doi.org/10.1038/ncomms2442).
- (82) Liu, Y.-H.; Li, Y.-Q.
Journal of Physics: Condensed Matter **2013**, *25*, 076005,
DOI: [10.1088/0953-8984/25/7/076005](https://doi.org/10.1088/0953-8984/25/7/076005).
- (83) Derras-Chouk, A.; Chudnovsky, E. M.
Journal of Physics: Condensed Matter **2021**, *33*, 195802,
DOI: [10.1088/1361-648X/abe351](https://doi.org/10.1088/1361-648X/abe351).
- (84) Raab, K.; Brems, M. A.; Beneke, G.; Dohi, T.; Rothörl, J.; Kammerbauer, F.; Mentink, J. H.; Kläui, M.
Nature Communications **2022**, *13*, 6982,
DOI: [10.1038/s41467-022-34309-2](https://doi.org/10.1038/s41467-022-34309-2).
- (85) Beneke, G.; Winkler, T. B.; Raab, K.; Brems, M. A.; Kammerbauer, F.; Gerhards, P.; Knobloch, K.; Krishnia, S.; Mentink, J. H.; Kläui, M.
Nature Communications **2024**, *15*, 8103,
DOI: [10.1038/s41467-024-52345-y](https://doi.org/10.1038/s41467-024-52345-y).
- (86) Brems, M. A.; Kläui, M.; Virnau, P.
Applied Physics Letters **2021**, *119*, 132405,
DOI: [10.1063/5.0063584](https://doi.org/10.1063/5.0063584).
- (87) Vizarim, N. P.; Reichhardt, C.; Venegas, P. A.; Reichhardt, C. J. O.
Journal of Magnetism and Magnetic Materials **2021**, *528*, 167710,
DOI: [10.1016/j.jmmm.2020.167710](https://doi.org/10.1016/j.jmmm.2020.167710).
- (88) Kern, L.-M. et al.
Nano Letters **2022**, *22*, 4028–4035,
DOI: [10.1021/acs.nanolett.2c00670](https://doi.org/10.1021/acs.nanolett.2c00670).
- (89) Riddiford, L. J.; Brock, J. A.; Murawska, K.; Hrabec, A.; Heyderman, L. J.

- Grayscale control of local magnetic properties with direct-write laser annealing,
arxiv: [2401.09314\[physics\]](https://arxiv.org/abs/2401.09314), 2024,
DOI: [10.48550/arXiv.2401.09314](https://doi.org/10.48550/arXiv.2401.09314).
- (90) Fultz, B.,
Phase Transitions in Materials;
Cambridge University Press: Cambridge, 2014,
DOI: [10.1017/CB09781107589865](https://doi.org/10.1017/CB09781107589865).
- (91) Fossheim, K.; Sudbø, A.,
Superconductivity: Physics and Applications;
John Wiley & Sons, Ltd: Chichester, 2004.
- (92) Von Grünberg, H.-H.; Keim, P.; Maret, G.
In *Soft Matter*;
John Wiley & Sons, Ltd: 2007, pp 41–86,
DOI: [10.1002/9783527682300.ch2](https://doi.org/10.1002/9783527682300.ch2).
- (93) Mermin, N. D.; Wagner, H.
Physical Review Letters **1966**, *17*, 1133–1136,
DOI: [10.1103/PhysRevLett.17.1133](https://doi.org/10.1103/PhysRevLett.17.1133).
- (94) Wagner, H.
Zeitschrift für Physik **1966**, *195*, 273–299,
DOI: [10.1007/BF01325630](https://doi.org/10.1007/BF01325630).
- (95) Kosterlitz, J. M.; Thouless, D. J.
Journal of Physics C: Solid State Physics **1972**, *5*, L124,
DOI: [10.1088/0022-3719/5/11/002](https://doi.org/10.1088/0022-3719/5/11/002).
- (96) Kosterlitz, J. M.; Thouless, D. J.
Journal of Physics C: Solid State Physics **1973**, *6*, 1181,
DOI: [10.1088/0022-3719/6/7/010](https://doi.org/10.1088/0022-3719/6/7/010).
- (97) Halperin, B. I.; Nelson, D. R.
Physical Review Letters **1978**, *41*, 121–124,
DOI: [10.1103/PhysRevLett.41.121](https://doi.org/10.1103/PhysRevLett.41.121).
- (98) Nelson, D. R.; Halperin, B. I.
Physical Review B **1979**, *19*, 2457–2484,
DOI: [10.1103/PhysRevB.19.2457](https://doi.org/10.1103/PhysRevB.19.2457).
- (99) Young, A. P.
Physical Review B **1979**, *19*, 1855–1866,
DOI: [10.1103/PhysRevB.19.1855](https://doi.org/10.1103/PhysRevB.19.1855).
- (100) Kapfer, S. C.; Krauth, W.
Physical Review Letters **2015**, *114*, 035702,
DOI: [10.1103/PhysRevLett.114.035702](https://doi.org/10.1103/PhysRevLett.114.035702).
- (101) Chui, S. T.

- Physical Review B* **1983**, *28*, 178–194,
DOI: [10.1103/PhysRevB.28.178](https://doi.org/10.1103/PhysRevB.28.178).
- (102) Kleinert, H.
Physics Letters A **1983**, *95*, 381–384,
DOI: [10.1016/0375-9601\(83\)90413-9](https://doi.org/10.1016/0375-9601(83)90413-9).
- (103) Glaser, M. A.; Clark, N. A.
In *Advances in Chemical Physics*;
John Wiley & Sons, Ltd: 1992, pp 543–709,
DOI: [10.1002/9780470141410.ch7](https://doi.org/10.1002/9780470141410.ch7).
- (104) Lansac, Y.; Glaser, M. A.; Clark, N. A.
Physical Review E **2006**, *73*, 041501,
DOI: [10.1103/PhysRevE.73.041501](https://doi.org/10.1103/PhysRevE.73.041501).
- (105) Chen, K.; Kaplan, T.; Mostoller, M.
Physical Review Letters **1995**, *74*, 4019–4022,
DOI: [10.1103/PhysRevLett.74.4019](https://doi.org/10.1103/PhysRevLett.74.4019).
- (106) Somer, F. L.; Canright, G. S.; Kaplan, T.; Chen, K.; Mostoller, M.
Physical Review Letters **1997**, *79*, 3431–3434,
DOI: [10.1103/PhysRevLett.79.3431](https://doi.org/10.1103/PhysRevLett.79.3431).
- (107) Jaster, A.
Physical Review E **1999**, *59*, 2594–2602,
DOI: [10.1103/PhysRevE.59.2594](https://doi.org/10.1103/PhysRevE.59.2594).
- (108) Mak, C. H.
Physical Review E **2006**, *73*, 065104,
DOI: [10.1103/PhysRevE.73.065104](https://doi.org/10.1103/PhysRevE.73.065104).
- (109) Lin, S. Z.; Zheng, B.; Trimper, S.
Physical Review E **2006**, *73*, 066106,
DOI: [10.1103/PhysRevE.73.066106](https://doi.org/10.1103/PhysRevE.73.066106).
- (110) Zahn, K.; Maret, G.
Physical Review Letters **2000**, *85*, 3656–3659,
DOI: [10.1103/PhysRevLett.85.3656](https://doi.org/10.1103/PhysRevLett.85.3656).
- (111) Huang, P.; Schönenberger, T.; Cantoni, M.; Heinen, L.; Magrez, A.; Rosch, A.; Carbone, F.; Rønnow, H. M.
Nature Nanotechnology **2020**, *15*, 761–767,
DOI: [10.1038/s41565-020-0716-3](https://doi.org/10.1038/s41565-020-0716-3).
- (112) Zázvorka, J.; Dittrich, F.; Ge, Y.; Kerber, N.; Raab, K.; Winkler, T.; Litzius, K.; Veis, M.; Virnau, P.; Kläui, M.
Advanced Functional Materials **2020**, *30*, 2004037,
DOI: [10.1002/adfm.202004037](https://doi.org/10.1002/adfm.202004037).

B. References

- (113) Meisenheimer, P.; Zhang, H.; Raftrey, D.; Chen, X.; Shao, Y.-T.; Chan, Y.-T.; Yalisove, R.; Chen, R.; Yao, J.; Scott, M. C.; Wu, W.; Muller, D. A.; Fischer, P.; Birgeneau, R. J.; Ramesh, R.
Nature Communications **2023**, *14*, 3744,
DOI: [10.1038/s41467-023-39442-0](https://doi.org/10.1038/s41467-023-39442-0).
- (114) Birch, M. T. et al.
Nature Communications **2020**, *11*, 1726,
DOI: [10.1038/s41467-020-15474-8](https://doi.org/10.1038/s41467-020-15474-8).
- (115) Nakajima, T.; Oike, H.; Kikkawa, A.; Gilbert, E. P.; Booth, N.; Kakurai, K.; Taguchi, Y.; Tokura, Y.; Kagawa, F.; Arima, T.-h.
Science Advances **2017**, *3*, e1602562,
DOI: [10.1126/sciadv.1602562](https://doi.org/10.1126/sciadv.1602562).
- (116) Qian, F.; Bannenberg, L. J.; Wilhelm, H.; Chaboussant, G.; Debeer-Schmitt, L. M.; Schmidt, M. P.; Aqeel, A.; Palstra, T. T. M.; Brück, E.; Lefering, A. J. E.; Pappas, C.; Mostovoy, M.; Leonov, A. O.
Science Advances **2018**, *4*, eaat7323,
DOI: [10.1126/sciadv.aat7323](https://doi.org/10.1126/sciadv.aat7323).
- (117) Zeissler, K.; Finizio, S.; Barton, C.; Huxtable, A. J.; Massey, J.; Raabe, J.; Sadovnikov, A. V.; Nikitov, S. A.; Brearton, R.; Hesjedal, T.; van der Laan, G.; Rosamond, M. C.; Linfield, E. H.; Burnell, G.; Marrows, C. H.
Nature Communications **2020**, *11*, 428,
DOI: [10.1038/s41467-019-14232-9](https://doi.org/10.1038/s41467-019-14232-9).
- (118) Zivieri, R.; Tomasello, R.; Chubykalo-Fesenko, O.; Tiberkevich, V.; Carpentieri, M.; Finocchio, G.
Physical Review B **2019**, *99*, 174440,
DOI: [10.1103/PhysRevB.99.174440](https://doi.org/10.1103/PhysRevB.99.174440).
- (119) Deuschländer, S.; Horn, T.; Löwen, H.; Maret, G.; Keim, P.
Physical Review Letters **2013**, *111*, 098301,
DOI: [10.1103/PhysRevLett.111.098301](https://doi.org/10.1103/PhysRevLett.111.098301).
- (120) Rothörl, J.
Particle-based computer simulations of magnetic skyrmions,
Ph.D. Thesis, Mainz: Johannes Gutenberg-Universität Mainz, 2024.
- (121) Guillamón, I.; Suderow, H.; Fernández-Pacheco, A.; Sesé, J.; Córdoba, R.; De Teresa, J. M.; Ibarra, M. R.; Vieira, S.
Nature Physics **2009**, *5*, 651–655,
DOI: [10.1038/nphys1368](https://doi.org/10.1038/nphys1368).
- (122) Roy, I.; Dutta, S.; Roy Choudhury, A. N.; Basistha, S.; Maccari, I.; Mandal, S.; Jesudasan, J.; Bagwe, V.; Castellani, C.; Benfatto, L.; Raychaudhuri, P.
Physical Review Letters **2019**, *122*, 047001,
DOI: [10.1103/PhysRevLett.122.047001](https://doi.org/10.1103/PhysRevLett.122.047001).

- (123) Sharma, R.; Rey, D.; Longchambon, L.; Perrin, A.; Perrin, H.; Dubessy, R. *Physical Review Letters* **2024**, *133*, 143401, DOI: [10.1103/PhysRevLett.133.143401](https://doi.org/10.1103/PhysRevLett.133.143401).
- (124) Zahn, K.; Lenke, R.; Maret, G. *Physical Review Letters* **1999**, *82*, 2721–2724, DOI: [10.1103/PhysRevLett.82.2721](https://doi.org/10.1103/PhysRevLett.82.2721).
- (125) Thorneywork, A. L.; Abbott, J. L.; Aarts, D. G. A. L.; Dullens, R. P. A. *Physical Review Letters* **2017**, *118*, 158001, DOI: [10.1103/PhysRevLett.118.158001](https://doi.org/10.1103/PhysRevLett.118.158001).
- (126) *Magnetic Microscopy of Nanostructures*; Hopster, H., Oepen, H. P., Eds.; NanoScience and Technology; Springer-Verlag: Berlin Heidelberg, 2005, DOI: [10.1007/b137837](https://doi.org/10.1007/b137837).
- (127) Oppeneer, P., *Theory of the Magneto-Optical Kerr Effect in Ferromagnetic Compounds*, 1999, DOI: [10.13140/2.1.3171.4083](https://doi.org/10.13140/2.1.3171.4083).
- (128) Soldatov, I. V.; Schäfer, R. *Physical Review B* **2017**, *95*, 014426, DOI: [10.1103/PhysRevB.95.014426](https://doi.org/10.1103/PhysRevB.95.014426).
- (129) Evico magnetics GmbH
Standard Magneto-Optical Kerr Microscope,
User Manual, Dresden: evico magnetics GmbH.
- (130) Soldatov, I. V.; Schäfer, R. *Review of Scientific Instruments* **2017**, *88*, 073701, DOI: [10.1063/1.4991820](https://doi.org/10.1063/1.4991820).
- (131) Allan, D. B.; Caswell, T.; Keim, N. C.; van der Wel, C. M. trackpy: Trackpy v0.4.1, 2018, DOI: [10.5281/zenodo.1226458](https://doi.org/10.5281/zenodo.1226458).
- (132) Allan, D. B.; Caswell, T.; Keim, N. C.; van der Wel, C. M.; Verweij, R. W. soft-matter/trackpy: v0.6.4, 2024, DOI: [10.5281/zenodo.12708864](https://doi.org/10.5281/zenodo.12708864).
- (133) Labrie-Boulay, I.; Winkler, T. B.; Franzen, D.; Romanova, A.; Fangohr, H.; Kläui, M. *Physical Review Applied* **2024**, *21*, 014014, DOI: [10.1103/PhysRevApplied.21.014014](https://doi.org/10.1103/PhysRevApplied.21.014014).
- (134) *Handbook of Sputter Deposition Technology*;

- Wasa, K., Kanno, I., Kotera, H., Eds.;
William Andrew Publishing: Oxford, 2012,
DOI: [10.1016/B978-1-4377-3483-6.00010-3](https://doi.org/10.1016/B978-1-4377-3483-6.00010-3).
- (135) *Handbook of Thin Film Deposition*;
Seshan, K., Ed.;
William Andrew Publishing: Oxford, 2012,
DOI: [10.1016/B978-1-4377-7873-1.00012-7](https://doi.org/10.1016/B978-1-4377-7873-1.00012-7).
- (136) Greene, J. E.
Journal of Vacuum Science & Technology A **2017**, *35*, 05C204,
DOI: [10.1116/1.4998940](https://doi.org/10.1116/1.4998940).
- (137) Schepis, D.; Seshan, K.,
Handbook of Thin Film Deposition,
2024.
- (138) Bhatnagar-Schöffmann, T. et al.
Applied Physics Letters **2023**, *122*, 042402,
DOI: [10.1063/5.0132870](https://doi.org/10.1063/5.0132870).
- (139) Geissler, M.; Xia, Y.
Advanced Materials **2004**, *16*, 1249–1269,
DOI: [10.1002/adma.200400835](https://doi.org/10.1002/adma.200400835).
- (140) Gruber, R.
Thermal Dynamics and Ordering of 2D Magnetic Skyrmions,
Master Thesis, Mainz: Johannes Gutenberg-Universität Mainz, 2021.
- (141) Büttner, F. et al.
Nature Physics **2015**, *11*, 225–228,
DOI: [10.1038/nphys3234](https://doi.org/10.1038/nphys3234).
- (142) Tipler, P. A.; Mosca, G.,
Tipler Physik: für Studierende der Naturwissenschaften und Technik;
Kersten, P., Ed.;
Springer: Berlin, Heidelberg, 2024,
DOI: [10.1007/978-3-662-67936-4](https://doi.org/10.1007/978-3-662-67936-4).
- (143) Lonsky, M.; Hoffmann, A.
APL Materials **2020**, *8*, 100903,
DOI: [10.1063/5.0027042](https://doi.org/10.1063/5.0027042).
- (144) Klose, C. et al.
Nature **2023**, *614*, 256–261,
DOI: [10.1038/s41586-022-05537-9](https://doi.org/10.1038/s41586-022-05537-9).
- (145) Klose, C.; Büttner, F.; Hu, W.; Mazzoli, C.; Beach, G. S. D.; Eisebitt, S.; Pfau, B.
Physical Review B **2022**, *105*, 214425,
DOI: [10.1103/PhysRevB.105.214425](https://doi.org/10.1103/PhysRevB.105.214425).
- (146) GmbH, S.

- Three-Axis Fluxgate Magnetometer,
User Manual, Bad Saarow: SENSYS GmbH.
- (147) Kalz, E.; Vuijk, H. D.; Abdoli, I.; Sommer, J.-U.; Löwen, H.; Sharma, A.
Physical Review Letters **2022**, *129*, 090601,
DOI: [10.1103/PhysRevLett.129.090601](https://doi.org/10.1103/PhysRevLett.129.090601).
- (148) Schwenke, P.; Spindler, E.; Vasyuchka, V. I.; Hamadeh, A. A.; Pirro, P.; Weiler, M.
Ratchet motion of magnetic skyrmions driven by surface acoustic sawtooth waves,
arxiv: [2503.09506](https://arxiv.org/abs/2503.09506) [cond-mat], 2025,
DOI: [10.48550/arXiv.2503.09506](https://doi.org/10.48550/arXiv.2503.09506).
- (149) Koshelev, A. E.; Vinokur, V. M.
Physical Review Letters **1994**, *73*, 3580–3583,
DOI: [10.1103/PhysRevLett.73.3580](https://doi.org/10.1103/PhysRevLett.73.3580).
- (150) Blatter, G.; Feigel'man, M. V.; Geshkenbein, V. B.; Larkin, A. I.; Vinokur, V. M.
Reviews of Modern Physics **1994**, *66*, 1125–1388,
DOI: [10.1103/RevModPhys.66.1125](https://doi.org/10.1103/RevModPhys.66.1125).
- (151) Valenzuela, S. O.; Bekeris, V.
Physical Review Letters **2001**, *86*, 504–507,
DOI: [10.1103/PhysRevLett.86.504](https://doi.org/10.1103/PhysRevLett.86.504).
- (152) Valenzuela, S. O.
Physical Review Letters **2002**, *88*, 247003,
DOI: [10.1103/PhysRevLett.88.247003](https://doi.org/10.1103/PhysRevLett.88.247003).
- (153) Kaji, T.; Maegochi, S.; Ienaga, K.; Kaneko, S.; Okuma, S.
Scientific Reports **2022**, *12*, 1542,
DOI: [10.1038/s41598-022-05504-4](https://doi.org/10.1038/s41598-022-05504-4).
- (154) Han, Y.; Ha, N. Y.; Alsayed, A. M.; Yodh, A. G.
Physical Review E **2008**, *77*, 041406,
DOI: [10.1103/PhysRevE.77.041406](https://doi.org/10.1103/PhysRevE.77.041406).
- (155) Seshadri, R.; Westervelt, R. M.
Physical Review B **1992**, *46*, 5150–5161,
DOI: [10.1103/PhysRevB.46.5150](https://doi.org/10.1103/PhysRevB.46.5150).
- (156) Goto, M.; Nomura, H.; Suzuki, Y.
Journal of Magnetism and Magnetic Materials **2021**, 167974,
DOI: [10.1016/j.jmmm.2021.167974](https://doi.org/10.1016/j.jmmm.2021.167974).
- (157) Qin, G.; Zhang, R.; Yang, C.; Lv, X.; Pei, K.; Yang, L.; Liu, X.; Zhang, X.; Che, R.
ACS Nano **2022**, *16*, 15927–15934,
DOI: [10.1021/acsnano.2c03046](https://doi.org/10.1021/acsnano.2c03046).
- (158) CARPi, N.; Minges, A.; Piel, M.
Journal of Open Source Software **2017**, *2*, 146,

- DOI: [10.21105/joss.00146](https://doi.org/10.21105/joss.00146).
- (159) Rohart, S.; Thiaville, A.
Physical Review B **2013**, *88*, 184422,
DOI: [10.1103/PhysRevB.88.184422](https://doi.org/10.1103/PhysRevB.88.184422).
- (160) Du, H.; Che, R.; Kong, L.; Zhao, X.; Jin, C.; Wang, C.; Yang, J.; Ning, W.; Li, R.; Jin, C.; Chen, X.; Zang, J.; Zhang, Y.; Tian, M.
Nature Communications **2015**, *6*, 8504,
DOI: [10.1038/ncomms9504](https://doi.org/10.1038/ncomms9504).
- (161) Diguët, G.; Ducharne, B.; El Hog, S.; Kato, F.; Koibuchi, H.; Uchimoto, T.; Diep, H. T.
Journal of Magnetism and Magnetic Materials **2023**, *579*, 170819,
DOI: [10.1016/j.jmmm.2023.170819](https://doi.org/10.1016/j.jmmm.2023.170819).
- (162) Finney, J. L.; Bernal, J. D.
Proceedings of the Royal Society of London. A. Mathematical and Physical Sciences **1997**, *319*, 479–493,
DOI: [10.1098/rspa.1970.0189](https://doi.org/10.1098/rspa.1970.0189).
- (163) Gruber, R.; Rothörl, J.; Fröhlich, S. M.; Brems, M. A.; Kammerbauer, F.; Syskaki, M.-A.; Jefremovas, E. M.; Krishnia, S.; Sudbø, A.; Virnau, P.; Kläui, M.
Imaging Topological Defect Dynamics Mediating 2D Skyrmion Lattice Melting,
arxiv: [2501.13151](https://arxiv.org/abs/2501.13151) [cond-mat], 2025,
DOI: [10.48550/arXiv.2501.13151](https://doi.org/10.48550/arXiv.2501.13151).
- (164) Pertsinidis, A.; Ling, X. S.
Nature **2001**, *413*, 147–150,
DOI: [10.1038/35093077](https://doi.org/10.1038/35093077).
- (165) Libál, A.; Reichhardt, C.; Reichhardt, C. J. O.
Physical Review E **2007**, *75*, 011403,
DOI: [10.1103/PhysRevE.75.011403](https://doi.org/10.1103/PhysRevE.75.011403).
- (166) Russell, E. R.; Spaepen, F.; Weitz, D. A.
Physical Review E **2015**, *91*, 032310,
DOI: [10.1103/PhysRevE.91.032310](https://doi.org/10.1103/PhysRevE.91.032310).
- (167) Rucker, F.; Bezvershenko, A.; Mettus, D.; Bauer, A.; Garst, M.; Rosch, A.; Pfeleiderer, C.
Shaking and pushing skyrmions: Formation of a non-equilibrium phase with zero critical current,
arxiv: [2504.01133](https://arxiv.org/abs/2504.01133) [cond-mat], 2025,
DOI: [10.48550/arXiv.2504.01133](https://doi.org/10.48550/arXiv.2504.01133).
- (168) Schall, P.; Weitz, D. A.; Spaepen, F.
Science **2007**, *318*, 1895–1899,
DOI: [10.1126/science.1149308](https://doi.org/10.1126/science.1149308).

- (169) Guillaumon, I.; Córdoba, R.; Sesé, J.; De Teresa, J. M.; Ibarra, M. R.; Vieira, S.; Suderow, H.
Nature Physics **2014**, *10*, 851–856,
DOI: [10.1038/nphys3132](https://doi.org/10.1038/nphys3132).
- (170) Schick, D.; Weißenhofer, M.; Rózsa, L.; Rothörl, J.; Virnau, P.; Nowak, U.
Physical Review Research **2024**, *6*, 013097,
DOI: [10.1103/PhysRevResearch.6.013097](https://doi.org/10.1103/PhysRevResearch.6.013097).
- (171) Gruber, R.; Rothörl, J.; Fröhlich, S. M.; Brems, M. A.; Sparmann, T.; Kammerbauer, F.; Syskaki, M.-A.; Jefremovas, E. M.; Krishnia, S.; Sudbø, A.; Virnau, P.; Kläui, M.
Skyrmion Lattice Domain Formation in a Non-Flat Energy Landscape,
arxiv: [2508.12988](https://arxiv.org/abs/2508.12988) [cond-mat], 2025,
DOI: [10.48550/arXiv.2508.12988](https://doi.org/10.48550/arXiv.2508.12988).
- (172) Fert, A.; Cros, V.; Sampaio, J.
Nature Nanotechnology **2013**, *8*, 152–156,
DOI: [10.1038/nnano.2013.29](https://doi.org/10.1038/nnano.2013.29).
- (173) Gruber, R.; Rothörl, J.; Fröhlich, S. M.; Brems, M. A.; Kammerbauer, F.; Syskaki, M.-A.; Jefremovas, E. M.; Krishnia, S.; Sudbø, A.; Virnau, P.; Kläui, M.
Nature Nanotechnology **2025**, 1–7,
DOI: [10.1038/s41565-025-01977-2](https://doi.org/10.1038/s41565-025-01977-2).
- (174) OpenAI et al.
GPT-4o System Card,
arxiv: [2410.21276](https://arxiv.org/abs/2410.21276) [cs], 2024,
DOI: [10.48550/arXiv.2410.21276](https://doi.org/10.48550/arXiv.2410.21276).
- (175) Gruber, R.; Rothörl, J.; Fröhlich, S. M.; Brems, M. A.; Kammerbauer, F.; Syskaki, M.-A.; Jefremovas, E. M.; Krishnia, S.; Sudbø, A.; Virnau, P.; Kläui, M.
Skyrmion Lattice Order Controlled by Confinement Geometry,
arxiv: [2508.15758](https://arxiv.org/abs/2508.15758) [cond-mat], 2025,
DOI: [10.48550/arXiv.2508.15758](https://doi.org/10.48550/arXiv.2508.15758).
- (176) Guo, Z.; Gruber, R.; Ksenzov, D.; Léveillé, C.; Pancaldi, M.; Pedersoli, E.; Spezzani, C.; De Ninno, G.; Capotondi, F.; Gutt, C.; Kläui, M.; Cros, V.; Reyren, N.; Jaouen, N.
Physical Review B **2025**, *112*, L020408,
DOI: [10.1103/1f11-n7dc](https://doi.org/10.1103/1f11-n7dc).

B.1. List of Acronyms

AFM	antiferromagnet
DMI	Dzyaloshinskii-Moriya interaction
DW	domain wall
EBL	electron beam lithography
FIB	focused ion beam
FM	ferromagnet
IBI	iterative Boltzmann inversion
iDMI	interfacial DMI
IP	in-plane
KTHNY	Kosterlitz-Thouless-Halperin-Nelson-Young
LL	Landau-Lifshitz
LLG	Landau-Lifshitz-Gilbert
LTEM	Lorentz transmission electron microscopy
MFM	magnetic force microscopy
MOKE	magneto-optical Kerr effect
MSD	mean squared displacement
OOP	out-of-plane
PMA	perpendicular magnetic anisotropy
QLRO	quasi-long-range order
SOC	spin-orbit coupling
SRT	spin reorientation transition

B.2. List of Figures

1.1. Chiral Domain Walls between OOP Domains	8
1.2. Magnetic Skyrmions	9
1.3. Different Skyrmion Sizes	10
1.4. Magnetic Exchange Coupling	12
1.5. Flux Closure State	15
1.6. Magnetization Alignment with External Field	17
2.1. Illustration of Dislocations	28
2.2. Illustration of Disclinations	29
2.3. Hexagonal Lattice Order	30
2.4. Strained Lattices	32
3.1. Magneto-Optical Kerr Effect	39
3.2. Schematic of a Kerr Microscope	40
3.3. Beam Path of the <i>evico</i> Kerr Microscope	41
5.1. Temperature Dependence of the Hysteresis Loop	82
5.2. Kerr Snapshots of Diffusing Skyrmions	84
5.3. Diffusion of Sparse Skyrmions in MAS763	86
5.4. Diffusion of Dense Skyrmions in MAS763	87
5.5. Detection of Diffusing Skyrmions	88
5.6. Parameter Variation for Detection of Diffusing Skyrmions	89
5.7. MSD for Varying AC Field Amplitude	90
5.8. MSD with Sliding-Window Analysis	91
5.9. Time Series of MSD and Diffusion Coefficient	92
5.10. Transmission of AC Currents in the Field Coil	93
5.11. Calibration of Coil Field Strength	94
8.1. Hysteresis Map	119
8.2. Kerr Microscopy Snapshots of Skyrmion Lattices	120
8.3. Skyrmion Lattice Statistics	121
9.1. Pattern Map of Sample FAB435p	137
9.2. Skyrmion Lattice in Triangular Confinement	138
9.3. Skyrmion Lattices in a Smaller Hexagon	140
9.4. Confinement Masking and Edge Detection	141
10.1. Kerr Images of Skyrmion Lattices	171
10.2. Skyrmion Detection Comparison	173
10.3. Effect of Vacancies and Interstitials on Lattice Order	174
10.4. G_T for Variations in the Reciprocal Lattice Vector	175

10.5. Bond Angles and Lengths of Neighbor Connections	176
10.6. Histogram of Skyrmion & Defect Occurrences	177
10.7. Measuring the Dislocation Diffusion	179
10.8. Time-Correlation of Topological Defect Occurrences	180
10.9. Reference Lattice Fit	181
10.10 Shear Energy Distribution	183
10.11 Melting by Skyrmion Shrinking under Field Excitation	185
10.12 Maps of Fluctuating Lattice Defects under Field Excitation	186
10.13 Formation of Spiral Magnetic Domains	187
C.1. Coloring of 3D Magnetization	214
C.2. Shear Fit with Statistics Cutoff	215
C.3. Shear Fit with Low-Energy Cutoff	216

C. Appendix

C.1. Additional Data

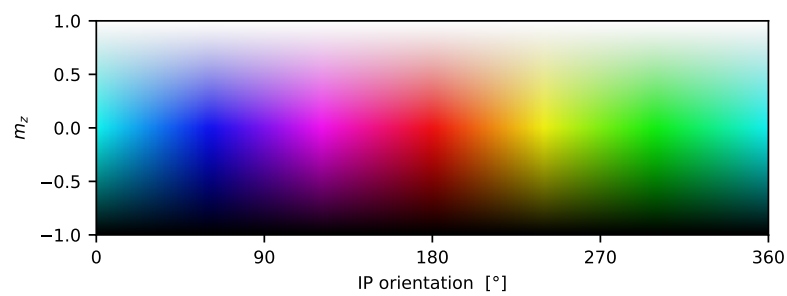


Figure C.1.: Coloring of 3D Magnetization. The color represents the IP orientation, the (color) saturation the IP magnitude and the lightness the OOP magnitude m_z of the magnetization.

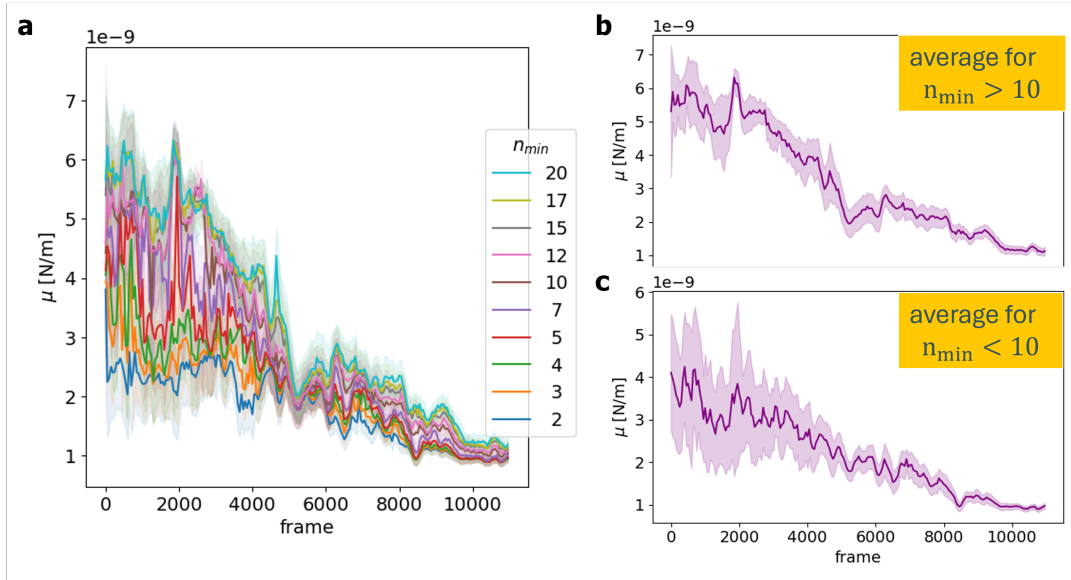


Figure C.2.: Shear Fit with Statistics Cutoff. (a) The cutoff n_{\min} sets a upper limit of the fit range, where the occurrences in the $10^8 \mu k_B T$ energy bins falls below n_{\min} . Note that the shear energies E_{shear} depends still on the shear modulus μ and is therefore not a true energy but a measure for the energy. For different cutoff values (different colors), the fit yields different values of μ . (b) Requiring a larger $n_{\min} > 10$ as minimum statistics causes a shorter fit range and yields robust results. (c) Choosing smaller cutoffs $n_{\min} < 10$ for the occurrences leads to larger fit ranges, which pick up noise at high energies, leading to an unstable fit. Data is shown as single-frame values and the rolling mean over 6.25 s.

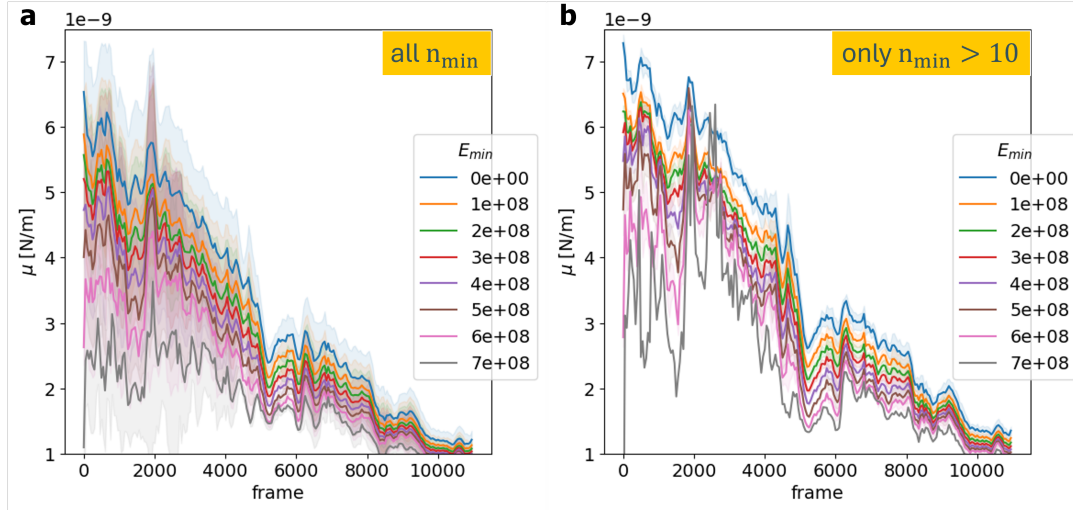


Figure C.3.: Shear Fit with Low-Energy Cutoff. (a) Introducing an energy cutoff E_{\min} determining the start of the fit range affects the resulting shear modulus μ . For smaller cutoffs, the peak at very low energies has an increasing influence, leading to larger values μ . (b) Taking into account the choice of the statistics cutoff $n_{\min} > 10$ as determined in Fig. C.2, the fit becomes more robust, especially for $1 < E_{\min}[10^8 \mu k_B T] < 6$. Data is shown as single-frame values and the rolling mean over 6.25 s. Note that the shear energies E_{shear} depends still on the shear modulus μ and is therefore not a true energy but a measure for the energy.

C.2. Code Availability

I have written Python scripts to detect and analyze skyrmion positions and trajectories, which are available for lab members as repositories on *eLabFTW* (📖 labbook database ID [7913](#)).

I have listed all measurements with their respective parameters for both experiments and data analysis in tables, which are also available for lab members on *eLabFTW* (📖 labbook database ID [7974](#)).

C.3. Use of Large Language Models

Writing this thesis, I have used large language models (between June and August 2025) as described in the following.

I have written a draft of all texts myself. I then used *GPT-4o* [174] to improve the writing style. I have only used the following prompt:

Prompt

Review the following paragraph for coherence and cohesion and to fit the integrity and style of a PhD thesis. The section [*serves as introduction to skyrmion stabilization*]. Keep the \LaTeX -code and referencing in your revised version, be especially careful to format subscripts " $_[\dots]$ " and spacings " $\backslash,$ " correctly and format hyphens as "-". The formatting functions " $\backslash\mathbf{}$ " and " $\backslash\mathrm{}$ " are custom-defined, you can keep them. All acronyms used with " $\backslash\mathrm{ac}$ " are predefined and should not be written in the full form.

[*INPUT PARAGRAPH*]

As indicated by the square brackets and the *italic* formatting, I provide a short description of the input type (in the presented example: "*introduction to skyrmion stabilization*") as well as my draft of the paragraph (here: stylized as "*INPUT PARAGRAPH*") within the single prompt.

Additionally, I used *GPT-4o* [174] to help with the formatting of this \LaTeX document. Example prompts are:

Prompt

When referencing preprints: How can I make sure the preprint server as well as the ArXiv ID are shown in the list of references using chem-acs and biber?

or

Prompt

How can I set the font of figure captions to sans-serif, figure label as bold, and the caption as left-aligned in plain (not hanging) format

In one case, I have asked *GPT-4o* [174] to suggest literature references for an effect that I have experienced (but that I have not found in publications on my own) with the following prompt:

Prompt

I stabilize magnetic skyrmions in thin film multilayer stacks. I experience that the spin reorientation transition is shifted to higher temperatures when geometric confinements

are introduced, and when the confinements become smaller. What is an appropriate (EXISTING!) reference to cite?

For the contribution to *The 2026 Skyrmionics Roadmap* shown in chapter 7, I generated an initial suggestion for the roadmap article using *GPT-4o* [174] with the following prompt:

Prompt

Write 1100 words for a contribution to the "Skyrmionics Roadmap 2026" on the topic of 2D skyrmion lattice phases. It should have three sections: Introduction, Relevance, Challenges

Since the output was mainly based on static skyrmion lattices and host materials, I used the output as basis only to develop the roadmap article. I ran the following command to improve the syntax:

Prompt

Based on your suggestion and my expertise, I have created the following text. Please review for coherence and cohesion, to fit the integrity of a review article.

For the Python code used for the data analysis, I have only used *GPT-4o* [174] for small optimizations and adjustments starting in June 2025. The vast majority of the code was however developed without using large language models. An example prompt that I have used is:

Prompt

How can i reduce the filesize of a 340*370 px black-white video with 11000 frames from 330 MB to 30 MB? I suggest using ffmpeg.
I have 16 fps and want to keep the framerate.
The video format is mp4. I would like to try libx264 encoding but still stay with 30 MB.

The German version of the Abstract is based on a translation of the English version using the AI chat of the Johannes Gutenberg-Universität Mainz (model *GPT OSS 120B*).

C.4. List of Publications with my Contribution

- **Skyrmion pinning energetics in thin film systems**
Raphael Gruber, Jakub Zázvorka, Maarten A. Brems, Davi R. Rodrigues, Takaaki Dohi, Nico Kerber, Boris Seng, Mehran Vafaei, Karin Everschor-Sitte, Peter Virnau & Mathias Kläui
Nature Communications **13**, 3144 (2022). DOI: [10.1038/s41467-022-30743-4](https://doi.org/10.1038/s41467-022-30743-4)
- **Constructing coarse-grained skyrmion potentials from experimental data with Iterative Boltzmann Inversion**
Yuqing Ge, Jan Rothörl, Maarten A. Brems, Nico Kerber, Raphael Gruber, Takaaki Dohi, Mathias Kläui & Peter Virnau
Communications Physics **6**, 30 (2023). DOI: [10.1038/s42005-023-01145-9](https://doi.org/10.1038/s42005-023-01145-9)
- **300-Times-Increased Diffusive Skyrmion Dynamics and Effective Pinning Reduction by Periodic Field Excitation**
Raphael Gruber, Maarten A. Brems, Jan Rothörl, Tobias Sparmann, Maurice Schmitt, Iryna Kononenko, Fabian Kammerbauer, Maria-Andromachi Syskaki, Oded Farago, Peter Virnau & Mathias Kläui
Advanced Materials **35**(17), 2208922 (2025). DOI: [10.1002/adma.202208922](https://doi.org/10.1002/adma.202208922)
- **Skyrmion automotion and readout in confined counter-sensor device geometries**
Kilian Leutner, Thomas Brian Winkler, Raphael Gruber, Robert Frömter, Johannes Güttinger, Hans Fangohr & Mathias Kläui
Physical Review Applied **20**, 064021 (2023). DOI: [10.1103/PhysRevApplied.20.064021](https://doi.org/10.1103/PhysRevApplied.20.064021)
- **Ultrafast dynamics of chiral spin structures in synthetic antiferromagnets**
Zongxia Guo, Raphael Gruber, Dmitriy Ksenzov, Cyril Léveillé, Matteo Pancaldi, Emanuele Pedersoli, Carlo Spezzani, Giovanni De Ninno, Flavio Capotondi, Christian Gutt, Mathias Kläui, Vincent Cros, Nicolas Reyren, & Nicolas Jaouen
Physical Review B **112**, L020408 (2025). DOI: [10.1103/1f11-n7dc](https://doi.org/10.1103/1f11-n7dc)
- **Persistent Homology-Based Indicator of Orientational Ordering in Two-Dimensional Quasi-Particle Systems Applied to Skyrmion Lattices**
Michiki Taniwaki, Thomas Brian Winkler, Jan Rothörl, Raphael Gruber, Chi-haru Mitsumata, Masato Kotsugi & Mathias Kläui
arXiv **2504**, 14688 (2025). DOI: [10.48550/arXiv.2504.14688](https://doi.org/10.48550/arXiv.2504.14688)

- **Real-Time Observation of Topological Defect Dynamics Mediating 2D Skyrmion Lattice Melting**
Raphael Gruber, Jan Rothörl, Simon M. Fröhlich, Maarten A. Brems, Fabian Kammerbauer, Maria-Andromachi Syskaki, Elizabeth M. Jefremovas, Sachin Krishnia, Asle Sudbø, Peter Virnau & Mathias Kläui
Nature Nanotechnology **20**, 1405-1411 (2025). DOI: [10.1038/s41565-025-01977-2](https://doi.org/10.1038/s41565-025-01977-2)
- **Skyrmion Lattice Order Controlled by Confinement Geometry**
Raphael Gruber, Jan Rothörl, Simon M. Fröhlich, Maarten A. Brems, Fabian Kammerbauer, Maria-Andromachi Syskaki, Elizabeth M. Jefremovas, Sachin Krishnia, Asle Sudbø, Peter Virnau & Mathias Kläui
Applied Physics Letters **127**, 212403 (2025). DOI: [10.1063/5.0299901](https://doi.org/10.1063/5.0299901)
- **Skyrmion Lattice Domain Formation in a Non-Flat Energy Landscape**
Raphael Gruber, Simon M. Fröhlich, Jan Rothörl, Maarten A. Brems, Tobias Sparmann, Fabian Kammerbauer, Maria-Andromachi Syskaki, Elizabeth M. Jefremovas, Sachin Krishnia, Asle Sudbø, Peter Virnau & Mathias Kläui
Communications Physics **9**, 29 (2026). DOI: [10.1038/s42005-025-02462-x](https://doi.org/10.1038/s42005-025-02462-x)
- **The 2026 Skyrmionics Roadmap**
Sabri Koraltan, Claas Abert, Manfred Albrecht, Maria Azhar, Christian Back, H el ene B ea, Max T. Birch, Stefan Bl ugel, Olivier Boule, Felix B uttner, Ping Che, Vincent Cros, Emily Darwin, Louise Desplat, Claire Donnelly, Haifeng Du, Karin Everschor-Sitte, Amalio Fern andez-Pacheco, Simone Finizio, Giovanni Finocchio, Markus Garst, Raphael Gruber, Dirk Grundler, Satoru Hayami, Thorsten Hesjedal, Axel Hoffmann, Aleř Hrabec, Hans Josef Hug, Hariom Jani, Jagannath Jena, Wanjun Jiang, Javier Junquera, Kosuke Karube, Lisa-Marie Kern, Joo-Von Kim, Mathias Kl aui, Hidekazu Kurebayashi, Kai Litzius, Yizhou Liu, Martin Lonsky, Christopher H. Marrows, Jan Masell, Stefan Mathias, Yuriy Mokrousov, Stuart S. P. Parkin, Bastian Pfau, Paolo G. Radaelli, Florin Radu, Ramamoorthy Ramesh, Nicolas Reyren, Stanislas Rohart, Shinichiro Seki, Ivan I. Smalyukh, Sopheak Sorn, Daniel Steil, Dieter Suess, Mykola Tasinkevych, Yoshinori Tokura, Riccardo Tomasello, Victor Ukleev, Hyunsoo Yang, Fehmi Sami Yasin, Xiuzhen Yu, Chenhui Zhang, Shilei Zhang, Le Zhao & Sebastian Wintz
arXiv **2601**, 16575 (2026). DOI: [10.48550/arXiv.2601.16575](https://doi.org/10.48550/arXiv.2601.16575)

C.5. Acknowledgements

Curriculum Vitae



JOHANNES GUTENBERG
UNIVERSITÄT MAINZ

